DEVELOPMENT OF A THIN FILM PRIMARY SURFACE HEAT EXCHANGER FOR ADVANCED POWER CYCLES

FINAL SCIENTIFIC/TECHNICAL REPORT

Overall Project Period 10/1/14 – 3/31/16
DOE Award No. DE-FE0024104
SwRI® Project No. 18.20746 / SwRI DUNS No. 00-793-6842

Prepared by:

Tim Allison, Ph.D.
(PI Contact: tim.allison@swri.org / 210-522-3561)
Griffin Beck
Jeffrey Bennett
Kevin Hoopes
Larry Miller

Prepared for:

U.S. Department of Energy
National Energy Technology Laboratory
626 Cochrans Mill Road
P.O. Box 10940
Pittsburgh, PA 15236-0940

June 29, 2016

SOUTHWEST RESEARCH INSTITUTE®
6220 Culebra Road
San Antonio, Texas 78238

DEVELOPMENT OF A THIN FILM PRIMARY SURFACE HEAT EXCHANGER FOR ADVANCED POWER CYCLES

FINAL SCIENTIFIC/TECHNICAL REPORT

Overall Project Period 10/1/14 – 3/31/16
DOE Award No. DE-FE0024104
SwRI® Project No. 18.20746 / SwRI DUNS No. 00-793-6842

Prepared by:

Tim Allison, Ph.D.
(PI Contact: tim.allison@swri.org / 210-522-3561)
Griffin Beck
Jeffrey Bennett
Kevin Hoopes
Larry Miller

Prepared for:

U.S. Department of Energy
National Energy Technology Laboratory
626 Cochrans Mill Road
P.O. Box 10940
Pittsburgh, PA 15236-0940

June 29, 2016

Approved:

Edgar B. Bowles, Jr.

Edgar B. Bowles, Jr., Director
Fluids & Machinery Engineering Department

DISCLAIMER

This report was prepared as an account of work sponsored by an agency of the United States Government. Neither the United States nor any agency thereof, nor any of their employees, makes any warranty, express or implied, or assumes any legal liability or responsibility for the accuracy, completeness, or usefulness of any information, apparatus, product, or process disclosed, or represents that its use would not infringe privately owned rights. Reference herein to any specific commercial product, process, or service by trade name, trademark, manufacturer, or otherwise does not necessarily constitute or imply its endorsement, recommendation, or favoring by the United States Government or any agency thereof. The views and opinions of authors expressed herein do not necessarily state or reflect those of the United States Government or any agency thereof.

ABSTRACT

A high-temperature design upgrade is investigated for an existing thin-film primary surface heat exchanger for a low-pressure CO_2 closed oxy-fuel Brayton cycle that is predicted to achieve over 50% thermodynamic efficiency. The cycle requires recuperator operation in CO_2 at a maximum 1,510°F (821°C), which is well above the existing design temperature. In order to accomplish reliable operation at this higher temperature, alternative materials and coatings were evaluated via strength properties and short-term laboratory-scale thermogravimetric corrosion tests in parallel with finite element and computational fluid dynamic analysis of multiple mechanical redesign options. These efforts have identified a preferred redesign option that maintains the creep and yield stress margins of the current design by changing the recuperator material to Haynes 282 and increasing sheet thickness by 40% for the counter-flow sheet and 75% for the hot side cross-flow corrugation sheet. Metallurgical analysis of the Haynes 282 test coupons showed evidence of intergranular attack that may cause long-term reliability problems in CO_2 service at these temperatures, but long-term testing in a flowing environment is recommended in order to understand accurately the severity of the attack. Detailed economic modeling of the existing air cycle recuperator and CO_2 cycle recuperator options was also completed, including costs for material, fabrication, fuel, maintenance, and operation. The analysis results show that the increased capital cost for high-temperature materials may be offset by higher cycle efficiencies, decreasing the overall lifetime cost of the system by over 12% even with slightly higher pressure drops in the new design. Finally, several test loop concepts were evaluated to determine the lowest-cost test setup for full-pressure full-temperature testing of a prototype high-temperature recuperator that maximizes the reuse of existing compression, heating, and cooling equipment and piping. A budgetary estimate of $1,013,000.00 was developed for the detailed design, construction, commissioning, and operation of a high-temperature recuperator module test loop.

TABLE OF CONTENTS

List of Figures

List of Tables

1. EXECUTIVE SUMMARY

This project objective is to develop a high-temperature design upgrade for an existing primary surface heat exchanger so that the redesigned hardware is capable of operation in CO_2 at temperatures up to 1,510°F (821°C) and pressure differentials up to 130 psi (9 bar). The heat exchanger is proposed for use as a recuperator in an advanced low-pressure oxy-fuel Brayton cycle that is predicted to achieve over 50% thermodynamic efficiency, although the heat exchanger could also be used in other high-temperature, low-differential pressure cycles. This report describes the progress to date, which includes continuing work performed to select and test new candidate materials for the recuperator redesign, final mechanical and thermal performance analysis results of various redesign concepts, and the preliminary design of a test loop for the redesigned recuperator including a budgetary estimate for detailed test loop design, procurement, and test operation.

A materials search was performed in order to investigate high-temperature properties of many candidate materials, including high-temperature strength and nickel content. These properties were used to rank the candidate materials, resulting in a reduced list of nine materials for corrosion testing. Multiple test rigs were considered and analyzed for short-term corrosion testing and Thermal Gravimetric Analysis (TGA) was selected as the most cost-effective option for evaluating corrosion resistance of the candidate materials. In addition, tantalum, niobium, and chromium coatings were identified as potential options for increased corrosion resistance. The test results show that many materials exhibit relatively low weight gain rates, and that niobium and tantalum coatings may improve corrosion resistance for many materials, while chromium coatings appear to oxidize and debond quickly. Metallurgical analysis of alloys was also performed, showing evidence of intergranular attack in 282 that may cause long-term reliability problems in CO_2 service at these temperatures. However, long-term testing in a flowing environment is recommended in order to understand accurately the severity of the attack.

Detailed economic modeling of the existing air cycle recuperator and CO_2 cycle recuperator options was also completed, including costs for material, fabrication, fuel, maintenance, and operation. The analysis results show that the increased capital cost for high-temperature materials may be offset by higher cycle efficiencies, decreasing the overall lifetime cost of the system. The economic analysis also examines costs associated with increased pressure drop and material changes for two redesign options. These results show that, even with slightly reduced performance and/or higher material costs, the lifetime cost per energy production may still be reduced by over 12%.

The existing recuperator design information was provided by Solar Turbines, Inc. via several models, drawings, and design handoff meetings. Multiple fluid/thermal and structural models were created in order to analyze critical recuperator performance and mechanical strength in critical areas throughout the redesign process. These models were analyzed for a baseline condition (consistent with current Mercury 50 operation) for validation purposes. Results are presented for heat transfer coefficients and pressure drops, matching well with the existing operational data. Simulation of higher-temperature CO_2 conditions was also performed, showing a slight expected increase in both heat transfer and pressure drop. Mechanical analysis results for critical areas on the cross-flow and counter-flow sheets have also been obtained for air and CO_2 cases. These results show similar stresses in both cases but significantly reduced safety factors for the CO_2 case due to reduced yield and creep rupture strengths of alloy 625 at the higher temperatures.

A concept brainstorm session and initial down-selection were completed in order to identify promising redesign options for further analysis. Detailed analysis of all promising redesign options

was performed via finite element and computational fluid dynamic simulations in order to characterize mechanical and thermal-fluid performance of each option. These options included material change, various sheet thickness configurations, pitch and phasing of cross-flow and counter-flow sheets, and separator sheets. The analysis results have identified two viable redesign options that maintain existing safety margins optimally through a material change to Haynes 282 and (A) sheet thickness increases of 40% on the counter-flow sheet and 75% on the hot side cross-flow corrugation sheet or (B) addition of a separator sheet in the counter-flow section while maintaining the original counter-flow sheet thickness and increasing the cross-flow corrugation sheet thickness by 90% to account for the increase in cell height. While both options satisfy mechanical stress constraints, the separator sheet design has a higher part count, slightly reduced heat transfer, and slightly higher pressure drop than the first option and is not preferred.

Finally, several test loop concepts have been developed for different full-scale and reduced-scale recuperator testing options. For each option, various loop components, such as heat exchangers, valves, heaters, and compressors, were evaluated in an effort to maximize utilization of existing resources. All concepts utilize an existing 3-MW CO_2 compressor, heater, and loop coolers, but the concepts vary by incorporating different amounts of new equipment for achieving various flow rates (all concepts operate at design pressure and temperature). The third concept achieves a 1 kg/s test without purchasing any costly equipment (coolers, heaters, blowers, etc.). Since the stacked cell design of the recuperator results in the same flow conditions at each core cell (even for a reduced-scale test). Thus, test loop Concept #3 was selected for the preliminary design. This loop design is detailed within the report, culminating in a budgetary estimate of $1,013,000.00 for the detailed design, construction, commissioning, and operation of a high-temperature recuperator test loop.

2. PROJECT ACCOMPLISHMENTS

This section describes the overall project and progress made on various project tasks through the end of the reporting period.

2.1 PROJECT OVERVIEW

2.1.1 PROJECT OBJECTIVE

The objective of the project is to develop a high-temperature heat exchanger design capable of operation in CO_2 at temperatures up to 1,510°F (821°C) and pressure differentials up to 130 psi (9 bar). The heat exchanger is proposed for use as a recuperator in an advanced low-pressure oxy-fuel Brayton cycle that is predicted to achieve over 50% thermodynamic efficiency, although the heat exchanger could also be used in other high-temperature, low-differential pressure cycles. The proposed heat exchanger concept is based on existing primary surface recuperators that are compact, low-cost, and have proven reliability and high effectiveness in automotive and gas turbine applications with low differential pressures.

2.1.2 PROJECT SCOPE

This project will increase the operating temperature range of the existing primary surface heat exchanger technology from the Solar Turbines, Incorporated Mercury™ 50 recuperator by accomplishing the following scope of work:

- Perform a mechanical redesign of a primary surface recuperator by selecting new high-temperature materials, analyzing structural changes to minimize thermal and mechanical stresses at higher operating temperatures, and evaluating coatings to minimize oxidation and carburization in CO_2. A system cost analysis will be performed for various redesign options in order to select a design that successfully achieves higher temperatures while keeping costs as low as possible.
- Perform laboratory-scale oxidation testing of high-temperature material and coating samples at temperatures above 1,510°F.
- Complete a preliminary design of a full-scale test loop for evaluating the heat exchanger concept so that cost and schedule can be established for any future performance validation efforts.

2.1.3 PROJECT TASKS

The following tasks and subtasks are identified in the Statement of Project Objectives:

- Task 1.0 Project Management & Reporting
- Task 2.0 System Analysis
  - Subtask 2.1 Thermodynamic Analysis
  - Subtask 2.2 Economic Analysis

- Task 3.0 Materials and Coatings Evaluation
  - Subtask 3.1 Review of Materials and Coatings
  - Subtask 3.2 Laboratory-Scale Coupon Test Rig Design & Fabrication
  - Subtask 3.3 Laboratory-Scale Coupon Testing
- Task 4.0 Recuperator Mechanical Redesign
  - Subtask 4.1 Development and Validation of Mechanical Model for Existing Recuperator
  - Subtask 4.2 Concept Study of Redesign Options for Higher Temperature
  - Subtask 4.3 Mechanical Design and Analysis of Selected Concepts
  - Subtask 4.4 Design Drawings and Quotes
- Task 5.0 Test Loop Preliminary Design
  - Subtask 5.1 Conceptual Design
  - Subtask 5.2 Preliminary Design

2.2 TASK 1 ACCOMPLISHMENTS – PROJECT MANAGEMENT & REPORTING

During the project, the Project Management Plan (PMP) was revised once to incorporate specific formatting and content requirements issued by the DOE. At this point, the PMP (Revision A) reflects the status of the project. All required reports have also been prepared and submitted in accordance with the "Federal Assistance Reporting Checklist."

2.3 TASK 2 ACCOMPLISHMENTS – SYSTEM ANALYSIS

This section describes the thermodynamic and economic analysis results that provide the recuperator redesign operating conditions and evaluate changes in recuperator design on the cycle and recuperator cost.

2.3.1 SUBTASK 2.1 – THERMODYNAMIC ANALYSIS

This subsection presents thermodynamic analyses of the overall cycle efficiency for the system as it was first proposed and was updated during the project to include more realistic pressure drops. The thermodynamic analysis will continue to be updated throughout the project as modifications are made to the recuperator design that change the heat transfer effectiveness and pressure drop. All thermodynamic cycle analyses were performed in Aspen Plus.

2.3.1.1 Cycle Overview

The heat exchanger is being designed for use as a recuperator in a closed-loop recuperated CO_2 oxy-fuel cycle. The cycle operates with CO_2 as the working fluid and uses combustion of oxygen and methane to provide heat directly to a turbine. Providing pure oxygen and methane will result in the exhaust being CO_2 and water. The water will be removed through a separator, and CO_2 produced by the reaction will be discharged from the system as pure CO_2, ready to be sequestered. Through sequestration and the use of pure methane, there will be no plant emissions to the atmosphere.

In addition to producing sequestration-ready CO_2 as a waste stream, one additional benefit of the proposed cycle is that the higher-cycle efficiency and increased density of CO_2 compared to air, result in a cycle volume flow that is approximately 70% that of an equivalent net power air cycle. The reduced volume flow allows for the use of smaller turbomachinery, potentially reducing equipment capital costs.

Although the proposed cycle is one example showing that increased thermodynamic efficiency can be achieved with a higher recuperator temperature, this conclusion is also true for other cycles and the proposed recuperator design can also be used in other high-temperature, low-differential pressure applications as well.

2.3.1.2 Original Cycle Analysis

The cycle was originally simulated during the proposal effort of this project using Aspen Plus to predict the cycle efficiency. First, a recuperated air Brayton cycle was created and tuned to reach an efficiency of 40.0%, the efficiency of the recuperated SOLAR® Mercury 50. The system maintained the published heat exchanger efficiency of 93%, existing firing temperature of 1,163°C, and cycle pressure ratio of 10:1. The same model was then reconfigured to simulate a CO_2 Brayton cycle for comparison. The recuperated CO_2 cycle achieved an efficiency of 47.7%. An organic Rankine cycle could be added as a bottoming cycle for the recuperated CO_2 system to bring the total system efficiency over 50%. A summary of the cycle efficiencies is shown in Table 2-1, and a screenshot of the recuperated model produced in Aspen Plus is shown in Figure 2-1. Please note that the Aspen Plus analysis is based upon using a unit mass flow, since efficiency is independent of the mass flow. This cycle will produce sequestration-ready CO_2 with a net efficiency of 47.7%, and could reach efficiency greater than 50% with the inclusion of an organic Rankine cycle.

Table 2-1. Cycle Efficiency Comparison

Modeling Parameters	
Compressor Isentropic Efficiency	80.0%
Turbine Isentropic Efficiency	83.3%
Heat Exchanger Effectiveness	93.0%
Cycle Analysis Results	
Cycle	Efficiency
Recuperated Air Brayton Cycle	40.0%
Oxy-Fuel Recuperated CO_2 Brayton Cycle	47.7%

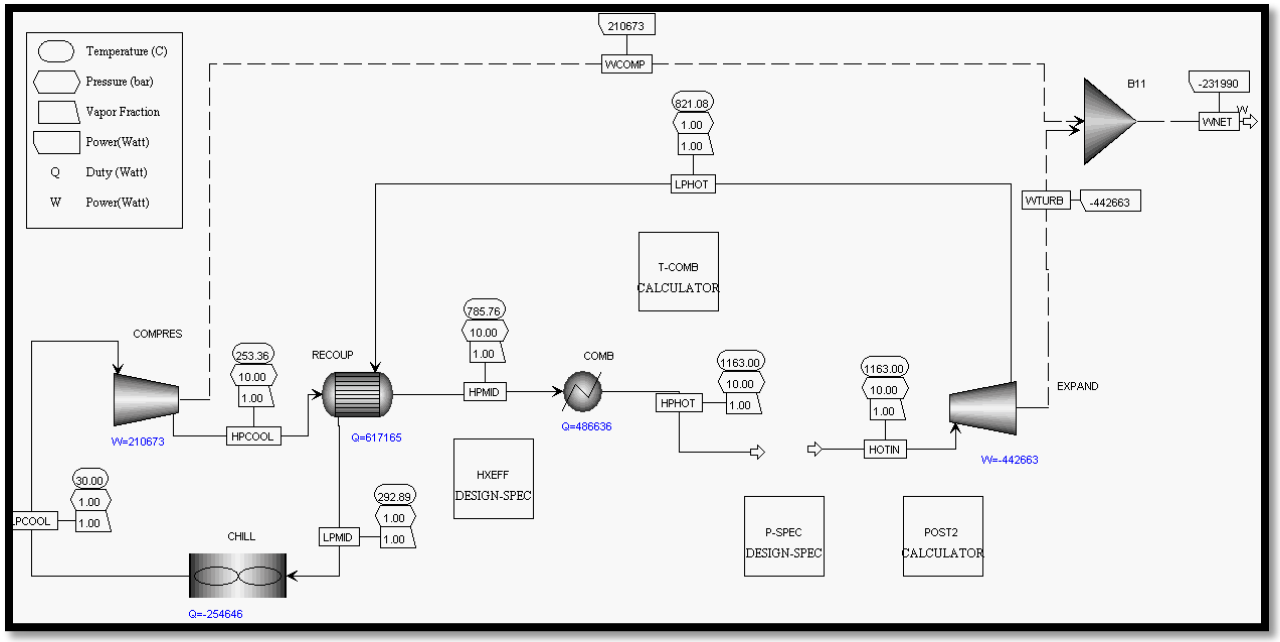

Figure 2-1. Recuperated Oxy-Fuel Cycle

2.3.1.3 Updated Cycle Analysis with Pressure Drops

The original cycle analysis was updated to account for measured pressure drops from the original recuperator design. The model was updated to have a 2.8% pressure drop across the air side and a 6.7% pressure drop across the exhaust side. Following the same procedure as the original thermodynamic analysis, compressor and turbine isentropic efficiencies were tuned to achieve 40% efficiency for a recuperated air Brayton cycle. Then the model was updated for an oxy-fuel recuperated Brayton cycle. The updated oxy-fuel cycle efficiency is 47.26%, a 0.5 percentage point reduction from the original prediction.

Table 2-2. Cycle Efficiency Comparison with Pressure Drops

Modeling Parameters	
Compressor Isentropic Efficiency	81.4%
Turbine Isentropic Efficiency	84.4%
Heat Exchanger Effectiveness	93.0%
Cycle Analysis Results	
Cycle	Efficiency
Recuperated Air Brayton Cycle	40.0%
Oxy-Fuel Recuperated CO_2 Brayton Cycle	47.26%

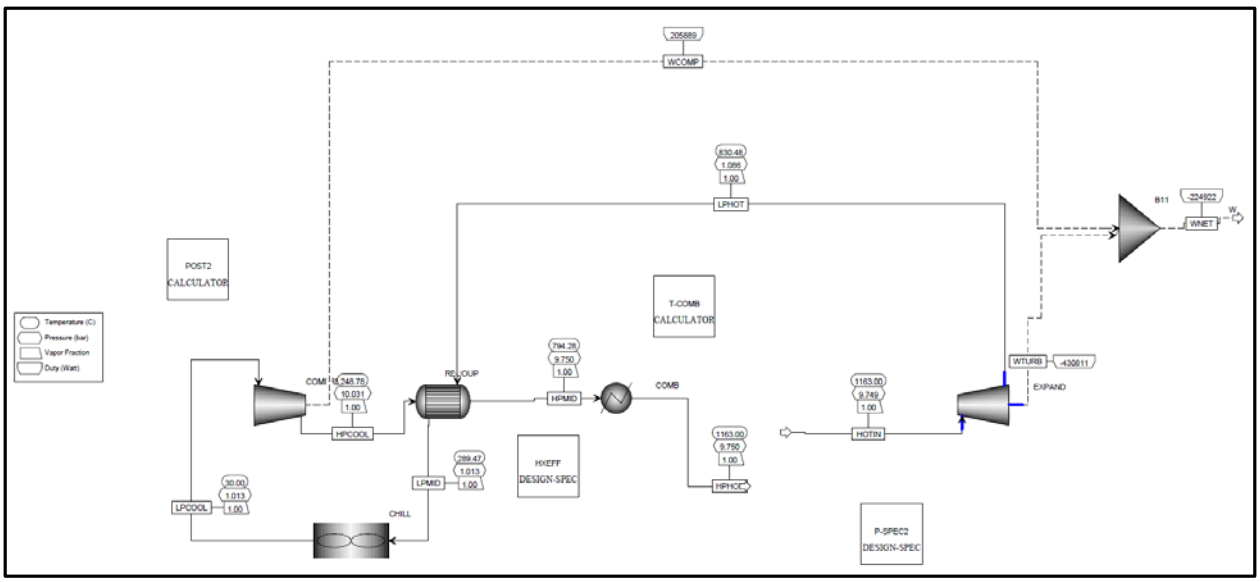

Figure 2-2. Recuperated Oxy-Fuel Cycle with Updated Pressure Drops

2.3.1.4 Heat Exchanger Design Conditions

The results of the Aspen Plus analysis with updated pressure drops have been used to determine the design conditions for the proposed heat exchanger. The proposed heat exchanger will use the turbine exhaust to pre-heat the compressor outlet flow, thus, reducing the amount of fuel necessary to bring the flow up to the flame temperature of 1,163°C. The turbine exhaust entering the heat exchanger will be at 830°C, and the compressor outlet flow at 249°C. The design has previously proven to operate at a heat exchanger effectiveness of 93%, which will result in the flow heading to the combustion chamber to be at a temperature of 794°C. This process then cools the turbine exhaust to a temperature of 290°C. The remaining heat could then be used in an organic Rankine cycle. A summary of the conditions are shown in Table 2-3.

Table 2-3. Heat Exchanger Design Conditions

Parameter	Hot Flow In (Turbine Exhaust)	Hot Flow Out	Cold Flow In (Compressor Discharge)	Cold Flow Out (to Combustor)
Temperature [°C]	830	290	249	794
Pressure [bar]	1.09	1.01	10.03	9.75

2.3.1.5 Cycle Analysis Update for Recuperator Redesigns

One of the initial redesign options of doubling the thickness of the sheets was simulated using CFD to predict the pressure drop, if the recuperator size would remain the same. This analysis found that the hot side would have a pressure drop 2.18 times higher, and the cold side 3.0 times higher. Cycle models were updated to predict the impact on cycle efficiency using these new pressure drop values. There are two ways to handle the change in pressure drop. Either the compressor pressure ratio can be increased or the turbine pressure ratio can be decreased. Both options were simulated and the results are shown below in Table 2-4. Either option results in an efficiency decrease of approximately 3%.

Table 2-4. Impact of Doubling Sheet Thickness on Cycle Efficiency

Configuration	Compressor Pressure Ratio	Turbine Inlet Pressure	Efficiency	Efficiency Change
[-]	[-]	[bar]	[%]	[%]
Case 1 - Maintain Original Pressure Drops	9.90	9.75	47.25	0.00
Case 2 - Maintain Compressor Pressure Ratio	9.9	9.189	44.21	-3.05
Case 3 - Maintain Turbine Inlet Pressure	10.505	9.75	44.06	-3.19

The recuperator pressure drop associated with a sheet thickness increase can be mitigated by increasing the number of cells in (and overall length of) the recuperator until the pressure drop is equivalent to the original design. The results of this option would match those previously presented for the CO_2 cycle. This approach will of course increase material cost; this increase is investigated and quantified in the next section.

2.3.2 SUBTASK 2.2 – ECONOMIC ANALYSIS

The purpose of this section is to estimate and compare the lifetime cost per energy production of the current and redesigned recuperator while keeping the cycle power production constant. The cost is broken down into four components, material cost, manufacturing cost, maintenance cost, and fuel cost. Next, the lifetime energy production is estimated. These results are combined to provide an estimate of total lifetime cost per energy production. This estimate does not account for the cost of the turbomachinery.

2.3.2.1 Cycle Analysis

This subsection compares the recuperated air Brayton and carbon dioxide Brayton cycles with the purpose of determining the size of the recuperators and the required heat input. The cycle analysis previously presented in this report analyzed each of these cycles using a mass flow rate of 1 kg/s in Aspen Plus. To compare the economics of each of these cycles, the recuperators are going to be compared while keeping the power output of the cycle constant. Table 2-5 takes the results of the cycle analysis and finds the corresponding mass flow and heat input required, if the cycle were to output 4.6 MW-e, to match the Mercury 50 power-set from which the recuperator design originates. The air cycle has an efficiency of 40% versus the 47.3% of the CO_2 cycle and as a result, the air cycle requires 11.85 MW of heat input, whereas the CO_2 cycle only needs 10.03 MW of heat input.

Next, the density of air and CO_2 were determined using NIST REFPROP at the conditions predicted for the recuperator. The density was combined with the necessary mass flows to calculate the required volume flow through the recuperators. In order to keep the velocities through the recuperator as similar as possible, the proportion of the volume flows was averaged at the predicted inlet and outlet conditions. The CO_2 recuperator requires 70.2% of the volume of the air recuperator, or a 29.8% reduction in size. This is shown in Table 2-6.

Table 2-5. Cycle Comparison for Economic Analysis

		Cycle	
		Recuperated Air Brayton	**Recuperated CO_2 Brayton**
Aspen Plus Cycle Analysis			
Cycle Inputs:			
Mass Flow	[kg/s]	1.0	1.0
Combustion Temperature	[C]	1,163	1,163
Results:			
Compressor Power	[kW]	346	206
Turbine Power	[kW]	592	431
Combustor Heat Input	[kW]	612	476
Efficiency Analysis:			
Cycle Power Out	[kW]	245	225
Cycle Power In	[kW]	612	476
Efficiency	[%]	40.0%	47.3%
Scaled to Designed Power Output			
Power Output	[kW-e]	4,600	4,600
Assumed Electrical Conversion Efficiency	[%]	97.0%	97.0%
Cycle Power Output	[kW]	4,742	4,742
Mass Flow	[kg/s]	19.4	21.1
Combustor Heat Input	[kW]	11,853	10,036

Table 2-6. Cycle Properties Comparison for Economic Analysis

Recuperated Air Brayton				
	Temperature	Pressure	Density	Flow Rate
	(°C)	(bar)	(kg/m³)	(m³/s)
Hot In	656.0	1.09	0.408	47.4
Hot Out	388.2	1.01	0.532	36.4
Cold In	368.1	10.03	5.427	3.6
Cold Out	636.7	9.73	3.712	5.2
Recuperated CO_2 Brayton				
	Temperature	Pressure	Density	Flow Rate
	(°C)	(bar)	(kg/m³)	(m³/s)
Hot In	830.5	1.09	0.523	40.3
Hot Out	289.5	1.01	0.951	22.2
Cold In	248.8	10.03	10.233	2.1
Cold Out	794.3	9.73	4.815	4.4
Flow Rate Comparison				
	Air	CO_2	CO_2/Air	
	(m³/s)	(m³/s)	Ratio	
Hot In	47.4	40.3	0.85	
Hot Out	36.4	22.2	0.61	
Cold In	3.6	2.1	0.58	
Cold Out	5.2	4.4	0.84	
		Average	0.72	

2.3.2.2 Material Cost

The recuperator is being redesigned with the goal of preserving as much of the design as possible in order to maintain its high effectiveness. Therefore, the design of each sheet will be similar, and the number of sheets will be adjusted to account for the difference in volume flows required by the two cycles. As presented in the previous section, the CO_2 cycle will require 72% of the original recuperator volume. The weight of the existing recuperator design was analyzed, as provided by Solar Turbines, to determine the amount of material required, and from this the total amount of material required for the recuperators was calculated as shown in Table 2-7.

Table 2-7. Volume Comparison of Air and Carbon Dioxide Recuperators

	Air Brayton	CO_2 Brayton	Units
Weight of Core	7,150	-	[#]
Weight of Associated Parts	3,350	-	[#]
Total Weight	10,500	-	[#]
Density (Alloy 625)	0.305	-	[lb/in^3]
Total Material Volume	34,426	24,787	[in^3]

Next, material prices were determined by requesting quotes from vendors. The recuperator currently used for the Mercury 50 is alloy 625, at an estimated cost of $22 per pound. Costs for alternative materials being considered are presented in Table 2-8. The current list of candidate materials could be as little as 29% less expensive than the current material to as high as 549% more expensive than the current material. Material prices were combined with the estimated material volume required for each recuperator to predict the total material cost of the recuperators, as shown in Table 2-9.

Table 2-8. Material Price Comparison

Material	Density (lb/in^3)	Cost ($/lb)	Cost Relative to 625 (%)
Inconel 625	0.305	22.00	0%
Hastelloy X	0.297	30.56	39%
Haynes 25 (L605)	0.330	62.29	183%
Haynes 230	0.330	51.79	135%
Haynes 282	0.299	32.78	49%
Haynes 263	0.302	56.78	158%
Haynes 617	0.302	35.00	59%
Haynes 188	0.324	142.86	549%
Incoloy 800H	0.287	15.63	-29%
309 SS	0.290	18.52	-16%
310H SS	0.285	24.82	13%

Table 2-9. Recuperator Cost Comparison for Air and Carbon Dioxide Recuperators

Material	Recuperated Air Brayton		Cost Relative to 625 (%)	Recuperated CO_2 Brayton		Cost Relative to Air 625 (%)
	Weight (lb)	Cost ($)		Weight (lb)	Cost ($)	
Inconel 625	10,500	231,000	0%	7,560	166,320	-28%
Hastelloy X	10,225	312,418	35%	7,362	224,941	-3%
Haynes 25 (L605)	11,361	707,607	206%	8,180	509,477	121%
Haynes 230	11,361	588,368	155%	8,180	423,625	83%
Haynes 282	10,293	337,419	46%	7,411	242,942	5%
Haynes 263	10,397	590,299	156%	7,486	425,015	84%
Haynes 617	10,397	363,885	58%	7,486	261,997	13%
Haynes 188	11,154	1,593,443	590%	8,031	1,147,279	397%
Incoloy 800H	9,880	154,380	-33%	7,114	111,154	-52%
309 SS	9,984	184,882	-20%	7,188	133,115	-42%
310H SS	9,811	243,534	5%	7,064	175,344	-24%

The material selection for the CO_2 recuperator is partly based on cost, but most importantly, the material is needed to provide the strength and oxidation resistance required for the high-temperature operating conditions. An option for obtaining oxidation resistance while using less expensive materials is to provide a protective coating over the base material. Of course, this method will have a manufacturing cost associated with it also. The Materials Engineering Department at SwRI has offered a rough estimate of coating costs using sputter deposition to deposit either niobium or tantalum on the surface of a metal sheet. The initial cost to coat a 3 ft. by 4 ft. sheet of material would be around $7,500, which would include some setup and development to ensure a uniform coating. Additional costs to coat a single 3 ft. x 4 ft. sheet (after the process is established) would be around $5,000.

Another coating option investigated was a hard chrome coating that Hohman Plating has experience applying. Hohman Plating estimated that the cost to apply hard chrome to a single sheet would cost roughly $5-$25 for an order of 1,000 sheets. There would be additional costs to set up the process. There were also concerns from Hohman Plating regarding the ability to provide an even coat considering the wavy pattern of the heat exchanger sheets.

The use of other coating methods or selection of a coating company that specializes in manufacturing may lower this process cost; however, it is apparent that the cost of a coating process could add significantly to the overall material cost for a large recuperator such as this.

2.3.2.3 Manufacturing Cost

Finally, manufacturing cost is another factor highly affected by a material change. If a material is selected that has a higher stiffness, the existing manufacturing equipment may not be able to form the folded heat transfer sheets and new equipment, such as dies and presses, would be required. Therefore, it is difficult to estimate the manufacturing cost at this stage. The number of manufacturing hours required per recuperator is an estimate provided by Solar. Table 2-10 estimates the cost for both recuperators assuming alloy 625 is used.

Table 2-10. Manufacturing Cost Estimate

Hourly Rates	**($/hr)**	**Ref.**
Welder Labor Rate	19.25	[1]
General Overhead Rate	48.125	Assumed
Variable Overhead Rate	10	Assumed
Capital Depreciation Rate	100	Solar Estimate
Total Hourly Rate	177.375	-
Total Manufacturing Cost		
	Recuperated Air Brayton	Recuperated CO_2 Brayton
Manufacturing Hours	1,000	720
Manufacturing Cost	$177,375	$127,638

2.3.2.4 Maintenance Cost

The recuperator design is practically maintenance free, with the exception of the tie bolts, which hold the sheets in place. Solar has estimated that every 30,000 hours of run time, the tie bolts need to be tightened. It was assumed that two specially-trained technicians would be required to perform the required maintenance.

Table 2-11. Estimated Maintenance Visit Cost

# of Technicians	**2**	**(#)**
Technician Rate [2]	$24.99	($/hr)
General Overhead	$124.95	($/hr)
Visit Cost	$ 2,399.04	($)

Table 2-12. Estimated Lifetime Maintenance Cost

Maintenance Interval	30,000	(hrs)
	3.42	(yr)
Recuperator Lifetime	12	(yr)
# of Maintenance Visits	4	(#)
Visit Cost	$ 2,399.04	($)
Total Maintenance Cost	$ 9,596	($)

2.3.2.5 Fuel Cost

The lifetime fuel cost for the recuperators was estimated by combining forecasted worldwide natural gas fuel prices with the required heat input from the cycle analysis. Natural gas price forecasts for 2020 are shown in Table 2-13. Cycle heat inputs from the previous analysis are combined with the design life of 12 years and the fuel prices in Table 2-14 to estimate the lifetime fuel cost. Fuel prices vary widely by region, from $5.2 to $13.0 per million British thermal unit. The recuperated CO_2 Brayton cycle has an efficiency 18% higher than the air Brayton cycle, thus, the air Brayton cycle requires 18% more fuel and an 18% higher fuel cost.

Table 2-13. Natural Gas Price Forecasts for 2020

Fuel Prices (Using 2020 forecasted prices) [3]		
U.S.	[$/mmBtu]	5.2
Europe	[$/mmBtu]	10
Japan	[$/mmBtu]	13

Table 2-14. Estimated Recuperator Lifetime Fuel Cost

		Recuperated Air Brayton	Recuperated CO_2 Brayton
Combustor Heat Input Rate	[MW]	11.85	10.04
Design Life	[yr]	12.00	12.00
	[hr]	105,192	105,192
Lifetime Combustor Heat Input	[MW-h]	1,246,849	1,055,747
	[MMBtu]	4,254,425	3,602,360
Lifetime Fuel Cost - US	[$]	$ 22,123,012	$ 18,732,272
Lifetime Fuel Cost - Europe	[$]	$ 42,544,253	$ 36,023,600
Lifetime Fuel Cost - Japan	[$]	$ 55,307,529	$ 46,830,680

2.3.2.6 Lifetime Cost per Energy Production and Summary

The material, manufacturing, maintenance, and fuel cost estimates previously discussed are combined in Table 2-15, to estimate the lifetime cost per energy production. The estimates are for 12 years of continuous power production and assume that the material for both air and CO_2 applications is alloy 625 without a coating (note that mechanical feasibility of alloy 625 at the higher CO_2 cycle temperatures is still being evaluated). This estimate also excludes the cost of the gas turbine package and costs associated with closed-loop piping and gas turbine modifications required to run the CO_2 Brayton cycle.

The results show that the fuel cost is the dominant factor, and, therefore, the recuperated CO_2 cycle costs $7 less per MWe-hr due to the efficiency of the cycle. Additionally, the increased density of CO_2 over air results in a 28% more compact heat exchanger, thus, lowering the material and manufacturing costs. After the material and coating selection is finalized, the material and manufacturing cost estimates will be updated.

Table 2-15. Lifetime Cost per Energy Production (Excludes Gas Turbine Package)

	Recuperated Air Brayton	Recuperated CO_2 Brayton	
Material	**625**	**625**	**282**
Material Cost	$231,000	$166,320	$242,942
Coating Cost	$0	$0	$0
Manufacturing Cost	$177,375	$127,638	$127,638
Maintenance Cost	$9,596	$9,596	$9,596
U.S. Fuel Cost	$22,123,012	$18,732,272	$18,732,272
Total Cost	$22,540,983	$19,035,827	$19,112,448
Lifetime Energy Production [MWe-hr]	483,883	483,883	483,883
Lifetime Cost Per Energy Production [$/MWe-hr]	**$46.58**	**$39.34**	**$39.50**

2.3.2.7 Updated Economic Analysis

CFD and cycle analyses of the successful redesigns showed that pressure drops would increase and, thus, efficiencies would decrease if the recuperator size were to remain the same. Therefore, the economic analysis was updated to include the expected cost of increasing the recuperator size to maintain pressure drops and, thus, efficiencies while making the geometry modifications. Based upon the cross-flow model analyzed, the redesign that increases the counter-flow sheet thickness will increase the material volume by 45% for an equivalent size recuperator. Using the CFD pressure drop predictions, the same redesign will require the number of sheets to be increased by 60% to maintain the same pressure drop. Similarly, the redesign with a separator sheet in the counter-flow region will increase the material volume by 124% for an equivalent size recuperator, and will require the number of sheets to be increased by 140% to maintain the same pressure drop. This analysis was used to update the material and manufacturing costs. Additionally, it was assumed that increasing the sheet thickness would increase manufacturing time per sheet by 20% due to increased time for bending the thicker sheets. Maintenance costs are expected to remain the same. A summary of the updated analysis is shown for the material costs in Table 2-16, manufacturing costs in Table 2-17, and a summary of the redesign against the original design in Table 2-18.

Table 2-16. Redesign Material Costs

	Recuperated Air Brayton	Recuperated CO_2 Brayton	
		Increased Counter-flow Sheet Thickness	Separator Sheet in Counter-Flow Region
Material	625	282	282
Price ($/lb)	22.00	32.78	32.78
Density (lb/in^3)	0.305	0.299	0.299
Volume	34,426	57,663	133,361
Material Price	$231,000	$565,171	$1,307,101

Table 2-17. Redesign Manufacturing Costs

	Recuperated Air Brayton	Recuperated CO_2 Brayton	
		Increased Counter-flow Sheet Thickness	Separator Sheet in Counter-Flow Region
Manufacturing Hours	1,000	1,382	2,072
Manufacturing Cost	$177,375	$245,066	$367,599

Table 2-18. Redesign Lifetime Cost Per Energy Production (Excludes Gas Turbine Package)

	Recuperated Air Brayton	Recuperated CO_2 Brayton	
		Increased Counter-flow Sheet Thickness	Separator Sheet in Counter-Flow Region
Material	**625**	**282**	**282**
Material Cost	$231,000	$565,171	$1,307,101
Manufacturing Cost	$177,375	$245,066	$367,599
Maintenance Cost	$9,596	$9,596	$9,596
US Fuel Cost	$22,123,012	$18,732,272	$18,732,272
Total Cost	$22,540,983	$19,552,106	$20,416,568
Lifetime Energy Production [MWe-hr]	483,883	483,883	483,883
Lifetime Cost Per Energy Production[$/MWe-hr]	**$46.58**	**$40.41**	**$42.19**

2.4 TASK 3 ACCOMPLISHMENTS – MATERIALS AND COATINGS EVALUATION

This section describes the effort to identify existing high-temperature materials that may be suitable for the recuperator redesign.

2.4.1 SUBTASK 3.1 – REVIEW OF MATERIALS AND COATINGS

The Mercury 50 recuperator is currently designed to perform in an Air Brayton cycle with maximum exhaust gas temperatures around 650°C (1,202°F) and maximum differential pressures around 9 bar (130 psi). Changing this recuperator design to operate in a CO_2 Brayton cycle would introduce a higher maximum operating temperature, around 820°C (1,508°F), while keeping the differential pressures the same. This change to a CO_2 environment along with an increase in temperature may require a material change in order to avoid corrosion, fatigue, and creep failures within the recuperator.

A rather large list of possible fabrication materials, which could be used to modify the Mercury 50 recuperator so it can function in this CO_2 Brayton cycle environment, has been produced for initial consideration. This initial list of materials was assembled from the Aerospace Structural Materials Handbook [Setlak, 2002 (1)], from manufacturer recommendations, and from material reviews performed for past projects. The initial materials considered are listed in Table 2-19. A source list for these materials is presented in Table 2-20.

Table 2-19. List of Materials Reviewed

309 Stainless Steel	Hiperco Alloy 50A	Invar 36	Pyromet 601
310H Stainless Steel	HPA Cobalt Alloy 6B/6K	Invar 42	Pyromet 625
330 Stainless Steel	HPA Cobalt Alloy 6BH	Kovar	Pyromet 680
AFA-OC6	Hy Mu 80	Monel 400	Pyromet 706
Alloy 60, NIT 60	Incoloy 800/800H	Monel K-500	Pyromet 751
AM 350	Incoloy 825	MP98T	Pyromet 80A
CMSX-4	Incoloy 901	Nickel 200/201	Pyromet 90
Custom 455	Inconel 100	Nitronic 30	Pyromet L605
Ferralium 255	Inconel 27-7MO	Nitronic 50 SS	Rene 41
Hastelloy C22	Inconel 600	Nitronic 60 SS	Rene 80
Hastelloy C276	Inconel 601	Permendur 2V	Rene 95
Hastelloy X	Inconel 617 (Haynes)	Permendur 49	Rene N5
Haynes 188	Inconel 625 (Haynes)	PH 13-8 Mo	Super Invar 32-5
Haynes 230	Inconel 706	PH 15-7 Mo	Waspaloy
Haynes 25 (L605)	Inconel 713	Pyromet 102	
Haynes 263	Inconel 718	Pyromet 41	
Haynes 282	Inconel X750 (Haynes)	Pyromet 600	

Table 2-20. Sources for Materials List

Author	Title	Date	Source
Stanley J. Setlak (4)	Aerospace Structural Metals Handbook, Edition: 39.1	2002	http://engineering.purdue.edu/IIES/MPHO/
CRS Holdings Inc. (5)	An Overview of Carpenter's High-Temperature Alloys	2006	www.cartech.com
Special Metal Corporation (6)	Product Handbook of High-Performance Alloys	2008	www.specialmetals.com
High Temp Metals (7)	High Temp Metals Data Library	Accessed 12/2/2014	www.hightempmetals.com/technicaldata.php
High Performance Alloys Inc. (8)	High Temperature Alloys	2007, Accessed 12/2/2014	www.hpalloy.com/alloys/hightemperature.html
Haynes International (9)	High-Temperature Alloys	Accessed 12/2/2014	www.haynesintl.com/htalloys.htm
Altemp Alloys (10)	Exotic, High Temperature Alloys & Super Alloys	2015, Accessed 12/2/2014	www.altempalloys.com/
Rolled Alloys (11)	Nickel Alloys	2014, Accessed 12/2/2014	www.rolledalloys.com/alloys/nickel-alloys/
Nickel Institute (12)	Nickel-Containing Materials – Properties	2011, Accessed 12/2/2014	www.nickelinstitute.org/NickelUseInSociety/MaterialsSelectionAndUse/Ni-ContainingMaterialsProperties

The review of these materials required that some initial criteria be met, the first of which was the availability of the material, including the available forms of the material. The material selected for this recuperator will be replacing the main heat transfer sheet that is folded into a corrugated sheet with a sinusoidal pattern. Availability in a sheet form is required for replacement of the current sheet material. The next criterion reviewed for these materials was the useful temperature range. The material needs to function well at 820°C (1,508°F) or higher, and not have major structural or corrosion problems at this temperature. Many sources were reviewed to determine the best materials to be used in a CO_2 environment at high temperatures [Mahaffey, Sept. 2014 (13)]; [de Barbadillo, Sept. 2014 (14)]; [Wright, June 2013 (15)]; [Lee, Sept. 2014 (16)]; [Pint, Sept. 2014 (17)]; [Saari, Sept. 2014 (18)], but almost all sources reviewed only presented testing information at temperatures around 600°C (1,112°F) instead of the 820°C (1,508°F) that is required for this design. The reference material that did cover higher temperatures was limited on the number of materials tested and, thus, did not cover all the materials reviewed for this application [Carlson, June 2014 (19)]. Another criterion is the workability or formability of the material, which can roughly be tied to the nickel content. Typically, the materials with higher nickel content will be less formable and, thus, the manufacturability of the corrugated heat transfer sheets will be a concern. The current manufacturing process for the Mercury 50 recuperator plates requires high forces to form the existing material (alloy 625) so higher stiffness in the materials reviewed could lead to manufacturing problems, such as broken forming equipment or decreased form accuracy.

Using the criteria discussed above, the initial list of materials was narrowed to just nine materials for final consideration. Knowing that some of these materials could be prohibitively expensive, some lower-cost materials were included in this list, namely the 309 and 310H stainless steels. In addition, the current recuperator material (alloy 625) was included in the list to offer a comparison of the newly considered materials and the current design. The reduced list of materials was then ranked from the best suspected fit (lowest number) to the worst suspected fit (highest number). Two material properties were used to rank these materials. The first property was the percentage of nickel. This property is tied to two conflicting material traits, the workability of the material, with higher nickel content typically decreasing the workability of the material, and the corrosion resistance, which increases with nickel content and is highly desirable in the environments that will be seen in this recuperator. For an initial material down-selection, low nickel content was preferred, giving a higher priority to workability. Corrosion resistance will be evaluated from the material testing. The second property used in the ranking process was the Sheet Rupture Life at approximately 870°C (1,598°F) and 100 hours. This specific point was used as it was common with almost all materials reviewed and offered a good comparison point just slightly above the design temperature for the recuperator. Both material properties used in ranking the materials were given equal weight. Some materials ranked equally and were thus counted as an equal fit. This reduced list of materials and the associated ranks for each material are presented in Table 2-21. A list of commonly available material properties for each of these down-selected materials is presented in Table 2-22.

Table 2-21. Reduced Materials List

Material	Rank	Max Working Temp.	% Nickel	SRL, 870ºC, 100 hrs.
Haynes 25	1	1,095°C	9-11	120 MPa
Haynes 188	2	1,095°C	20-24	99 MPa
Haynes 617	3	980°C	55	90 MPa
309 Stainless Steel	3	980°C	12-15	38 MPa
Hastelloy X	4	1,095°C	49	73 MPa
Haynes 263	4	1,204°C	52	97 MPa
Incoloy 800/800H	4	1,100°C	30-35	48 MPa
310H Stainless Steel	5	1,035°C	19-22	38 MPa
Haynes 625	6	980°C	55-61	59 MPa

Table 2-22. Material Properties for Down-selected Materials

			Hastelloy X	Haynes 188	Haynes 25 (L605)	Haynes 263	Incoloy 800/800H	Haynes 617	Haynes 625	309 SS	310H SS
	Solidus Temp.		1,260°C	1,315°C	1,330°C	1,300°C	1,357°C	1,332°C	1,275°C	?	?
	Max Service Temp.		1,095°C	1,095°C	1,095°C	1,204°C	1,100°C	?	980°C	980°C	1,035°C
	% Nickel		49	20-24	9-11	52	30-35	55	55-61	12-15	19-22
Dynamic Modulus of Elasticity (Gpa)	@ 700-800°C	Temp [°C]	**700**	**760**	**700**	**700**	**760**	**700**	**760**	**760**	**760**
		DME (Gpa)	150	172	173	176	145	166	158	134	141
	@ 800-900°C	Temp [°C]	**800**	**900**	**800**	**800**	**871**	**800**	**871**	**871**	**871**
		DME (Gpa)	143	161	163	166	132	157	146	124	132
	@ 900-1,000°C	Temp [°C]	**982**	**982**	**900**	**900**	Not Available	**900**	**982**	Not Available	Not Available
		DME (Gpa)	141	154	154	154	X	149	129	X	X
Sheet Rupture Life 900-1,000°C	Temp [°C]		**982**	**980**	**980**	Not Available	Not Available	**980**	**982**	**900**	Not Available
	Point 1	Hours	10	10	10	X	X	Not Available	Not Available	X	
		Stress [Mpa]	45	63	81	X	X	X	X	X	
	Point 2	Hours	100	100	100	X	X	X	100	X	
		Stress [Mpa]	26	37	50	X	X	X	15	X	
	Point 3	Hours	1,000	1,000	1,000	X	X	1,000	1,100	1,000	
		Stress [Mpa]	8	17	28	X	X	14	12	15	
	Point 4	Hours	10,000	Not Available	Not Available	X	X	X	X	X	
		Stress [Mpa]	8	X	X	X	X	X	X	X	

Table 2-22. Material Properties for Down-selected Materials (Continued)

			Hastelloy X	Haynes 188	Haynes 25 (L605)	Haynes 263	Incoloy 800/800H	Inconel 617	Alloy 625	309 SS	310H SS
Sheet Rupture Life 1,000-1,100°C	Temp [°C]		**1,093**	**X**	**1,093**	X	X	**1,095**	**1,093**	**1,000**	
	Point 1	Hours	10	X	10	X	X	20	70	1,000	
		Stress [Mpa]	17	X	38	X	X	30	12	8	
	Point 2	Hours	100	X	100	X	X	1,000	300	10,000	
		Stress [Mpa]	8	X	19	X	X	7	7	4	
	Point 3	Hours	1,000	X	Not Available	X	X	10,000	Not Available	100,000	
		Stress [Mpa]	4	X	X	X	X	6	X	1.5	
	Point 4	Hours	Not Available	X	X	X	X	Not Available	X	X	
		Stress [Mpa]	X	X	X	X	X	X	X	X	
			Hastelloy X	**Haynes 188**	**Haynes 25 (L605)**	**Haynes 263**	**Incoloy 800/800H**	**Inconel 617**	**Alloy 625**	**309 SS**	**310H SS**
Tensile Properties	Temp [°C]		**760**	**760**	**760**	**760**	**760**	**760**	**760**	**760**	**760**
	0.2% YS ksi		34	39	35	75	14	36	55	22	21
	UTS ksi		67	90	84	105	32	70	88	35	38
	% Elong		53%	63%	28%	33%	78%	92%	70%	39%	54%
	Temp [°C]		**871**	**871**	**871**	**871**	**871**	**871**	**871**	**871**	**871**
	0.2% YS ksi		28	36	34	32	16	30	35	21	16
	UTS ksi		45	60	47	51	21	41	52	18	22
	% Elong		59%	64%	30%	55%	83%	99%	69%	50%	56%
	Temp [°C]		**982**	**982**	**982**	**982**	**982**	**982**	**982**	**982**	**982**
	0.2% YS ksi		13	19	18	13	10	16	11	--	8
	UTS ksi		26	35	33	25	12	22	25	11	12
	% Elong		66%	59%	40%	72%	100%	93%	108%	--	93%

Moving forward with material selection, one other consideration will be used in the final ranking of these materials, the unit cost of each material. Material suppliers (hpalloy.com/ michlinmetals.com/ altempalloys.com) have been contacted and costing information has been requested. Upon completion of ranking, the material list may be reduced to the top six materials, and these materials will go on to weight change testing at the operating temperature and in a CO_2 environment.

In addition to the base material selection, several types of coatings have been reviewed. The use of coatings on the heat exchanger surfaces could broaden the selection of base materials to include some less expensive or more workable options. With aid from the Materials Department at Southwest Research Institute, various coating material types were reviewed, including ceramics, alumina forming coatings, and high corrosion resistant metals. Experience from previous coating tests, which used each of these types of coatings on flexible thin bodies, led to the conclusion that both ceramic and alumina forming coatings have a much higher chance of failure when compared to the high corrosion resistant metals. This increased chance of failure is due to their brittle nature and the differences between thermal expansion ratios of these coatings

and the base materials. It was determined that both niobium and tantalum would provide a high degree of corrosion resistance while matching closely the thermal expansion ratios of the base materials being tested. Two coated sample sets were prepared, one set with a coating of niobium, and the other with a coating of tantalum.

2.4.2 SUBTASK 3.2 – LABORATORY-SCALE COUPON TEST RIG DESIGN & FABRICATION

The final materials from the material review and down selection process will be tested for oxidation and corrosion in a CO_2 environment at the expected operating temperature of 820°C (1,508°F). Many different ideas have been considered for the testing of these materials, but three main testing concepts have arisen as the most appropriate and most feasible for low-cost weight change testing at temperature and in a CO_2 environment. These testing concepts include building an in-house test chamber that flows CO_2 and combustion gas through tubes of each material; using an existing tube furnace for material test with low flow capabilities; or using Thermal Gravimetric Analysis (TGA) equipment owned by another SwRI division on campus.

The initial intention for this material testing was to test each material in the same environment it would see during operation of the recuperator. The worst expected environment is a temperature of 820°C (1,508°F) with CO_2 flowing past at a nominal velocity of roughly 85 feet per second. Each testing option has its strengths and weaknesses when it comes to material testing for this specific environment. Each of these is discussed below.

2.4.2.1 Testing in an Existing Tube Furnace

The Materials Department at SwRI has material testing equipment that is used on a regular basis; however, much of this equipment is specialized for a specific material test setup. One piece of equipment that is available for high-temperature testing in different gaseous environments is a tube furnace, such as the one depicted in Figure 2-3. The tube of this furnace is roughly 2.5” in diameter and has a section of tube nearly one foot long that is entirely encompassed by the furnace. This would allow several samples to be placed in the furnace for heating at once. These samples could be commercially produced samples that would provide a high level of consistency of weight and surface area for each sample tested. This furnace also has connections to allow the introduction of various gasses into the tube, so testing could be conducted in a CO_2 environment.

One possible shortcoming of this furnace is that the available flow of gas is very low and, thus, the actual operating conditions in the recuperator, specifically the flow velocity, cannot be met using this test equipment. In addition, weight measurements of each sample will have to be performed with separate measurement equipment adding time and complexity to the testing process.

Figure 2-3. Tube Furnace Available on SwRI Campus

2.4.2.2 Testing with Thermal Gravimetric Analysis (TGA)

The Fire Technology and the Chemical Engineering divisions at SwRI both have TGA machines that are often used for testing of various material types. The Fire Technology division has been contacted and information on their equipment and capabilities has been provided. The available equipment is a Jupiter® simultaneous thermal analyzer (STA) 449 F3 with a silicon carbide furnace. Technical information for this equipment is provided in Table 2-23 and Table 2-24 with an image presented in Figure 2-4. Testing with this equipment would require a one-day baseline run with no material and roughly one and a half days of testing for each material. Three sample runs would be performed for each material to ensure consistency of each run. Each sample would be a small piece of material less than 35 grams. To ensure an accurate comparison between samples, each sample would need to have a similar physical shape to ensure that the surface area was consistent among samples. The program for this equipment would ramp the temperature up for each sample at a consistent ramping rate, and the associated software would record the mass change in a consistent format that would be easily comparable between individual runs. These mass measurements are incorporated in the existing test equipment, greatly simplifying the measurement portion of the testing. This equipment would also provide the ability to apply a cover gas for the testing, so testing could be performed in a CO_2 environment.

Similar to the existing tube furnace, this equipment performs each test run at low gas flow rates and, thus, cannot match the flow velocities expected in the recuperator.

Table 2-23. STA 449 F3 Technical Specifications

Item: STA 449 F3 Jupiter – Simultaneous Thermal Analyzer TGA DSC
Temperature range: -150°C to 2,400°C Heating and cooling rates: 0.001 K/min to 50 K/min (dependent on furnace) Weighing range: 1 µgram to 35 grams TG resolution: 0,1 µgram (over entire weighing range) DSC resolution: < 1 µW (dependent on sensor) Measuring Range Cp measuring range: 0 to 5 J/(g*K) Atmospheres: inert, oxidizing, reducing, static, dynamic Switch valve for two purge gases and one protective gas Mass flow control for three gas channels (optional) Vacuum-tight assembly up to 10^{-4} mbar TGA-DSC and TGA-DTA sample carriers for real simultaneous operation (http://www.netzsch-thermal-analysis.com/us/products-solutions/simultaneous-thermogravimetry-differential-scanning-calorimetry/sta-449-f3-jupiter.html#!tabs/technique)

Table 2-24. STA 449 F3 Furnace Specifications

Type of Furnace	Temperature Range	Cooling System
Silver	**-120°C to 675°C**	Liquid nitrogen
Silver	**-150°C to 1,000°C**	Liquid nitrogen
Platinum	RT to 1,500°C	Forced air
Silicon carbide	**RT to 1,600°C**	**Forced air**
Rhodium	RT to 1,650°C	Forced air
Graphite	RT to 2,000°C	Tap or chilled water
Water vapor	RT to 1,250°C	Forced air
High-speed	RT to 1,250°C	Forced air
Tungsten	RT to 2,400°C	Tap or chilled water

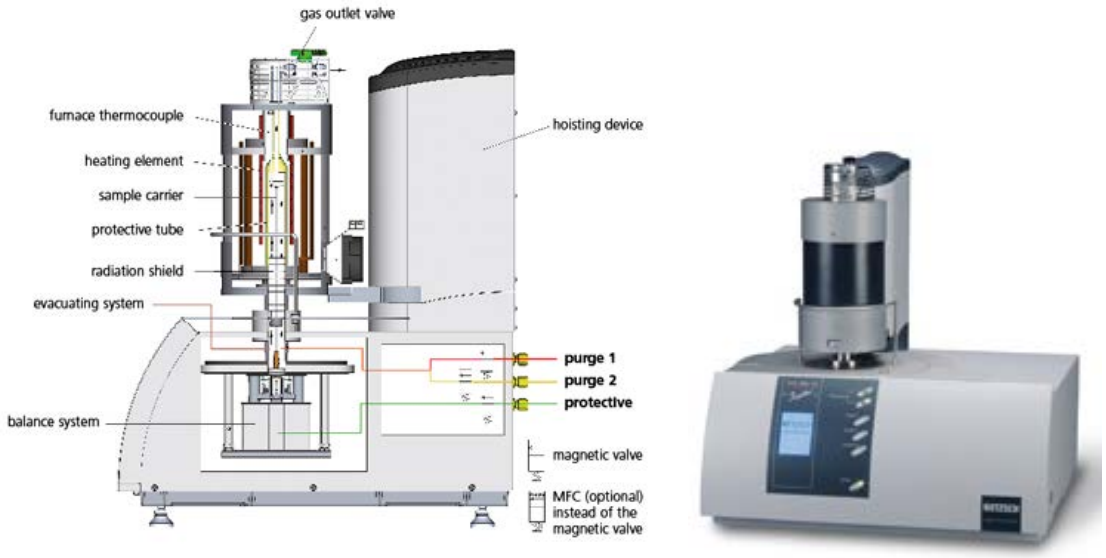

Figure 2-4. Jupiter 449 F3 TGA Machine Available on SwRI Campus

2.4.2.3 Testing with In-House Built Chamber

Having a test chamber specially built for this testing is the only option of the three that would allow material testing to be performed in a flowing environment similar to that expected in the actual recuperator with flow velocities around 85 f/s. Two options have been explored for this type of test chamber, a test fixture consisting of a gas mixing chamber and a single larger pipe diameter (2”-3” ID) material chamber, such as that depicted in Figure 2-5, and a gas mixing chamber that transitions to flowing through multiple small diameter tubes (3/16” ID) made from each of the test materials, such as that depicted in Figure 2-6.

Figure 2-5. Single-tube Test Chamber

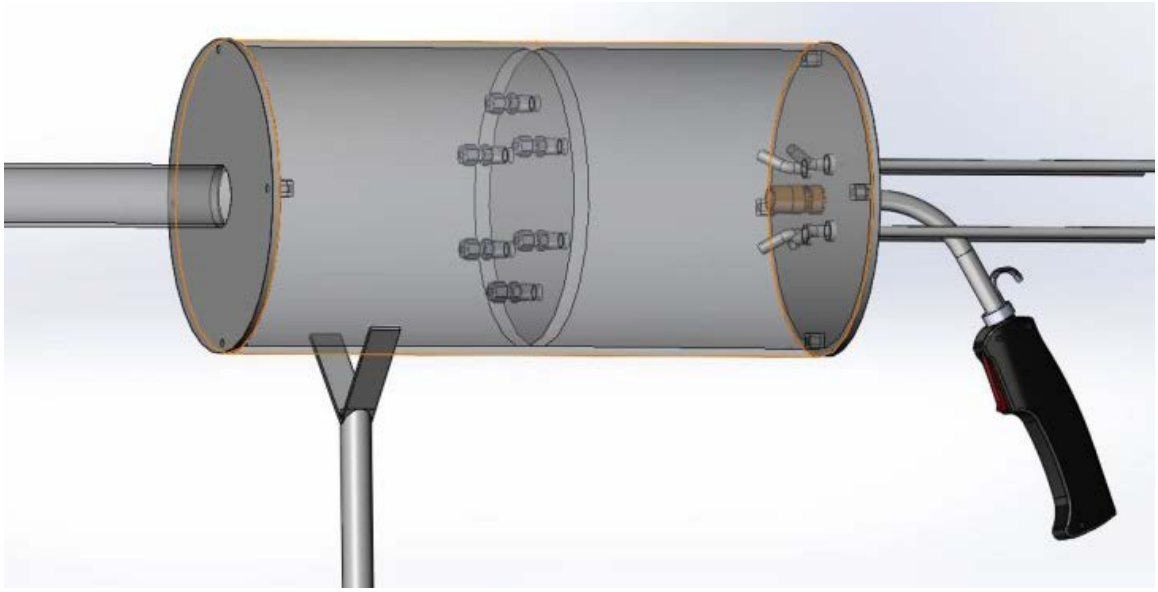

Figure 2-6. Multi-tube Test Chamber

The single-tube test chamber design is a simple construction and could be used to test commercially available material test coupons; however, there are a few operational aspects that may make this a less desirable option. In using a single in-line tube for the test chamber, the materials being tested would need to be configured in-line, one behind the other. This positioning could change the flow pattern around successive material samples leading to an uneven exposure between the various samples. This formation also may affect the actual temperature seen by each successive sample with the samples nearest the mixing chamber seeing higher temperatures than the samples furthest from the mixing chamber. Another concern with this design is the amount of heat input and cover gas required to reach desired flow rates for this testing. To reach a velocity of approximately 85 f/s in a 2.25" pipe, the total volume flow of gas would need to be around 140 cfm. Assuming this gas is provided at ambient temperatures, and using the sensible heat equation:

$$h_s = c_p \rho q \, dt \quad (1)$$

Where h_s = sensible heat in BTU/hr, c_p = the specific heat at temperature in BTU/lb_f, ρ = density at temperature in lb/ft^3, q = flow rate in cfh, and dt = temperature change in Fahrenheit.

Using this equation, the sensible heat required would be around 117,600 BTU/hr. Assuming an oxy-acetylene heat source, the fuel consumption to meet this heat input would be around 88 cfh of oxygen and 80 cfh of acetylene, which is equal to the maximum heat output of a #8 Victor heating tip, see Table 2-25. A large acetylene bottle contains around 368 ft^3 of gas and costs $378. A dewar of oxygen contains 5,500 ft^3 of gas and costs $116. Counting the volumes of each of these fuels and the available flow rates for each, and assuming a week of testing, 37 acetylene bottles and three dewars of oxygen would be required to perform this testing, and a total of 13,400 ft^3 of acetylene and 14,800 ft^3 of oxygen would be consumed. At a calculated cost of \$0.34/ft^3 for acetylene and \$0.02/ft^3 for oxygen, the cost of fuel gases alone would be over $5,000 for this testing. CO_2 would also be required at a rate of 147 cfm, with its associated cost.

In an effort to reduce testing costs, similar calculations have been made using methane and oxygen as the combustion gases. To achieve similar heating values, 129 cfh of methane and 269

cfh of oxygen would be required, leading to a total of 21,700 ft^3 of methane and 45,200 ft^3 of oxygen being consumed for a weeklong test. The total volume of methane and of oxygen is much higher due to the lower heating value of methane when compared to acetylene; however, since the cost of methane is so much lower than acetylene ($0.0094 /$ft^3$ vs. $0.34 /$ft^3$ respectively) the overall fuel gas cost would decrease to just over $1,200.

Table 2-25. Victor Heating Nozzle Specifications

Tip Size	Acetylene Pressure Range PSIG	Oxygen Pressure Range PSIG	Acetylene ft³/hr Min	Acetylene ft³/hr Max	Oxygen ft³/hr Min	Oxygen ft³/hr Max	BTU per Hour Min	BTU per Hour Max
4	6 - 10	8 - 12	6	20	7	22	8,820	29,400
6	8 - 12	10 - 15	14	40	15	44	20,580	58,800
8	10 - 15	20 - 30	30	80	33	88	44,100	117,600
10	12 - 15	30 - 40	40	100	44	110	58,800	147,000
12*	12 - 15	50 - 60	60	150	66	165	88,200	220,500
15*	12 - 15	50 - 60	90	220	99	244	132,300	323,400
*www.victortechnologies.com								

The multi-tube test chamber design, though still simple in construction, avoids some of the concerns presented by the single-tube design. With this design, the sample materials are the actual tubes through which the CO_2 flows. These tubes could be placed in a circular pattern around a bulkhead plate, ensuring an equal flow and similar flow pattern for each sample. Each sample would also be equidistant from the heat source, ensuring an equal temperature at each specimen. The required gas flow rate could also be much lower for this design, depending on the ID of the sample tubes used. Assuming the use of six samples, each with a 3/16" ID, calculations similar to those above have been made for an approximate 85 f/s flow velocity. The overall gas flow required, including fuel gas and additional CO_2, would be only 5.52 cfm and, the heat input required would be around 4,400 BTU/hr, which matches half the minimum heating value of a #4 Victor heating tip. Continuing the assumption of an oxy-acetylene heat source, the fuel consumption would be around 4 cfh of oxygen and 3 cfh of acetylene. In comparison to the 13,400 ft^3 of acetylene and 14,800 ft^3 of oxygen from the single 2.25" tube above, this setup would use a total of 500 ft^3 of acetylene and 600 ft^3 of oxygen. The cost of fuel gases for this scenario would be around $400 for a week of testing.

Again, calculations have been made using methane and oxygen as the feed gases. To achieve similar heating values, 5 cfh of methane and 10 cfh of oxygen would be required, leading to a total of 800 ft^3 of methane and 1,700 ft^3 of oxygen being consumed for a weeklong test. Using $0.0094 /$ft^3$ for the cost of methane and $0.02 /$ft^3$ for oxygen, the overall fuel gas cost for this test setup would be around $125.

One concern when considering the multi-tube test was the possibility of pressurizing the mixing chamber due to the flow restrictions presented by the small diameter tubing. To alleviate these concerns, the flow pattern and the pressure drop through a single 0.0625" diameter tube with a flow velocity of 85 ft/s, gas density of 0.949×10^{-3} slug/ft^3, and dynamic viscosity of 9.135×10^{-7} lb s/ft^2 were calculated using the equation:

$$p_1 - p_2 = f*(1/D)*(1/2)*\rho*V^2 \quad (2)$$

Where f = friction factor (0.095507), D = inner diameter, ρ = density, and V = Velocity.

The Reynolds number for this flow was around 460, which placed the flow pattern in the laminar range. The pressure differential across the tube was around 0.44 psi, which includes a reentrant inlet loss of 0.013 psi and an exit pressure loss of 0.016 psi using K factors of 0.78 and 1.0, respectively. The inlet and exit losses were calculated using Equations 3 and 4, as noted below. This low pressure loss means that very low pressures are required to meet the desired 85 ft/s flow velocities through each tube.

$$dp_{inlet} = K_{inlet}*(1/2)*\rho*V^2 \quad (3)$$

$$dp_{exit} = K_{exit}*(1/2)*\rho*V^2 \quad (4)$$

From the initial information for each of these material test options, the best option for low flow rate testing appears to be the TGA equipment owned by the Fire Technology division. This equipment could provide short testing times and good accuracy and repeatability.

The best option for high-flow rate testing appears to be the in-house-built multi-tube test chamber. This test rig could provide a true-to-life environment for material testing and consists of a fairly simple design and build.

2.4.3 SUBTASK 3.3 – LABORATORY-SCALE COUPON TESTING

Thermal Gravimetric Analysis was selected as the method for performing material testing. Though this equipment only provides a low flow environment, it proved to be highly repeatable, quick, and inexpensive for this type of testing. This weight change testing was performed using a Netzsch STA449 F3 with a silicon carbide furnace and alumina crucibles. An example of this equipment can be seen in Figure 2-3. Specifications for the STA 449 F3 and for various furnaces have been presented in Section 2.4.2.2 as shown in Tables 2-21 and 2-22. Background research into the possible oxidation and carburization rates of some of the materials being tested lead to an initial testing time of five hours. It was assumed that this duration at the required temperature would allow enough oxidation to occur on each sample to allow for a meaningful weight loss/gain comparison with the chosen testing equipment.

The Netzsch STA449 F3 uses crucibles that are 3 mm deep and have an inner diameter of only 5.75 mm. An example of these crucibles, as mounted in the Netzsch TGA machine, is shown in Figure 2-7 a. and b. To fit this available volume, the samples of each material were cut down to approximately 5 mm x 3 mm x 1 mm cubes (see Figure 2-8). The samples were initially cut using a wet saw; however, the dimensional accuracy required could not be maintained, so later samples were cut using a wire EDM machine to ensure proper accuracy of the samples. All samples used in the final testing results were deburred and polished with 600-grit polishing strips to obtain a uniform surface finish on all samples. To ensure that the surface area of each sample was known, two measurements were made on each set of faces and the averages of those measurements were used to calculate volumes and surface areas. Each sample was cleaned with acetone and DI water prior to testing to ensure no contamination was present on the samples.

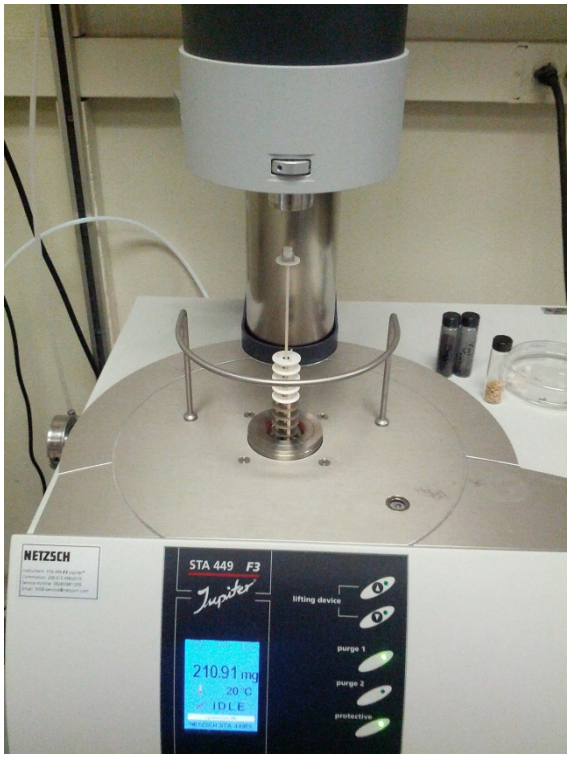

a. b.

Figure 2-7. a. and b. Sample Crucibles Mounted in Netzsch TGA Machine

Figure 2-8. Sample Measuring 3 mm x 5 mm x 1 mm Inside the Crucible

Upon reviewing the test sample dimensional quality and the results obtained from testing, it was determined that the samples used in the first two baseline runs were of low quality and did not offer enough uniformity to instill confidence in the testing results. The samples for the third run were prepared with more dimensional accuracy and uniformity, and subsequently provided much

more confidence in the testing results. A typically prepared sample is presented in Figure 2-9. The results of the third run (-3) will be presented here with the first and second runs being considered only as pre-test runs. Two additional dimensionally precise sample sets have been prepared (-11 and -12) and tested to confirm check repeatability of run 3 test results. In the third run, alloy 800H was eliminated due to the very high weight gains seen in the previous testing, and the 309H and 310H stainless steels were eliminated due to chromium migration and material sensitization that occurs in the desired temperature range. Material sample dimensions are presented in Table 2-26 for the -3, -11, and -12 run (uncoated) samples as well as the niobium- and tantalum-coated samples. The niobium and tantalum sample dimensions are the dimensions prior to coating. The coating process deposits a layer of material around 4 microns thick on the outer surfaces of the samples.

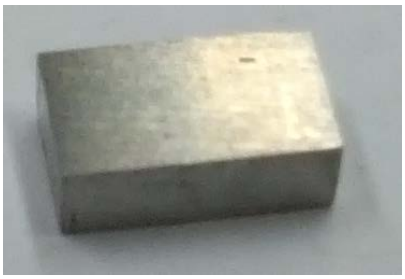

Figure 2-9. Typically Prepared Sample of Inconel 625

Table 2-26. Run 3 Material Sample Dimensions

Sample	Direction	Average (mm)	Area (mm^2)	Area (in^2)	Volume (mm^3)
188 – 3	L	4.9289	55.5402	0.0861	24.2614
	W	2.9883			
	D	1.6472			
188 – N	L	4.9911	55.6721	0.0863	24.2482
	W	2.9655			
	D	1.6383			
188 – T	L	5.0038	56.1334	0.0870	24.5353
	W	2.9883			
	D	1.6408			
282 – 3	L	5.0546	47.9695	0.0744	17.3699
	W	2.8664			
	D	1.1989			
282 – N	L	5.0292	54.0244	0.0837	22.9412
	W	2.8804			
	D	1.5837			

Sample	Direction	Average (mm)	Area (mm^2)	Area (in^2)	Volume (mm^3)
282 – T	L	5.1079	54.4150	0.0843	23.0989
	W	2.8600			
	D	1.5812			
230 – 3	L	4.8895	52.7159	0.0817	22.3972
	W	2.8423			
	D	1.6116			
230 – N	L	4.9276	53.2483	0.0825	22.6771
	W	2.8600			
	D	1.6091			
230 – T	L	4.9098	52.8907	0.0820	22.4749
	W	2.8448			
	D	1.6091			
625 – 3	L	4.9515	54.8584	0.0850	23.8158
	W	2.9223			
	D	1.6459			
625 – N	L	4.9378	53.8855	0.0835	23.1748
	W	2.8715			
	D	1.6345			
625 – T	L	4.9403	54.0253	0.0837	23.2585
	W	2.8804			
	D	1.6345			
263 – 3	L	3.9141	81.1812	0.1258	49.4705
	W	3.9027			
	D	3.2385			
263 – N	L	3.9370	81.2401	0.1259	49.4886
	W	3.9091			
	D	3.2156			
263 – T	L	3.9370	81.1381	0.1258	49.4057
	W	3.8964			
	D	3.2207			
617 – 3	L	4.9428	65.0405	0.1008	33.3406
	W	2.8372			
	D	2.3774			
617 – N	L	4.9428	65.1695	0.1010	33.4421
	W	2.8473			
	D	2.3762			
617 – T	L	4.9327	64.6886	0.1003	33.0672
	W	2.8258			
	D	2.3724			

Sample	Direction	Average (mm)	Area (mm^2)	Area (in^2)	Volume (mm^3)
25 – 3	L	4.9619	54.5358	0.0845	23.6429
	W	2.8816			
	D	1.6535			
25 – N	L	4.9530	54.8791	0.0851	23.8092
	W	2.9274			
	D	1.6421			
25 – T	L	4.9606	54.7643	0.0849	23.7321
	W	2.9134			
	D	1.6421			
X – 3	L	4.9492	46.8470	0.0726	16.8796
	W	2.8448			
	D	1.1989			
X – N	L	4.9441	46.6894	0.0724	16.8225
	W	2.8321			
	D	1.2014			
X – T	L	4.9428	46.2178	0.0716	16.5467
	W	2.8042			
	D	1.1938			

The test program used to evaluate each sample provided an initial temperature ramp rate of 40°C per minute up to 820°C. The temperature was then held at 820°C for five hours, after which the material was allowed to cool back to ambient temperature. An example of the test program can be seen in Figure 2-10.

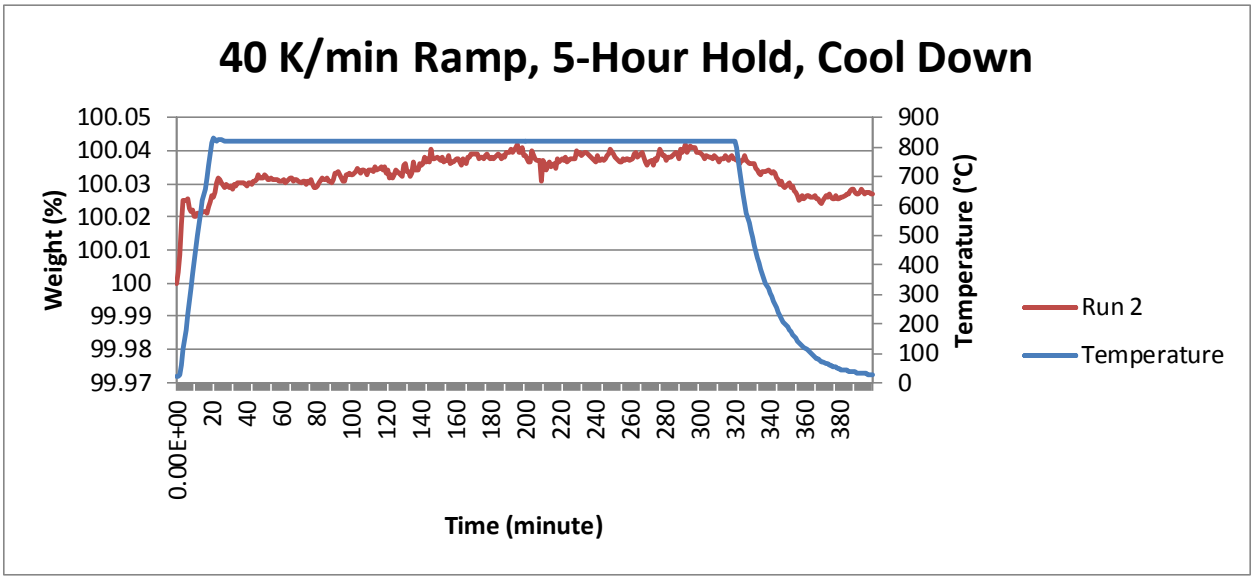

Figure 2-10. Test Program with 40 K/min Ramp Rate, 5-Hour Hold and Cool-down to Ambient

The results obtained from the testing equipment showed weight loss/gain for each sample in milligrams and in weight percentage. For initial comparison purposes, the weight percentage for each sample was inserted into a single graph for each set of tests (see Figure 2-11). Though this graph gives some sense of how the materials react in the environment of interest when compared to each other, minor anomalies can occur within the chamber that may affect the exact weight measurements obtained via the TGA machine during a run. In addition, the weight change comparison with the TGA machine is not a true comparison between the individual samples because the surface area is not included as a parameter of weight change. Since the initial weight and size of each sample varied slightly, the results needed to be converted to a form that was not biased by these differences. To accomplish this, the results were used to calculate and show a weight loss/gain rate per surface area, in this case per in^2. The rate was calculated using the initial measured weight and the final measured weight as these were deemed to be more accurate than the TGA readout. The initial and final measured weights were measured using the same scale, a Pinnacle Balance by Denver Instrument model PI-225D.

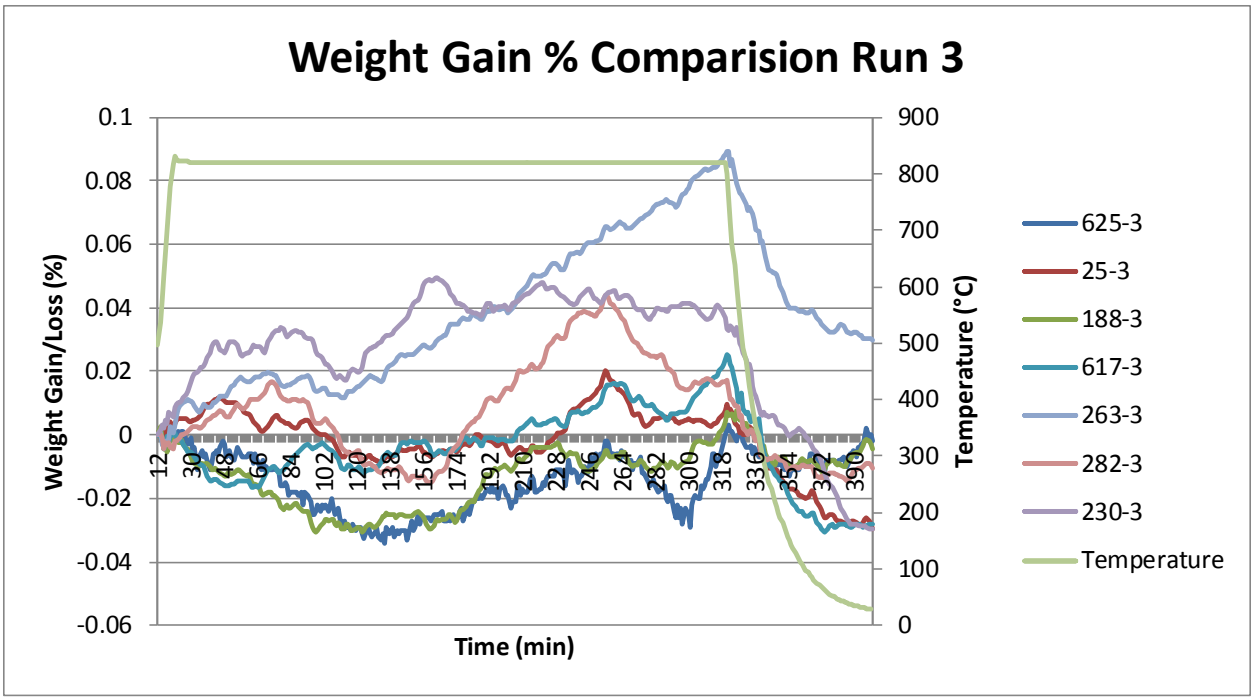

Figure 2-11. Run 3 Weight Change Percentage Comparison Data from Netzsch STA Program

Figure 2-12 shows the rate changes in milligrams per in^2 per hour for the three uncoated test runs with Figure 2-13 showing the average of these runs. The averaged results of these three runs show that alloys 188, 617, and 230 have weight gain rates equal to or less than alloy 625, and that alloys 25, 263, X, and 282 have higher weight gain rates. Although the results of this testing show that alloys 25, 263, X, and 282 have a much higher initial (five hour) oxidation rate, the long term oxidation rate of some of these materials may still be acceptable and long-term testing of these materials is recommended before ruling out any of these materials for this application. The standard deviations for runs -3, -11, and -12 are shown as error bars in Figure 2-13, while the top of the box shows the 75th percentile and the bottom of the box shows the 25th percentile. The weight change variation among the three tests is very large for some samples (e.g., Hastelloy X).

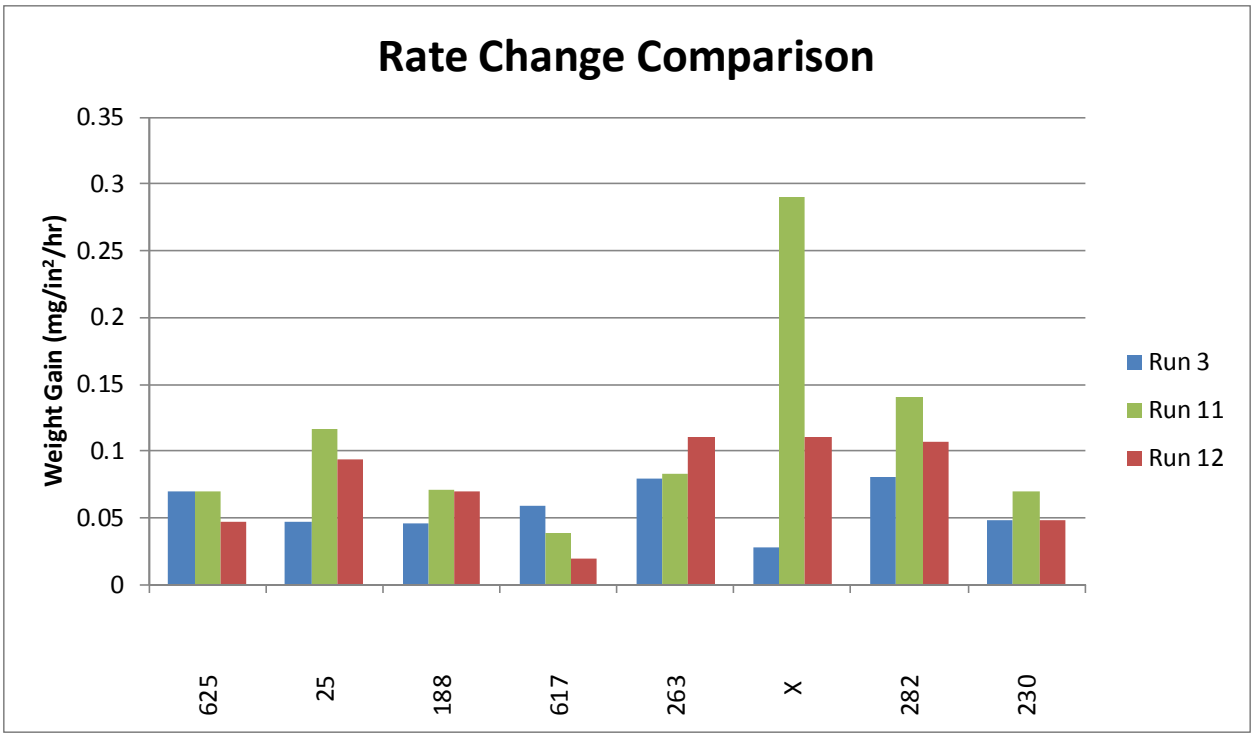

Figure 2-12. Run 3 Weight Change Rate Calculated Using Sample Surface Area

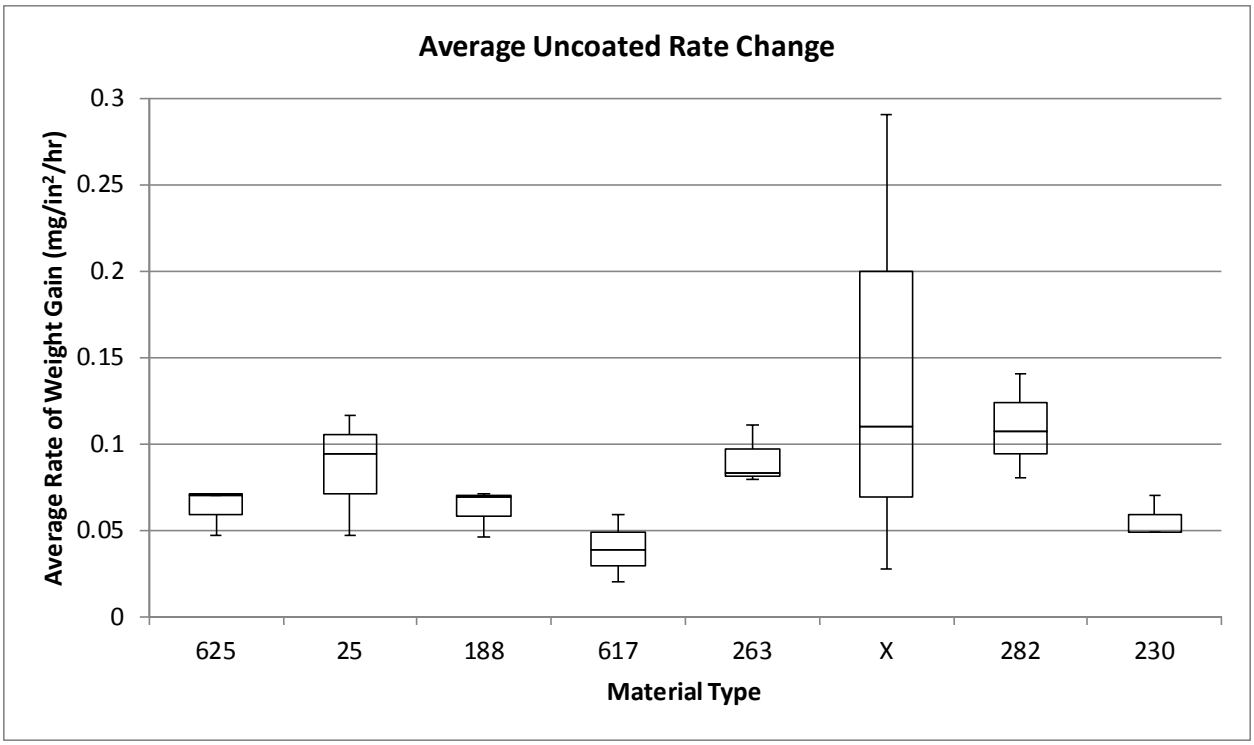

Figure 2-13. Average Weight Change Rate with Standard Deviations and 25th and 75th Percentiles

High magnification images were taken of some of the samples in an effort to measure the thickness of the oxidation layer on the samples. Figure 2-14 shows the oxidation layer on the 625-12 sample. Typical oxidation layer thicknesses measured via visual magnification ranged from around 0.5 microns up to 2 microns. Using these oxide layer thicknesses and the surface area of the samples, and assuming most of the oxidation was a simple nickel oxide (NiO), the minimum and maximum weight gain for several samples were calculated and compared to the measured weight gains. The measured weight gains for most of the samples were within these calculated estimates; however, all of the actuals were near the lower limits. These lower values could indicate that the corrosion layer was a different form of oxide or carbide than the originally assumed NiO, or it could indicate that there was a loss of material through some form of selective leaching.

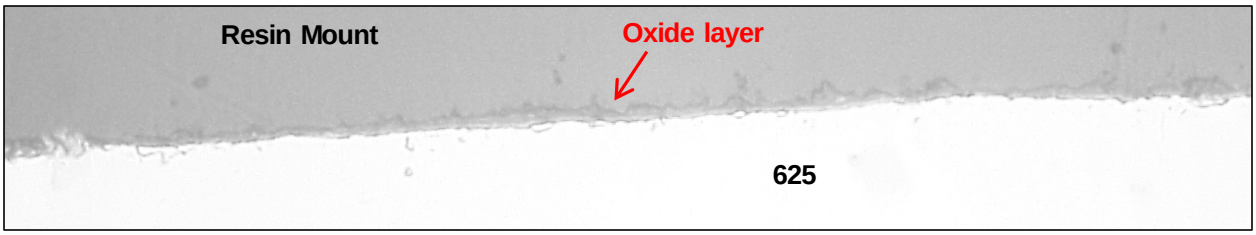

Figure 2-14. 1,000X Magnification of 625-12 Oxidation Layer

Alloy 625 and 282 samples were viewed using a Scanning Electron Microscope (SEM) (Figure 2-15). The results of this analysis showed the formation of a thin oxide film on the surface of both samples. The chemical nature of this film is discussed later with the Energy Dispersive Spectroscopy (EDS) analyses.

The SEM images also showed some form of intergranular attack (IGA) occurring on the alloy 282 sample with a more modest grain boundary attack occurring on the alloy 625 (Figure 2-15). The IGA occurring on the alloy 282 samples after five hours of exposure time penetrated roughly 2 to 3 µm into the material. Aside from the loss of material that can occur from IGA, this degradation mode can be detrimental when the material is in a stressed state. When under a tensile stress, IGA can become stress concentrators and act as initiation points for stress corrosion cracking, which could ultimately lead to early failure of the material. So far, the effects of this IGA have not been addressed by any of the sCO_2 material tests as these tests are typically performed with the material in an unstressed state. Thus, initiation of SCC in these environments has not been seen or studied. Verbal communications with some material test engineers have indicated that this initial IGA may be shallow enough to render it inconsequential, and that the initial IGA may be halted by the formation of the protective oxide layers, while other material researchers have voiced concerns and believe that further testing is required. Further testing of the material should be performed with this in mind, and some tests should be performed with the materials in a similar stressed state as would be found in components used for a sCO_2 power cycle loop (i.e., thermal/mechanical stresses on piping and associated connections).

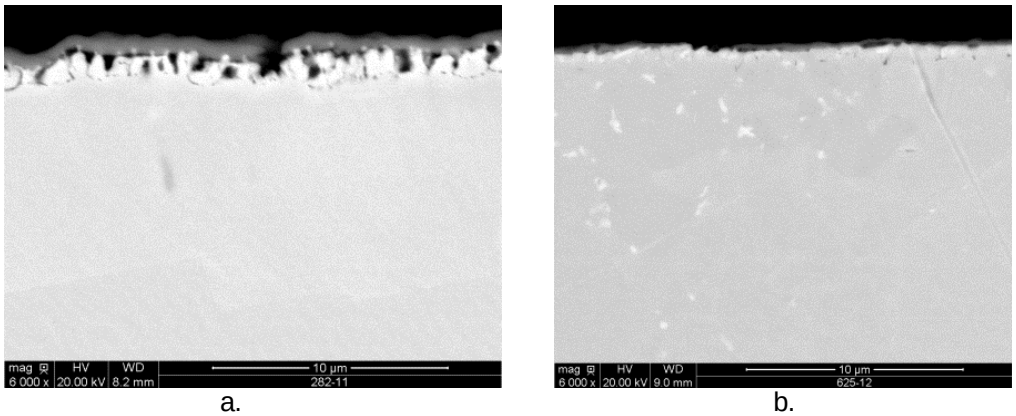

a. b.

Figure 2-15. SEM View of Grain Boundary Attack on a) Haynes 282 and b) Inconel 625 at 820°C in CO_2 Gas after Five Hours of Exposure

In light of the IGA seen on the alloy 282 samples, one 5-hour test run was performed with alloy 740, another high-strength super alloy being considered for supercritical CO_2 applications, and one that was considered a good substitute should alloy 282 show signs of concern in the atmosphere tested. Though only one test sample of alloy 740 was run, the weight change results are compared to that of the other materials in Figure 2-16. The rate of weight gain for this one sample does not show a large deviation from that of the other materials tested and is very comparable to the average weight change in alloy 282. Alloy 740 also showed IGA occurring on the surface of the sample and penetrating up to 5 µm into the material after only five hours of testing (Figure 2-20). EDS analysis was also performed on this test sample and the results are discussed later in this section.

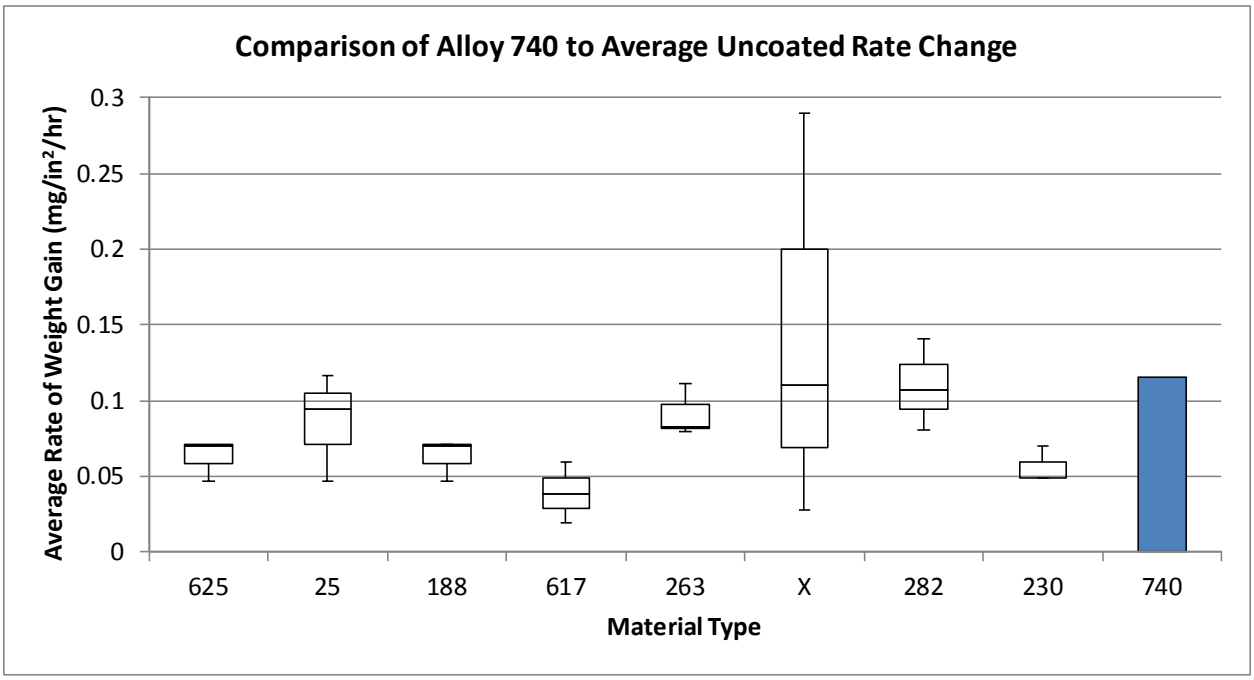

Figure 2-16. Comparison of the Single 5-Hour Test Weight Change Results of Alloy 740 with the Average Weight Change Rate of the Other Materials Tested

Energy Dispersive Spectroscopy analysis was performed on the 5-hour exposed samples of the 282, 625, and 740 materials and dot plots of the alloys' elemental composition were made (see Figure 2-17 for alloy 282 SEM and dot plot views). The oxide layers on the alloy 282 sample contained relatively high amounts of chromium, titanium, and oxygen. These elements would be expected to form in the oxide layer and possibly act as protective barriers for the underlying material. Note that there was a depletion of chromium and titanium out of the base material below the oxide film. Relatively high concentrations of aluminum were present in the area of IGA with a slight depletion zone just below it. This suggests possible migration of aluminum to form an oxide layer on the surface of the material. It is unclear how the depleted regions affected the corrosion resistance properties of the alloy. Some carbon buildup appeared to be occurring on the outer oxide layer; however, the carbon did not appear to have a large presence in the base material, indicating that material carburization was not occurring at the time in this alloy. Elemental analysis of the unexposed base metal and oxide layer of the 5-hour exposure 625 sample are presented in Figure 2-18 and Figure 2-19.

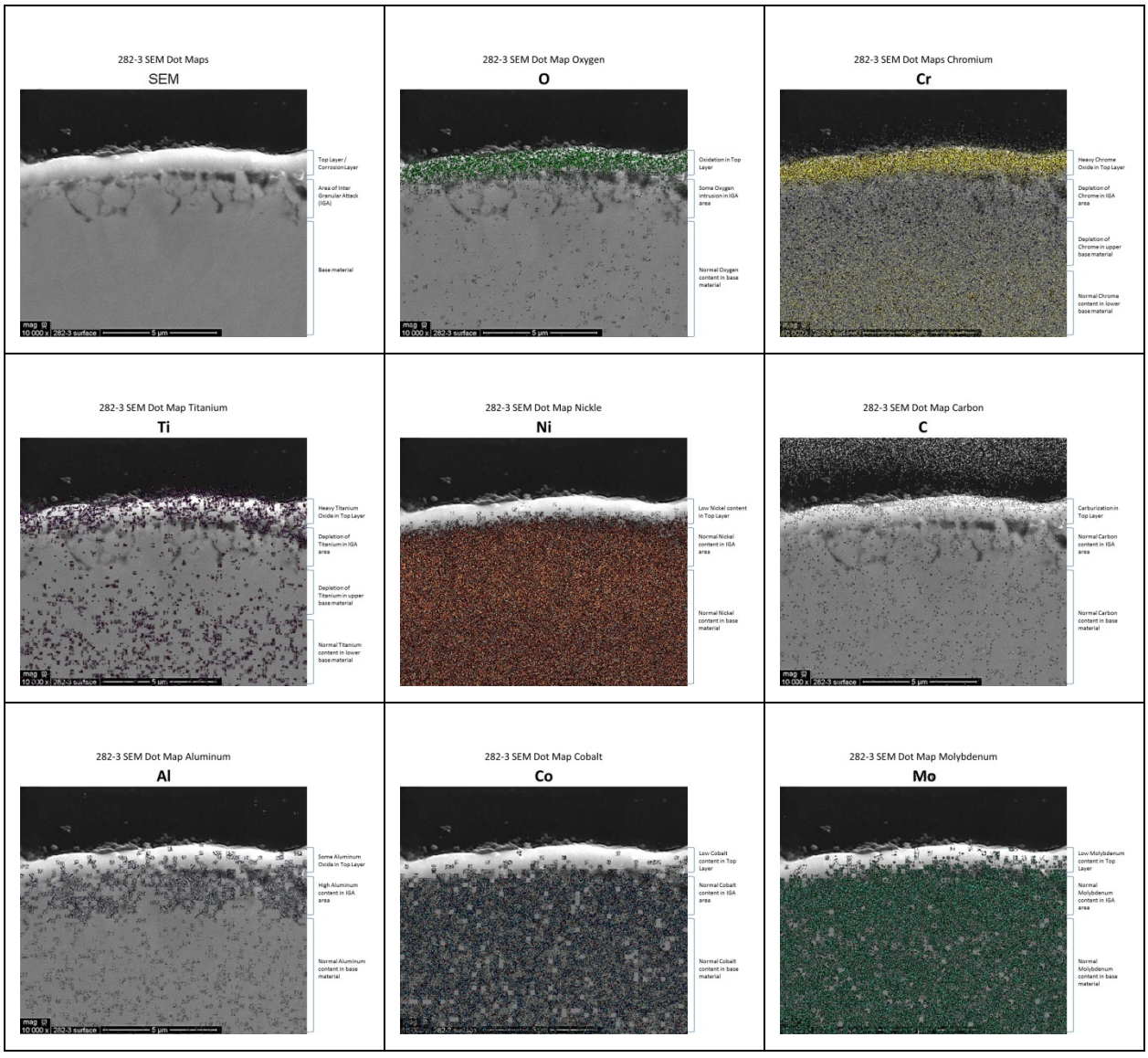

Figure 2-17. SEM View and EDS Dot Map for Alloy 282 at 810°C in CO_2 gas after a 5-Hour Exposure Test

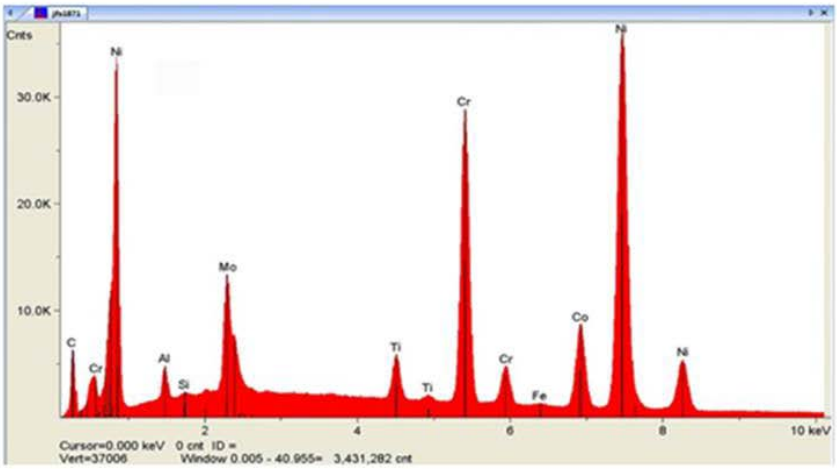

Elt.	Conc. (wt%)
Al	2.35
Si	0.47
Ti	2.28
Cr	19.45
Fe	0.22
Co	10.20
Ni	56.38
Mo	8.66

Figure 2-18. Elemental Analysis for Alloy 282 Base Metal Prior to Exposure Test

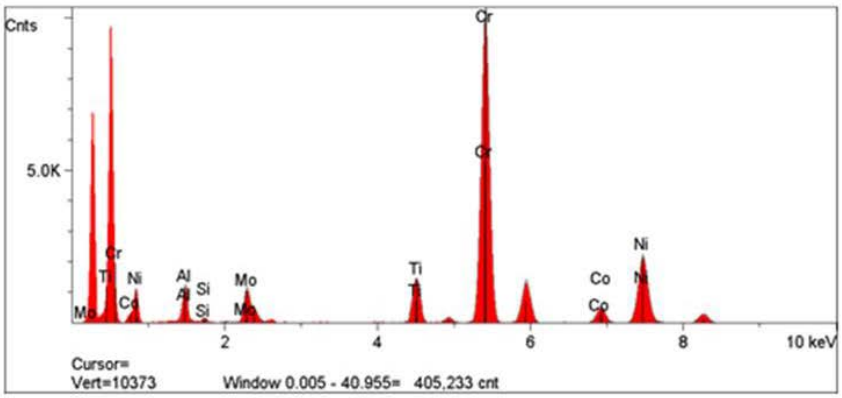

Elt.	Conc. (wt%)
Al	4.97
Si	0.60
Ti	5.11
Cr	53.41
Co	5.30
Ni	25.73
Mo	4.88

Figure 2-19. Elemental Analysis of Oxide Layer on Alloy 282 at 820°C in CO_2 Gas after a 5-Hour Exposure Test

The EDS dot plot analysis of the 5-hour exposure test of alloy 740 (Figure 2-20) shows a thick upper oxide layer consisting mostly of chromium oxide with some titanium oxide interspersed. A lower oxide layer has formed around the areas of IGA. This lower oxide layer consists mainly of aluminum oxide with some titanium oxide interspersed. The area of IGA shows chromium depletion and may have a slightly higher concentration of molybdenum than that of the base material. Just below the IGA area is a shallow band of aluminum depleted material. Carbon is fairly evenly distributed through the material showing no signs that carburization is occurring.

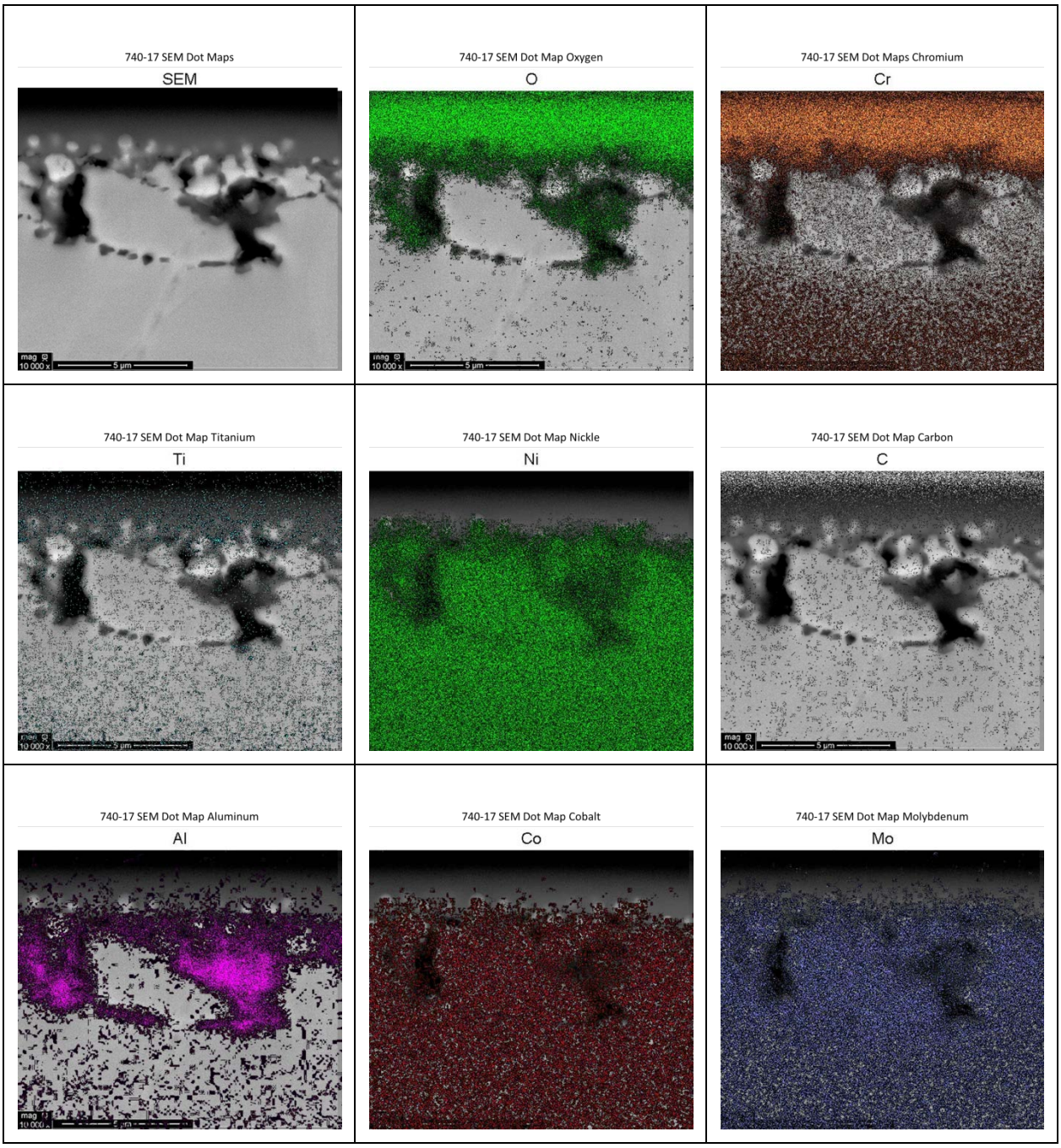

Figure 2-20. SEM View and EDS Dot Map for Alloy 740 at 810°C in CO_2 gas after a 5-Hour Exposure Test

The EDS analysis of the 5-hour alloy 625 test samples showed that the oxide layer that formed on the surface of this material was a chromium oxide without the titanium that was present in the 282 alloy (Figure 2-21). A small band of chromium depletion could be seen just below the material surface in the area of the observed IGA. One prominent feature appearing in the alloy 625 samples that was not present in the alloy 282 was the initial formation of carbides in the base material. Though the carbide formations were not analyzed in this study, the initial SEM image clearly showed the formation of carbides as white nodules in the base material and near the

sample surface. The phase changing of alloy 625 and the formation of carbides at various temperatures have been studied and are fairly well understood [Floreen, 1994 (27)]. Elemental analysis of the unexposed base metal and oxide layer of the 5-hour exposure 625 sample are presented in Figure 2-22 and Figure 2-23.

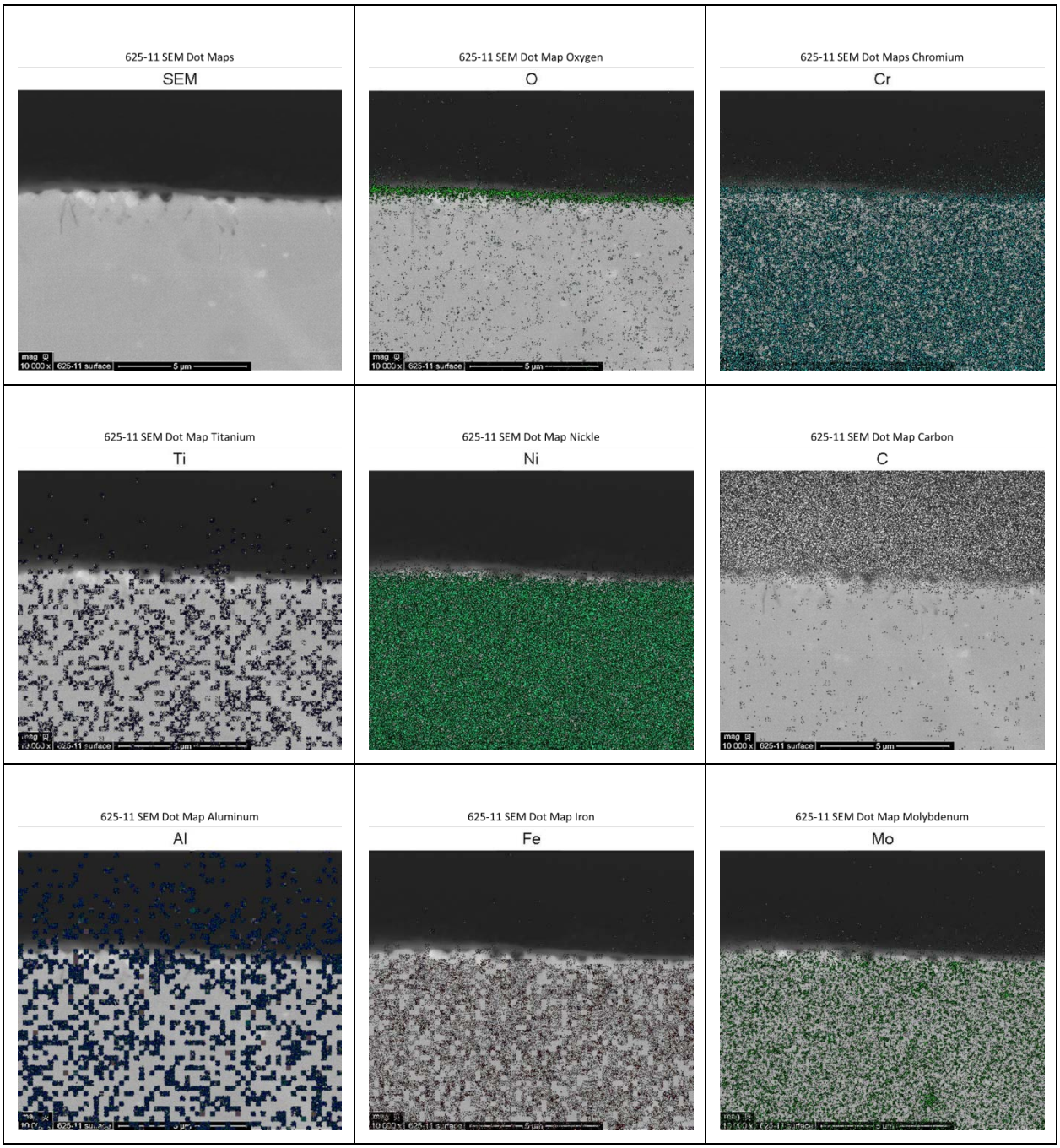

Figure 2-21. SEM View and EDS Dot Map for Alloy 625 at 810°C in CO_2 gas after a 5-Hour Exposure Test

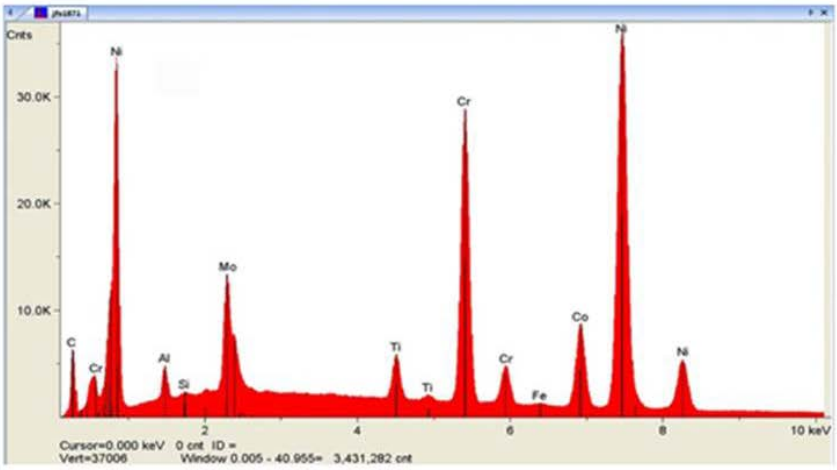

Elt.	Conc. (wt%)
Al	2.35
Si	0.47
Ti	2.28
Cr	19.45
Fe	0.22
Co	10.20
Ni	56.38
Mo	8.66

Figure 2-22. Elemental Analysis for Alloy 625 Base Metal Prior to Exposure Test

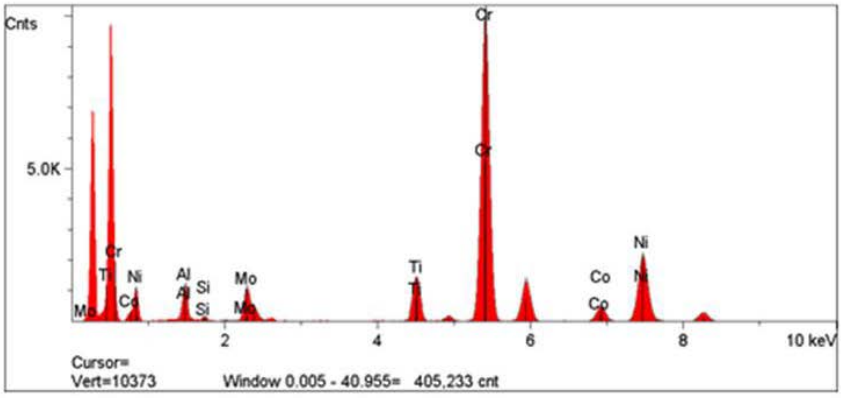

Elt.	Conc. (wt%)
Al	4.97
Si	0.60
Ti	5.11
Cr	53.41
Co	5.30
Ni	25.73
Mo	4.88

Figure 2-23. Elemental Analysis of Oxide Layer on Alloy 625 at 820°C in CO_2 Gas after a 5-Hour Exposure Test

To better understand the progression of the degradation observed in the 5-hour tests, one sample of alloy 282 and one sample of alloy 625 were prepared and tested for almost a week (169 hours for 282 and 158 hours for 625) under the same environmental conditions as the previous samples (40°C/min ramp rate to 820°C then hold in slow flow CO_2). These samples were characterized using the SEM and EDS analysis. The results of these longer tests were compared to the 5-hour test sample results. The images of alloy 282 in the SEM appeared to have less IGA present than the 5-hour test and the outer oxide layer appeared to be thinner (Figure 2-24). The makeup of the outer oxide layer was chromium oxide and titanium oxide, and an aluminum oxide layer had formed as an inner oxide layer. The material just below the sample surface showed a slight depletion of chromium and titanium, though this depletion was much less evident than with the 5-hour samples. This band showed a depletion of aluminum, which may be tied to the formation of the aluminum oxide layer. No large concentrations of carbon were present in the base material, indicating that carburization had not occurred to that point.

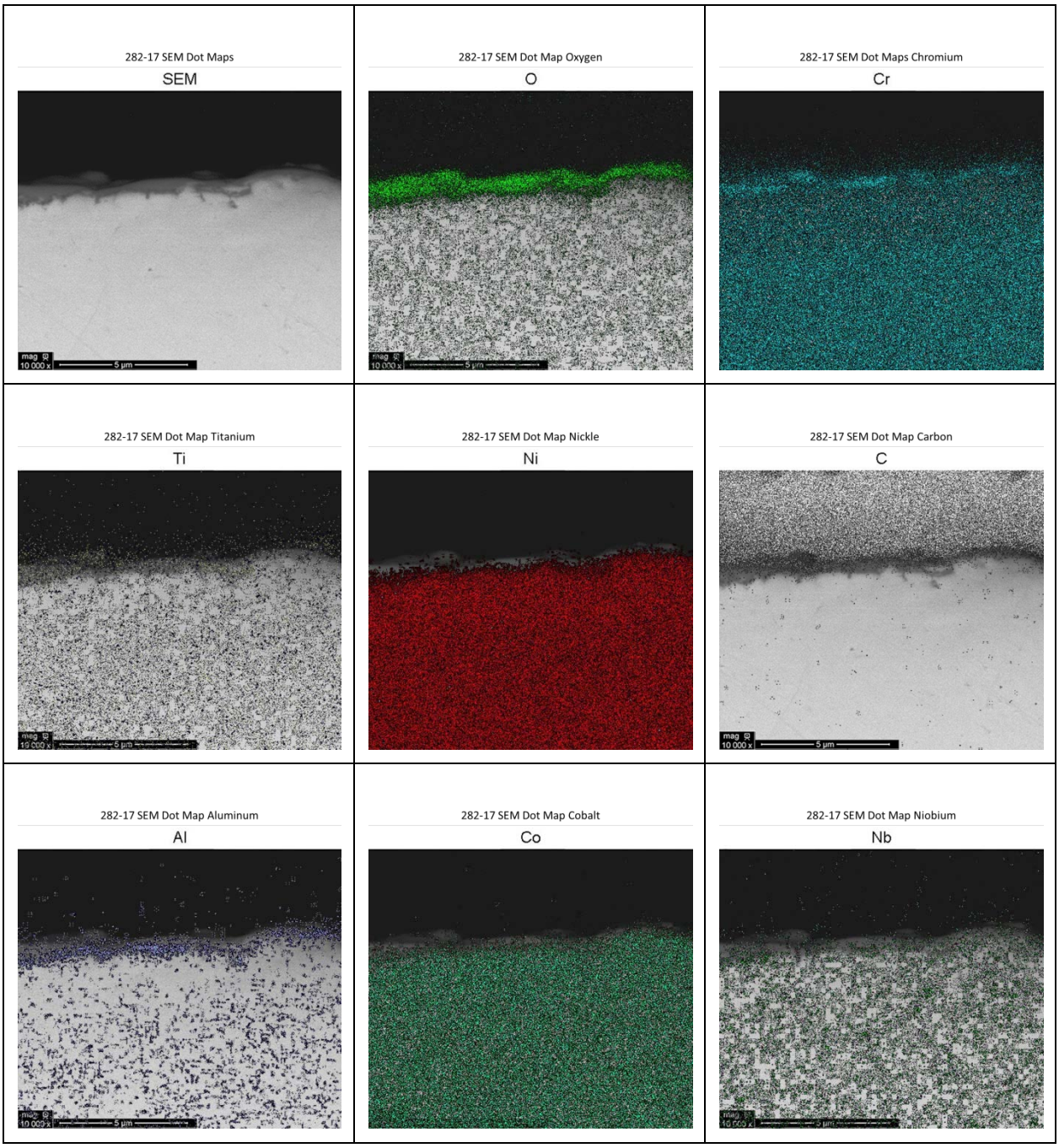

Figure 2-24. SEM View and EDS Dot Map for Alloy 282 at 820°C in CO_2 gas after a 169-Hour Exposure Test

The SEM images of the alloy 625 sample exposed for one week showed that the oxide layer was much thicker than it was with the 5-hour exposure (Figure 2-25). In addition, the surface of this sample, though prepared similar to the other samples, had pitting that gave the appearance of possible grain fallout. The outer oxide layer appeared to be formed almost solely of chromium oxide. No depletion of the various elemental components was evident in this sample. Relatively large nodules of molybdenum, niobium, and silicon carbides were present both in the base material and towards the surface. Overall, the activity seen in these two materials, when exposed

to 820°C, appeared to be similar to the results of material tests performed by others at lower temperatures but for longer exposure times [Pint, March 2016a (25)]; [Pint, March 2016b (26)].

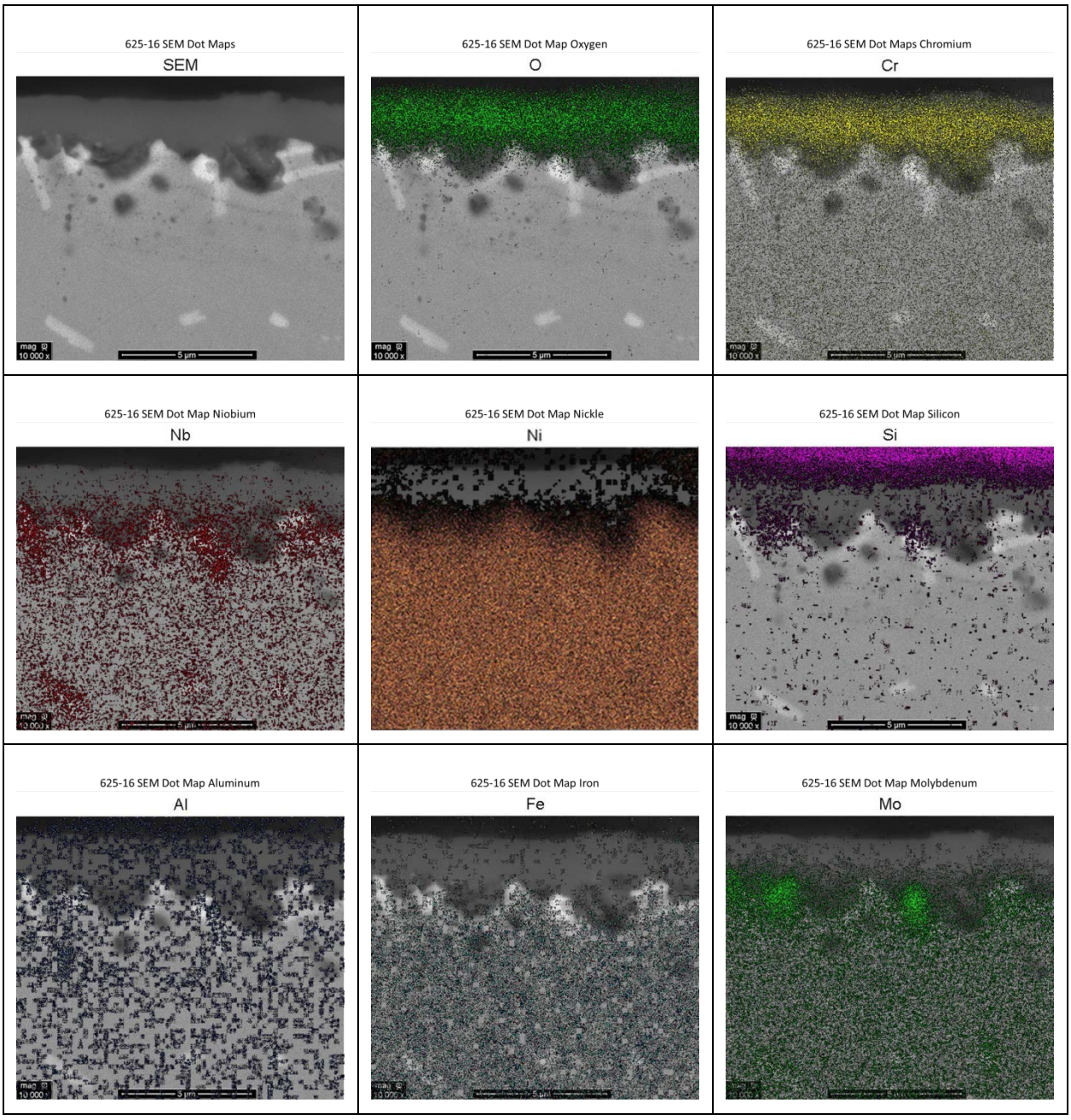

Figure 2-25. SEM View and EDS Dot Map of Alloy 625 at 820°C in CO_2 Gas after a 158-Hour Exposure Test

Two sets of test samples were prepared for additional testing incorporating protective coatings. The first set had been coated with niobium and the second set had been coated with tantalum. The deposition process used on these samples was Plasma Vapor Deposition (PVD), sometimes called sputtering. These samples were tested using the same program setup that was used for the uncoated samples, and a comparison of weight change rates was made for each of these

runs. Figure 2-26 shows the weight gain comparison between the averages of the uncoated samples, the niobium-coated samples, and the tantalum-coated samples.

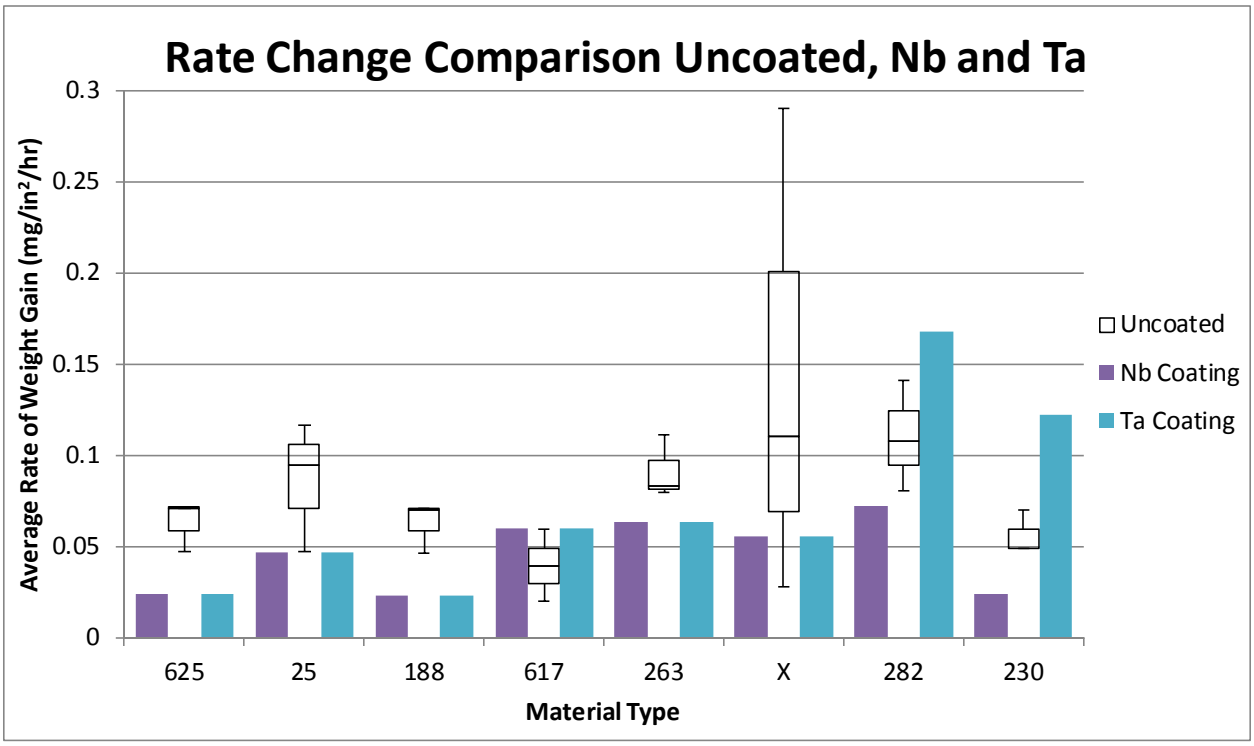

Figure 2-26. Weight Gain Rate Comparison for Average Uncoated, Niobium-Coated, and Tantalum-Coated Samples

The results of this comparison showed that the tantalum-coated samples appeared to have a higher rate of weight gain on alloys 617, 282, and 230, whereas, the niobium-coated samples showed decreased weight gain rates in seven of the eight samples with the only increased rate of weight gain occurring in alloy 617. However, these results were from only one run of the niobium and tantalum samples and, thus, no statistical significance can be associated with these results. In addition, these samples have not been viewed using SEM nor has EDS analysis been performed, so the underlying structure and boundary interactions in these samples are as yet unknown.

Three additional coated sample sets were prepared with a layer of chromium, applied by a nickel chrome plating process. An initial 5-hour test was performed on one of the chrome coated 625 samples. This test used the same test parameters as the tests performed on the niobium and tantalum coated samples. During this test, the nickel chrome plating turned black, lost adhesion to the base metal, and flaked off the sample. The samples were sent back to the plating company for adhesion testing and it was determined that the plating process and adhesion were correct at ambient temperatures. The company then exposed one set of samples to 820°C in air for five hours and the plating turned black, lost adhesion, and flaked off the samples. Figure 2-27 a) and b) show the flaked sample after our testing and after the temperature test performed by the provider. It was determined that the chrome plating was oxidizing at the elevated temperatures and was losing the bond with the base nickel coating. Based on these results, the tests of chrome-plated samples were stopped and no further testing with chrome plating has been performed.

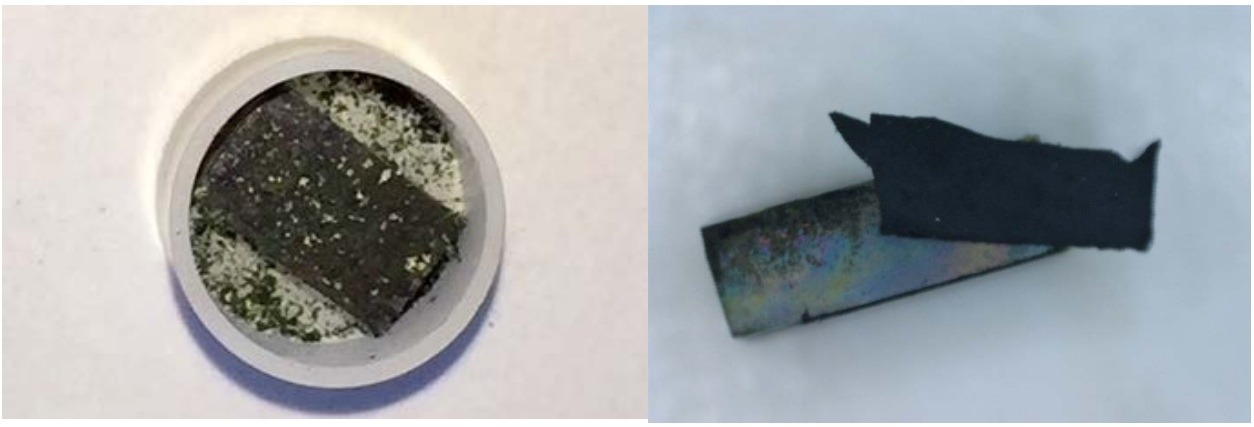

a) b)

Figure 2-27. Chrome Plating Detachment after 820°C Exposure for Five Hours on a) Alloy 625 Sample Tested at SwRI, b) Material Samples Exposed at Plating Vendor Facility

In summary, the 5-hour test results from this work indicated that all materials tested had equal or lower initial weight gain rates compared with alloy 625. The weight gain rates were reasonably low and indicated that the materials may be a decent fit for the high-temperature CO_2 recuperator under consideration for this project. Intergranular attack was observed in test samples of alloys 282 and 740, but the long-term effects of this attack cannot be evaluated with short-term testing in a low-flow environment. Other considerations for any of these materials include the mechanical properties at elevated temperatures, and the cost and availability of the material. This work also shows that the use of niobium and tantalum coatings may be beneficial in these environments, effectively expanding the list of usable materials in high-temperature CO_2, assuming cost of material and processing is not prohibitive. Chrome-coated 625 sample testing showed that the chrome plating oxidizes and de-bonds quickly within a 5-hour test and may not be suitable for this application.

These test results provide only a comparative view of the initial weight change rate of these materials (5-hour exposure for all tested materials and 7-day exposure for alloys 625 and 282) while this equipment is expected to run for hundreds of thousands of hours. In addition, some of these initial rates of weight gain may decrease drastically with time while others may remain high, leading to a much shorter time to oxidation layer breakaway. An example diagram of oxidation leading to breakaway is presented in Figure 2-28; however, the curve shape may differ for various materials and may also depend on the gas flow rate across the material. To understand fully how any of these materials would perform for the life of the recuperator, testing should be performed for a much longer period (typically 10,000 or 100,000 hours) in this environment, and startup and shutdown thermal cycles should be taken into consideration.

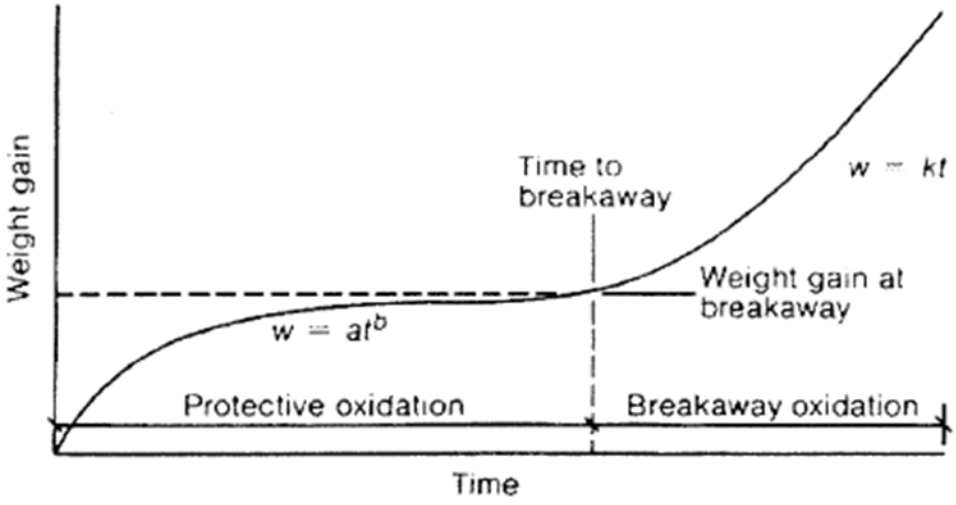

Figure 2-28. Diagram of Oxidation Leading to Breakaway Growth [Rowlands (20)]

2.5 TASK 4 ACCOMPLISHMENTS – RECUPERATOR MECHANICAL REDESIGN

This section describes the modeling and redesign effort to upgrade the recuperator design to operate at the conditions developed in Task 2 (Section 2.3.1).

2.5.1 SUBTASK 4.1 – DEVELOPMENT AND VALIDATION OF MECHANICAL MODEL FOR EXISTING RECUPERATOR

This section presents the model development and analysis results for the existing Mercury 50 recuperator. The recuperator core is the primary region where new operating conditions are expected to require significant design changes and challenging design work. Thus, the proposed analysis approach will focus on using the localized model approach discussed above in order to evaluate recuperator effectiveness, pressure drop, and mechanical stresses. Detailed analysis of the ducting, tie rods, and overall recuperator assembly will not be performed, since existing design methodology is expected to be sufficient for the new operating conditions.

The model geometry and material information were provided by Solar Turbines, Inc. and are discussed in Section 2.5.1.1. Due to the large number of small geometric features, it is not computationally possible to model the entire recuperator in a single model (fluid or structural). Thus, analysis is performed on critical/representative areas within the recuperator and results are scaled up to the full-size recuperator model (this approach is consistent with practices in the literature as presented in Section 2.5.1.2). This section discusses the fluid/heat transfer models and structural models separately in Sections 2.5.1.3 and 2.5.1.3.1, respectively.

2.5.1.1 Existing Recuperator Design

The existing recuperator for the Mercury 50 gas turbine was developed in the 1990s and has been used successfully and reliably for many years. The technology has also been licensed and applied to a number of micro-turbines. These recuperators are composed of air cells constructed from 0.004 - 0.008 inch thick sheets of alloy 625 folded into a corrugated pattern, as shown in Figure 2-29. This folded shape maximizes the primary surface area that is in direct contact with

the gas turbine exhaust and compressor discharge gas streams. Pairs of these sheets are welded together around the perimeter to form air cells. There are no internal welds or joints within the air cells. Groups of these cells are sandwiched together via an arrangement of clamping bars and are welded to intake and discharge headers to form the recuperator assembly.

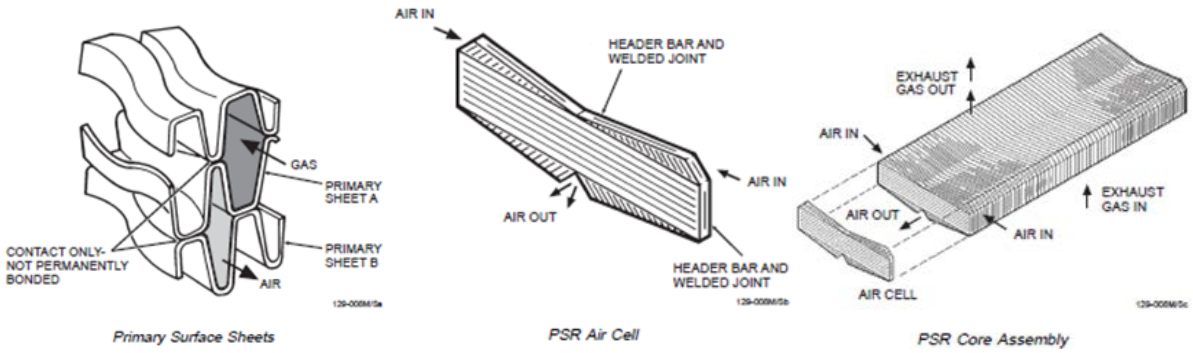

Figure 2-29. Existing Primary Surface Recuperator Design Overview [Solar Turbines (21)]

The primary surface recuperator design has several major advantages over traditional plate-fin and shell-and-tube heat exchangers. The clamped design allows the assembly to flex freely, minimizing stresses at weld locations due to thermal transients, and avoiding low-cycle fatigue failures. The contact surfaces provide multiple friction interfaces for energy absorption, reducing the risk of high-cycle fatigue. In addition, to improved reliability, primary surface recuperators are significantly smaller and lighter than competing technologies and have superior heat transfer effectiveness (92 - 93%) compared to competing technologies, as illustrated in Figure 2-30.

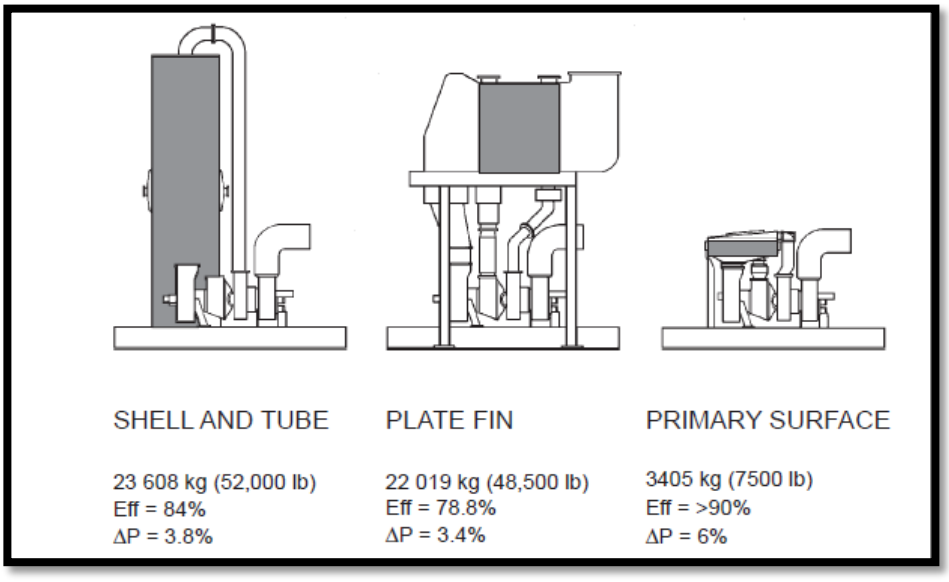

Figure 2-30. Recuperator Technology Comparison [Solar Turbines (17)]

Detailed geometry for the existing recuperator core design was provided by Solar Turbines, through a collection of solid models and drawings for the folded sheets in the recuperator core. This file handoff was accompanied by several teleconference discussions and a design handoff

meeting at Solar Turbine's facility in order to view recuperator hardware and obtain clarifications regarding the overall core construction and assembly. The air and exhaust flow paths through the core are shown in more detail in Figure 2-31. This figure shows a half of the air cell from Figure 2-29 since the two sides are symmetric. The air and exhaust gases enter and exit through a triangular intake and exit through cross-flow sections (brown), and the majority of heat transfer occurs in the counter-flow (yellow) section. The cross-flow sections use corrugated sheets to guide the air/gas flow evenly across the center section. These corrugations also provide stiffness to support the nine (9) bar differential pressure load from air to gas sections. These sheets are shown in the isometric view or a single cell in Figure 2-32. The cross-flow-guide sheets end where they meet the counter-flow section, where the primary surface sheet pattern shown in Figure 2-29 begins.

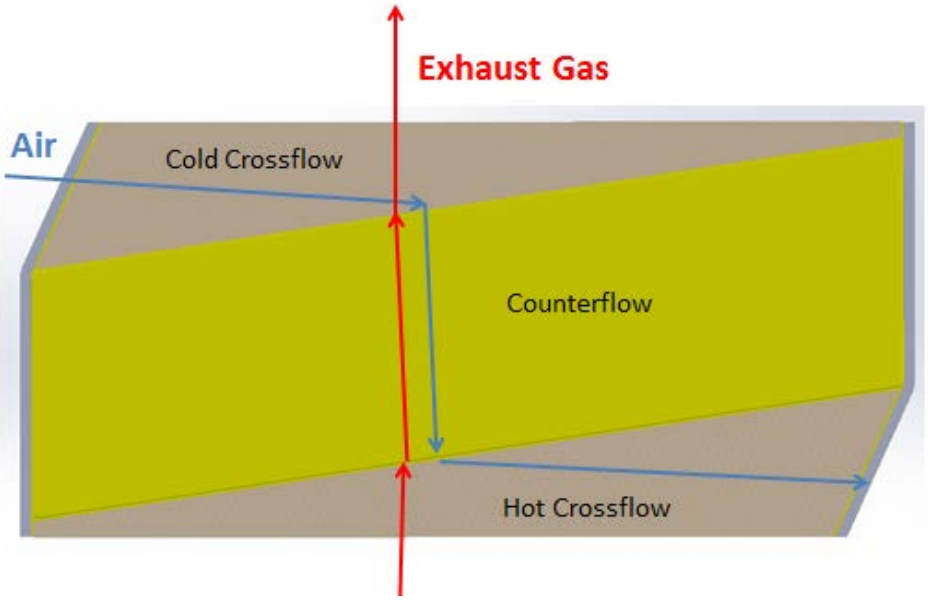

Figure 2-31. Side View of Recuperator Gas Flow Paths

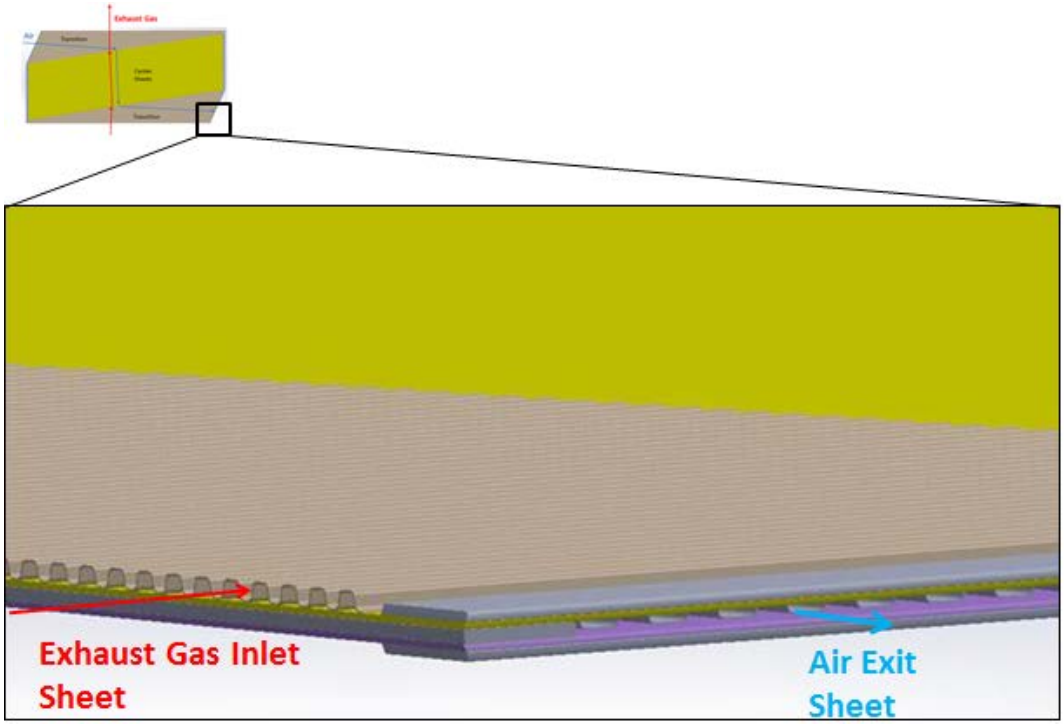

Figure 2-32. Isometric View of Recuperator Inlet / Exit Corrugated Sheets (Single Cell)

The entire recuperator is assembled by stacking multiple cells together and using tie rods to apply a compressive load to the overall assembly. The compressive tie rod load is supported by the header bars along the sides (shown in grey in Figures 2-31 and 2-32) and not by the transition sheets or primary surface sheets (these support the differential pressure load and thermal loads). The header bars are also welded along the boundaries of each cell in order to prevent leakage between air and the exhaust gases. The entire stacked assembly is then welded to air inlet and exit ducts along the inlet and outlet surfaces and exhaust gas ducting is welded along the remaining edges in order to direct the inlet and exit exhaust flow. The final assembly is shown installed with a Mercury 50 gas turbine in Figure 2-33.

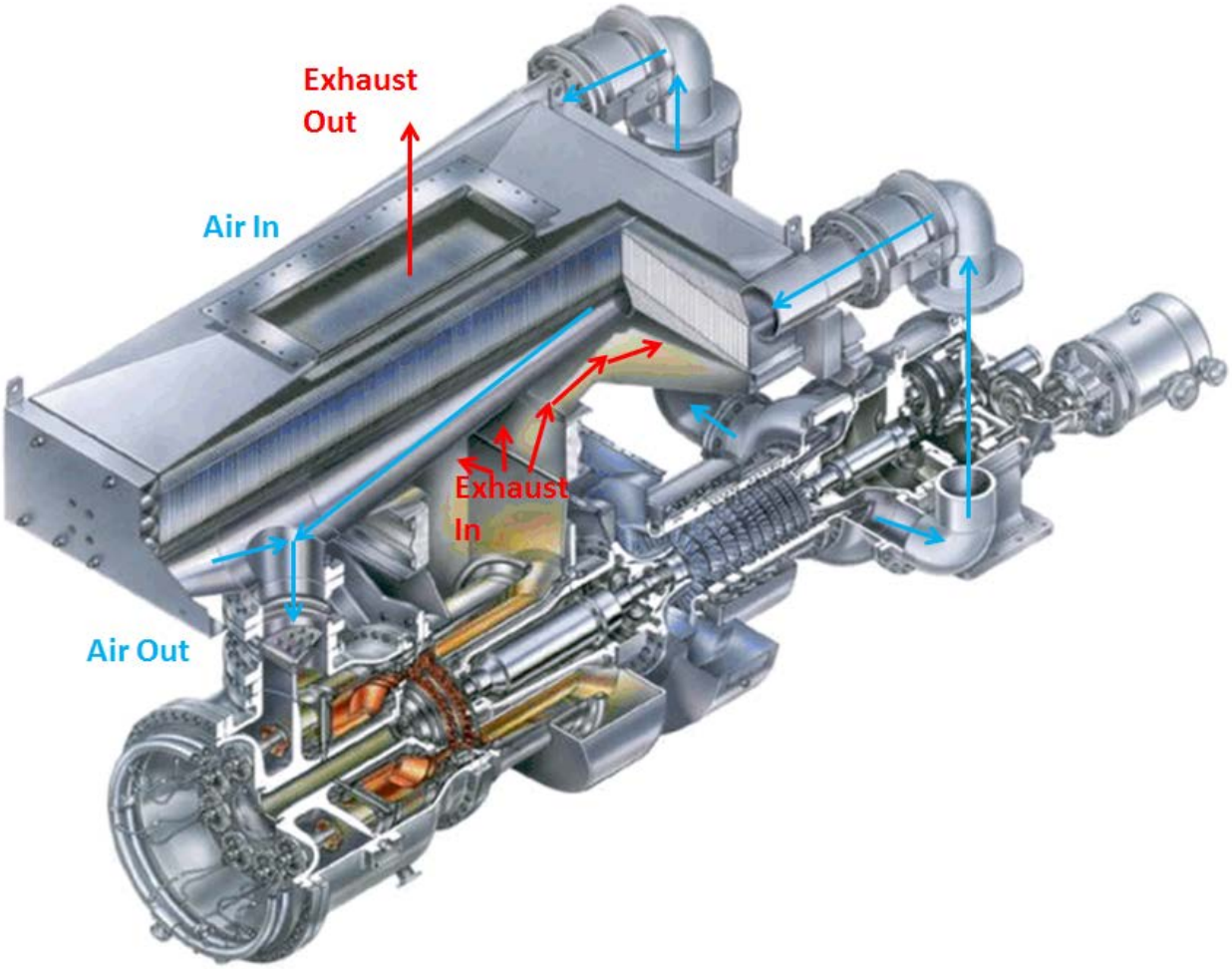

Figure 2-33. Installed Recuperator Assembly

2.5.1.2 Literature Review of Complex Recuperator Modeling Approach

In theory, analyzing a complex geometry recuperator is very similar to modeling a simple recuperator. The only difference is that in a complex geometry recuperator, different parts of the heat exchanger are modeled computationally to determine inputs to a simple 1D or 2D temperature model, whereas simple models have well known friction factors and Nusselt numbers. [Abdulbasit (22)] and [Mylavarapu (23)] both incorporate this strategy in predicting the effectiveness of fairly complex heat exchanger geometries. Abdulbasit models a single corrugated channel having different shapes and cross sections using ANSYS CFX. Using these complex flow results, Abdulbasit determines heat transfer coefficients, Reynolds number, and Nusselt number for the flows in the entrance region and the fully-developed flow region in each tube cross section. He then applies the results to a model of the whole recuperator and compares the results to measurement. Generally, he obtains good agreement with the results. A cross section of the flow profile obtained in his analysis is shown in Figure 2-34 and correlated friction factor to Reynolds number is shown in Figure 2-35.

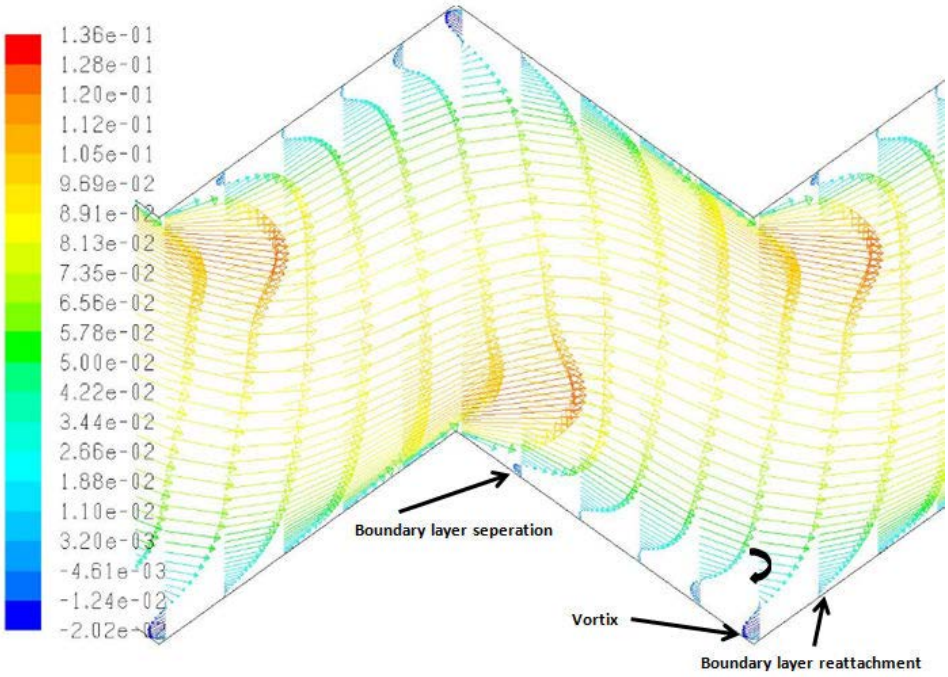

Figure 2-34. Flow Velocities for Fully-developed Flow Regions 0

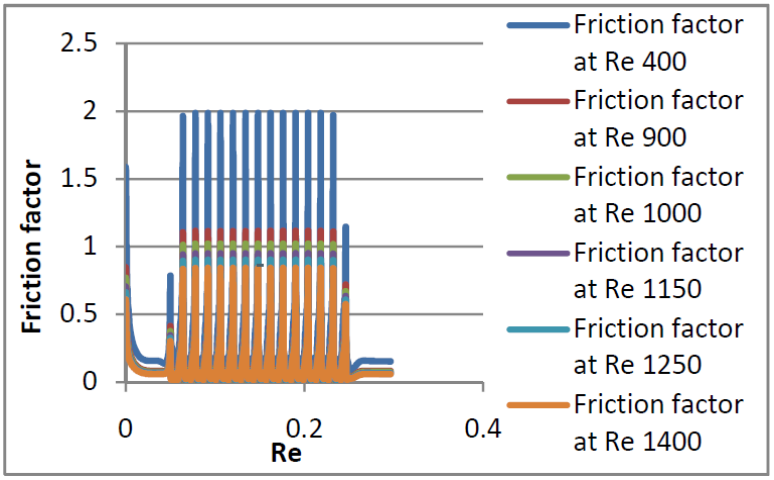

Figure 2-35. Correlation between Friction Factor and Reynolds Number 0

2.5.1.3 Fluid/Heat Transfer Models

In order to analyze the performance of the heat exchanger as a system, information about the heat transfer performance of both the hot and cold sides of the heat exchanger is needed for both the cross-flow and counter-flow regions.

For the heat exchanger model, this heat transfer information takes the form of an overall heat transfer coefficient (HTC) that is a combination of the HTC on the hot side, the HTC on the cold

side, as well as the thermal resistance provided by the separator sheets. It is anticipated that these HTCs will be different for each zone in the heat exchanger and, also, be a function of fluid temperature. For a simple geometry, the evaluation of the HTCs would be a simple task of consulting a published correlation. As no correlation exists for the unique recuperator geometry, a more in-depth analysis is needed. By using Computational Fluid Dynamics (CFD), the HTCs can be approximated on both the hot and cold sides of the heat exchanger.

There are several different methods that could potentially be used to evaluate the heat transfer performance of a particular geometry from the recuperator. Three of these are a fluid-only model with constant surface heat flux, a fluid-only model with constant surface temperature, and a fluid and solid conjugate heat transfer model. The first two methods make use of Newton's law of cooling and only differ in which quantities are specified, and which are calculated during the simulation. The conjugate heat transfer method computes the fluid in both the hot and cold sides of the heat exchanger along with the temperature distribution in the separator sheet. The resultant outlet temperatures can then be used to derive a bulk HTC.

Due to the similarity to anticipated temperature profiles and simulation simplicity, the constant wall temperature method was chosen. In this method, the wall temperature is held constant and the bulk temperature and resultant wall heat fluxes are calculated as part of the CFD solution. In the cross-flow sections of the heat exchanger, a single fixed temperature was used while in the counter-flow section of the heat exchanger a linearly varying temperature profile was used.

The following sections provide details about this computational method using the cold side of the cross-flow region as an example. The same methodology for pre-processing and post-processing was used for the other sections as well for both air and CO_2.

2.5.1.3.1 Geometry

Figure 2-36 below shows one period of the air-side flow path in the cross-flow region:

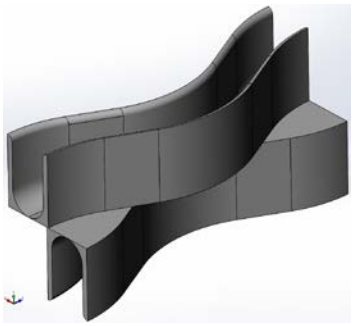

Figure 2-36. Air-side Flow Path in the Cross-flow Region

As can be seen in the figure, only one period was extracted from the solid model. Using the CFD preprocessor, it is trivial to duplicate a mesh of a single period to make a simulation of as many periods as desired. Also, the model was cut to take advantage of periodicity so that only one flow channel is needed to be meshed. Figure 2-37 shows an image of the computational mesh.

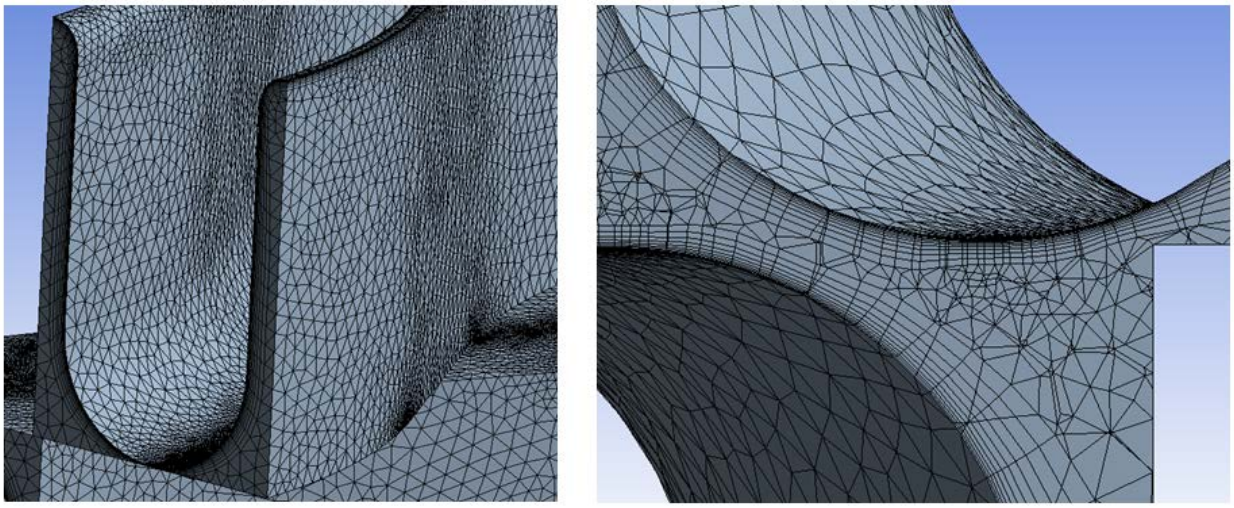

Figure 2-37. Detail of Boundary-layer Inflated Tetrahedral Mesh

As can be seen in the figure, the mesh is comprised of a triangular surface mesh that is inflated with prism layers. Between these prism layers, a free tetrahedral mesh was used. The mesh shown has approximately 1 million elements per period with 10 layers of boundary layer inflation.

The other sections of the heat exchanger were cut and meshed with a similar level of refinement. Due to the resultant wall Y+ values, as well as a mesh independence study, this level of refinement was deemed acceptable.

2.5.1.3.2 Boundary Conditions and Simulation Parameters

As the heat transfer split between the entrance, cross-flow, and exit regions of the heat exchanger was not specified, it was assumed that 80 percent of the temperature change occurred in the counter-flow section of the heat exchanger. By simulating the flow through the heat exchanger at a wide range of temperatures, the impact of temperature can be included in the resultant expression for the HTC.

As it was not anticipated that the HTC would be a very strong function of inlet pressure, and the pressure range for the entire heat exchanger is small, for simplicity, the inlet pressure was modeled as the mean total pressure between the inlet and outlet for all cases. The calculation for per-section mass flow assumed that there was a uniform distribution of mass flow through all the flow channels. For the cross-flow sections, the equation for the applied wall temperature was calculated assuming a linear variation in temperature on the opposing side of the heat exchanger. For the cross-flow sections, the wall temperature was fixed at the anticipated wall temperature on the other side of the heat exchanger.

Since the Reynolds number is based on the average velocity and using a characteristic length equal to the distance between the separator sheets in one, the straight sections at the inlet was below 500, the flow in the counter-flow regions is laminar, and no turbulence model was used. In the cross-flow regions, the hot side of the heat exchanger was also laminar, but the cool side of the exchanger was turbulent. This is due to the small entrance and exit width as shown in Figure 2-31. In these simulations, the SST turbulence model was used.

For the air simulations, an ideal gas with temperature dependent fits for specific heat, thermal conductivity, and viscosity was used. For the CO_2 simulations, the CO_2 properties were calculated beforehand in REFPROP and tabulated.

2.5.1.3.3 Solution Procedure

ANSYS CFX 16.0, which uses a finite volume method to solve the Reynolds-averaged Navier-Stokes equations, was used to obtain a steady-state fluid/heat transfer solution. To track solution progress, outlet temperature as well as wall friction force were monitored. Once these quantities reached a steady-state solution and the equation residuals were reduced, the simulation was terminated. Figure 2-38 shows the equation residuals and the computed outlet temperature for a typical simulation as it progressed.

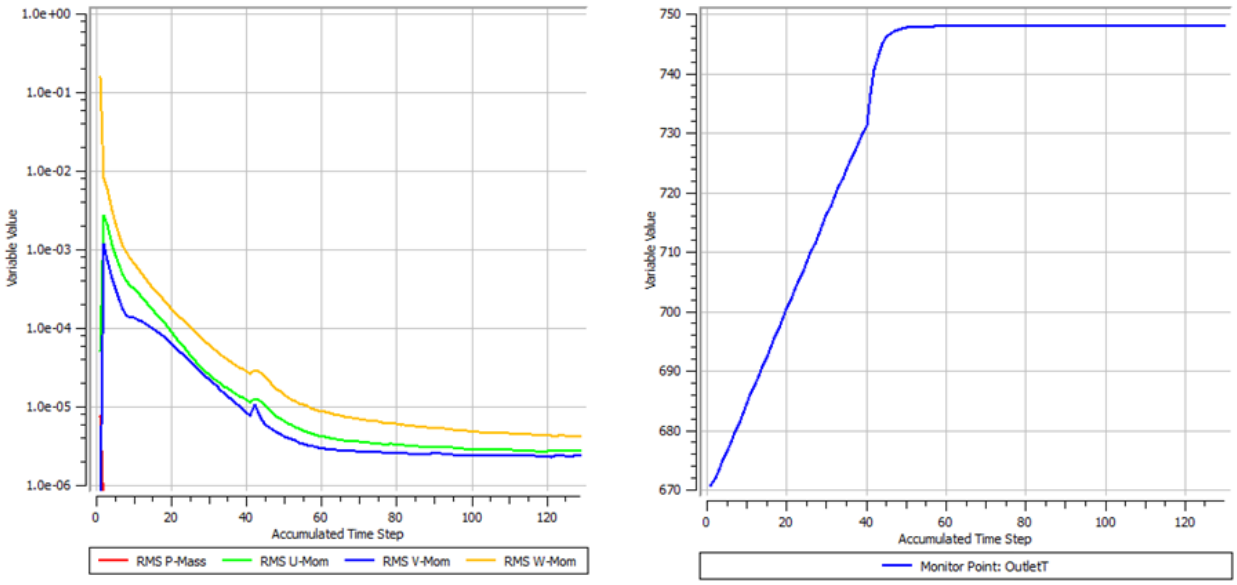

Figure 2-38. Typical simulation progress for the cold side of the cross-flow region. The left image shows the equation residuals as a function of simulation time step and the image on the right shows the outlet temperature as a function of simulation time step.

Notice that the simulation reaches a smooth steady-state solution with a relatively low value for the equation residuals.

2.5.1.3.4 Post Processing Technique

In order to post process the simulation results, a script was created that interrogates the solution between any number of arbitrary planes. At these planes, the script calculates the mass flow averaged temperature to get a bulk mean temperature for the section. It then uses these planes to divide the wall. The area averaged wall temperature and wall heat flux is then computed on the wall section in-between these two interrogation planes. Using this method the period-averaged HTC can be calculated. This same script was used for all sections of the heat exchanger.

2.5.1.3.5 Heat Transfer Results

Using the simulation procedure and post processing technique described above, simulations using air and CO_2 were ran for the hot and cold side of the heat exchanger in the cross-flow and counter-flow regions.

Figure 2-39 shows heat transfer results for both the air and CO_2 for the hot and cold sides of the counter-flow section of the heat exchanger. The results are presented as HTC/k in order to remove the effect of temperature dependent thermal conductivity.

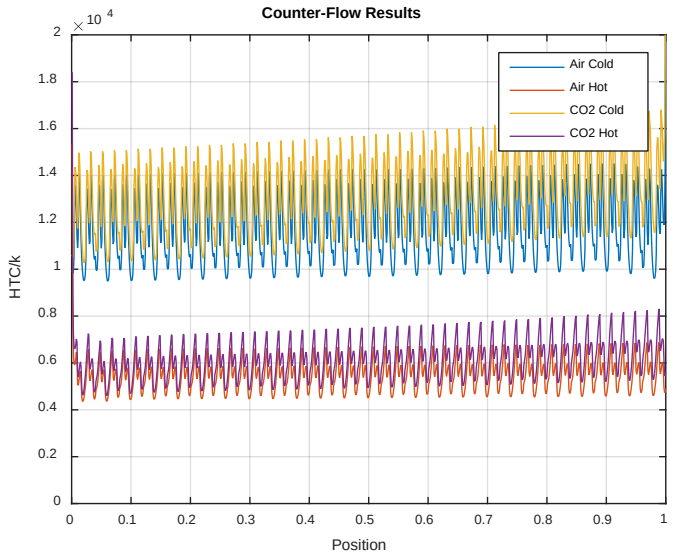

Figure 2-39. Heat Transfer Results for Counter-Flow Section for Air and CO_2

Average values for HTC/k are presented in Table 2-27 for air and CO_2 for the counter-flow region of the heat exchanger. While it is clear in Figure 2-39 that that there is some variation in HTC/k with position, this variation is small. For example, fitting a line to the cold CO_2 data results in an average change in HTC/k of 1,800 [1/m] or 13% over the entire length of the heat exchanger. Further refinement to these data could be made to take into account changes in other temperature dependent parameters, such as Prandtl number and viscosity.

The results shown in Table 2-27 indicate that heat transfer coefficients for CO_2 are expected to be slightly higher than for air, resulting in slightly improved heat transfer effectiveness for the CO_2 cycle application.

Table 2-27. Average HTC/k Values for Air and CO_2 for the Counter-flow Region

Region	Mean HTC/k [1/m]
Cold Air	11,793
Cold CO_2	13,167
Hot Air	5,495
Hot CO_2	6,195

Figure 2-40 shows heat transfer results for air and CO_2 for the cross-flow region. As in the results for the counter-flow region, the results are presented as HTC/k to remove variation with respect to thermal conductivity. It is interesting to note that the laminar cases all converge to the same HTC/k value as anticipated. It is also interesting to note that one of the cases, namely the hot air inlet case, diverges from this value near the end of the heat exchanger. Since the simulation converges to the same steady-state HTC/k value as the other simulations, it is assumed that the divergence later on is the result of a numerical error.

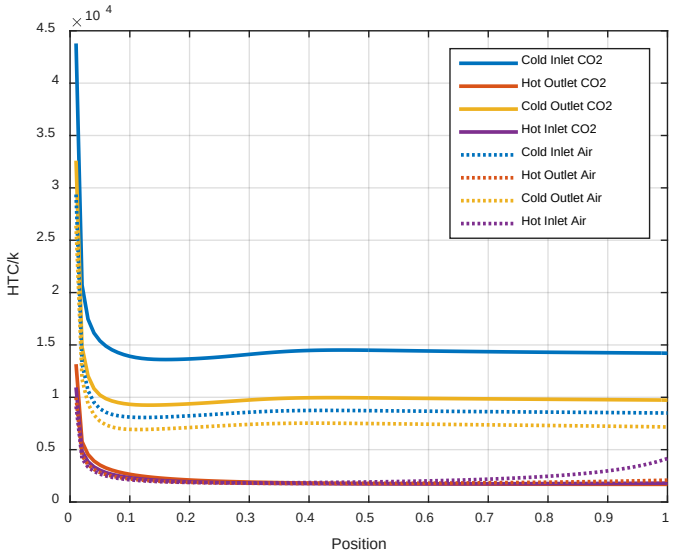

Figure 2-40. Heat Transfer Results for the Cross-flow Region for Both Air and CO_2

Steady-state values for HTC/k are presented in Table 2-28.

Table 2-28. Steady-State HTC/k Values for Air and CO_2 in the Cross-flow Region

Region	Steady State HTC/k [1/m]
Cold Inlet CO_2	14,300
Hot Outlet CO_2	1,800
Cold Outlet CO_2	9,900
Hot Inlet CO_2	1,800
Cold Inlet Air	8,600
Hot Outlet Air	1,800
Cold Outlet Air	7,400
Hot Inlet Air	1,800

2.5.1.3.6 Pressure Drop Results

By interrogating the simulations used for the heat transfer modeling described previously, the total pressure drop through the heat exchanger predicted by the CFD simulations can be quantified. This total pressure loss is shown in Table 2-29, along with experimental data from an existing air recuperator. To obtain these data from the CFD result, the pressure drop per unit length of the

cross-flow and counter-flow regions was evaluated and then a mean length through the actual heat exchanger geometry was used to calculate the total predicted pressure drop. It should be noted that the experimental data includes losses from ducting as well as the transition from the cross-flow to the counter-flow region of the heat exchanger while the CFD data does not. Thus, the calculated pressure losses for the air cycle match reasonably well with experimental data. The CO_2 simulations show increased pressure drop over the air case, which will be incorporated in to future CO_2 cycle models.

Table 2-29. Predicted Total Pressure Loss and Experimental Data

Region	Total Pressure Loss	Experimental Data
Air Cold	2.08%	2.8%
Air Hot	5.58%	6.7%
CO_2 Cold	2.60%	-
CO_2 Hot	5.68%	-

2.5.1.3.7 Overall Heat Transfer Model

Knowledge of the heat transfer coefficients and friction factors is insufficient to predict overall heat transfer and pressure drop since the thermal conductivity of the primary surface film must also be considered. In addition, thermal conductivity, HTCs, and friction factors are expected to vary with temperature and, thus, change significantly along the entire flow path. In this section, an element-wise modeling method is described for incorporating thermal conductivity and length-varying air and exhaust gas-side HTCs for overall heat exchanger performance.

In the proposed model, temperatures, pressures, HTCs, friction factors, and thermal conductivity are assumed to be constant over a single element along an average flow path through the recuperator. The element length can be arbitrarily selected in the cross-flow sections since the flow path does not vary along the length. In the counter-flow section, a single lengthwise period is considered to be an element. For a particular element i (where i increases from cold side to hot side), the following heat transfer relationships may be applied:

$$\dot{\boldsymbol{Q}}_{\boldsymbol{i}} = \frac{\boldsymbol{k_i A_i}\left(\boldsymbol{T_{wall,EG,i}} - \boldsymbol{T_{wall,AIR,i}}\right)}{\boldsymbol{t_i}} \quad (5)$$

$$\dot{\boldsymbol{Q}}_{\boldsymbol{i}} = \boldsymbol{h_{EG,i} A_i}\left(\boldsymbol{T_{avg,EG,i}} - \boldsymbol{T_{wall,EG,i}}\right) \quad (6)$$

$$\dot{\boldsymbol{Q}}_{\boldsymbol{i}} = \boldsymbol{h_{AIR,i} A_i}\left(\boldsymbol{T_{wall,AIR,i}} - \boldsymbol{T_{AIR,avg,i}}\right) \quad (7)$$

$$\dot{\boldsymbol{Q}}_{\boldsymbol{i}} = \dot{\boldsymbol{m}}_{\boldsymbol{EG}} \boldsymbol{C_{p,EG,i}}\left(\boldsymbol{T_{EG,i}} - \boldsymbol{T_{EG,i+1}}\right) \quad (8)$$

$$\dot{\boldsymbol{Q}}_{\boldsymbol{i}} = \dot{\boldsymbol{m}}_{\boldsymbol{AIR}} \boldsymbol{C_{p,AIR,i}}\left(\boldsymbol{T_{AIR,i+1}} - \boldsymbol{T_{AIR,i}}\right) \quad (9)$$

$$\boldsymbol{T_{avg,EG,i}} = \boldsymbol{0.5} * \left(\boldsymbol{T_{EG,i}} + \boldsymbol{T_{EG,i+1}}\right) \quad (10)$$

$$\boldsymbol{T_{avg,AIR,i}} = \boldsymbol{0.5} * \left(\boldsymbol{T_{AIR,i}} + \boldsymbol{T_{AIR,i+1}}\right) \quad (11)$$

In Equations 5 through 11, k is the thermal conductivity, h is a heat transfer coefficient, $\dot{Q}$ is heat transfer, $\dot{m}$ is mass flow, A is total element wall area, t is the wall thickness, and C_p is the specific heat at constant pressure. Subscripts AIR and EG denote the air exhaust gas, respectively. The

relationships above comprise a system of seven equations and seven unknowns, which can be solved for each element, accounting for changes in thermal conductivity and heat transfer coefficients with temperature and Reynolds number at each element. Pressure drop across each element can similarly be calculated with an element-wise friction factor.

This modeling approach was applied to the existing recuperator counter-flow geometry and cold-side temperatures using the heat transfer coefficient values shown in Table 2-27 and temperature-dependent thermal conductivity of Inconel 625, as shown in Figure 2-41. The resulting temperature distributions through the counter-flow section are shown in Figure 2-42. These calculations show that the modeled heat transfer coefficient values result in approximately 68% of the temperature change in the counter-flow section. Examination of the relative HTC/k values for each section indicates that this is reasonable.

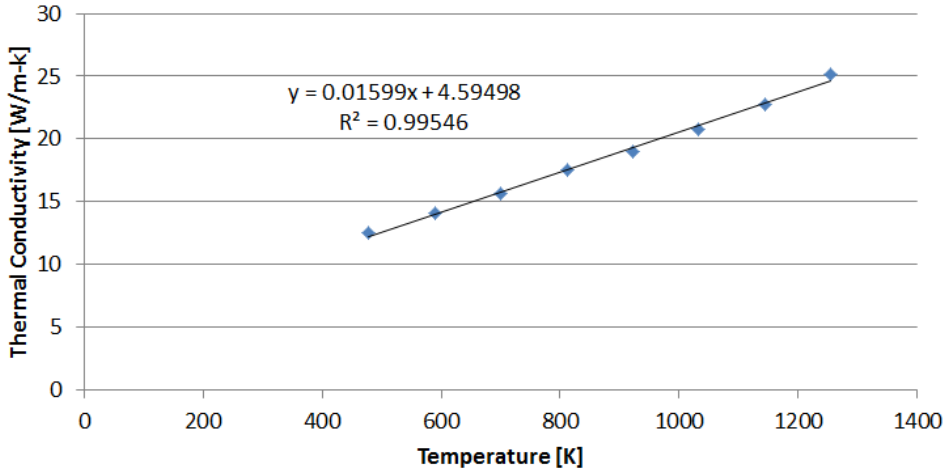

Figure 2-41. Inconel 625 Thermal Conductivity

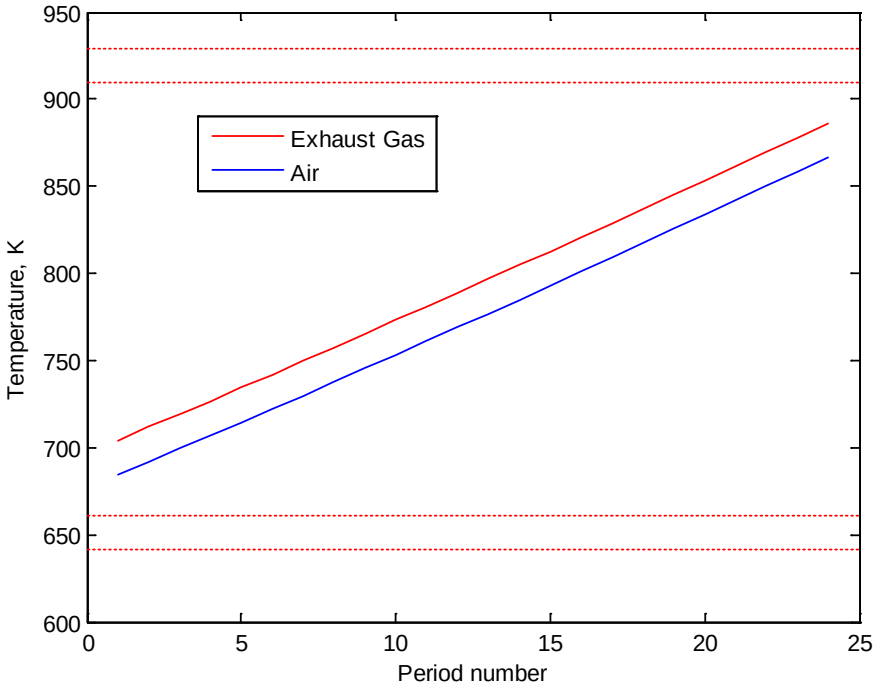

Figure 2-42. Overall Heat Exchanger Counter-Flow Model Temperature Outputs

2.5.1.4 Structural Models

This section presents structural models that have been developed for evaluating material stresses at several critical locations within the recuperator:

1. Exhaust gas inlet sheet (highest temperature region; corrugated guide sheets support pressure load)
2. Counter-flow sheets away from the header bars (still high temperatures and pressure loading)
3. Clamp joint where primary surface sheets clamp into header bars near exhaust gas inlet (high temperatures; locations of previous thermal fatigue failures in older recuperator designs)

2.5.1.4.1 Exhaust Gas Inlet Sheet Model

A model of the gas side cross-flow sheet has been created to evaluate deformation and creep life in the existing recuperator gas inlet design. This model is positioned at a distance from the header bars to eliminate any stress concentrations that would occur due to the transition from header bar to sheet. The model consists of an upper sheet, a lower sheet, and a corrugated support section, each measuring 0.544” wide and 0.375” deep (see Figure 2-43). Dimensions for the sheets and corrugation sections have been taken from the solid models provided by Solar.

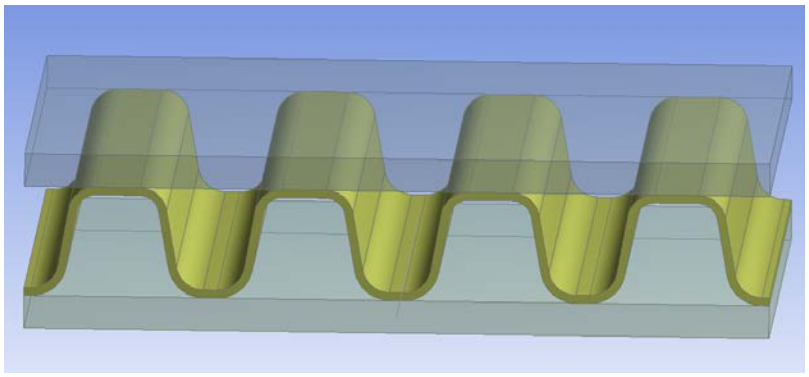

Figure 2-43. Three-Body Exhaust Gas Inlet Sheet Model

The model has been analyzed with six different mesh densities in order to demonstrate a solution that is not mesh dependent. The most coarse mesh used around 122,500 nodes and incorporated 1 elements across the corrugated sheet (Figure 2-44), while the most fine mesh consisted of around 1,270,000 nodes and incorporated 4 elements across the corrugated sheet (Figure 2-45). The mesh has been refined at the regions where contacts will occur to help ensure accurate results in the critical regions. The meshes for all three bodies have been created using a sweep feature starting from the +Z face and sweeping in the –Z direction.

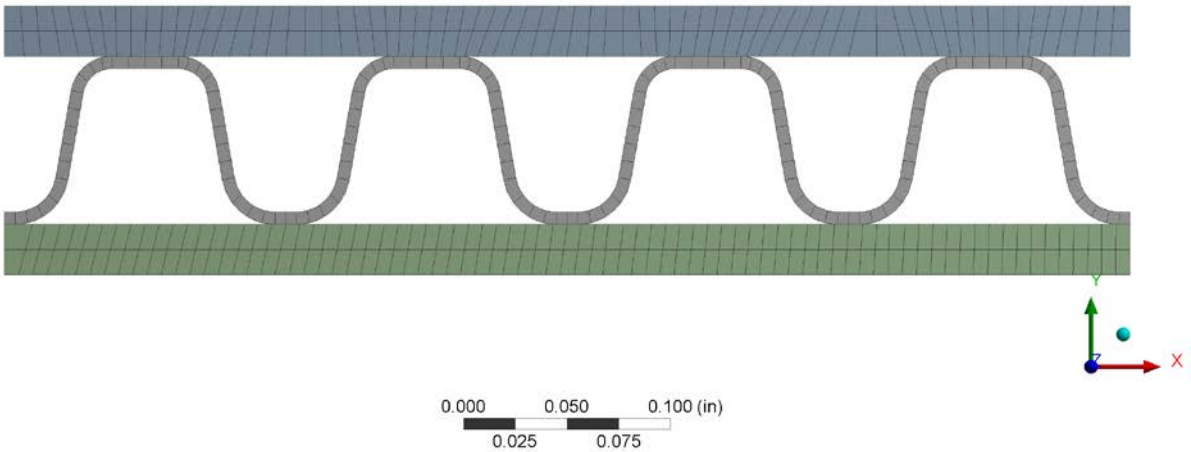

Figure 2-44. Exhaust Gas Inlet Sheet Model, Low Resolution Mesh

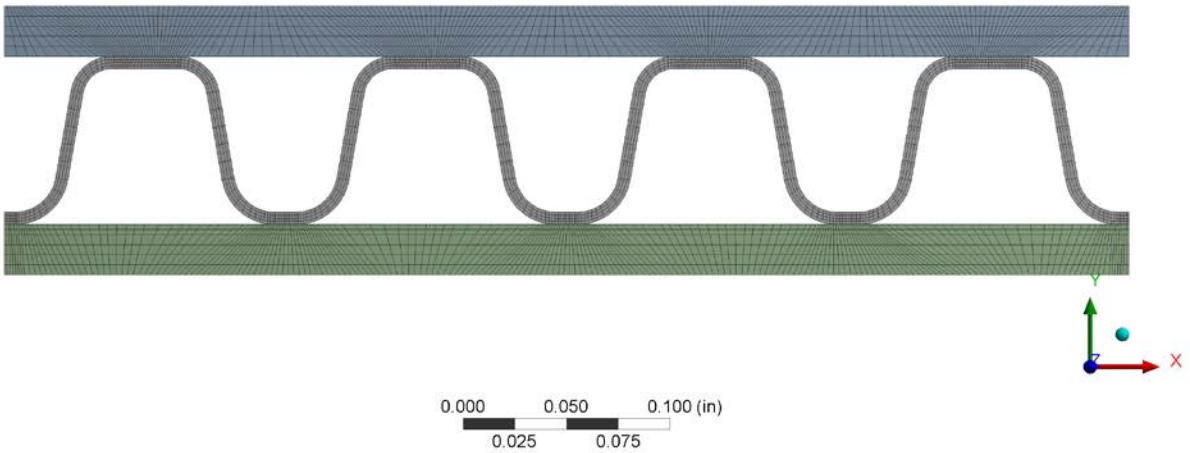

Figure 2-45. Exhaust Gas Inlet Sheet Model, High Resolution Mesh

Each of these models has been set up with Linear Periodic Symmetry on all three components in the X-direction and a regular symmetry constraint on the –X face, which is the same as the low side on Linear Periodic constraint. A regular symmetry constraint has been applied to the +Z face of all three components with the –Z faces being left free (i.e., the model is approximating the center section of the counter-flow region).

Loading has been applied to the model in two time steps. In the first step, a normal pressure of 9 bar (130 psi) has been applied to the top surface of the upper plate and bottom surfaces of the lower plate. This pressure is the differential pressure seen between the air side and exhaust side of the current recuperator. In the second step, a thermal condition of 1,208°F has been applied to all three bodies to simulate the highest expected working temperature of the current recuperator. Frictional contacts have been applied to all touching surfaces between the corrugated sheet and the upper and lower sheets. The friction coefficient used for these contacts is 0.2. Since the external forces being applied to this model are equal, the only other constraint on the model is the use of weak springs, which are automatically applied to keep the model from moving in space.

The stress and total deformation results calculated for the high-resolution model are shown in Figures 2-46 and 2-47. These results show a maximum equivalent stress of 12,475 psi and a maximum deformation of 0.0062068" for the high-resolution model. To demonstrate that the solution is mesh independent, the analysis was performed on six meshes ranging from 122,500 nodes to 1,270,000 nodes. Figure 2-48 plots the maximum stress from each model in the corrugated sheet and the sheets on either side. The results show that the model with 600,000 nodes has converged to the final solution. The stress results are compared with yield and creep rupture stresses in Section 2.5.1.5, indicating that these stresses are within failure limits (as expected for the baseline case with the existing recuperator design).

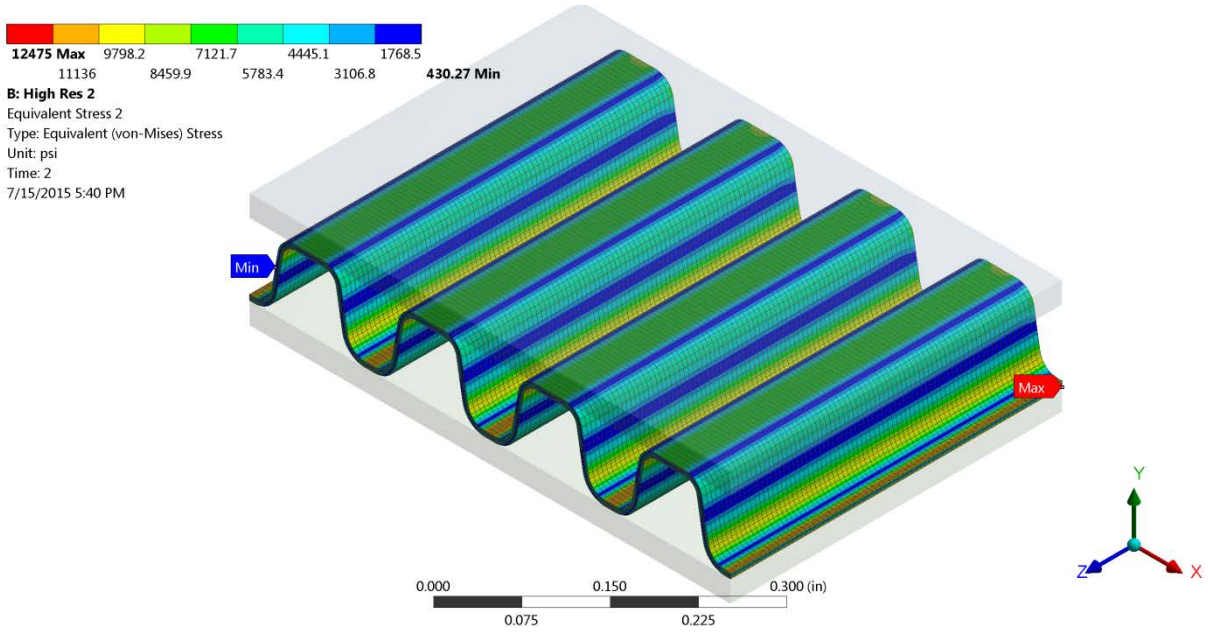

Figure 2-46. Stress Pattern, High Resolution Exhaust Gas Inlet

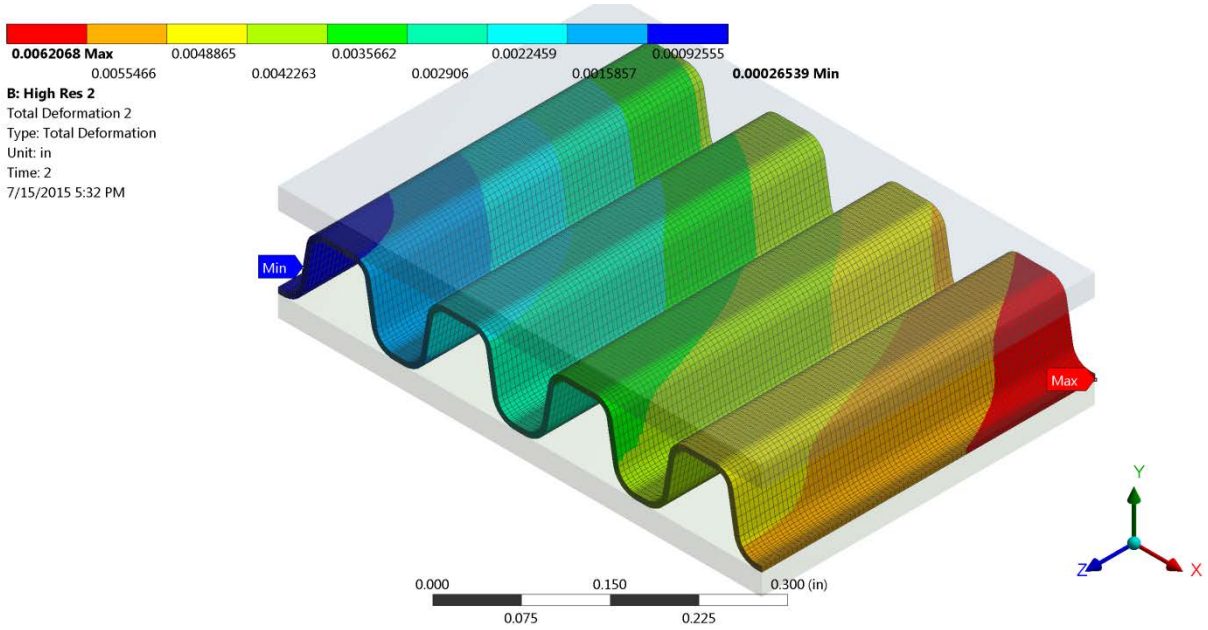

Figure 2-47. Total Deformation Pattern, High Resolution Exhaust Gas Inlet

After the model was run at the current recuperator conditions, it was simulated at the conditions predicted for using carbon dioxide as the working fluid. The pressure difference across the recuperator remains at 9 bar, but the temperature increases from 1,208°F to 1,526°F. These simulations found that the resulting stresses at CO_2 conditions are nearly identical to those at air conditions, as shown in Figure 2-46. The major difference is that the material creep and yield limits have lowered significantly, resulting in a much lower safety factor, as shown in Figure 2-64.

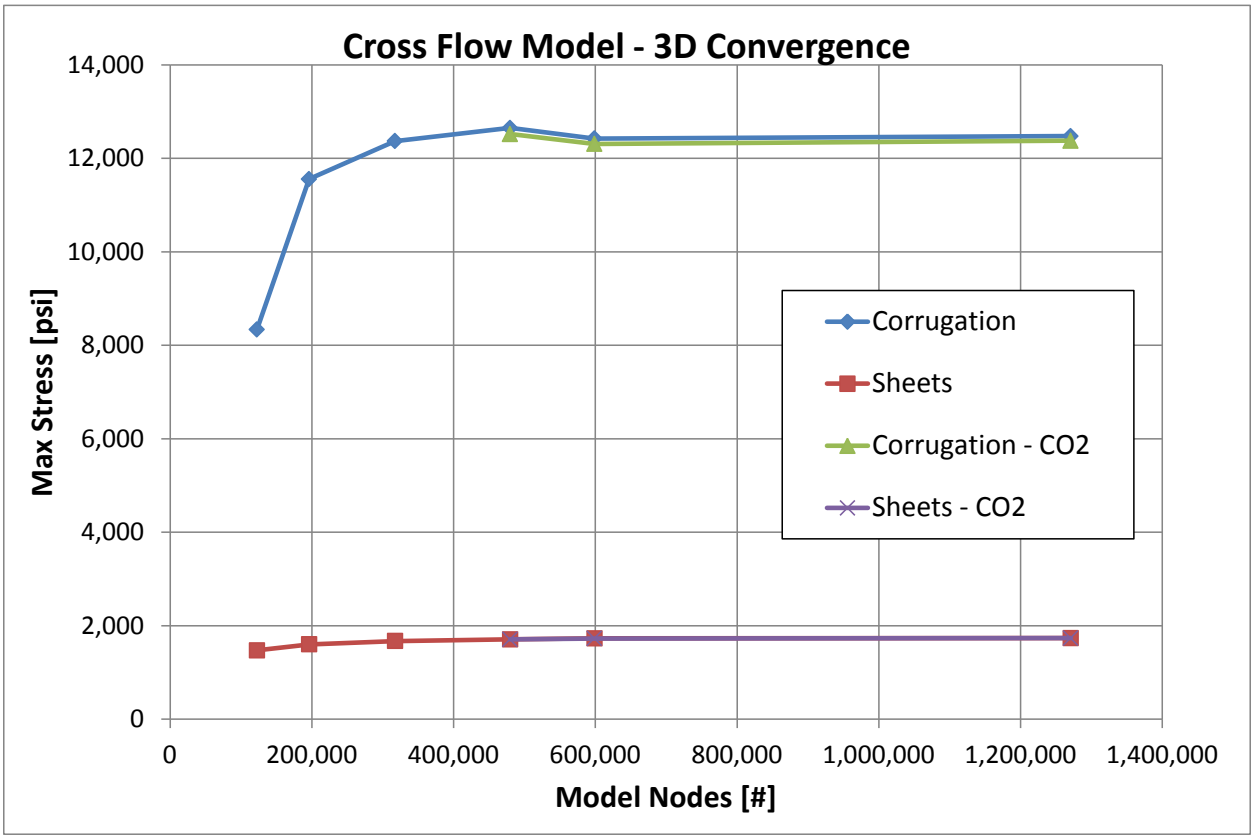

Figure 2-48. Mesh Convergence Study

2.5.1.4.2 Counter-flow Sheet Model

A model of the counter-flow heat transfer sheet has been created to evaluate deformations and stresses in the existing recuperator primary heat exchanger sheet design. Similar to the cross-flow model, this model is positioned at a distance from the header bars to eliminate any stress variations that would occur due to the transition from header bar to sheet. The model consists of an upper corrugated sheet and a lower corrugated sheet each, measuring 0.5216" wide and 0.38" deep (see Figure 2-49). Dimensions for the sheets and corrugation sections have been taken from the heat transfer sheet drawings provided by Solar.

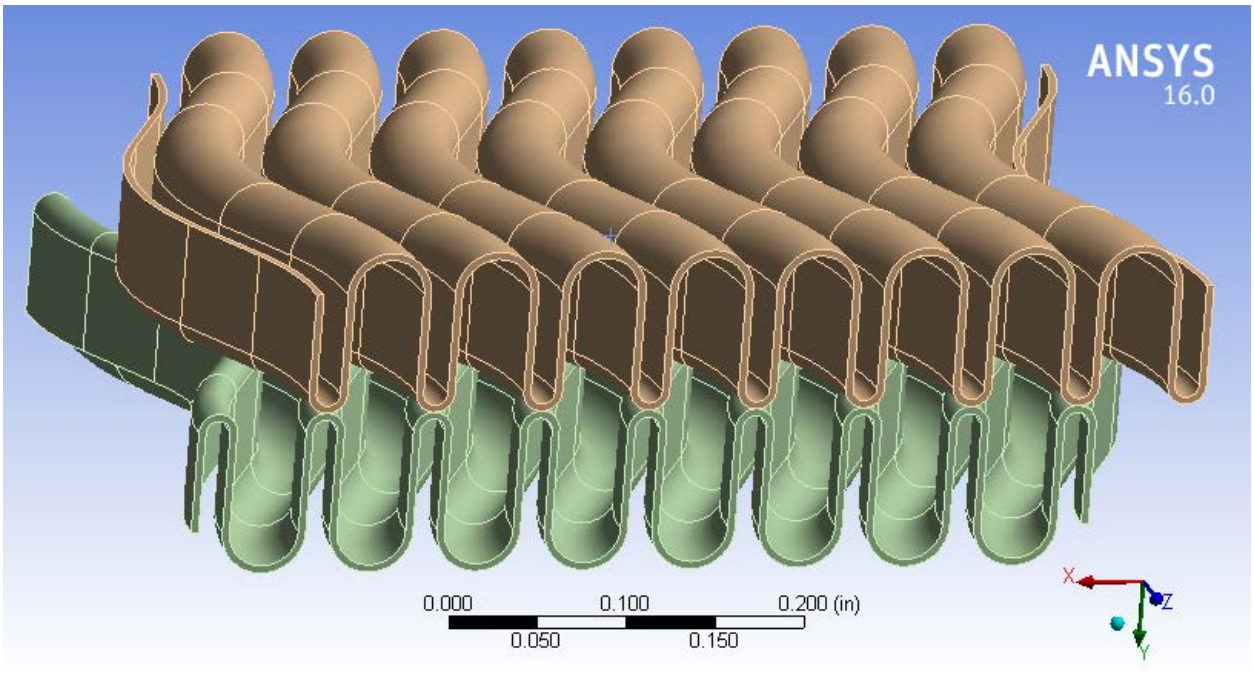

Figure 2-49. Counter-flow Model

This model was analyzed with three different mesh densities. The lowest mesh density model consisted of approximately 497,000 nodes and incorporated two elements across the corrugated sheet thicknesses (Figure 2-50). The middle mesh density model consisted of approximately 2,106,000 nodes and incorporated three elements across the corrugated sheet thicknesses (Figure 2-51). The highest mesh density model consisted of approximately 3,500,000 nodes and incorporated four elements across the corrugated sheet thicknesses. The mesh has been refined at the boundaries where contacts will occur to help ensure accurate results in these critical regions. The meshes for both bodies have been created using a sweep feature starting from the +Z face and sweeping in the –Z direction.

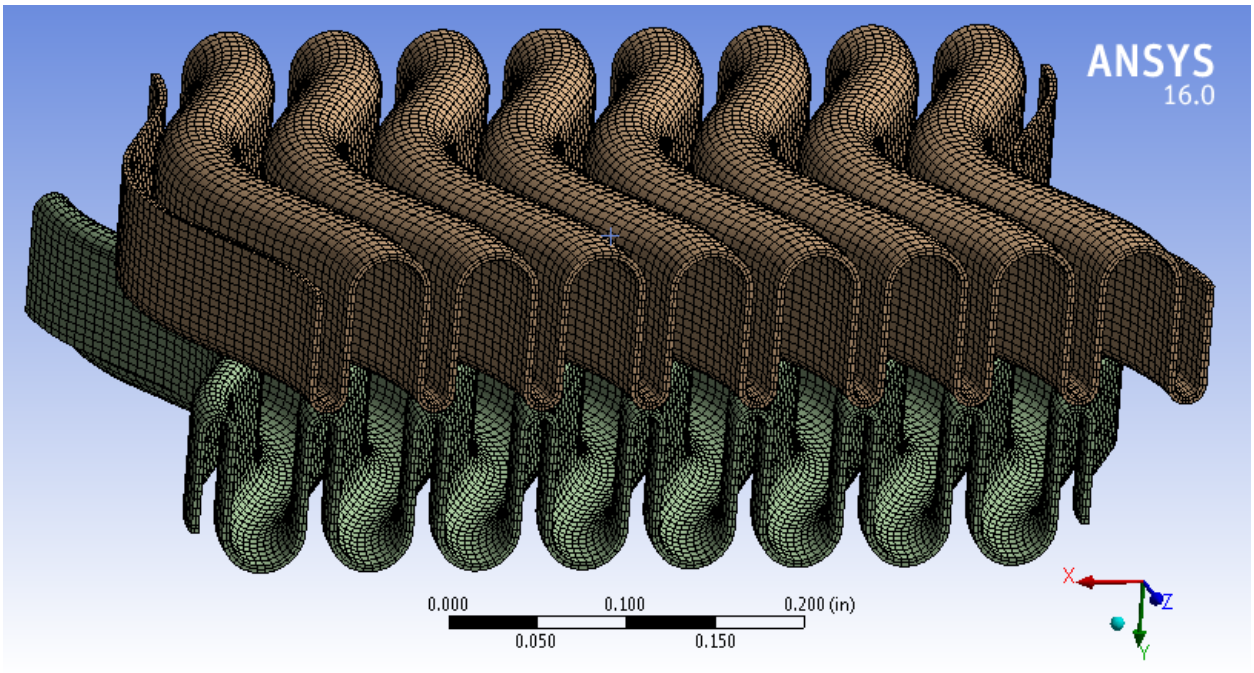

Figure 2-50. Coarse Mesh Counter-flow Model

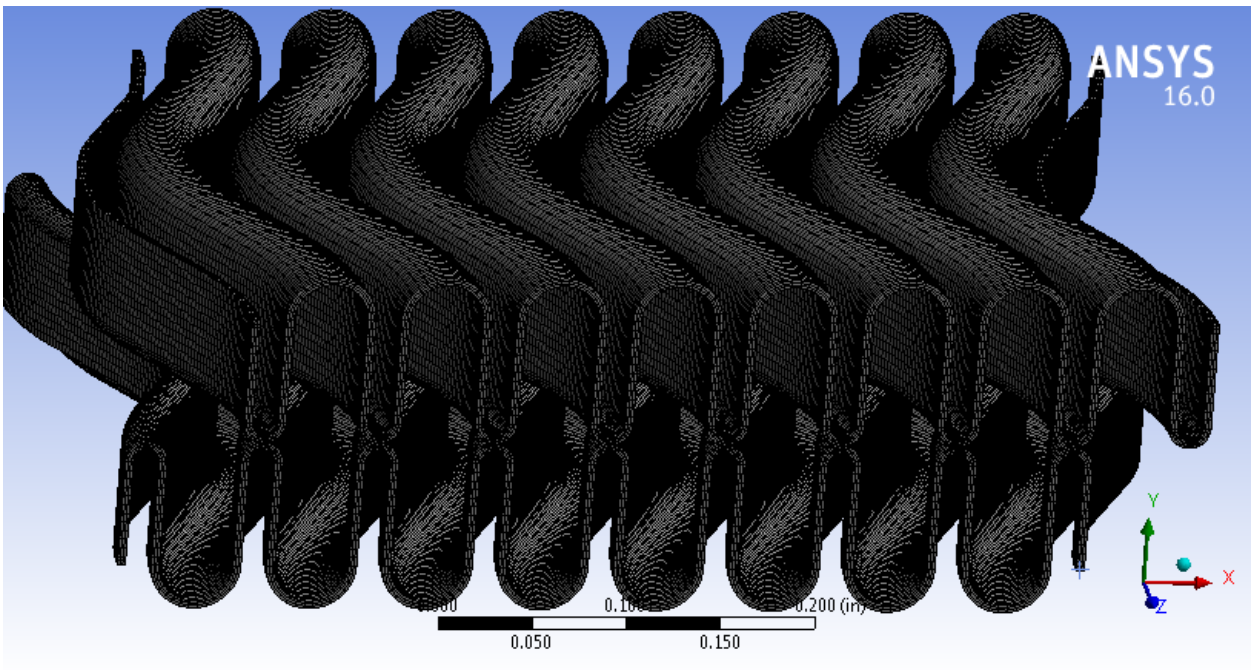

Figure 2-51. Fine Mesh Counter-flow Model

Each of these models has been set up with Linear Periodic Symmetry on both components in the Z direction. Linear periodic boundaries cannot be applied in more than one direction at a time, so frictionless supports have been applied to the +Y and –Y edge surfaces of each sheet in order to

offer some constraint in the Y direction and to reduce the bending forces that would otherwise be seen due to the geometry of the free edges in the X direction. Though the forces on this model are symmetric, the simulation would not converge without a constraint in the X direction, so one face on the –X side of each body was constrained with a fixed constraint.

Loading has been applied to this model in two separate steps. In the first step, a normal pressure of 9 bar (130 psi) has been applied to the top surface of the upper corrugated sheet and to the bottom surfaces of the lower corrugated sheet. This pressure is the differential pressure seen between the air side and exhaust side of the current recuperator. In the second step, a thermal condition of 1,200°F has been applied to both bodies to simulate the highest expected working temperature of the existing recuperator. Frictional contacts have been applied to all touching surfaces between the two corrugated sheets. The friction coefficient used for these contacts is 0.2. Since the external forces being applied to this model are equal between the top and bottom surfaces, the only other constraint on the model is the allowance of weak springs, which are automatically applied, if needed, to keep the model from moving in space.

The deformation and stress results of this simulation are examined in the four center periods of each body in order to ignore edge effects from the applied boundary conditions, which occur on the outer two periods. These results are shown for the low-resolution model in Figures 2-52 through 2-54. The deformation results are mainly due to thermal growth and show that deflections are generally small enough that they do not affect the flow path significantly. The maximum equivalent stress exists on the opposite side of the sheets where the top and bottom sheets contact.

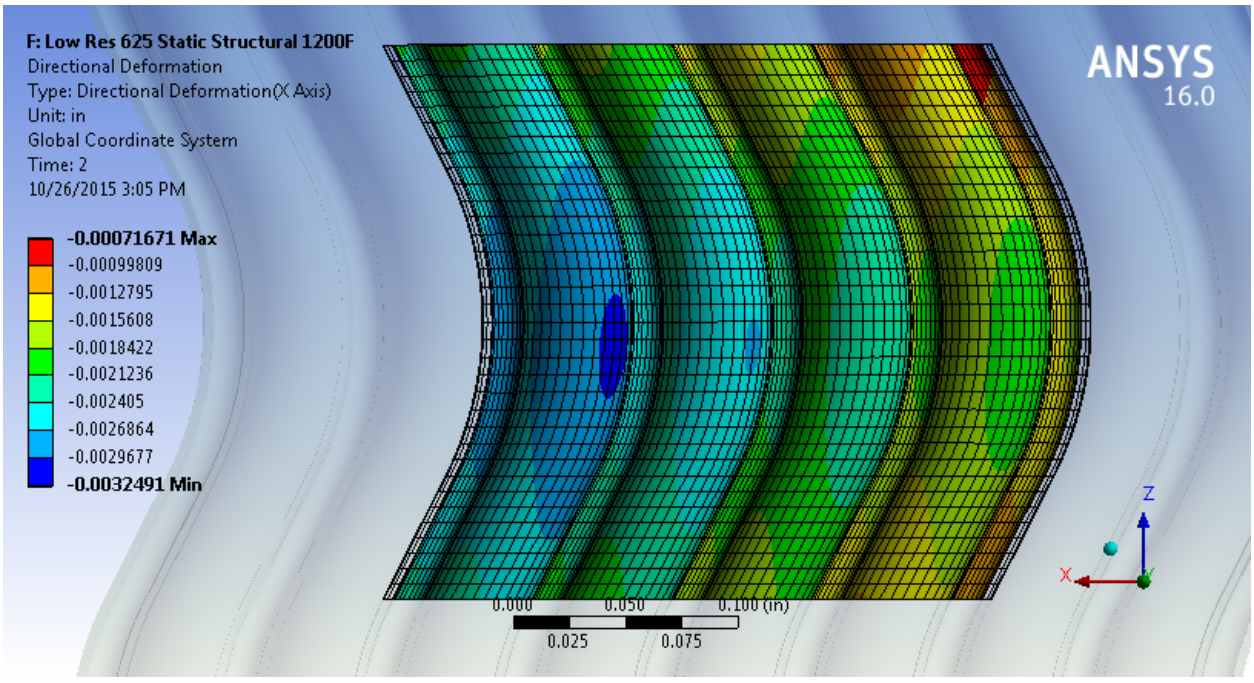

Figure 2-52. Counter-flow Sheet X-Displacements, Mid-Resolution Mesh

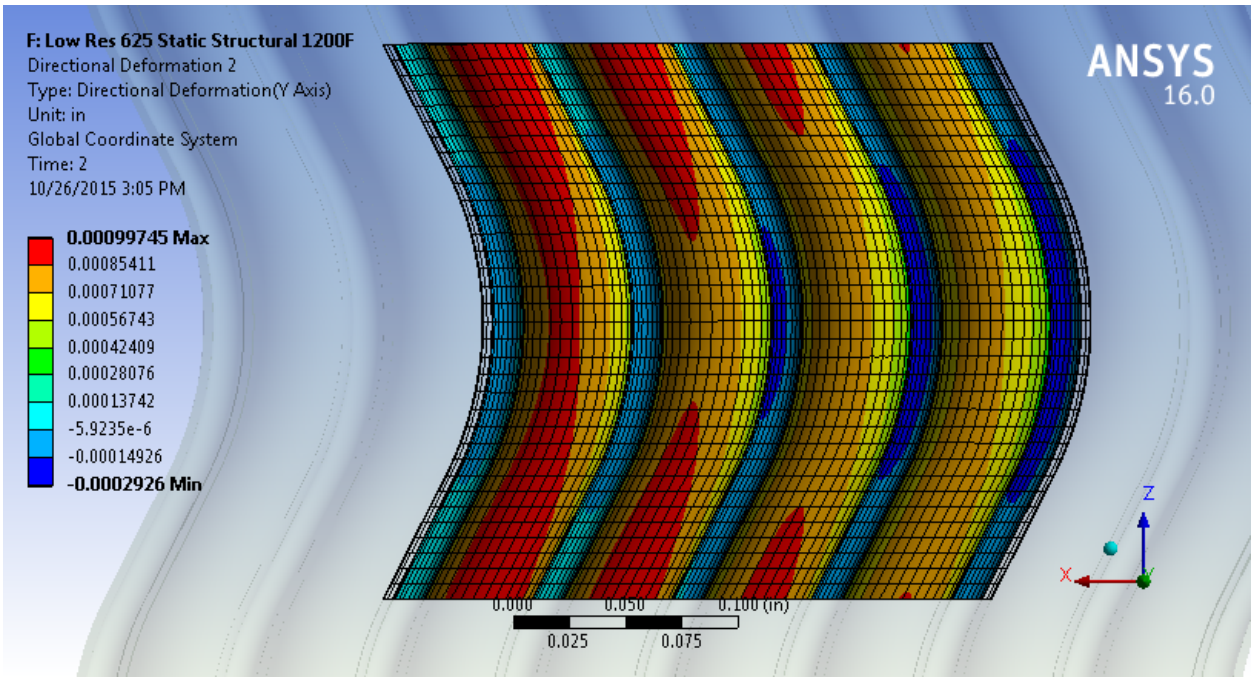

Figure 2-53. Counter-flow Sheet Y-Displacements, Mid-Resolution Mesh

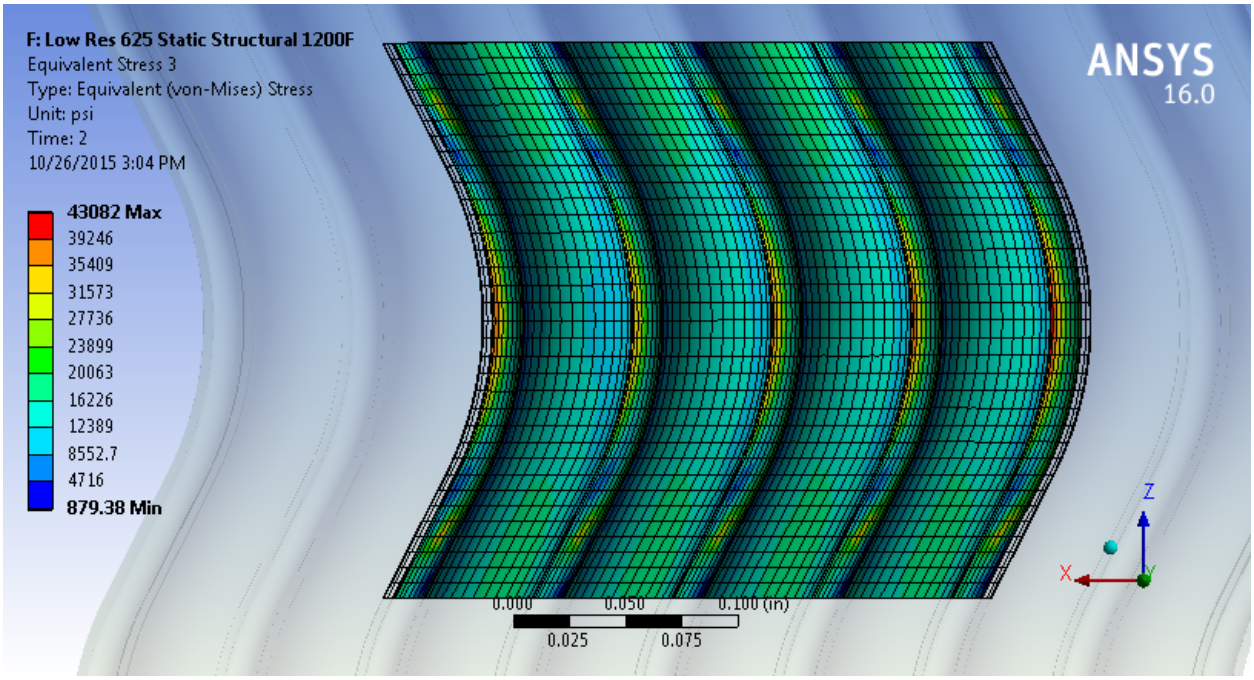

Figure 2-54. Counter-flow Sheet Equivalent Stresses, Mid-Resolution Mesh

A mesh-independent study was performed with the three different resolution models and the normalized results show that the percent change in stress from the low-resolution model to the mid- and high-resolution models is less than 2.5% (see Figure 2-55). The difference in total

deformation for the models is also extremely low. Because these values change little between all three models, it appears that mesh-independent results are being presented. The stress patterns throughout the center sections also appear to be uniform, indicating that the boundary conditions are not significantly affecting results near the center section of the model and, thus, are being applied correctly for this analysis.

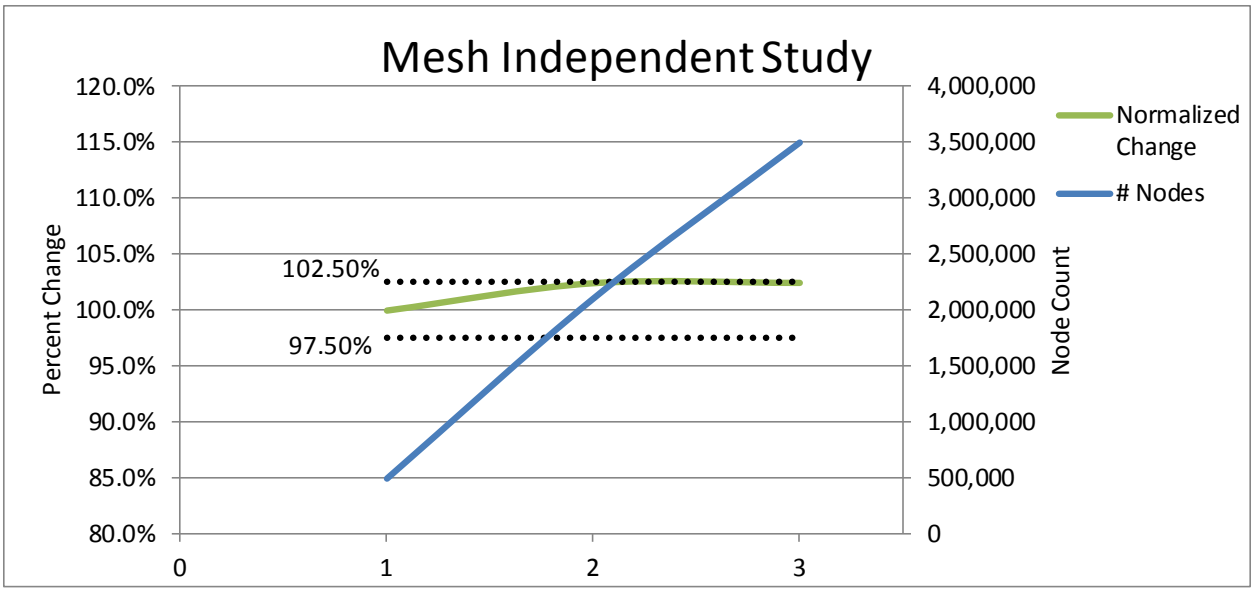

Figure 2-55. Counter-flow Sheet Mesh Independence Study

2.5.1.4.3 Clamp Joint Corner Model

In previous recuperator designs, the bottom left corner of the recuperator sheets where the clamp joint is located (see Figure 2-56) was prone to cracking due to thermal fatigue. Therefore, stresses at this area are modeled, and changes due to the recuperator redesign options will be monitored throughout this project. This subsection presents the evaluation of the existing corner at baseline operating conditions.

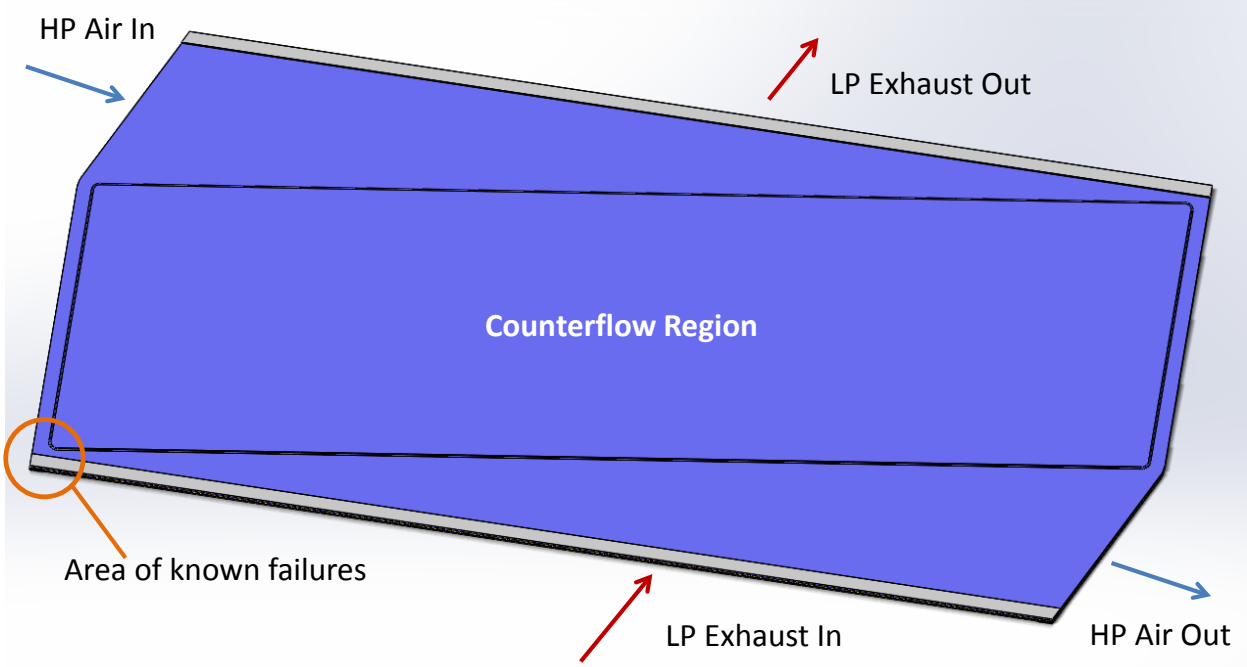

Figure 2-56. Location of Clamp Joint Corner Model

A solid model of the corner was constructed in SolidWorks 2015 and analysis was performed in ANSYS Workbench 16. The major model components are labeled on top of a coarse mesh in Figure 2-57. Low-pressure (14.5 psia) exhaust enters between the top and bottom sheets and travels through the corrugation towards the counter-flow region of the heat exchanger. Meanwhile, high-pressure air (145 psia) exits the counter-flow region and travels above the top sheet, and below the bottom sheet towards the exit of the heat exchanger. The pressure differential (130.5 psi) is represented in the model by a pressure condition applied to the faces wetted by the high pressure. The exterior edges of the bars and sheets are welded, thus, the pressure differential can also seep in-between the bars and sheets. An exploded view of the model, from the back, is shown in Figure 2-58 with the area highlighted where the differential pressure is applied.

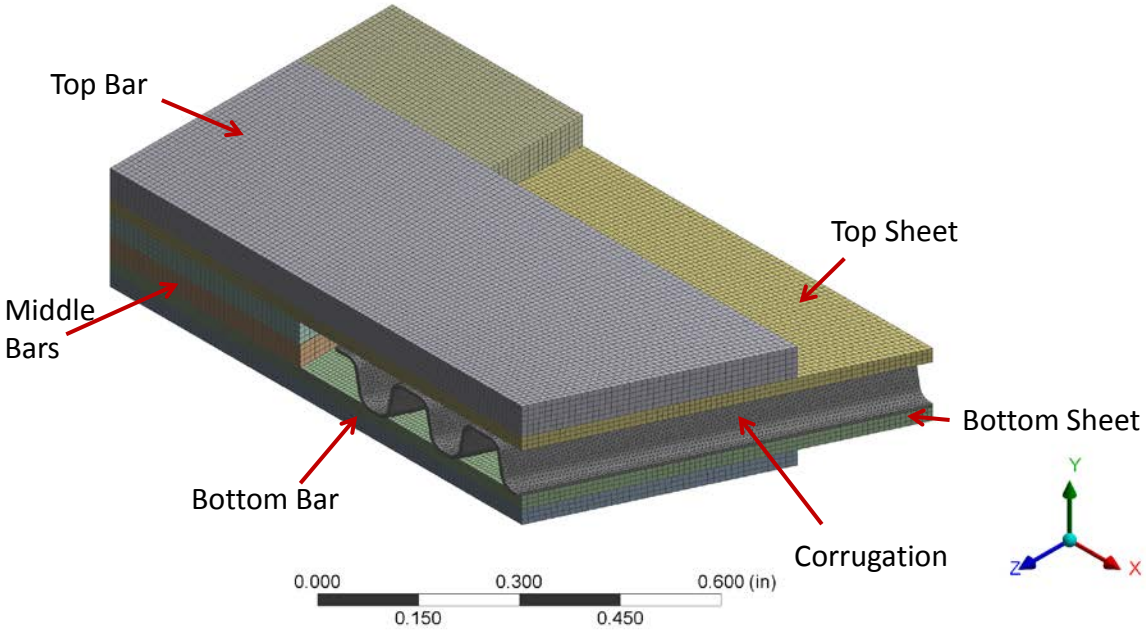

Figure 2-57. Clamp Joint Corner Model – Medium Mesh (Front View)

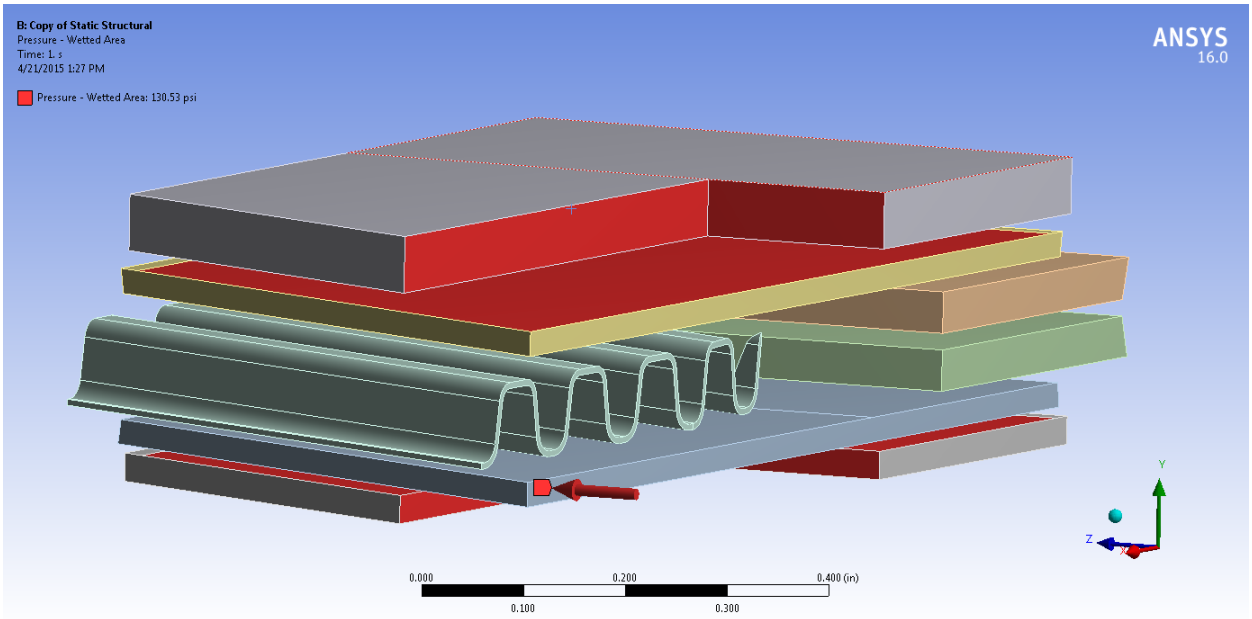

Figure 2-58. Clamp Joint Corner Model – Pressure Differential (Back View)

In addition to the exterior welds, the recuperator is held together with a 35,000 pound force distributed over the regions of stacked bars, as shown in Figure 2-59. The total area covered by this force is 15.1 in^2, thus the pressure on these faces is 2,322 psi. This pressure is applied to the portion of the top bar that sits above the middle bars. The remaining portion of the top bar experiences the pressure differential of 130.5 psi to represent the next layer. The back, side, and bottom faces of the model remain planar through the use of frictionless boundary conditions. The corner is modeled at a temperature of 1,148°F to represent the current operating conditions.

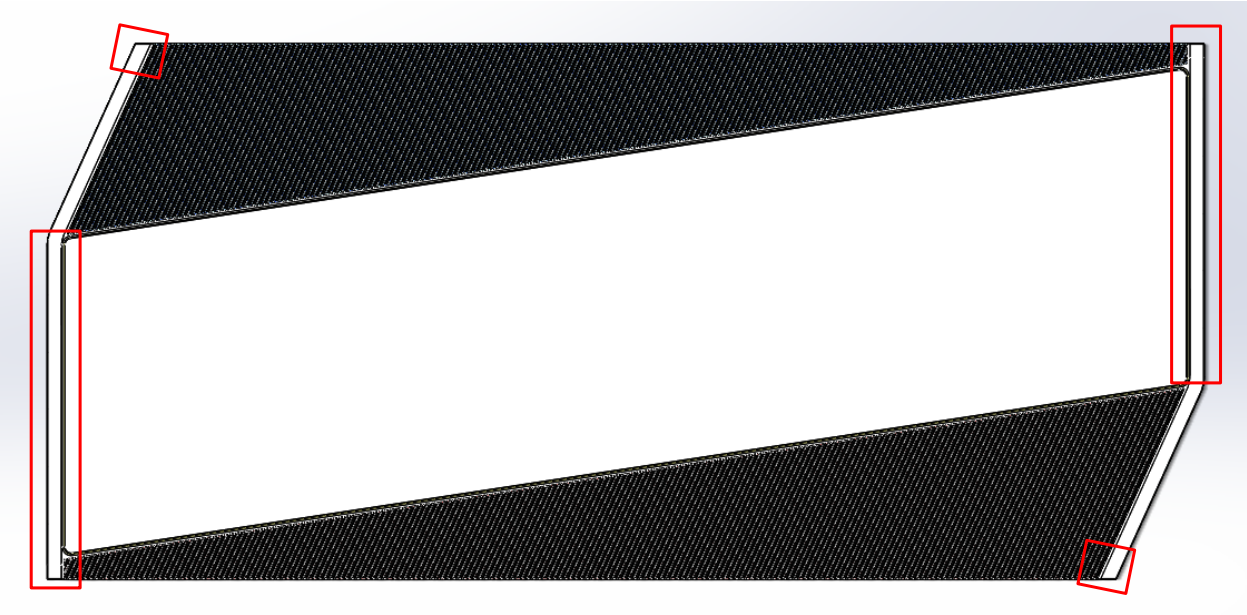

Figure 2-59. Locations of Clamping Load Path

The model has two primary types of frictional contact. First is the contact between the corrugation and the top and bottom sheets. The corrugation is expected to move due to the temperature and pressure loading. This contact region is shown in Figure 2-60. Second is the contact between the top bar and top sheet or the bottom bar and bottom sheet. The edges of these components are welded together, but there is room for pressure to enter, thus, causing movement between them. This contact is shown in Figure 2-61. Both contact regions are shown with the status of the regions after the model has been run using the coarse mesh. The results show that corrugation remains in contact (sliding/sticking). Meanwhile, the sheet and bar contact region remains in contact where the preload is applied and separates where there is only the pressure differential applied.

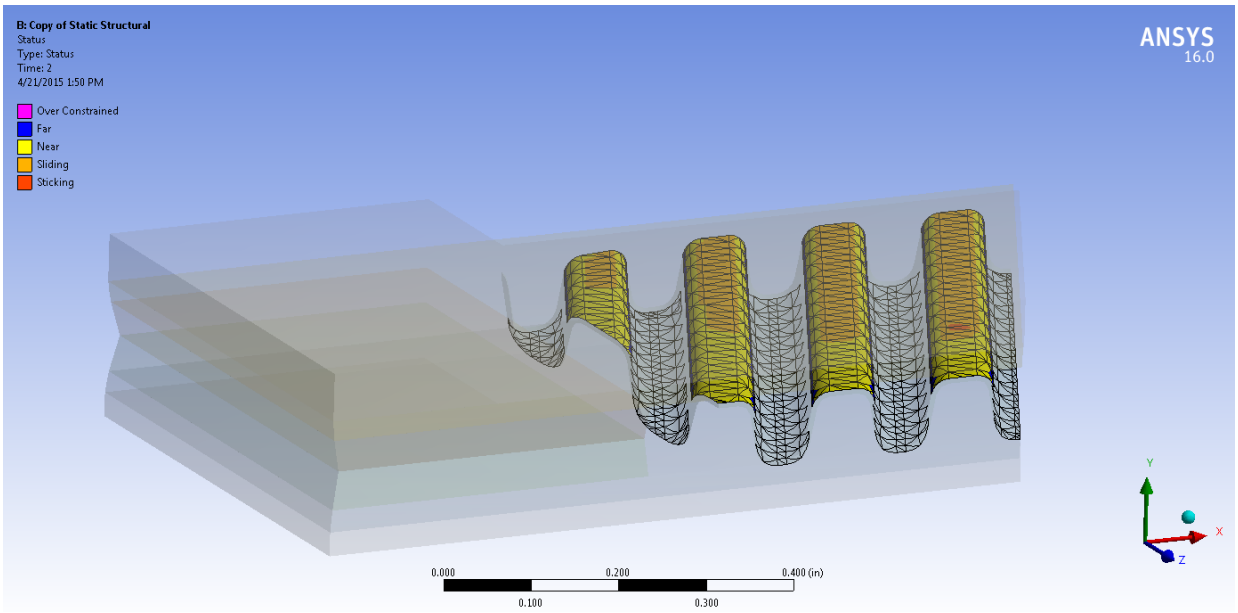

Figure 2-60. Clamp Joint Corner Model – Corrugation/Sheet Contact Region

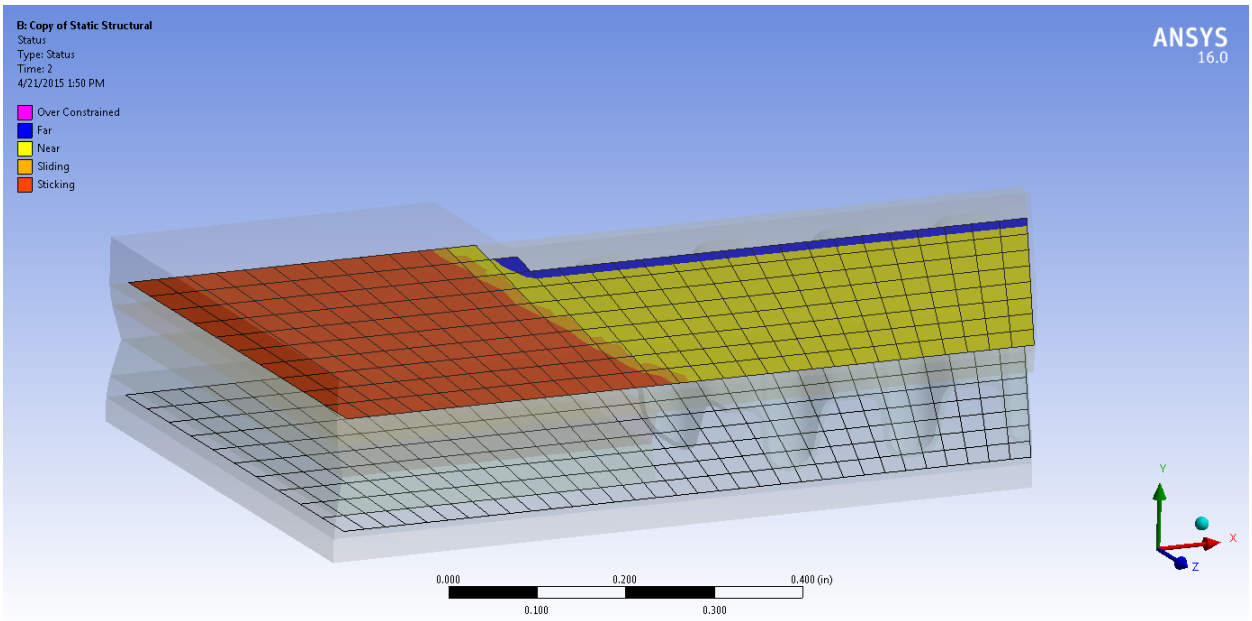

Figure 2-61. Clamp Joint Corner Model – Bar/Sheet Contact Region

This model has been simulated using two different mesh densities. Results using a low mesh density are shown in Figure 2-62 and a higher density in Figure 2-63. Both exhibit a high-stress area located in the region where cracking has previously occurred in old recuperator designs. This region represents the transition from the area where clamping forces are applied to the open corrugation area.

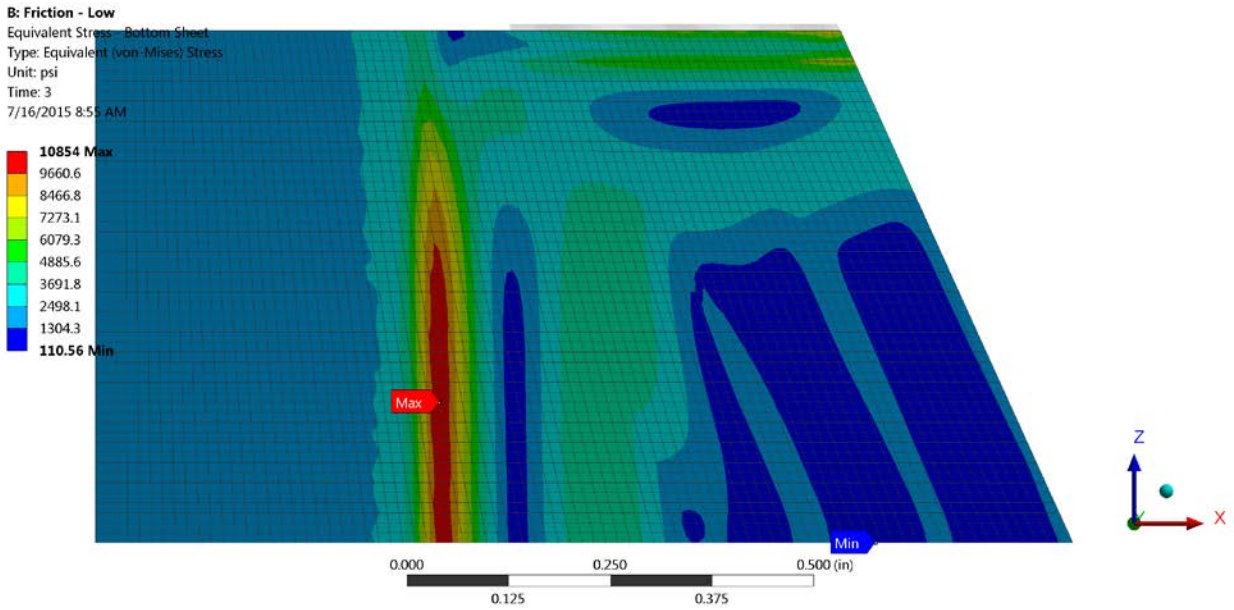

Figure 2-62. Clamp Joint Corner Model – Bottom Sheet Initial Results

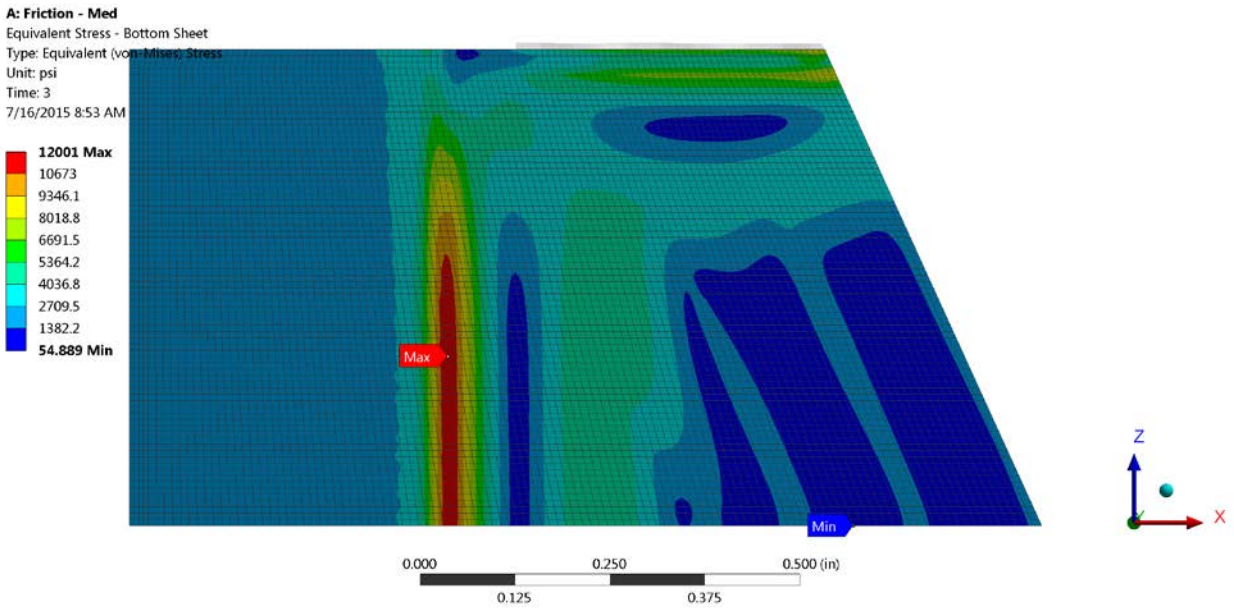

Figure 2-63. Clamp Joint Corner Model – Refined Mesh Results

More recent discussions with Solar have indicated that cracking in this region was likely more related to low-cycle fatigue during thermal transients, not creep stress at steady operating conditions. Since this project is focusing primarily on analysis of the recuperator core and does not include the effect of thermal transients on the overall recuperator, the low-cycle fatigue stresses are not modeled. Thus, remaining work focuses on the other two regions in terms of determining the success of a recuperator redesign.

2.5.1.5 Evaluation of Mechanical Stresses – Baseline Geometry

The maximum stress results for each mechanical model are compared against the temperature-dependent yield stresses and creep rupture stresses for alloy 625 in Figure 2-61. These results show that stresses in the exhaust gas inlet sheet and near the clamp joint are below yield and creep rupture limits for the original design conditions, as would be expected for an existing design. The maximum stress in the counter-flow model for the baseline case is below the yield strength of the material at this temperature, and is also just below the 10,000-hr creep rupture stress of approximately 50 ksi. These stress results are higher than expected for the established baseline design, and are not indicative of actual operating conditions as the physical equipment has more than 200,000 hours of operating time on it without seeing creep rupture problems.

One possible explanation is that the predicted stresses are correct and are at the 100,000 hour rupture stress, but the stress limits for creep rupture may be significantly different for tensile and compressive loads. The area of highest stresses in the model is a section that is in compression rather than in tension, and most creep models have been performed for tensile load cases. These tensile cases cause voids and cracking along grain boundaries which lead to rupture. Compressive loading, however, may not produce the same rupture results or may produce them at a much slower rate. Stresses in other materials have been found to have a substantially longer time to creep failure when applied in compression as compared to tension. For example, one study focusing on the tensile and compressive creep behavior of die cast magnesium alloy found that “the creep rate in compression is lower than that in tension by about one order of magnitude for all pairs tested under the same stress magnitude” [Agnew, 24]. The remaining work with the counter-flow section stresses is directed toward identifying a design that maintains the existing safety factors.

The exhaust corrugation model has been run for the carbon dioxide conditions and it was found that while the stresses are nearly constant the yield and creep strength are much lower at the elevated temperatures. Therefore, the design must be altered to safely run at the carbon dioxide conditions. The design approach will be to maintain a similar safety factor as the current recuperator when operating at the increased temperatures.

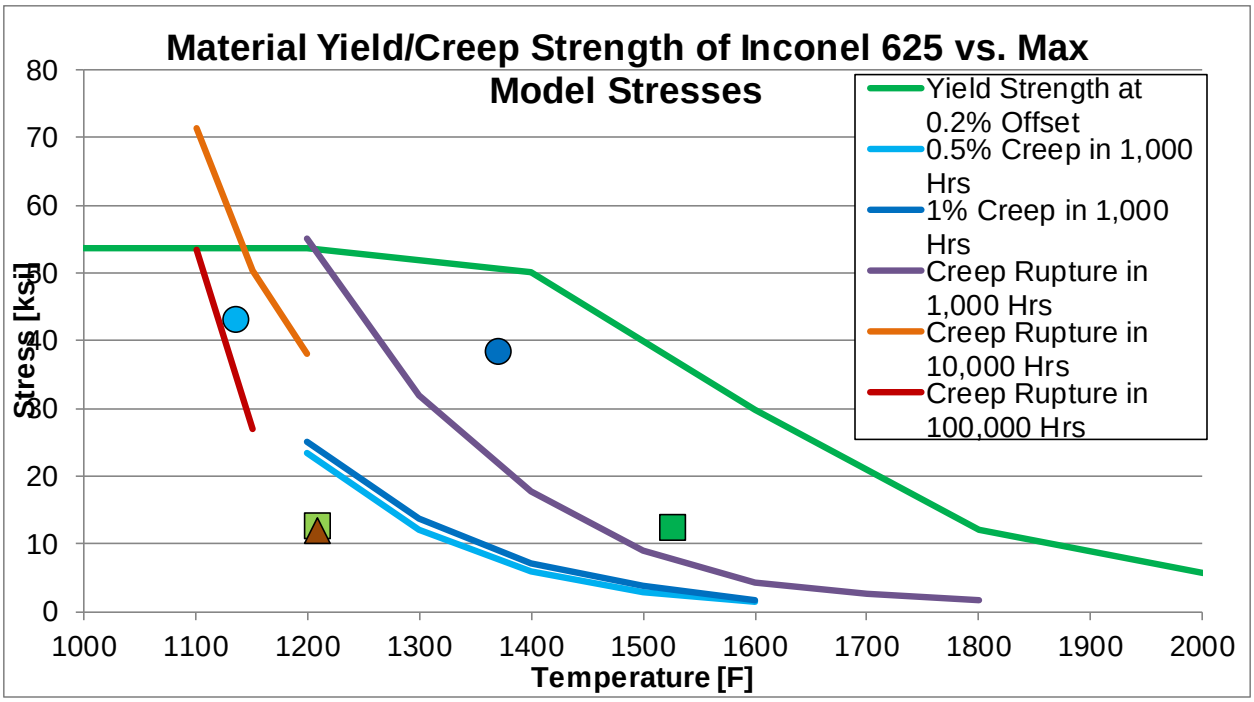

Figure 2-64. Comparison of Mechanical Stresses with Alloy 625 Yield and Creep Limits

2.5.2 SUBTASK 4.2 – CONCEPT STUDY OF REDESIGN OPTIONS FOR HIGHER TEMPERATURE

The baseline analysis results, described in the previous section, show similar stresses in the cross-flow and counter-flow regions for both the baseline and hot (CO_2) operating conditions, but significantly reduced safety creep and yield safety factors associated with reduction of material strength at the higher temperature condition. These results highlight the necessity of design changes for higher-temperature operation. A conceptual design brainstorm session and down-selection meeting was held involving senior engineering staff at SwRI and recuperator design and manufacturing engineers at Solar Turbines in order to develop a short list of redesign options for further evaluation. The brainstorm and down-selection results are summarized in Table 2-30. Concepts indicated were selected for further analysis and validation based on potential for successful manufacturing, effective stress reduction, and cost-effectiveness.

The final redesign is likely to require a material change to improve high-temperature creep and yield strength. In order to compare the alternative materials selected for this project, the yield and the 1,000-hour creep rupture strength curves for each material have been plotted as a function of temperature. The yield strength plot is shown in Figure 2-65 and the creep rupture strength plot is shown in Figure 2-66. 1,000-hour creep rupture strength was selected as the creep metric because all of the materials of interest had this measurement available. The yield stress plot shows that Haynes 263, Haynes 282, and Haynes 25 all have a higher limit than alloy 625 at 1,526°F. However when looking at both plots, it is clear that the creep rupture strength decreases more quickly than the yield strength and is, thus, the limiting factor when preserving yield and creep safety factors for the updated design. All of the materials plotted have creep rupture strength higher than alloy 625 at the temperature of interest.

Based upon the economic analysis, it has been determined that recuperator material cost is relatively insignificant when compared with the fuel savings of installing the recuperator in a higher efficiency cycle. Therefore, Haynes 282 has been selected for further redesign investigation as it offers the highest creep rupture strength at the conditions expected in the CO_2 cycle. This preliminary material selection is subject to verifying availability and manufacturability of Haynes 282 sheets.

Table 2-30. Recuperator Concept Listing and Down-Selection for Further Analysis

Area	Number	Description	Notes	Representative Image	Analyze?
Overall	1	Material change to Haynes 282	Confirm ductility relative to Alloy 625 and availability of sheet-form Haynes 282		Y
	2	Increase recuperator length to lower DP	No risk; higher cost		Y
Cross-flow Sheet	3	Increase crossflow corrugated sheet thickness	Higher pressure drop, improved heat transfer if pitch is maintained		Y
	4	Decrease crossflow corrugated sheet pitch	Higher pressure drop, improved heat transfer. Assume counterflow sheet air-side width is smallest manufacturable width		Y
	5	Solid supports at regular crossflow sheet channel intervals	Assembly/attachment of supports, increased pressure drop		N
	6	Hollow (circular/oval) support tubes at regular crossflow sheet channel intervals	May provide lower pressure drop compared to solid supports and / or increased thickness / reduced pitch of counterflow sheet		Y
	7	Change shape of crossflow sheet folds - wider at base to reduce bending stresses at max stress location	Turning angle not a toleranced dimension		Y
Counter-flow Sheet	8	Increase crossflow sheet thickness			Y
	9	Flat contacts in counterflow sheets	Manufacturing with existing equipment is questionable		N
	10	Only fold counterflow sheets in thicker counterflow region to avoid decreasing crossflow area	Concerns about stretching sheet in folding process		N
	11	Change streamwise phasing of counterflow sheets to improve contact area	Contact faces could be slightly out of phase or exactly in phase		Y
	12	Incorporate separator sheet between counterflow sheets to distribute contact stresses (perhaps perforated and/or with turbulators)			Y
	13	Insert nested support sheets in counterflow section to provide additional strength without decreasing crossflow area	Concerns about matching tolerances between existing sheets and support sheets; mismatch resulting in high stresses and poor heat transfer		N

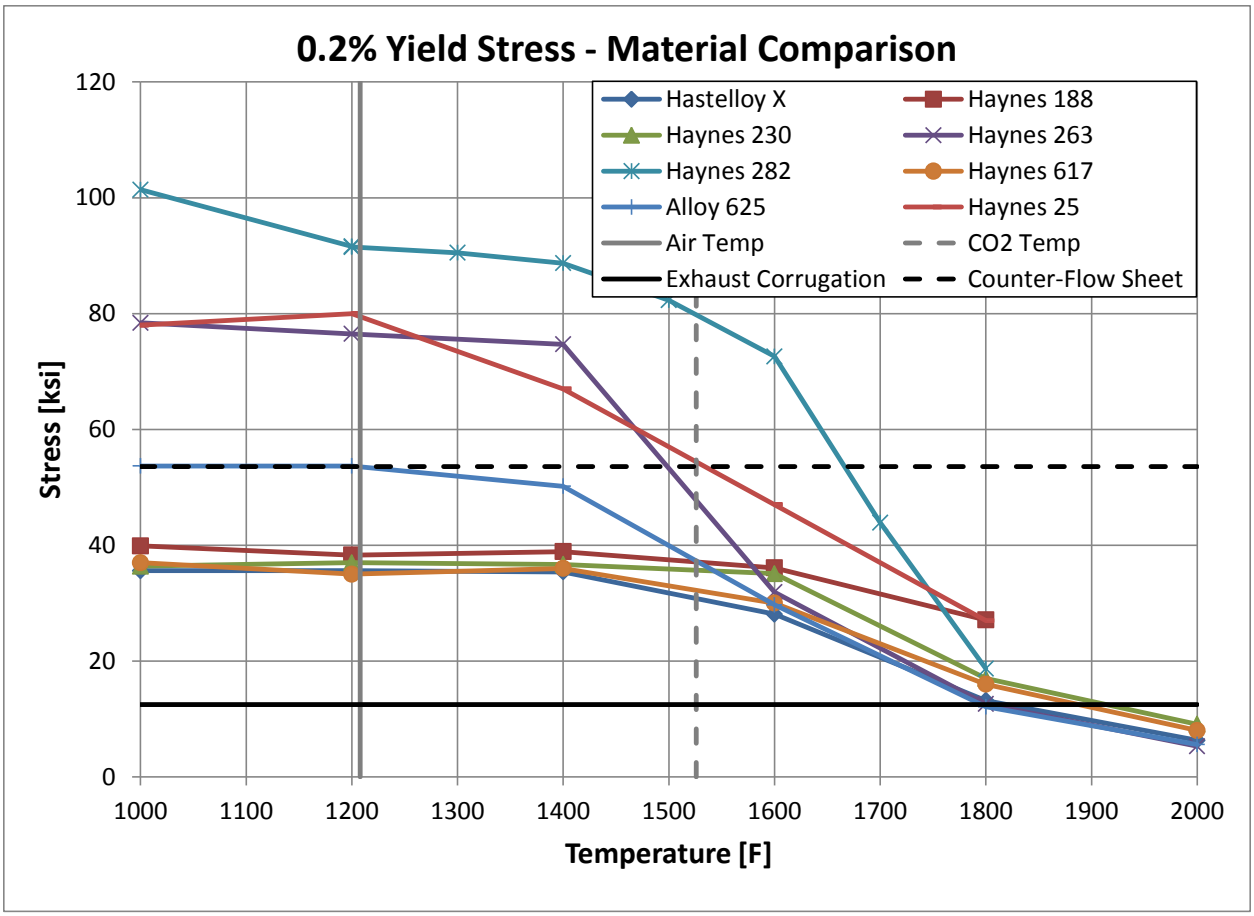

Figure 2-65. Comparison of Yield Limits for a Variety of Materials

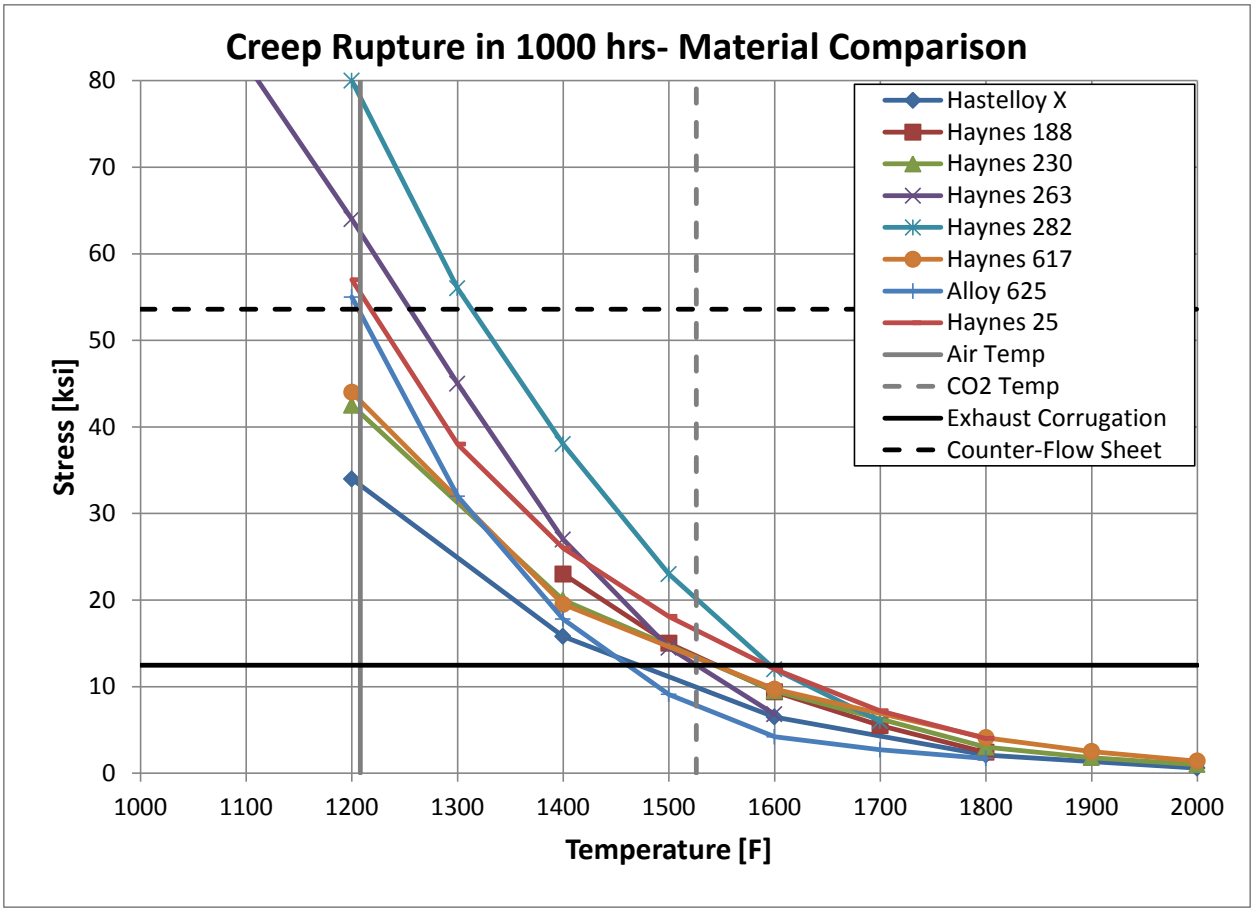

Figure 2-66. Comparison of 1,000 Hour Creep Rupture Limits for a Variety of Materials

2.5.3 SUBTASK 4.3 – MECHANICAL DESIGN AND ANALYSIS OF SELECTED CONCEPTS

Analysis of the down-selected concepts is currently underway, and multiple concepts for both the cross- and counter-flow sections have been completed to date. The following subsections provide preliminary analysis results for heat transfer performance and mechanical strength for concepts for both areas.

2.5.3.1 Counter-flow Sheet Redesign

The intent of this work is to develop a high-temperature heat exchanger design capable of operation in CO_2 at temperatures up to 1,510°F (821°C) and pressure differentials up to 130 psi (9 bar). To accomplish this goal, the counter-flow regions of the existing primary surface heat exchanger would need to go through a redesign to handle this combination of temperature and pressure. For the initial redesign, it was determined that an increase in material thickness would be required. In discussions with Solar Turbines, the point was made that the existing folding equipment used to create the counter-flow sheets may be able to handle sheet material thicknesses up to twice the thickness of the original design. This was used as the thickness criteria for the initial redesign.

The existing model was used to create a new design with the counter-flow sheet thickness twice that of the original. The corrugated sheets in the redesigned model measure 0.0084” thick instead of the original 0.0042” thickness. The overall height of the corrugated sheet and the depth of the

model were both kept the same. The number of corrugation periods in the model and the bend radius of each corrugation were also kept the same; however, the overall width of the model increased due to the increased material thickness. Minor changes were also required in the sinusoidal pattern of the folds to ensure these patterns remained aligned with the opposing sheet in accordance with the original design intent.

The initial analysis run on this new, thicker model (2X model) used the same loads and temperatures as the existing high-temperature run, which consisted of 130 psi pressures on the top and bottom surfaces of the model, and a temperature load of 1,510°F. The constraints used in the initial 2x model analysis were also kept the same as the initial baseline analysis. See Section 2.5.1.4.2 for a full description of baseline loads and constraints. The results of these runs showed some anomalies occurring on the edges of the model in the Z direction (see Figure 2-67). These edges have a Linear Periodic constraint applied to them which forces these two faces to react to any loads as if they were the same face; however, neither face has a symmetry constraint applied, so both faces, though reacting similarly, were experiencing high localized stress at points of contact along the edge due to bending effects.

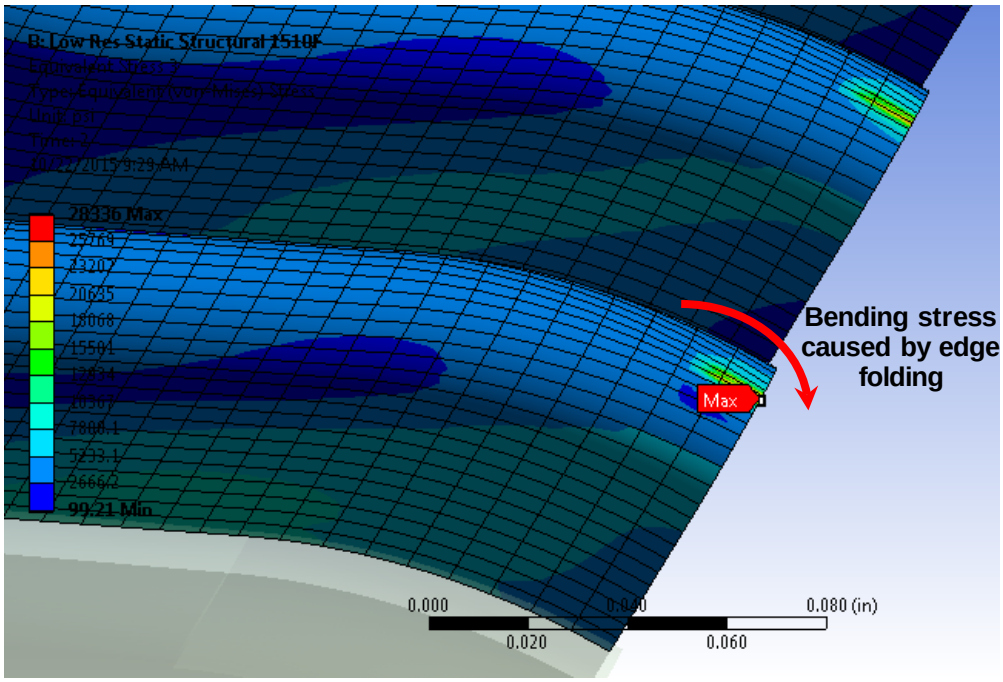

Figure 2-67. Edge Anomalies in Z Direction, 2X Model

To correct the high bending stress seen on the sheet edges, a symmetry constraint was applied to the +Z face on both models and the analysis for each was rerun. The results of this run seemed to correct the high edge stresses seen in the 2X model; however, the original model would not converge.

It was determined that the models could be simplified to removing some of the non-linear analysis requirements that were present in the original models. This simplification was accomplished by removing the thermal load and applying material properties at 820°C to the corrugated sheets. This simplification would allow for better convergence in the models while imposing symmetry restraints and keeping the original analytical intent, which included capturing the material stress relaxation at temperature. The results of the simplified models were compared to that of the

original models to ensure the simplified modeling approach remained accurate. The stress patterns and results from this analysis matched closely with the original analysis without symmetry (see Figure 2-68 a. and b.). The stress magnitude also seemed reasonable with an overall stress decrease from 43,082 psi to 40,044 psi, which is expected due to the symmetry constraint changing the dynamics of the contact interactions.

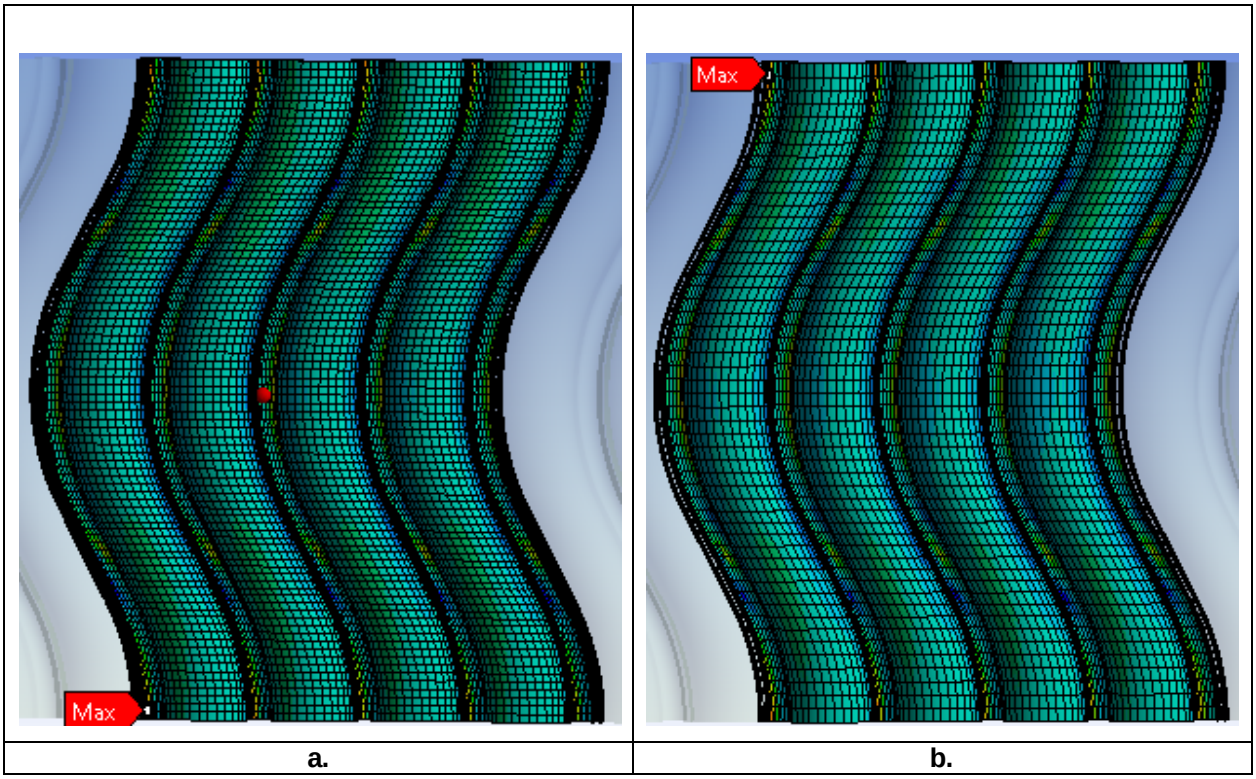

a. b.

Figure 2-68. Stress Pattern of a. Original Thickness Model with Symmetry and 1,200°F Material Properties b. Original Thickness Model with no Symmetry

With the knowledge that the simplified symmetry models match well with the original baseline models, analysis was continued with the simplified 2X symmetry model and subsequent models of varying thickness and design. The first set of models varied only the thickness of the counter-flow sheets using sheet thicknesses of 1.2, 1.3, 1.4, 1.5, and 2 times thicknesses. The results of these analyses were compared to the baseline analysis with a goal of keeping similar creep and yield safety factors for the increased thickness models in CO_2, as are found in the original model with air. The 2X model using alloy 625 at the CO_2 temperatures did not meet the safety factors of the original model in air, so the sheet material was changed to Haynes 282. With the increased strength of this new material, several material thickness iterations were made in an attempt to find the smallest material thickness (to keep good machinability) that would still meet the required safety factor for both yield strength and creep. These iterations included sheet thicknesses of 2, 1.5, 1.4, 1.3, and 1.2 times thicknesses. The thinnest sheet of 282 to still meet the safety factor requirements was the 1.4X sheet. Two additional designs were modeled in an effort to meet these requirements. The first of these was a model with the corrugations of the top and bottom sheets perfectly in line, creating lines of contact down the center of each trough (Figure 2-69). A thickness of 1.4X was used and the results of the analysis met the required stresses; however, this design was deemed unrealistic as the inherent variation in the placement of these sheets was quite large and would not allow for the precise alignment of the top and bottom sheets with the required precision. A major change in the assembly process of the

recuperator would be required to meet the precise alignment requirements of this design. The second design used a separator sheet between the top and bottom corrugated sheets (Figure 2-70). This separator sheet acts as an additional support where the top and bottom corrugations cross, effectively reducing the stresses at those points. Three variations with the separator sheet were analyzed starting with a corrugated sheet thickness of 1.4X and a separator sheet thickness of 0.0042", and working down to a corrugated sheet of original thickness and a separator sheet thickness of 0.003". This combination was the thinnest material that still met the safety factor criteria.

A graphical comparison of the safety factors associated with each of these redesign options is presented in Figure 2-71. For the safety factor comparison, yield stress and creep stress were evaluated at 1,136°F for the air condition and at 1,371°F for the CO_2 condition. These temperatures represent the expected high temperatures at the counter-flow section of the recuperator.

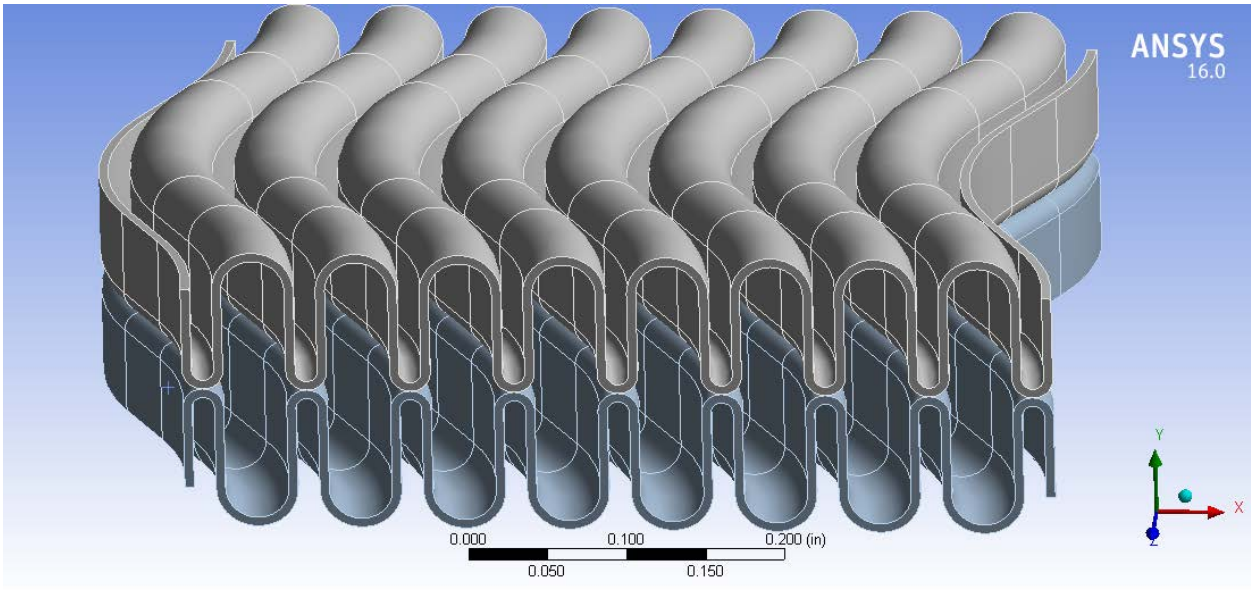

Figure 2-69. Counter-flow Section Redesign with In-phase Corrugations

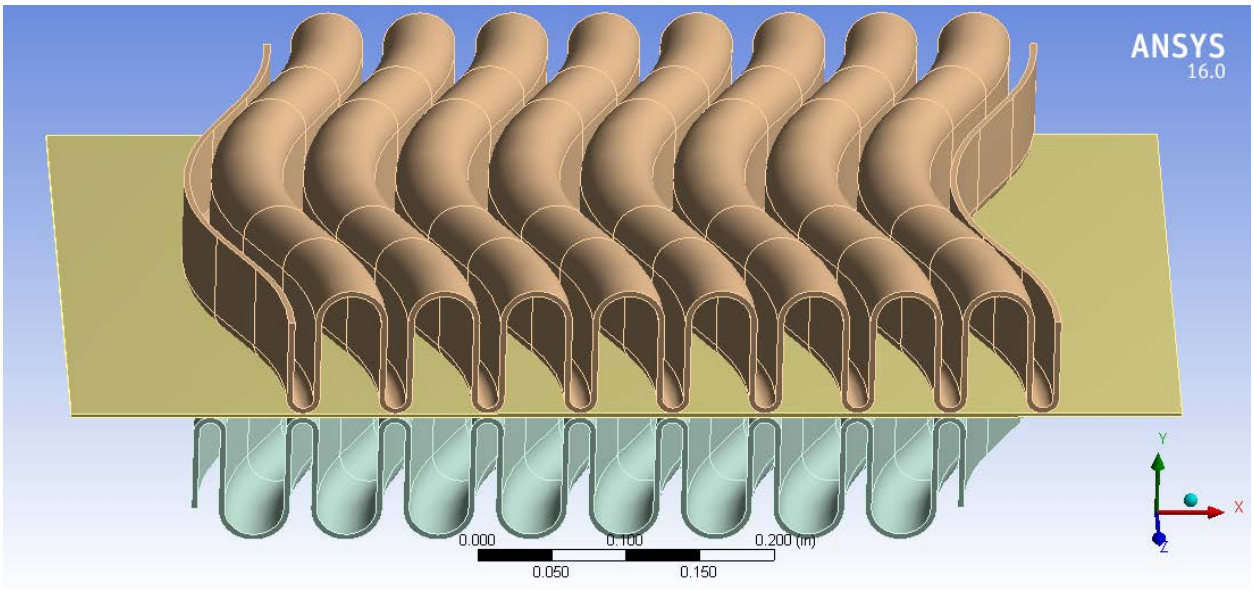

Figure 2-70. Counter-flow Section Redesign with Separator Sheet

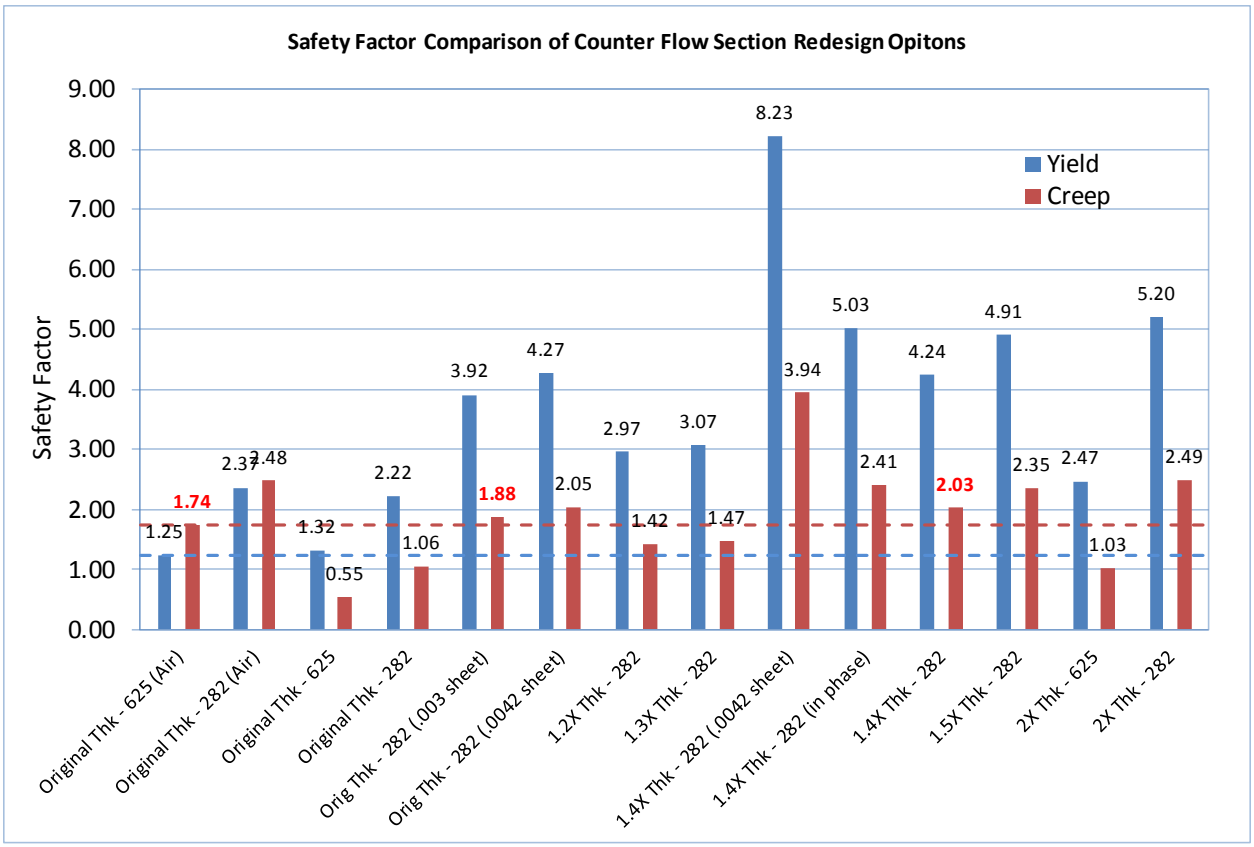

Figure 2-71. Safety Factor Comparison of Counter-flow Redesign Options

From these redesigns, it appears that the two options that optimally maintain the yield and creep safety factors of the original design in air are the separator sheet with 0.003" thickness and the original design with 1.4X the existing sheet thickness. Both of these redesigns also include a material change from alloy 625 to Haynes 282. The analysis for the design with a separator sheet was performed with a flat unperforated separator sheet for simplicity. Another variation for this redesign concept is to use a perforated separator sheet to allow air exchange between the top and bottom chambers, thus, maximizing mixing flow and heat transfer; however, any perforations in the separator sheet could be positioned between the contact points of the upper and lower corrugated sheets creating stress risers in those areas. The stress risers would potentially negate the stress lowering effect of the separator sheet, making this an unacceptable option. This phenomenon is difficult to model accurately, since the recuperator design does not allow for precise positioning of the counter-flow sheets relative to separator sheet perforations. With these difficulties in mind, the separator sheet was designed to be unperforated.

2.5.3.2 Cross-flow Section Redesign

During the course of the project, the team brainstormed a variety of redesign approaches and selected four for detailed investigation. The four redesign approaches investigated included: 1) increasing the thickness of the corrugation, 2) adjusting the corrugation pitch, 3) adjusting the angle of corrugations, and 4) adding support tubes. The following four sections describe each of these approaches along with their impact on the stress levels. This is followed by as summary section, and the last section presents two successful redesigns.

Each redesign option required a new finite element model for analysis. To ensure that each simulation accurately predicts the redesign performance, mesh convergence studies were performed for each new model. An overview of the model convergence is shown in Figure 2-72 for the corrugation stress levels. A complimentary analysis was performed to ensure convergence in the sheet stress levels. A material change did not necessitate the need for a new model, but for completeness, those results have also been included.

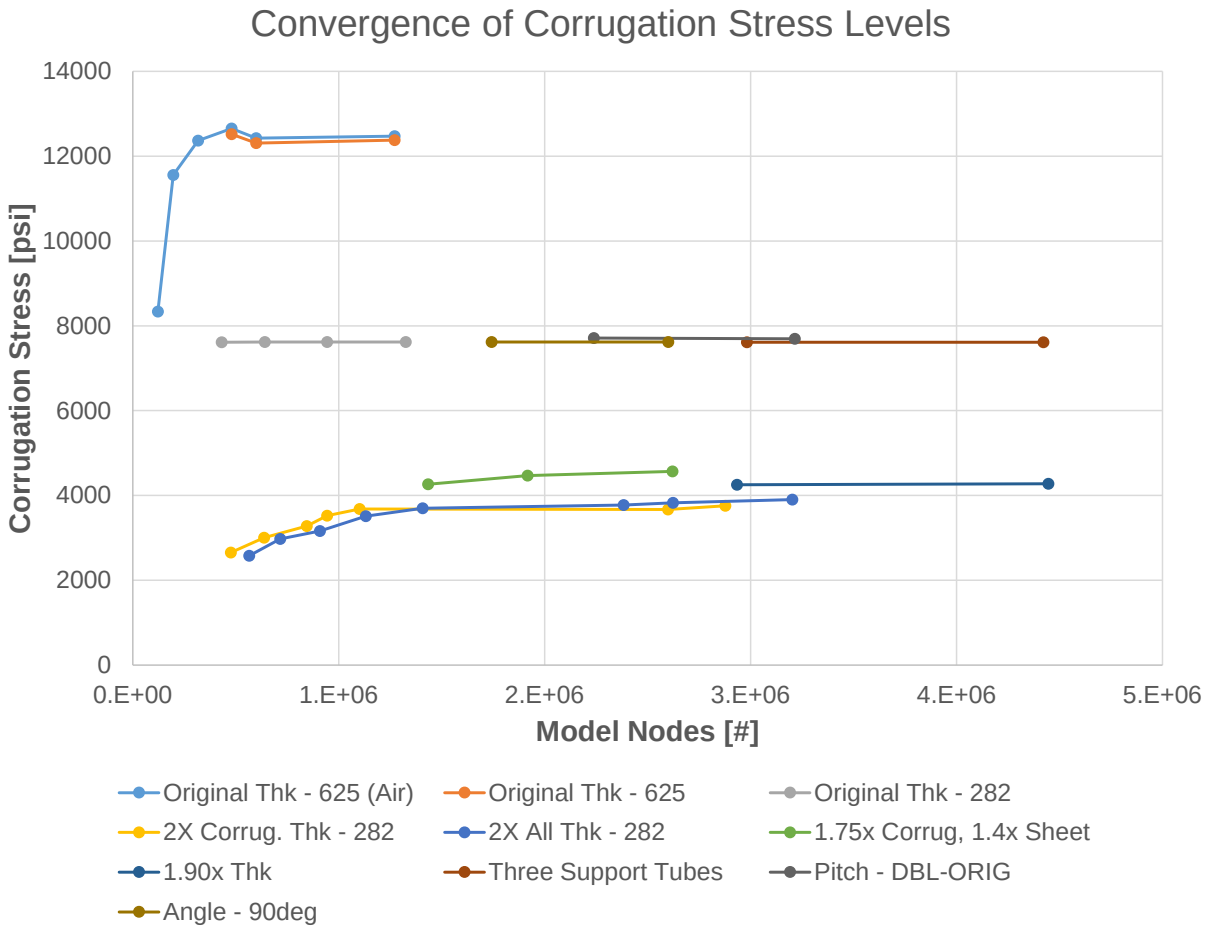

Figure 2-72. Overview of Model Convergence

2.5.3.2.1 Increased Corrugation Thickness

This section presents the results of increasing the corrugation thickness for CO_2 conditions. The results for doubling corrugation thickness are shown in Figure 2-73 for using 625 and Figure 2-74 for 282, using the current design's counter-flow sheet thickness. The stress levels and stress fields are very similar despite using the different materials. Doubling the corrugation thickness greatly reduced the maximum stresses. The maximum stresses occurred at the inside of the corrugation bends for both design options. Another double corrugation case (not shown) was performed where the corrugation contact area, instead of corrugation bend angles remained constant. This redesign did not greatly change the stress levels.

The impact of increasing the thickness of the counter-flow sheets on corrugation stresses is also presented for CO_2 conditions. The flat sheets in the exhaust corrugation models represent counter-flow sheets that have been pressed flat, so the counter-flow sheet thickness affects the available space for corrugation height in the cross-flow section. Thus, various geometries were analyzed in order to determine the optimal corrugation thickness for various counter-flow sheet thicknesses. Simulation results with twice the current counter-flow sheet thickness are shown below in Figure 2-75 for using 625, and Figure 2-76 for 282. Again, the stress levels and stress fields were quite similar despite using the different materials. Similar to doubling only the corrugation thickness, the maximum stresses occurred at the inside of the corrugation bends for

both design options. Doubling the thickness of everything reduced the stress levels in the sheets while slightly increasing the stress levels of the corrugation. A third, double-all case (not shown), was performed where the corrugation contact area, instead of corrugation bend angles remained constant. This option did not greatly change the stress levels. These simulations have shown that increasing the corrugation thickness reduces the maximum stresses.

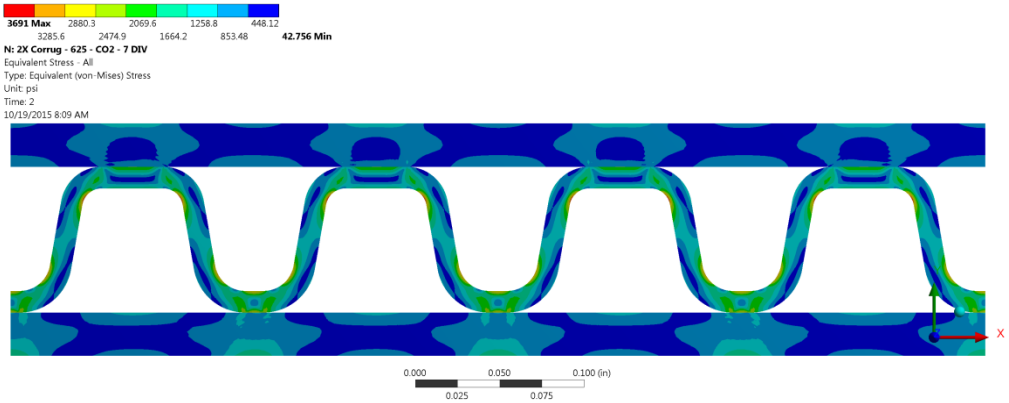

Figure 2-73. Stress Distribution for 2X Corrugation Thickness – 625 @ CO_2 Conditions

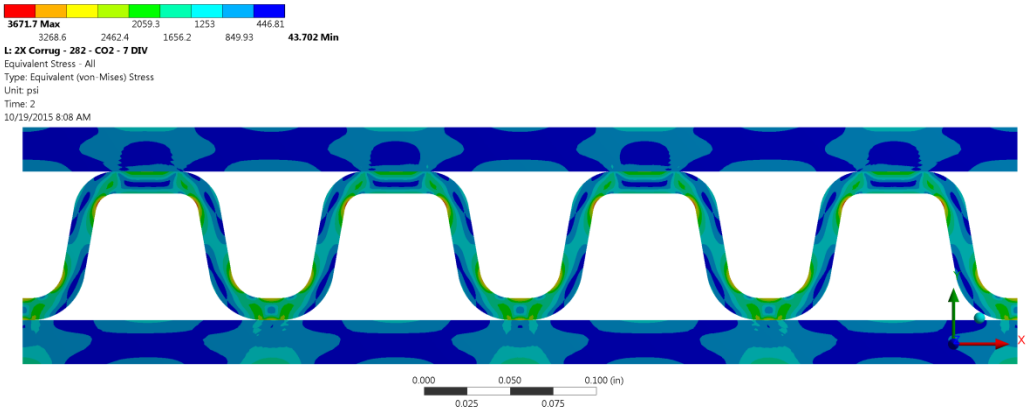

Figure 2-74. Stress Distribution for 2X Corrugation Thickness – 282 @ CO_2 Conditions

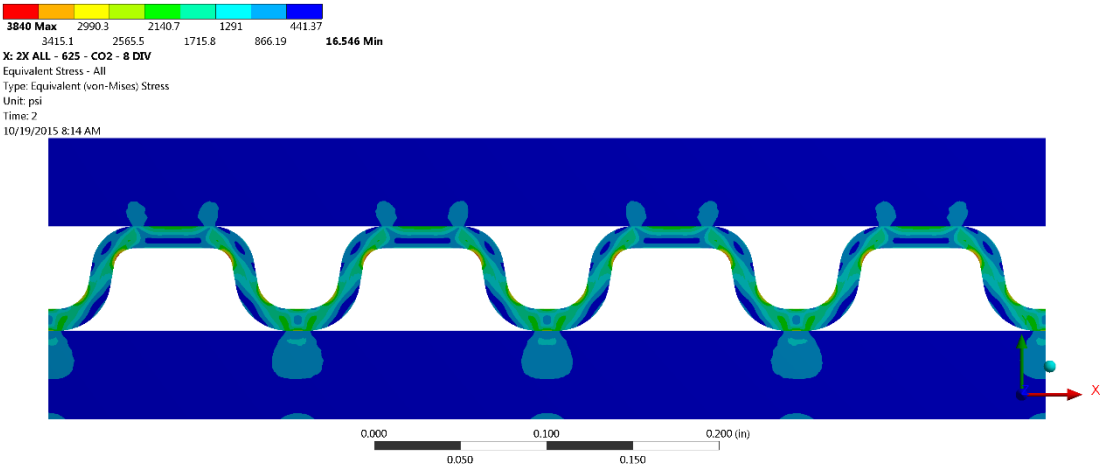

Figure 2-75. Stress Distribution for 2X Thickness of Corrugation and Sheets - 625 @ CO_2 Conditions

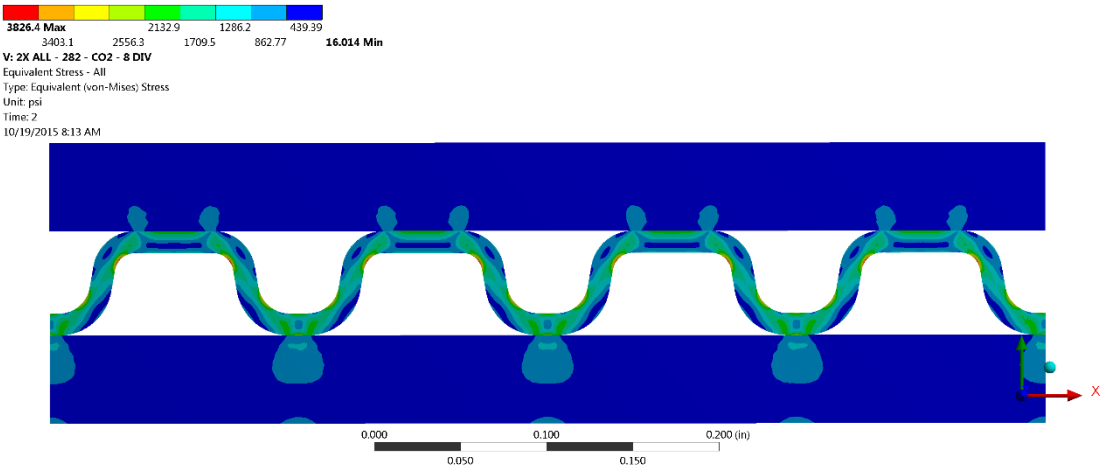

Figure 2-76. Stress Distribution for 2X Thickness of Corrugation and Sheets - 282 @ CO_2 Conditions

2.5.3.2.2 Pitch Modifications

Alternative redesign options were made to vary the pitch of corrugations in the cross-flow section. These designs were variations of the original thickness levels and run for CO_2 conditions with 282 as the material. The first option, shown below in Figure 2-77, halved the contact area of the corrugation with the upper sheet. The second redesign reduced the contact areas of the upper and lower corrugation to a minimum, as shown in Figure 2-78. A third redesign was created that doubled the contact areas of the upper corrugation, as shown in Figure 2-79. All redesign options resulted in stress levels quite similar to the original pitch.

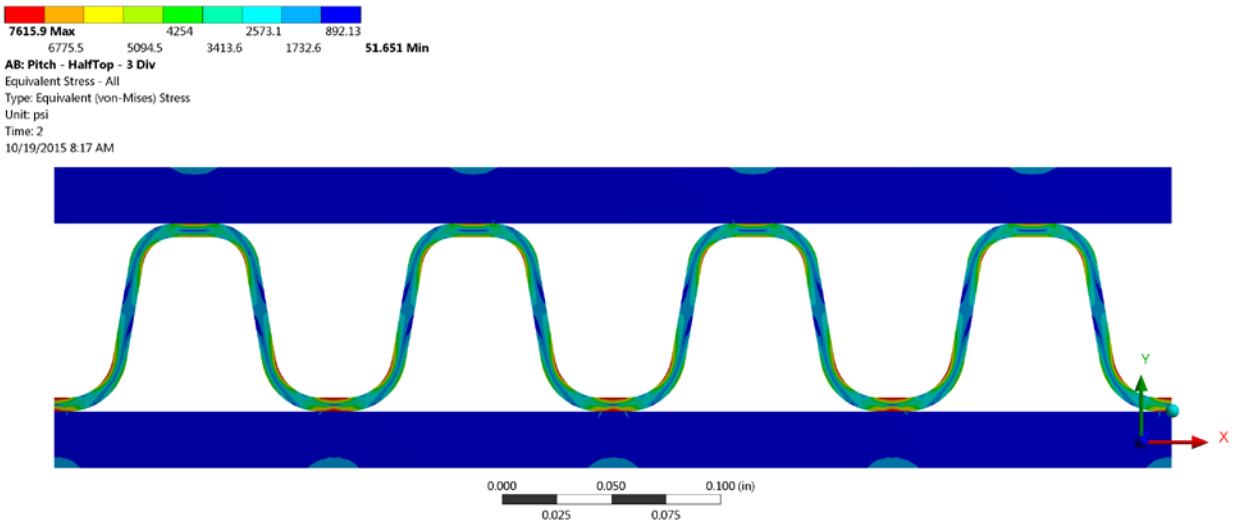

Figure 2-77. Stress Distribution for Pitch Half Top – 282 @ CO_2 Conditions

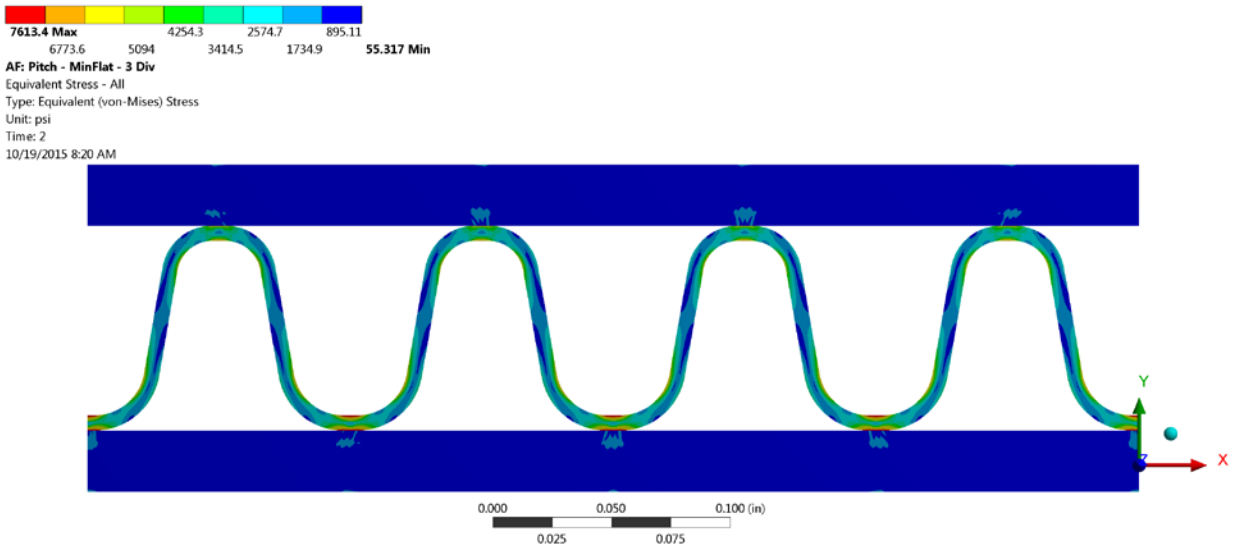

Figure 2-78. Stress Distribution for Pitch Minimum Flats – 282 @ CO_2 Conditions

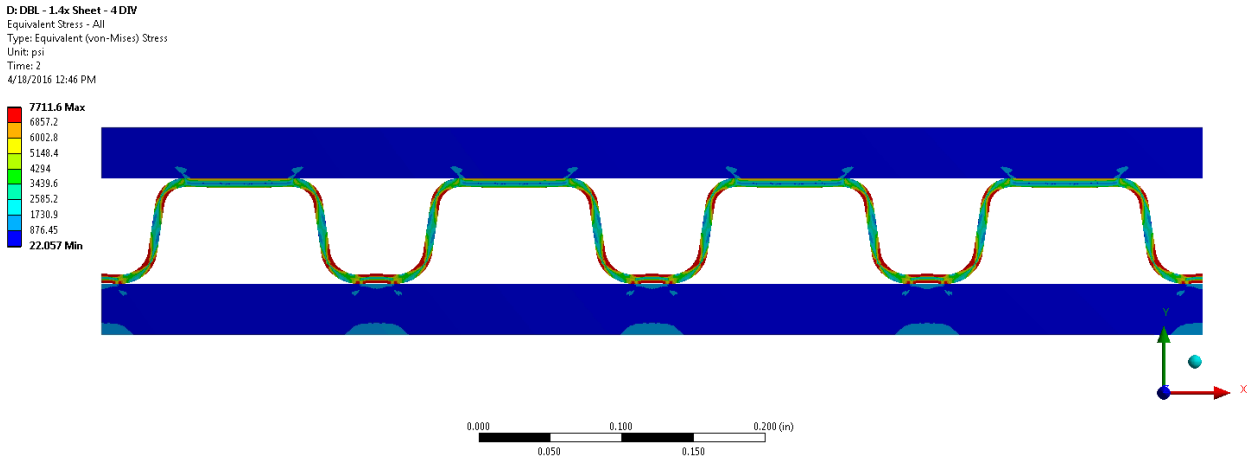

Figure 2-79. Stress Distribution for Pitch Double Top – 282 @ CO_2 Conditions

2.5.3.2.3 Angle Modifications

This section presents the results of changing the pitch of the corrugation angles using Haynes 282 and the current design's counter-flow sheet thickness. The angle of the corrugation ranged from 70°, shown in Figure 2-80, to 90°, shown in Figure 2-81. Not shown are the 75° and 85° cases that ranged in stress levels between the cases shown. For all the cases, the corrugation area that contacted the lower sheet remained the same while the contact area on the upper sheet changed with respect to the uniform and symmetric angle modifications. The overall sheet length remained the same for all cases. The resulting stress levels provided little change over the range of angles, with stress concentrations transitioning from the lower contact area at 70° to the corrugation bends as the angle increases to 90°.

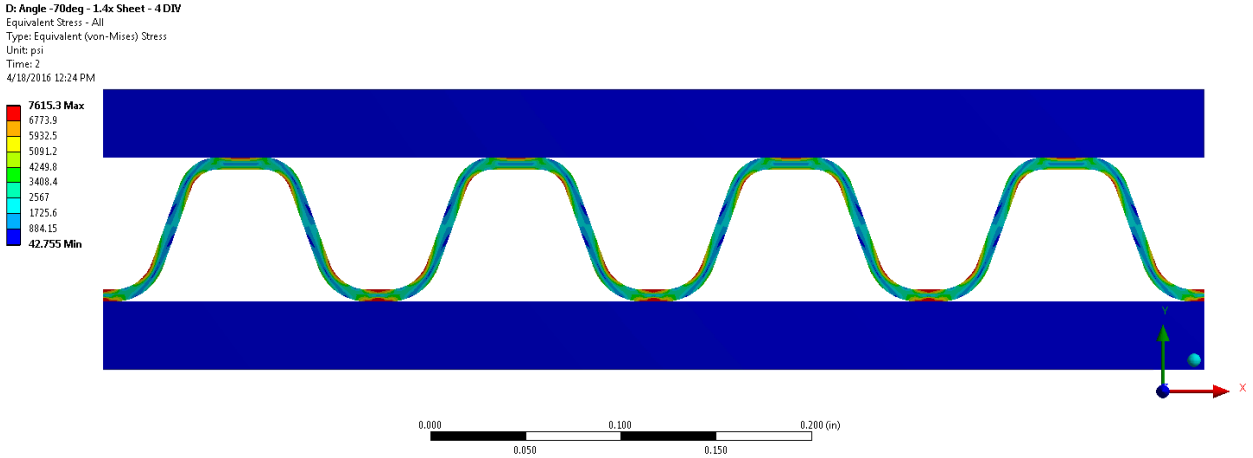

Figure 2-80. Stress Distribution for 70° Corrugation Angle - 282 @ CO_2 Conditions

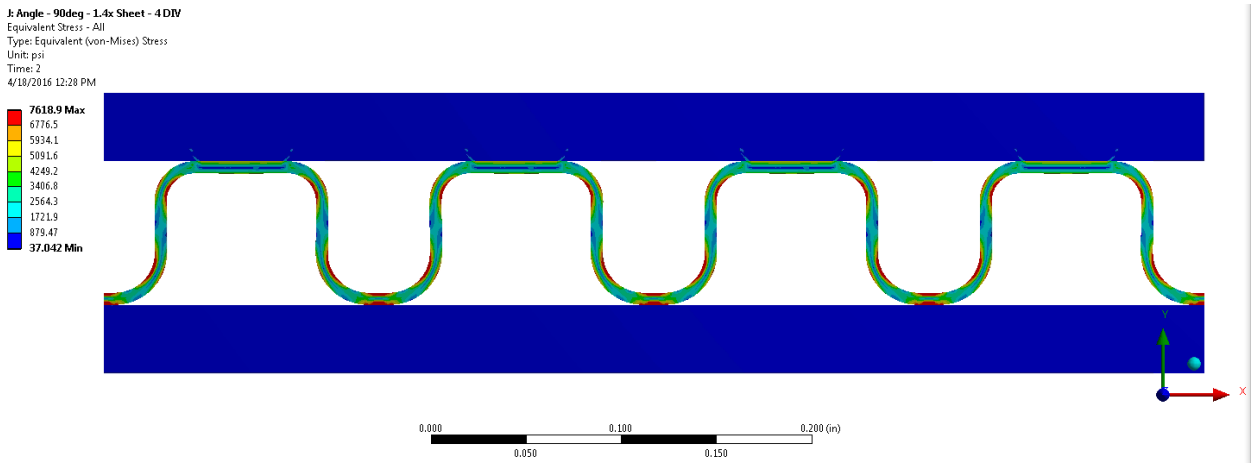

Figure 2-81. Stress Distribution for 90°Corrugation Angle - 282 @ CO_2 Conditions

2.5.3.2.4 Support Tube Modifications

One series of modifications included the use of hollow support tubes at regular cross-flow sheet channel intervals. The curves of the square tubing edges matched those of the corrugation bends. The tubing was comprised of the Haynes 282 material with the same thickness as the corrugation. The hollow tubes were placed underneath the corrugation, making contact with the face of the lower sheet. Four options of tube quantities are presented with one, two, three, and five tubes spaced along the length of the sheet with even distribution along the x-axis. Figure 2-82 through Figure 2-85 demonstrate the geometry of the one-tube design through the five-tubes design, respectively. While the tubes provided added support with minimized pressure loss, the overall stress level of the corrugation remained similar to those as other designs. As expected, the option with five tubes, representing a tube for every opening under the corrugation, resulted in the lowest stress levels of all of the support tube modification options.

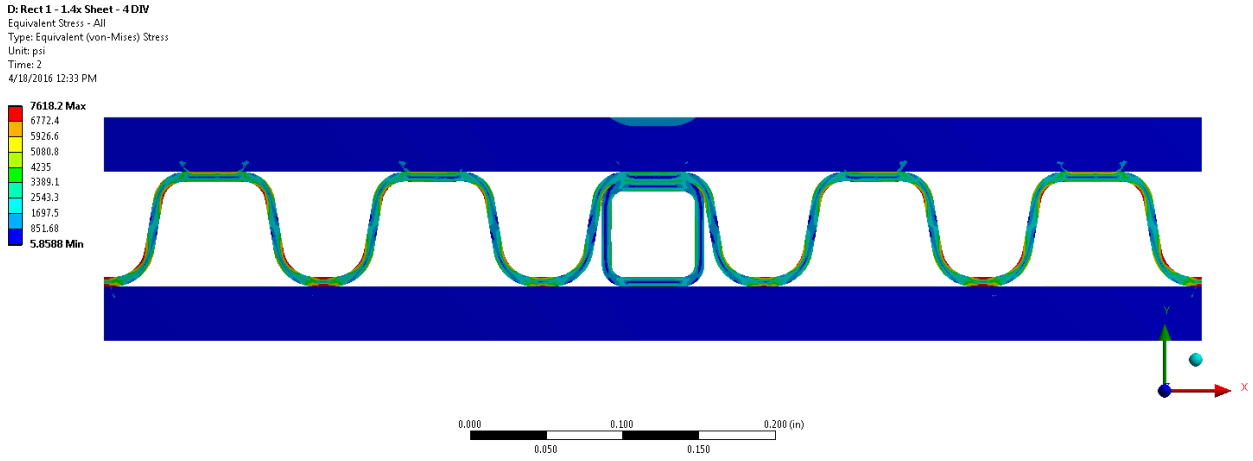

Figure 2-82. Stress Distribution for One Support Tube - 282 @ CO_2 Conditions

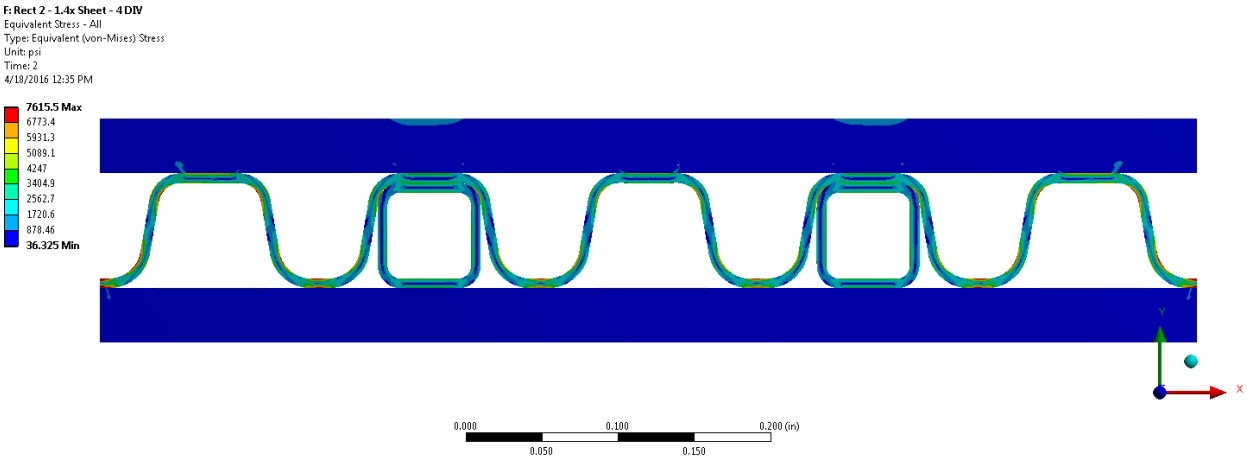

Figure 2-83. Stress Distribution for Two Support Tubes - 282 @ CO_2 Conditions

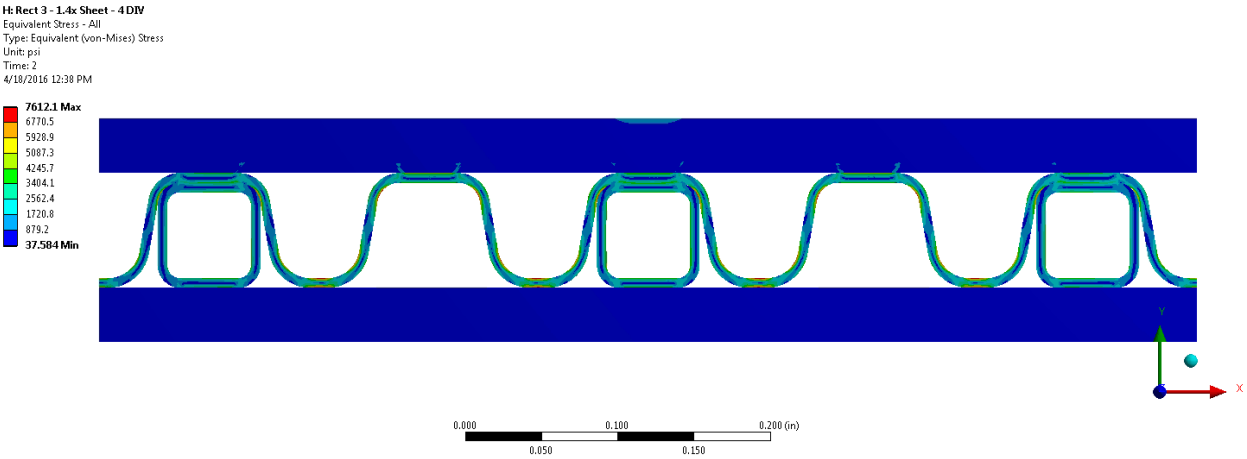

Figure 2-84. Stress Distribution for Three Support Tubes - 282 @ CO_2 Conditions

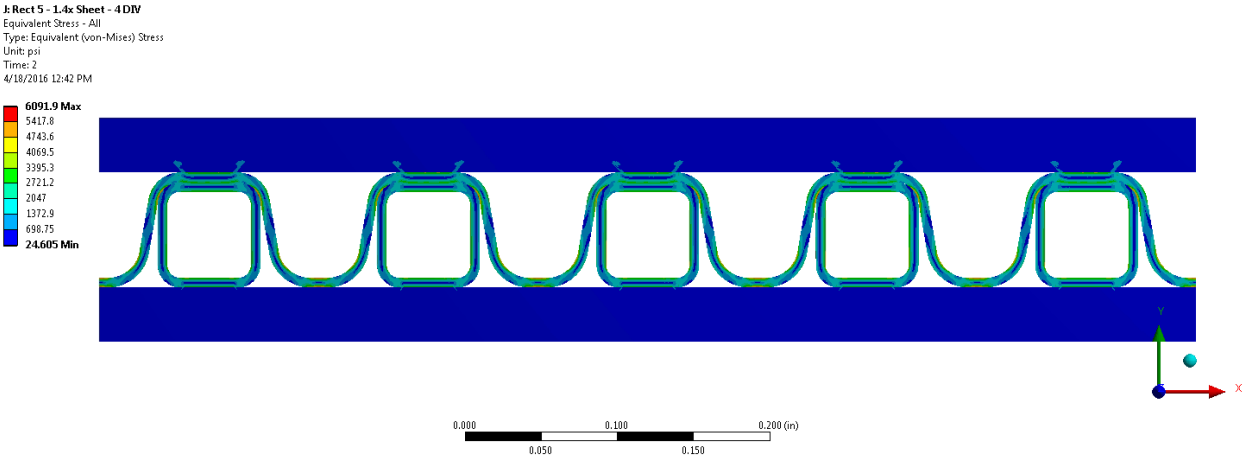

Figure 2-85. Stress Distribution for Five Support Tubes - 282 @ CO_2 Conditions

2.5.3.2.5 Comparison of Redesign Approaches

This section compares the safety factor of the four redesign approaches: 1) increasing the thickness of the corrugation, 2) adjusting the corrugation pitch, 3) adjusting the angle of corrugations, and 4) adding support tubes. The redesigns are compared to the safety factor of the original design in two graphs.

Figure 2-86 shows only the impact of increasing the thickness and has various combinations of sheet and corrugation thicknesses. Figure 2-87 compares the remaining redesign approaches and keeps corrugation at its original thickness and the sheets at 1.4 times the original thickness. The graphs clearly show that of the redesign approaches investigated, only increasing the corrugation thickness had a significant impact on the safety factor.

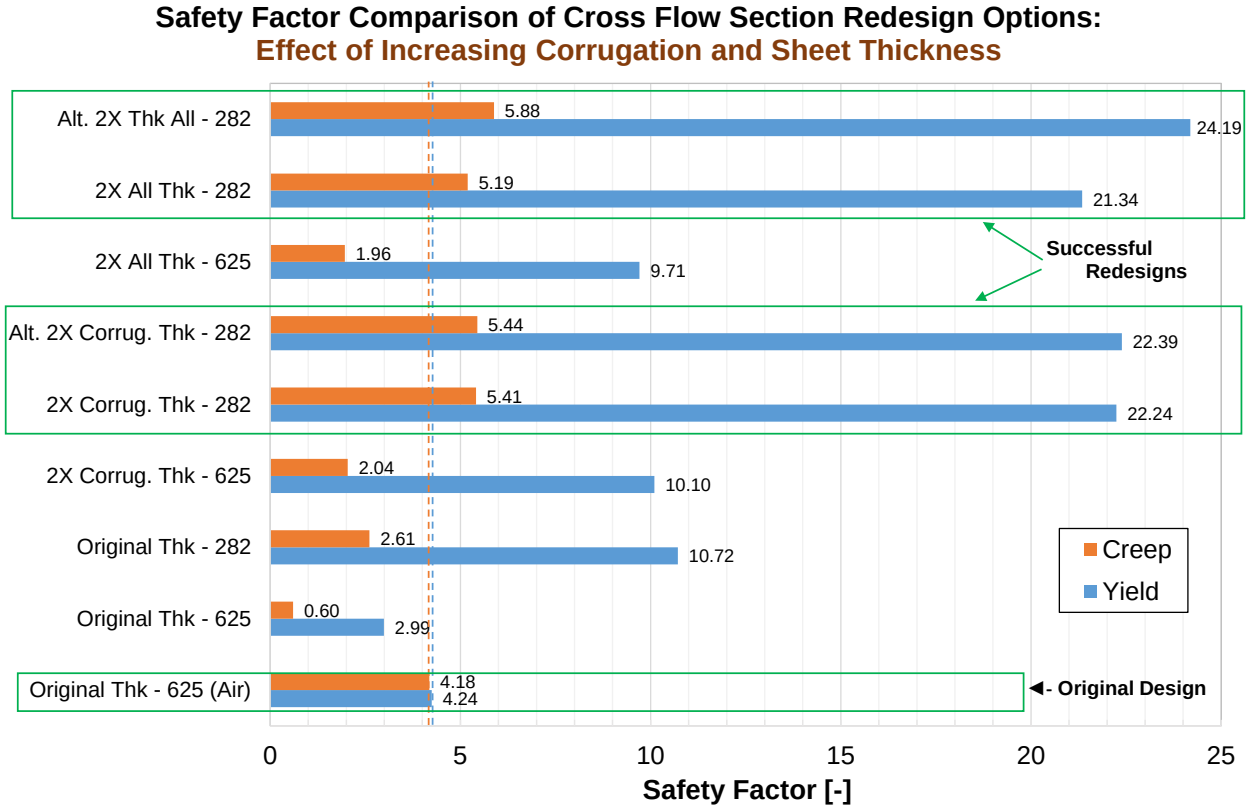

*All cases are run at CO_2 Cycle Conditions unless otherwise noted

Figure 2-86. Comparison of Exhaust Corrugation Redesign Approaches – Part 1

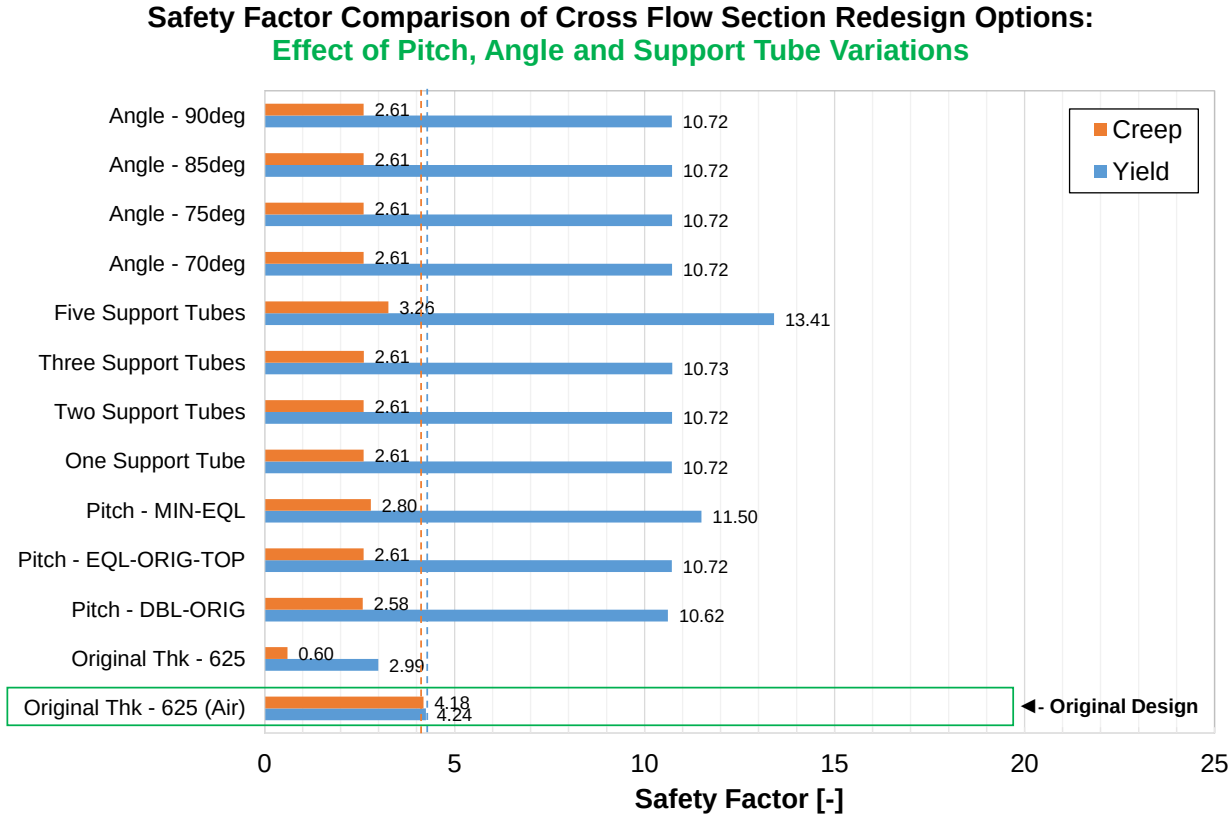

Figure 2-87. Comparison of Exhaust Corrugation Redesign Approaches – Part 2

2.5.3.2.6 Successful Redesigns

The previous section described two successful approaches for redesigning the counter-flow region of the heat exchanger, namely to 1) increase the counter-flow sheet thickness to 1.4 times the original and 2) insert an additional separator sheet in between the counter-flow sheets. This section focuses on applying the cross-flow redesign approach of increasing the corrugation thickness to find a suitable solution to complement both counter-flow solutions. The goal of these analyses was to determine which redesign maintained the safety factor of the original recuperator, while using the least amount of material in order to minimize recuperator cost.

2.5.3.2.6.1 Increased Counter-flow Thickness

As described previously, the optimal counter-flow sheet thickness of 1.4 times the original value was determined for the new design conditions. A parametric study was performed holding constant the counter-flow sheet thickness and varying the thickness of the corrugation sheet. A variety of corrugation thicknesses between one and two times the original thickness were investigated. Previous analyses showed that alloy 625 would not be an acceptable material within this range, thus, Haynes 282 was investigated exclusively. In addition to investigating changing the corrugation thickness, several pitch modifications were also analyzed. An overview of the results is presented below in Figure 2-88. The best redesign option to date is the 1.75 times original thickness corrugation. The stress distribution of this configuration is shown in Figure 2-89.

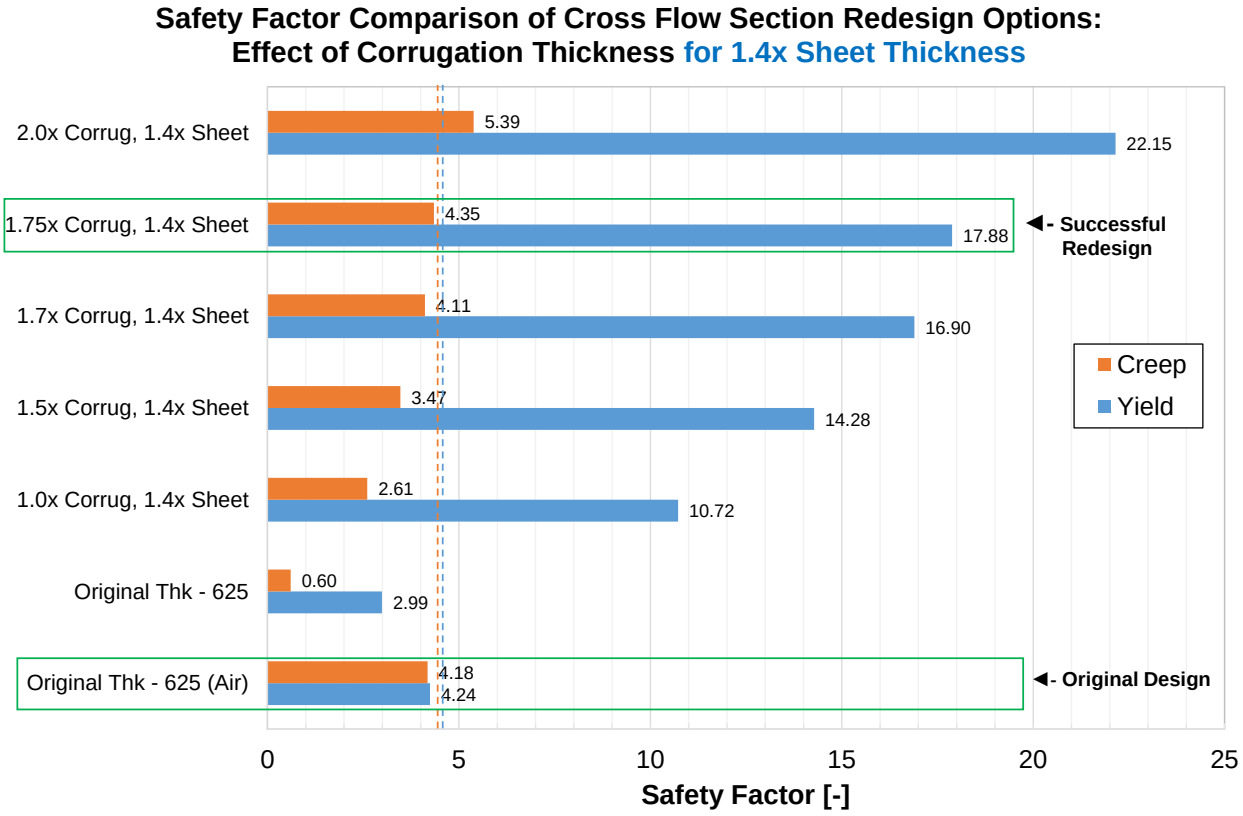

*All cases are run at CO_2 Cycle Conditions unless otherwise noted **Variations shown use a sheet with 1.4x the original thickness

Figure 2-88. Cross-Flow Redesign Analysis Summary – with 1.4x Sheet (Haynes 282)

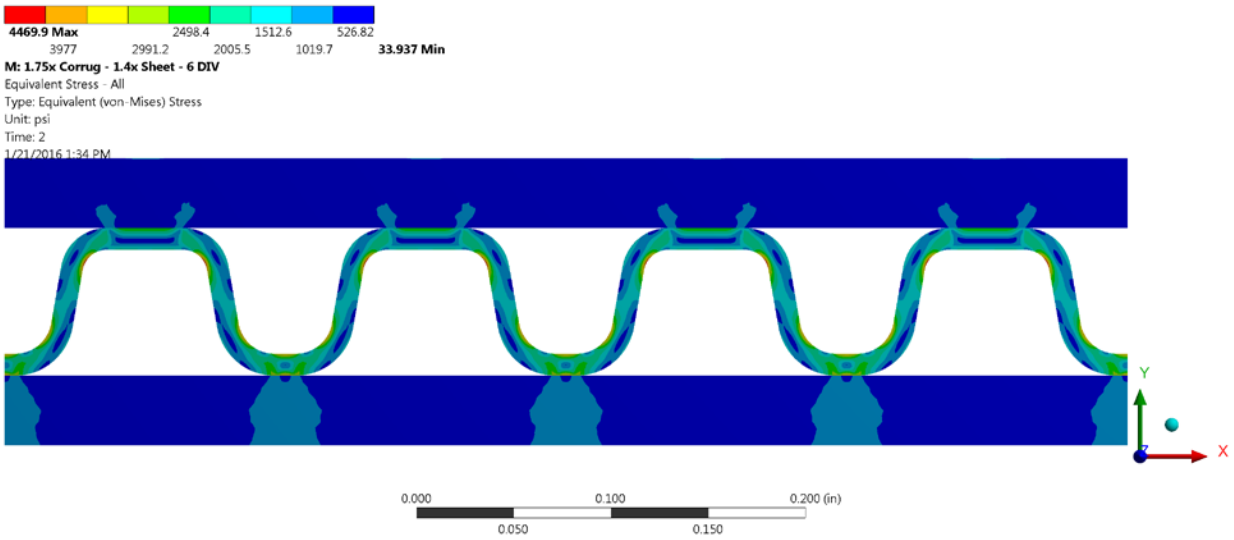

Figure 2-89. Stress Distribution for 1.75x Corrugation – Optimal Cross-Flow Redesign

2.5.3.2.6.2 Increased Counter-flow Height

In order to accommodate the insertion of a separator sheet into the counter-flow region of the heat exchanger, the height of the corrugation was increased by 0.003". A parametric study was performed with this new height, varying the thickness of the corrugation sheet between one and two times the original thickness. As with the previous study, only Haynes 282 was investigated and the corrugation pitch remained constant. A comparison of the variations is shown in Figure 2-92. The best redesign option to date is the 1.9 times original thickness corrugation. The stress distribution of this configuration is shown in Figure 2-91.

Both redesign options increase the sheet thickness of the cross-flow section, and the first design incorporates a counter-flow sheet thickness 40% thicker than that of the original design. Based on conversations with Solar, it is likely that either of these changes can be accommodated by the existing forming machines. The 40% thicker cross-flow sheet design maintains the current part count and assembly process being used on the existing air Brayton cycle recuperator, where the separator sheet concept introduces an additional component.

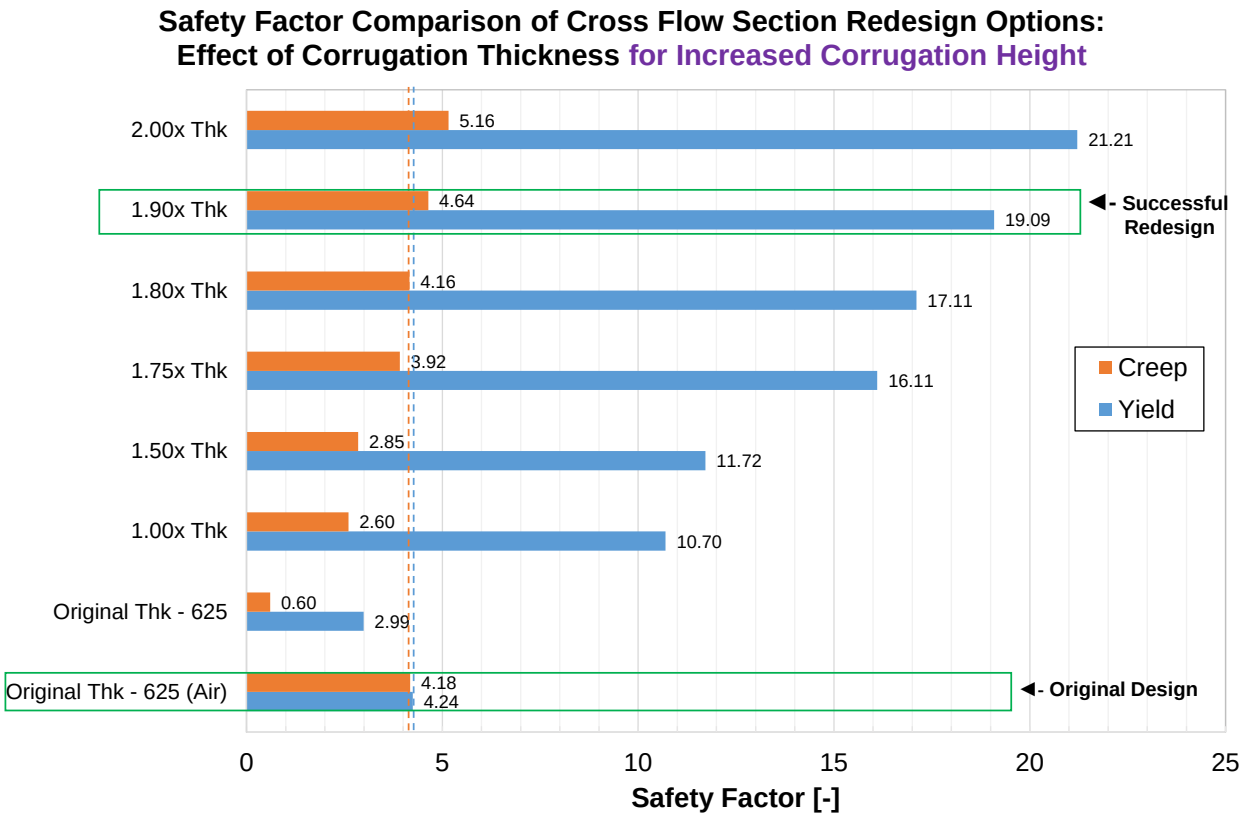

*All cases are run at CO_2 Cycle Conditions unless otherwise noted **Variations shown use a sheet with the original thickness

Figure 2-90. Cross-Flow Redesign Analysis Summary – with Separator Sheet (Haynes 282)

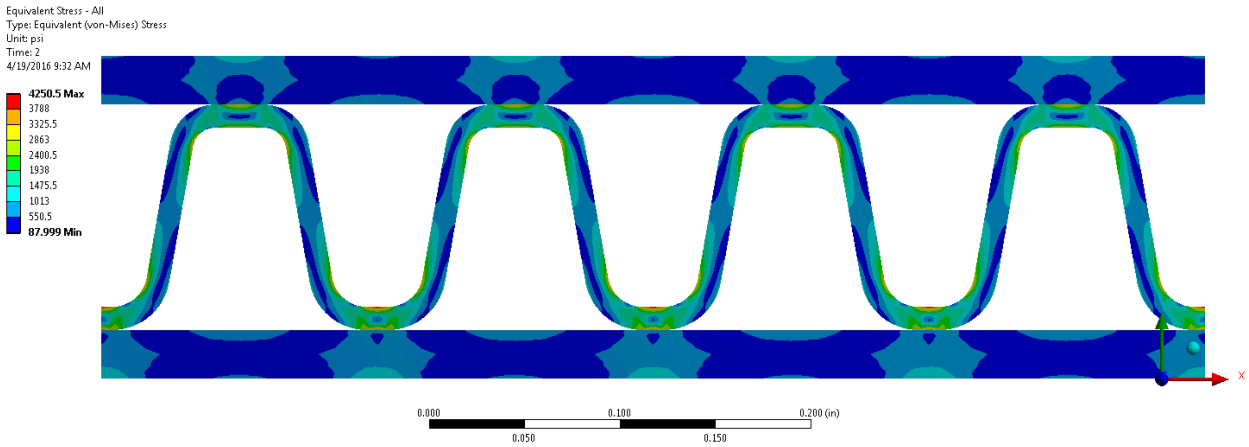

Figure 2-91. Stress Distribution for 1.9x Corrugation – Optimal Cross-Flow Redesign

2.5.3.3 Aerothermal Performance of Optimal Redesign Options

2.5.3.3.1 Heat Transfer Results

Using the simulation procedure and post-processing technique used for the previous simulations, new models were created to test the effect of the new geometry configurations discussed previously in this report. In this section and in the plot legends, the different geometry configurations for all the tested geometries are referred to by their respective corrugation thicknesses. Table 2-31 lists these thicknesses and a more complete geometric description for each case.

Table 2-31. Geometry Details for Geometric Cases Simulated

Corrugation Thickness	Geometric Description
1.00x	1.00x sheet thickness, 1.00x corrugation thickness: Baseline geometry.
2.00x	2.00x sheet thickness, 2.00x corrugation thickness
1.90x	1.00x sheet thickness, 1.90x corrugation thickness: Includes the addition of a non-perforated separator sheet.
1.75x	1.40x sheet thickness, 1.75x corrugation thickness

For the 1.90x case, models were created for the hot side of the counter-flow section, as well as the hot inlet of the cross-flow section. A model of the cold side of the counter-flow region was not created, as the sheet thickness in the 1.90x configuration is the same as in the original geometry. It was assumed that with the same sheet thickness, the heat transfer performance and pressure drop would be similar to the original case.

For the 1.75x case, models were created for both the hot and cold sides of the counter-flow section as well as the hot inlet of the cross-flow section.

Figure 2-39 shows heat transfer results in the counter-flow region for all of the cases that were simulated. The results are presented in terms of HTC/k in order to remove the effect of temperature-dependent thermal conductivity.

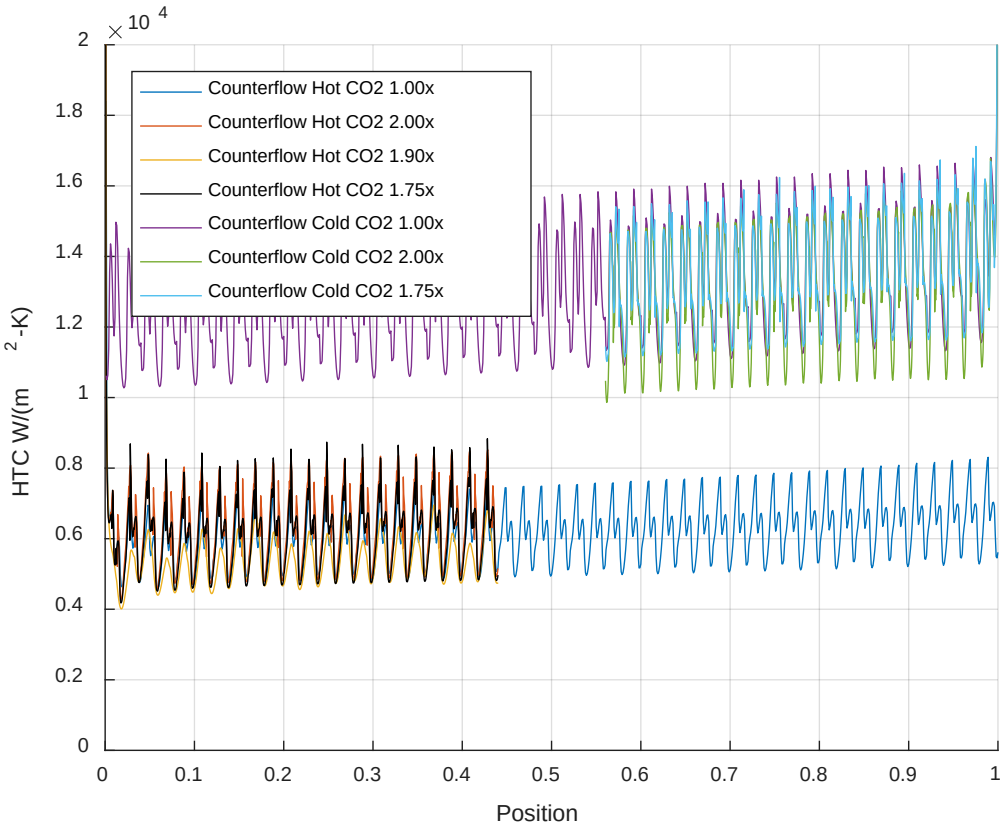

Figure 2-92. Heat Transfer Results for Counter-flow Section for Air and CO_2

Notice that the results for HTC are very similar between all of the versions of the geometry. Although the flow is moving much faster in the modified versions of the geometry, since the flow is laminar, the resultant Nusselt number is not a strong function of flow velocity, but it is a strong function of shape. This accounts for the relatively small change in HTC/k between the different geometric configurations.

Figure 2-2 shows in detail the results from the 1.00x case and the 1.90x case, which contained the separator sheet. Notice that in the 1.90x configuration, the HTC was reduced and the periodic nature of the HTC values was different from the 1.00x case. Both of these differences can be attributed to the addition of the non-perforated separator sheet, as it does not allow flow to move between the two out-of-phase sections of the hot side of the counter-flow region. This has the effect of reducing the mixing and, thus, the heat transfer.

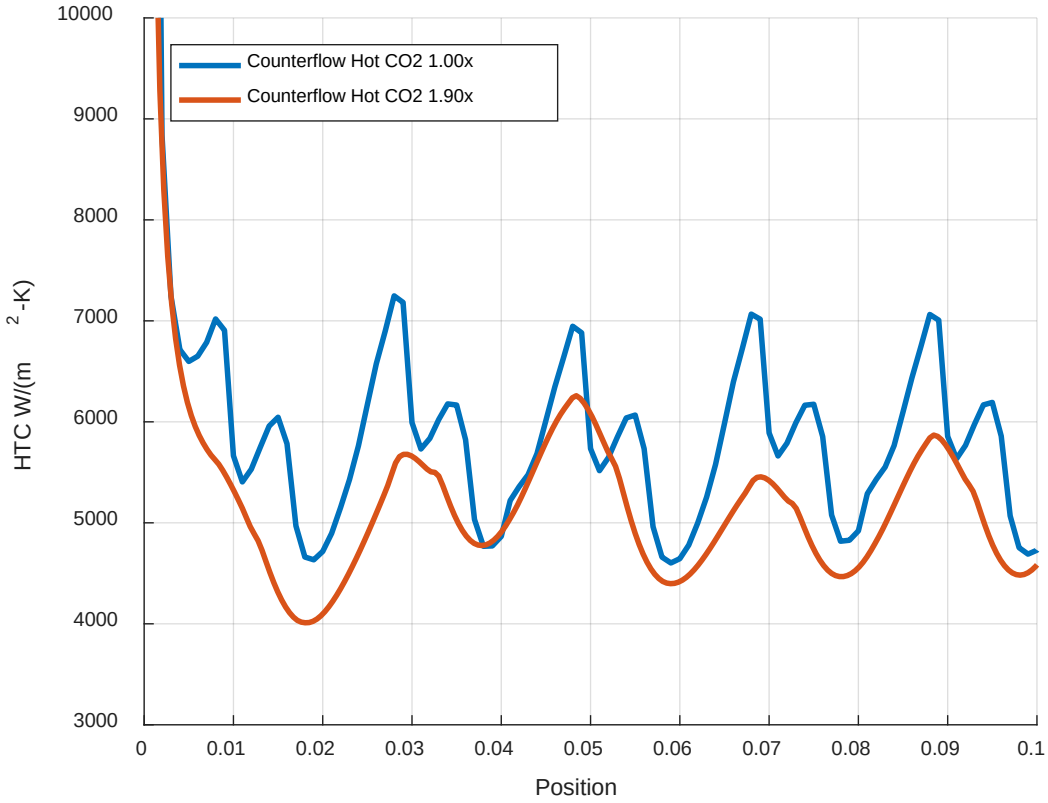

Figure 2-93. Detail of Heat Transfer Results for Counter-Flow Section

Average values for HTC/k are presented in Table 2-27 for the counter-flow region of the heat exchanger, including results from the air simulations.

Table 2-32. Average HTC/k Values for Air, Standard CO_2, and Modified CO_2 for the Counter-flow Region

Region	Mean HTC/k [1/m]
Cold Air	11,793
Cold CO_2 1.00x	13,167
Cold CO_2 2.00x	12,750
Cold CO_2 1.90x (Separator Sheet)	11,793
Cold CO_2 1.75x (Increased Counter-Flow Sheet Thickness)	12,998
Hot Air	5,495
Hot CO_2 1.00x	6,195
Hot CO_2 2.00x	6,869
Hot CO_2 1.90x (Separator Sheet)	5,696
Hot CO_2 1.75x (Increased Counter-Flow Sheet Thickness)	6,565

Figure 2-40 shows heat transfer results for the hot inlet section of the cross-flow region. As in the results for the counter-flow region, the results are presented as HTC/k to remove variation with respect to thermal conductivity.

As before, the flow in this section is laminar, so the change in heat transfer coefficient between the standard and modified cases can largely be attributed to changes in flow channel cross section shape. As discussed previously, it was assumed that the divergence from a steady-state value later on in one of the modified geometry cases was the result of a numerical error in the post processing routine. The steady-state values for HTC/k for the standard and modified geometries are shown in Table 2-34.

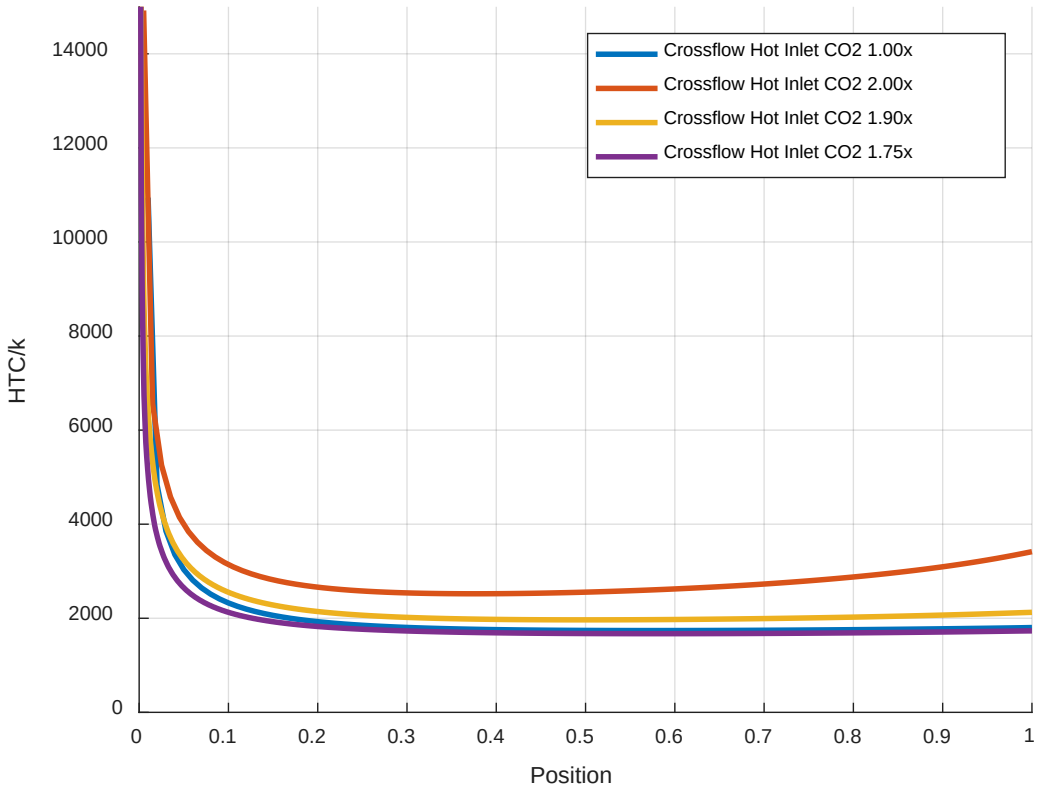

Figure 2-94. Heat Transfer Results for the Hot Inlet of the Cross-flow Region for Both the Standard and Modified CO_2 Cases

Table 2-33. Average HTC/k Values for Hot Inlet of the Cross-flow Region

Region	Mean HTC/k [1/m]
Hot Air	1,800
Hot CO_2 1.00x	1,750
Hot CO_2 2.00x	2,500
Hot CO_2 1.90x (Separator Sheet)	2,000
Hot CO_2 1.75x (Increased Counter-Flow Sheet Thickness)	1,700

2.5.3.3.2 Pressure Drop Results

By interrogating the simulations used for the heat transfer modeling described previously, the total pressure drop through the heat exchanger predicted by the CFD simulations could be quantified and compared between the standard and modified geometries. For the sections not explicitly modeled, namely the other cross-flow regions, the pressure drop ratio from the hot inlet simulation was used. The results from this study are shown in Table 2-34. Once the modified geometry is defined in more detail, further simulations can be done to create a refined estimate of the total pressure drop through the entire machine.

Table 2-34. Estimated Total Pressure Drop Compared to Baseline

Case	Hot	Cold
1.00x	1.0	1.0
2.00x	2.2	3.0
1.90x (Separator Sheet)	2.4	1.0
1.75x (Increased Counter-Flow Sheet Thickness)	1.5	1.6

The increased pressure drop in the 2.00x case can largely be attributed to the decreased flow area and, thus, increased flow velocity. Although the corrugation sheet thickness was reduced to the baseline level in the 1.90x case, the addition of the non-perforated separator sheet accounted for the increase in pressure drop on the hot side. The cold-side pressure drop of the 1.90x case remained the same as the baseline configuration due to their geometric similarity. As anticipated, the 1.75x case produced additional pressure drop when compared to the baseline 1.00x case, but not as much as the 2.00x case.

2.5.3.3.3 Redesign Performance Summary

The results described in the two previous subsections showed that the redesign option with increased counter-flow sheet thickness (1.75x increase in cross-flow corrugation thickness) exhibits 10-20% better heat transfer performance in the counter-flow section and only a 7% reduction in heat transfer in the cross-flow section. The separator sheet design (1.9X increase in cross-flow corrugation thickness) has heat transfer coefficients very similar to the existing recuperator design. The pressure drops for both redesign options significantly exceed the baseline case, but the increased thickness design is superior to the separator sheet design. Based on these analysis results and its reduced component count, the increased-thickness design was selected as the best redesign option for higher-temperature operation.

2.5.4 SUBTASK 4.4 – DESIGN DRAWINGS AND QUOTES

Revised drawings of the redesigned counter-flow sheets and cross-flow section corrugations were prepared and submitted to Solar for a budgetary quote for fabrication. The drawings were not submitted to other vendors due to the specialized manufacturing required.

2.6 TASK 5 ACCOMPLISHMENTS – TEST LOOP PRELIMINARY DESIGN

This section describes work that has been performed to design a full-scale test loop for evaluation of the redesigned recuperator.

2.6.1 SUBTASK 5.1 – CONCEPTUAL DESIGN

In the original proposal, a full-scale test loop was recommended for the recuperator tests rather than a lab-scale test to replicate fully the corrosive environment and mechanical stresses experienced under normal operating conditions. A potential full-scale test loop concept was presented (Figure 2-95) that utilized several existing components at SwRI: the CO_2 compressor, cooler, and a 1.92-MW heater (purchased early 2015). The following sections describe the work completed to date to develop further the full-scale test loop design and to verify the existing components' applicability to the test scenario. Additionally, work completed to size additional, necessary major components and to obtain budgetary quotes will be detailed.

Alternate test loop concepts will be identified that would primarily use existing components and require few new components. These concepts could potentially offer a lower-cost alternative to the full-scale, closed-loop concept described first.

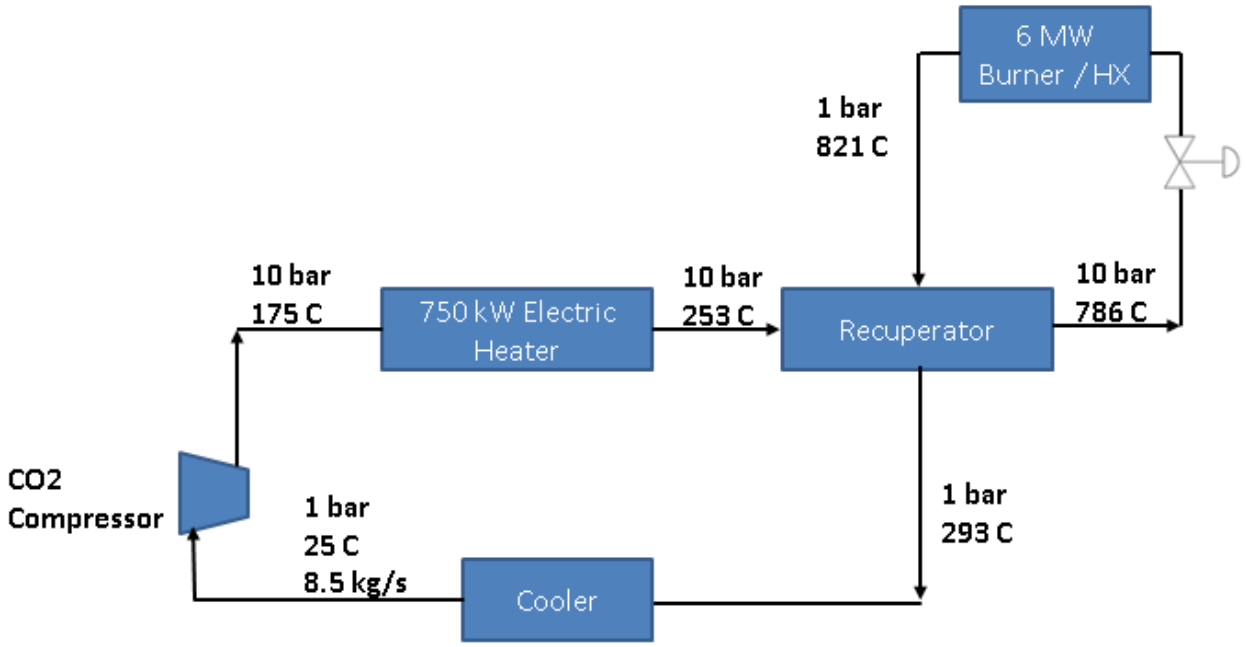

Figure 2-95. CO_2 Recuperator Test Loop Concept (Original Proposal)

2.6.1.1 Selection of Test Loop Flow Rates

The proposal presented ASPEN Plus cycle simulations of the Mercury 50 operating with both air and CO_2 as the working fluid. Those simulations yielded unit mass power and heat values for the cycle and are summarized in Tables 2-35 through 2-36.

In Table 2-35, the mass flow rate of the Mercury 50 (17.7 kg/sec) was applied to the unit mass values to generate the total power and heat loss for the air cycle.

Table 2-35. ASPEN Plus Air Cycle Results

	ASPEN Simulation [MW]	**Mercury 50 [MW]**
Compressor Power	0.355	6.3
Recuperator Heat Xfer	0.272	4.8
Heat Input	0.625	11.1
Turbine Work	0.605	10.7
Power Output	0.250	4.4
Heat Loss	0.374	6.6
Air Mass Flow (kg/s)	**1.0**	**17.7**

In Table 2-36, the results of the CO_2 simulation are shown along with several calculated cycles at varying CO_2 mass flows. For the calculated cycles, the objective was to have a variable of the CO_2 cycle equal the same variable of the air cycle and then determine which of the cycle conditions could be replicated on the full-scale test loop. For example, a CO_2 cycle with mass flow of 17.7 kg/sec equals the mass flow of the air cycle (other power and heat values are different). A cycle with 19.1 kg/sec flow of CO_2 has an equivalent power output to the air cycle.

Table 2-36. ASPEN Plus CO_2 Cycle Results

	ASPEN Simulation [MW]	**Equal Mass Flow [MW]**	**Equal Volume Flow [MW]**	**Equal Power Output [MW]**	**Equal Recuperator Power [MW]**
Compressor Power	0.211	3.7	5.7	4.0	1.6
Recuperator Heat Xfer	0.617	10.9	16.7	11.8	4.8
Heat Input	0.487	8.6	13.1	9.3	3.8
Turbine Work	0.443	7.8	12.0	8.4	3.5
Power Output	0.232	4.1	6.3	4.4	1.8
Heat Loss	0.255	4.5	6.9	4.9	2.0
CO_2 Mass Flow (kg/s)	1.0	17.7	27.0	19.1	7.8

For all but the "equal recuperator power" cycle, the required mass flows greatly exceeded the flow capability of the CO_2 compressor (maximum of 7.1 kg/sec for pressure ratio of 10:1 for flow of CO_2). Therefore, utilizing the existing CO_2 compressor in the test loop will yield tested recuperator power (the heat exchanged between the exhaust gas stream and combustor inlet stream) that is roughly equal the recuperated heat of the air cycle (providing some equivalency between the two cycles). The stacked-layer design of the recuperator core allows for relatively straightforward scalability in its design. Testing of a scaled-down design at full temperature and pressure is still expected to provide the same thermal and mechanical loading on the recuperator core and can, thus, provide sufficient validation for the recuperator core design. Thus, lower-scale test concepts will also be evaluated in order to maximize the use of existing components and keep test costs to a minimum.

2.6.1.2 Modeling of Closed-Loop Test System (Concept #1)

With a target mass flow identified, a high-level model of the closed-loop design concept (referred to as Concept #1) was generated in Microsoft Excel to understand the power requirements of each component. A diagram of the model is shown in Figure 2-97. A summary of the power and heating/cooling requirements for major loop components from the Excel model is provided in Table 2-37 (note that existing items are indicated with an *).

The Excel model utilized basic thermodynamic relationships to calculate power and heating/cooling values by calculating the product of the fluid enthalpy rise and the mass flow (Equation 12).

$$\boldsymbol{P, Q = \dot{m}\Delta h} \tag{12}$$

Expansion from high-side pressure (10 bar) to low-side pressure (1 bar) was assumed to be isenthalpic. Finally, the reported recuperator effectiveness of 93% was utilized to determine the high-pressure outlet enthalpy (Equation 13).

$$\boldsymbol{\eta_{eff} = \frac{(h_{LP\_i} - h_{HP\_i})}{(h_{LP\_i} - h_{HP\_o})}} \tag{13}$$

Table 2-37. Summary of Excel Model Power/Heat Calculations

	P_in [bar]	P_out [Bar]	T_in [°C]	T_out [°C]	Pwr/Heat Exch [kW]
Compressor*	1.0	10.0	50.0	175.0	798.8
Low Temp Heater*	10.0	10.0	175.0	253.1	565.0
Control Valve	10.00	1.00	784.3	783.9	0
High Temp Heater	1.0	1.0	784.0	821.0	330.0
Cooler*	1.0	1.0	295.0	50.0	1,693.6

The Excel values are generated using the specified mass flow of 7.1 kg/sec with CO_2 as the working fluid. Fluid properties were generated using REFPROP v9.0 embedded in the Excel model. It should be noted that the given values are for steady-state conditions at full operating

temperatures. Additionally, most of the values are calculated on an ideal basis (see Equations 12 and 13) and the actual components would require some additional margin to account for process inefficiencies as well as the expected warm-up transient.

Calculations of the warm-up transient have not been made at this time; however, it is understood that the loop will require a warm-up period during test startup. During this transient, the loop temperature will begin operation at some relatively low temperature, and increase in temperature as heat added by the low- and high-temperature heaters is recuperated, and as the piping and components are heated. Additional calculations will be made to understand the transient event as well as to estimate the recuperator effectiveness at the lower temperature gradients to avoid prolonged warm-up times.

Each component listed in the table will be discussed in the following paragraphs.

The closed loop test Concept #1 is represented schematically in Figure 2-96. In the figure, existing equipment is indicated by the green shading and required equipment is indicated with red shading.

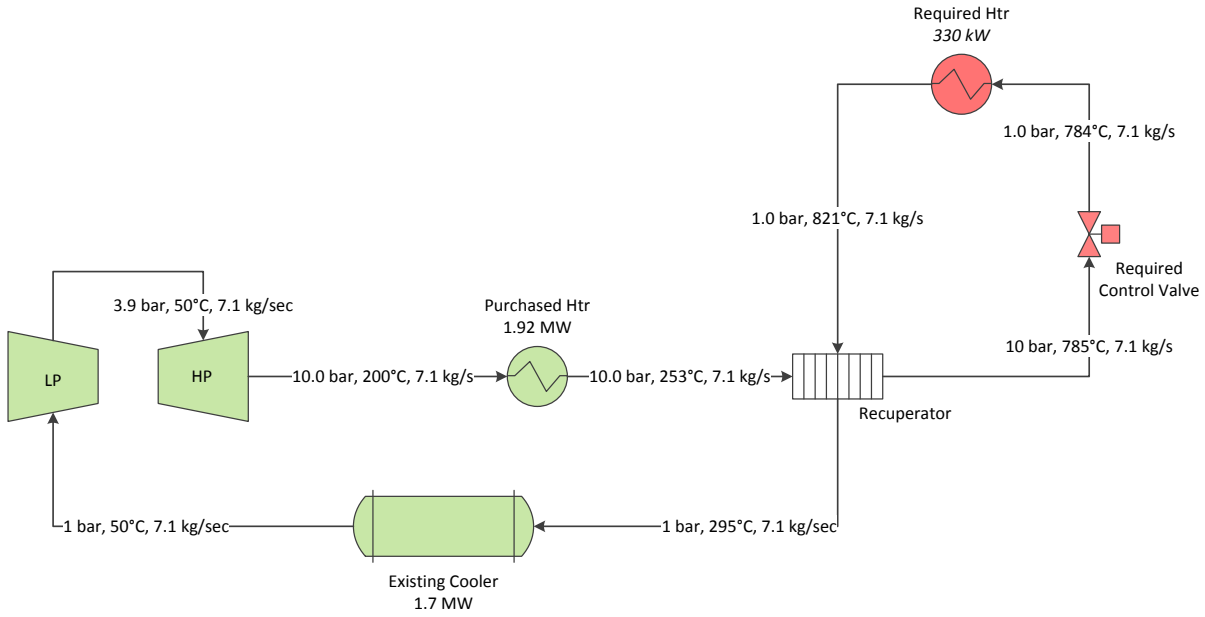

Figure 2-96. Closed Loop Test Concept #1

The primary technical challenge of the first concept is the temperature extremes that must be tolerated by the valve and process heater downstream of the recuperator on the high pressure side. The high temperature of 785°C requires highly specialized components which, based on initial estimates received, are also very costly components.

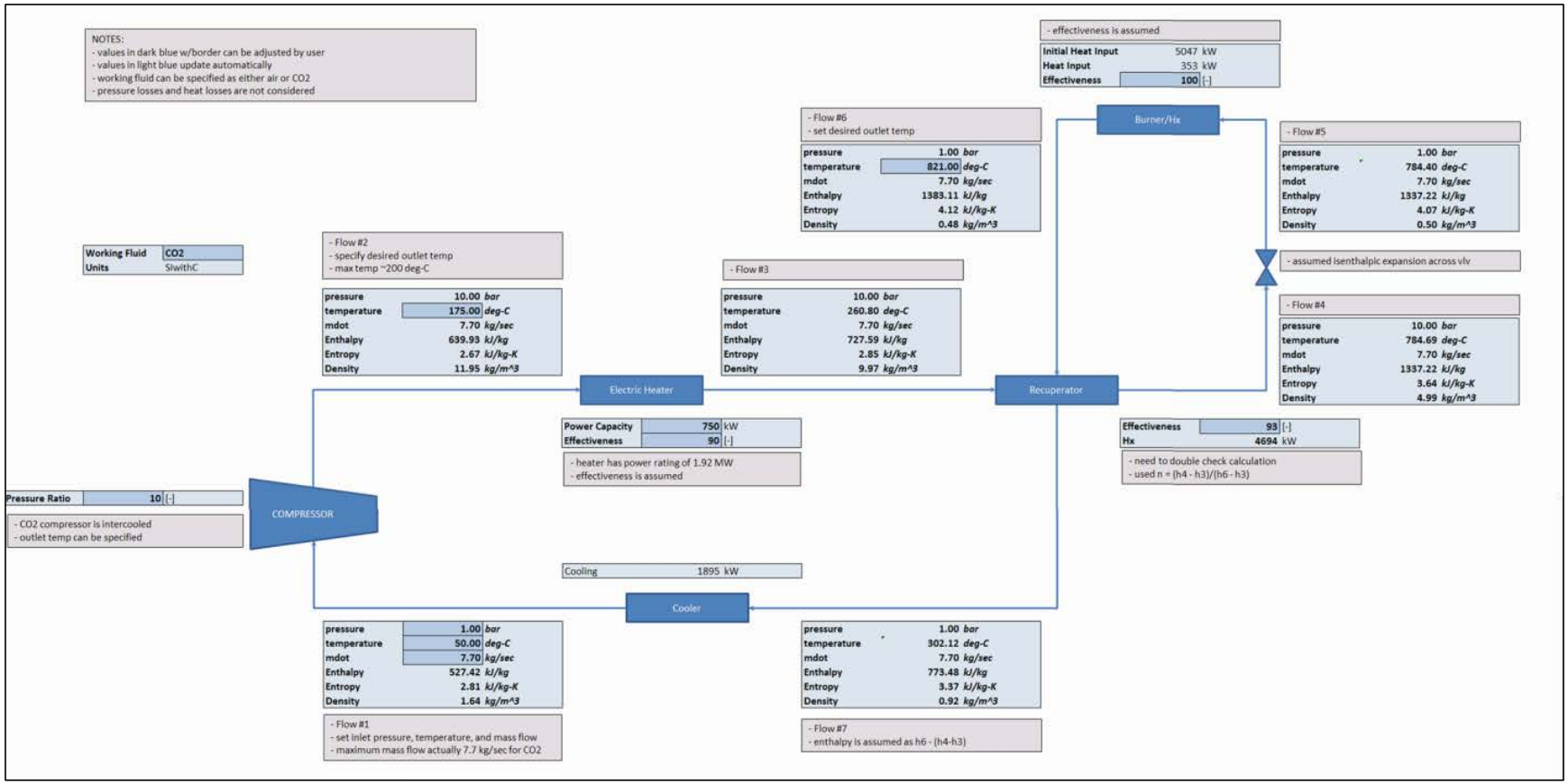

Figure 2-97. Excel Model of Closed-Loop Test Concept #1

CO_2 Compressor

The CO_2 compressor installed at the SwRI Turbomachinery Research Laboratory was previously detailed in the appendix of the proposal document and is shown in Figure 2-98. For the specific application to the current loop concept, the compressor is capable of providing 7.1 kg/sec at a PR of 10:1 at a controlled outlet temperature (currently specified at 175°C with a maximum outlet temperature of 200°C).

Figure 2-98. 3-MW CO_2 Compressor Located at SwRI Turbomachinery Research Laboratory

Low Temperature Heater

In the first closed-loop design concept, the heat required to boost the high-pressure CO_2 flow from 175°C to approximately 253°C is nominally 615 kW. A 1.92-MW Sylvania-OSRAM electric heater is currently on order by SwRI (shown in Figure 2-99, note the diagram shown depicts air as working fluid). The closed-loop Concept #1 will utilize that heater for the low-temperature heater. Maximum inlet and outlet temperatures of the heater are limited to 538°C and 816°C, respectively. While the maximum outlet temperature is very near the required temperature of 821°C, the heater will not be suitable as the high-temperature heater due to maximum temperature limitations of the heater inlet.

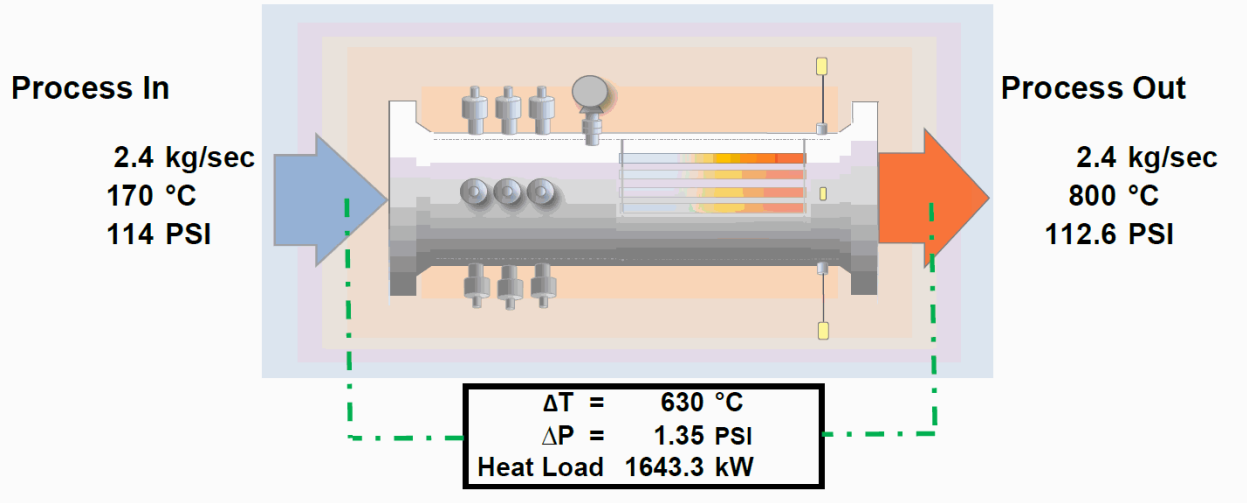

Figure 2-99. Purchased Sylvania-OSRAM Heater Flow Diagram

Control Valve/Orifice

For the closed-loop Concept #1, a control valve or orifice will be required to set the loop back-pressure. From an operational standpoint, a control valve is preferred so that compressor operating points can be adjusted. Control valves currently installed in the flow loop cannot be applied due to the elevated temperatures currently in the loop design (minimum valve inlet temperature of 785°C for valve installed upstream of the high-temperature heater). At the time of this reporting, several requests for a budgetary quote have been submitted. Several of the vendors contacted were not able to offer valves due to temperature limitations. Several other vendors that manufacture severe service valves appropriate for the application have not supplied a budgetary quote at the time of this report.

MOGAS Industries, Inc. furnished a budgetary quote for a control valve with the temperature and flow capacity required. The quoted valve is an 8-inch diameter rotary ball-valve with a control element installed in the valve seat with a maximum operating temperature of 900°C (an 11% margin above the target temperature of 785°C and 10% margin above the worst case temperature of 821°C, if the valve is positioned downstream of the heater). The budgetary quote for the valve is $305,000. A cross section of the proposed valve is shown in Figure 2-100.

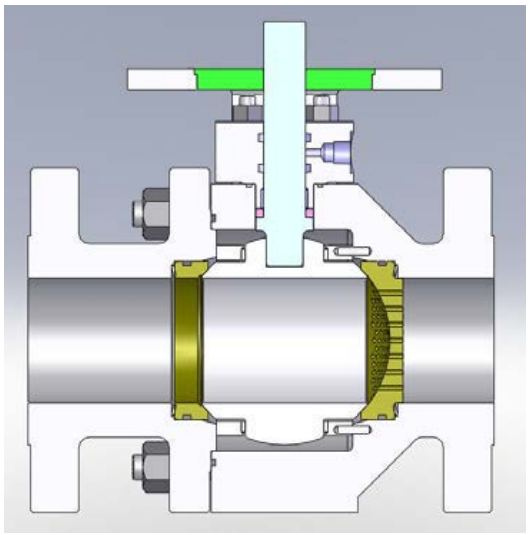

Figure 2-100. Cross Section of Control Valve Offered by MOGAS

A preliminary calculation was made to estimate the required valve flow coefficient (C_v) using the formulas given in ANSI/ISA s75.01 (as shown in Equation 14, in modified form to solve for C_v and to include the anticipated choked flow). The anticipated C_v is approximately 270.

$$C_v = \frac{Q_{scfh}}{906.7 P_1}\sqrt{\frac{G_g T_1 Z}{x}} \tag{14}$$

The alternative to using a control valve would be to insert an orifice plate. The orifice plate is less desirable from the operational perspective because it offers no control for tuning system back-pressure; however, the orifice plate likely offers significant cost savings compared to the control valve. Preliminary sizing suggests a β of 0.5772, but does not account yet for thermal expansions, which will be quite significant due to the high-operating temperatures.

High-Temperature Heater

The power requirement to heat the 785°C flow of CO_2 up to 821°C was calculated to be approximately 360 kW under steady operating conditions. As was stated previously, this calculation does not account for a warm-up transient (heating the loop from ambient temperatures to the operational temperature) and would likely benefit by some over-sizing. Additional estimates and calculations should be made to better understand the recuperator effectiveness during the warm-up transient to appropriately size the heater to achieve a loop heat-up time that is sufficiently fast.

Several requests for budgetary quotes have been solicited at the time of this reporting and some have been received. Sylvania-OSRAM supplied a budgetary estimate of $350,000 for a 400 kW heater operating on 500 Amp, 3Φ, 600 V panel (the test laboratory is currently supplied with 3 Φ, 480 V and 3 Φ 4,160 V). The quoted heater is similar in design to the purchased low-temperature heater, but with materials designed for the high-inlet/outlet temperatures.

Cooler

The existing shell/tube heat exchanger is utilized in the current loop design concept to remove additional heat in the low-pressure CO_2 flow after it passes through the recuperator. Excel calculations estimate that 1.8 MW of heat will be rejected from the cooler.

The cooler was designed for operation at a much higher pressure (140 bar) and has a design temperature of 260°C. Communications with the manufacturer confirmed that the cooler can be operated at the higher inlet temperature of 295°C due to the greatly reduced inlet pressure (approximately 1-1.5 bar).

Sizing calculations provided by the manufacturer indicate a cooling capacity of approximately 2.5 MW; however, due to the different flow conditions and working fluid, additional calculations will be requested to confirm the cooler is capable of the desired heat rejection.

2.6.1.3 Alternative Loop Concepts

Additional efforts have begun to identify possible test loop design concepts that could offer a cost savings over the closed-loop concept detailed above. These efforts are focused on maximizing the use of existing components in the loop while maintaining (or nearly maintaining) the temperature and pressure differentials expected in the actual cycle.

Test Loop Concept #2 and #2$_{alt}$

Because of the elevated temperatures, the second loop concepts considered below still require additional purchased components to cool the flow of hot CO_2 to temperatures compatible with the other existing components.

The loop Concepts #2 and #2$_{alt}$ are shown in Figure 2-101. In the figure, existing components are shown in green, necessary additional components are shown in red, and optional components are shown in yellow. Note that the second of the two concepts is simply a variation of the first concept that requires the addition of the optional components (those shown in yellow) to achieve the expected operating temperatures. Also, note that the displayed temperature values include the additional heating components.

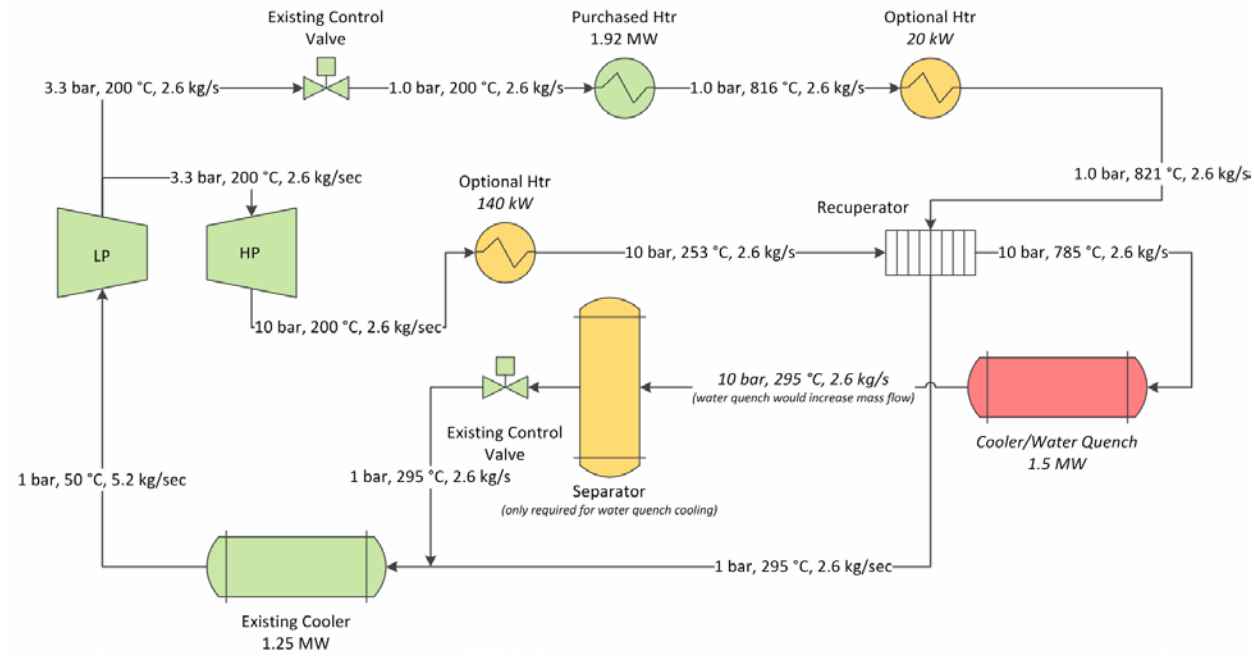

Figure 2-101. Closed Test Loop Design Concept #2 and #2$_{alt}$

In Concepts #2 and #2$_{alt}$, the mass flow through the high- and low-pressure sides of the recuperator is reduced from a maximum of 7.7 kg/sec to 2.6 kg/sec (approximately 1/3 of the maximum loop flow capacity). As described earlier, it is believed that the recuperator can be scaled down, such that the pressure and temperature differentials are equivalent and the mass flow through the plate sections is also equivalent. The alternate concepts utilize the compressor sections semi-independently to create low- and high-pressure loops that split after the first compressor section (identified as the "LP" compressor) and merge again at nearly atmospheric pressure prior to entering the existing cooler.

The first concept, Concept #2, utilizes only existing components, with the exception of a cooler or a water-quench and separator to cool the high-temperature CO_2 prior to expanding the flow back to the suction pressure. In this concept, the temperature differentials are not achieved due to limitations of the heater (maximum outlet temperature of approximately 816°C) and the temperature limitation of the compressor (maximum outlet temperature of 200°C). Nevertheless, the concept does achieve temperatures that are close to the anticipated operation and only requires the addition of a cooling mechanism.

Current work is focused on identifying possible cooling mechanisms for the recuperator outlet flow on the 10-bar side. Many standard coolers are not capable of the elevated inlet temperature of 785°C; however, inquiries will be made to determine the cost of such a cooler. Alternatively, a water-quenching system and separation/drying system could potentially be used. In this concept, water would be sprayed directly into the high-temperature CO_2 flow to cool the flow. The water/CO_2 mixture would then pass through a separation mechanism. Potential drawbacks to this approach include the formation of carbonic-acid and introduction of a humid mixture to the closed system. Additional work will investigate the viability of this option.

It should be noted that the existing heater is utilized more effectively in this option. In the closed-loop option described in detail in the previous sections, the heater utilized roughly 1/3 of its capacity. In the alternative arrangement described in this section, the heater is utilized to its full capacity to generate a majority of the required system heating.

Lastly, a second alternative concept, Concept #2_{alt}, would utilize the components previously described, but also add two heaters to achieve the desired temperature differentials more closely. The first heater would be positioned on the high-pressure side to bring the temperature at the outlet of the HP compressor from 200°C to the desired 253°C. Budgetary quotes have not been obtained but this heater is expected to be a comparatively low-cost item due to the minimal power requirement and the low inlet and outlet temperatures. The second optional heater would be placed on the low-pressure side after the existing heater to boost temperature from 816°C to 821°C. While the power requirement for this heater is very low, the elevated temperatures are expected to increase the cost of this item.

Similar to the first concept, the second set of test loop concepts also face the technical challenge of high inlet temperatures (785°C) at the inlet of the cooler or water quench.

Test Loop Concept #3

As described above, both of the closed-loop test concepts described in the previous sections face the technical challenge of having high gas temperatures at the inlets to some of the required process equipment. These high temperatures require the use of highly specialized and costly equipment. A third test loop concept was generated that decreases the impact of those high gas temperatures that exist at the outlet of the recuperator on the high-pressure side. The third concept is diagrammed in Figure 2-102. Existing items are shaded green and required items are shaded red.

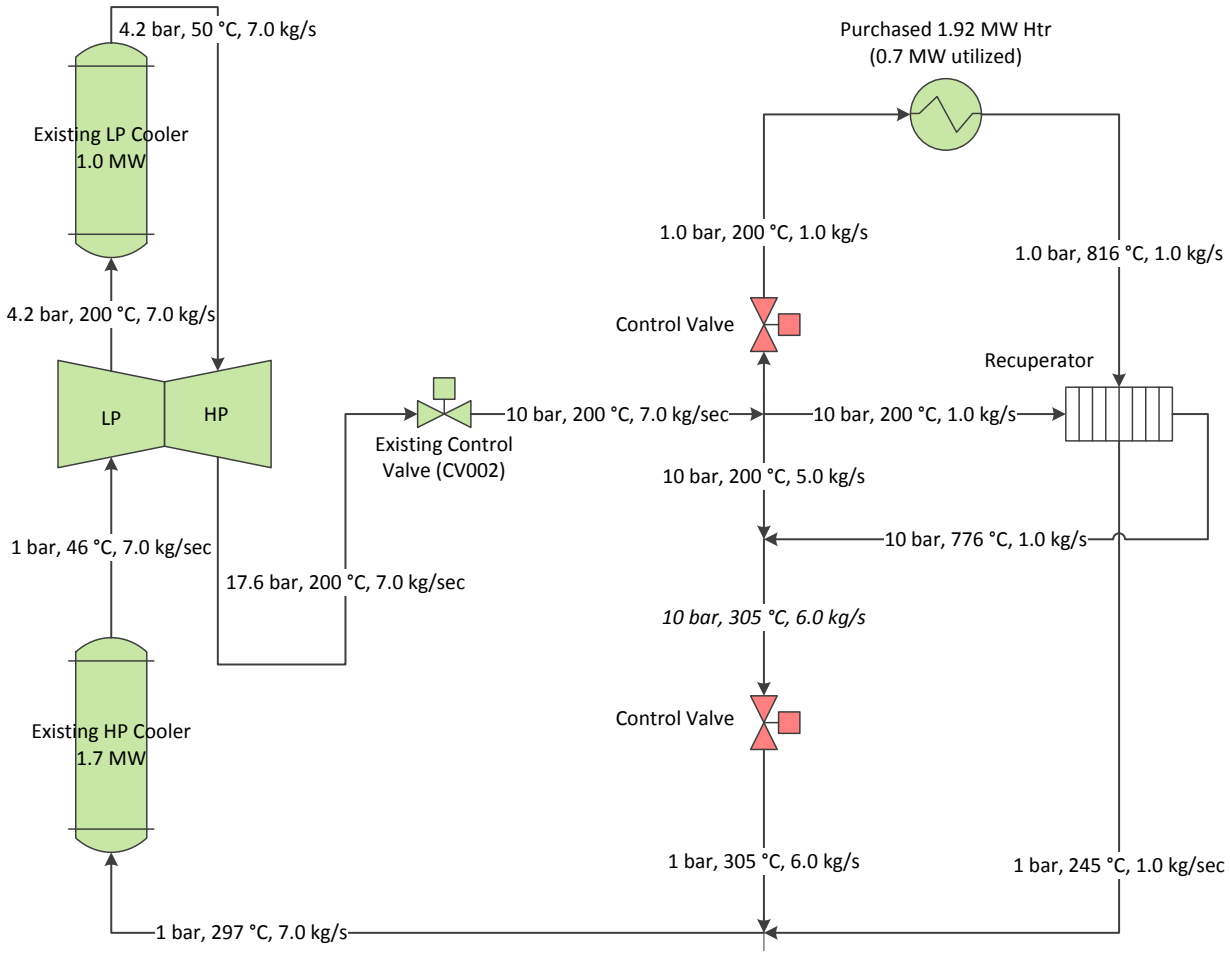

Figure 2-102. Closed Loop Test Concept #3

In the third concept, the existing CO_2 compressor would be utilized to nearly the maximum flow capacity at 7.0 kg/sec. The anticipated operating points at each stage are plotted in Figure 2-103 along with test data for the CO_2 compressor. The test points were generated during operation with CO_2 as the working fluid. It can be observed that additional flow could be achieved using the CO_2 compressor; however, for the purposes of the conceptual design discussion, the 7.0 kg/sec will be maintained. The flow exiting the high-pressure stage would be at an elevated pressure of 17.6 bar and a temperature of approximately 200°C. Temperature would be maintained, piping would likely require some insulation, and pressure would be decreased using the existing control valve. Initial calculations indicate that the existing 6" Dyna-Flo control valve is sufficient to control the flow and decrease pressure to 10 bar. The anticipated operating point is plotted along with the valve Cv curve as shown in Figure 2-104.

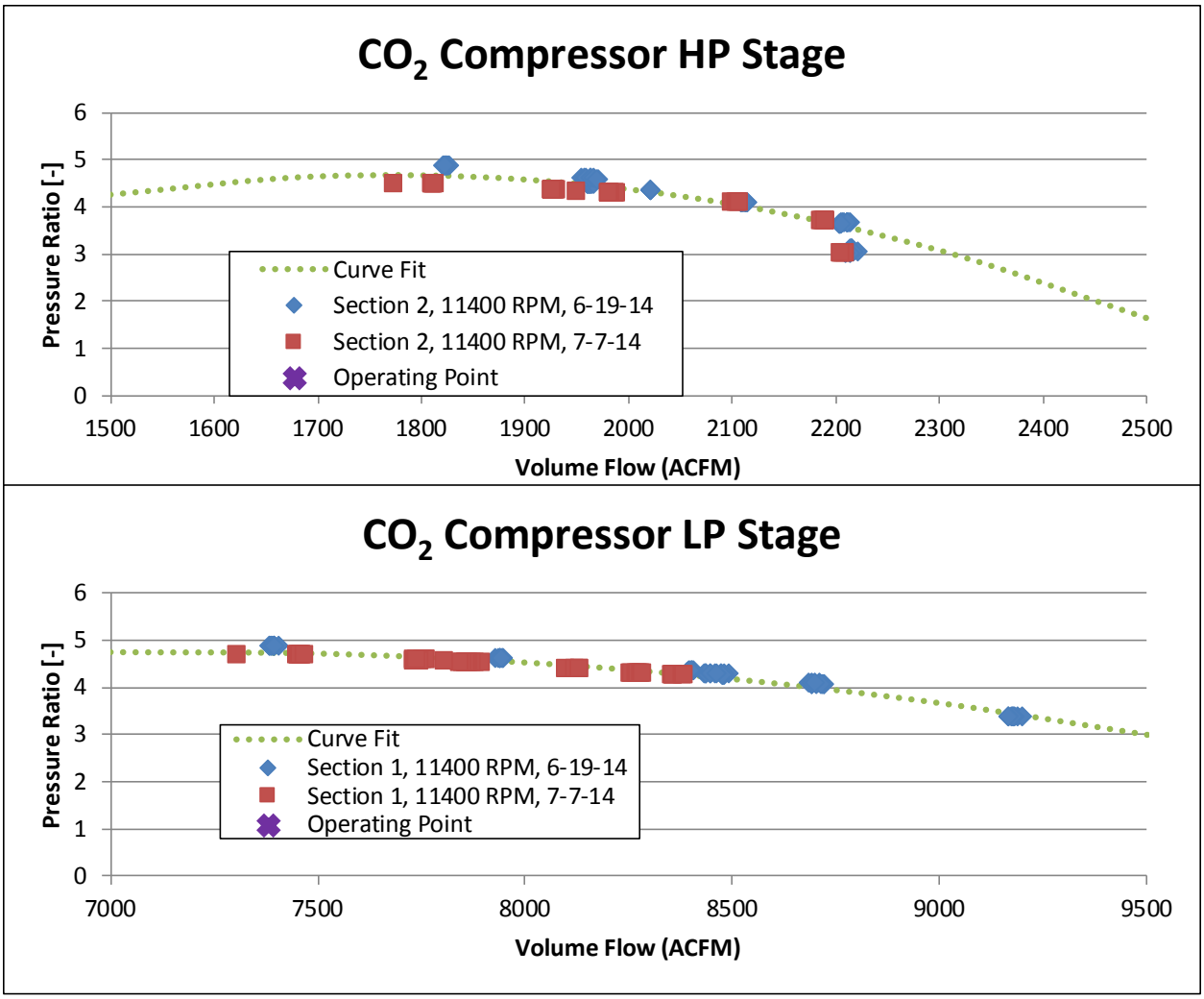

Figure 2-103. Loop Concept #3 Anticipated CO_2 Compressor Operating Point

The flow after the control valve (10 bar, 7.0 kg/sec, 200°C) would then be split into three different streams. The first stream would be piped directly to the recuperator inlet to deliver CO_2 at 1.0 kg/sec, 200°C, and 10 bar. It should be noted that the inlet flow temperature and flow rate are both less than the original test points described in the original project narrative. The flow rate through the recuperator on both the high- and low-pressure side in this concept is approximately 14% of test loop Concept #1 and 38% of Concept #2. It should be noted though, because of the stacked-layer design of the recuperator core, the test flow can easily be scaled down and still provide usable test data. Testing of a scaled-down design at full temperature and pressure is still expected to provide the same thermal and mechanical loading on the recuperator core and can, thus, provide sufficient validation for the recuperator core design.

In this concept, the temperature entering the recuperator is 53°C less than the anticipated operating conditions. Additional heating could be implemented to increase the temperature of the recuperator inlet stream but would require the use of an additional heater. Additional flow, for this concept, could not be achieved.

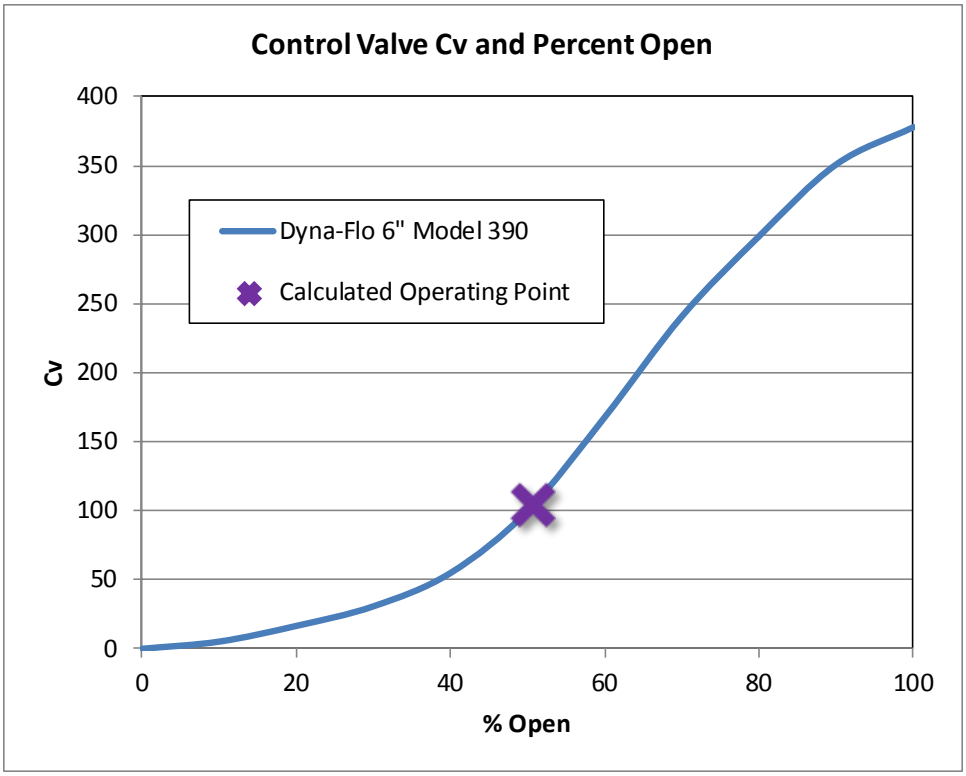

Figure 2-104. Existing HP Control Valve Cv Curve

The second stream would be directed to the existing 1.92-MW heater after dropping pressure across another control valve. Inlet conditions to the Sylvania-OSRAM heater would be 1.0 bar, 1.0 kg/sec, and 200°C. Using 0.7 MW of power (36% of the heating capacity) under steady-state conditions, the heater would supply a stream to the low-pressure side of the recuperator at 1.0 kg/sec, 1.0 bar, and 816°C. The supplied temperature is slightly less than the anticipated operating condition of 821°C; however, based on discussions with engineering at Sylvania-OSRAM, it may be possible to achieve the additional 5°C of heating required to exactly equal 821°C. As the test loop design matures and a loop concept is selected, additional inquiries will be made to better understand the actual process temperatures that can be achieved using the heater under the anticipated test conditions.

The final stream (10 bar, 5.0 kg/sec, 200°C) would be utilized for cooling the outlet stream from the recuperator on the high-pressure side. By mixing the two streams at some point downstream of the recuperator outlet, the temperature of the recuperator outlet gas is reduced from 776°C to 305°C. The cooled/mixed CO_2 would then flow through another control valve to drop the pressure down to the 1 bar low-pressure operating condition before mixing with the recuperator low-pressure outlet stream.

There are two primary benefits of Concept #3. First, the cooling mechanism described above allows for lower temperature operation downstream of the recuperator and relaxes the temperature requirements for downstream equipment. The second benefit is the few additional components required for the concept. In the current iteration, only two additional control valves would be needed (not including piping, insulation, and instrumentation).

Due to the low cost of Concept #3, and because the stacked cell design of the recuperator allows for straightforward sub-scale testing at lower overall flow rates (matching the mass flow per cell as a full-scale test), Concept #3 is considered to be the best candidate for minimizing test cost in a future test effort.

2.6.1.4 Anticipated Site Layout Prior To Recuperator Tests

Efforts have been made to understand the anticipated test site layout at the SwRI Turbomachinery Research Laboratory around the time that the recuperator tests would likely take place. It is recognized that, in addition to the cost of the required test loop components, some of the required piping, electrical wiring, or other auxiliary items can increase project costs significantly.

Work performed by SwRI for another project effort determined that the electrical wiring required for the Sylvania-OSRAM heater is particularly costly. It is anticipated that, prior to the recuperator tests, the heater will be installed within a Mixed Gas Lab (MGL) that is located within SwRI's Turbomachinery Research Laboratory. The anticipated layout is shown in Figure 2-105, where the heater is connected to the CO_2 compressor via 6" supply and 8" exhaust piping as shown. Regardless of which test loop concept is selected for further development, it is strongly recommended that the design incorporate the anticipated layout to avoid the large expense of relocating the heater.

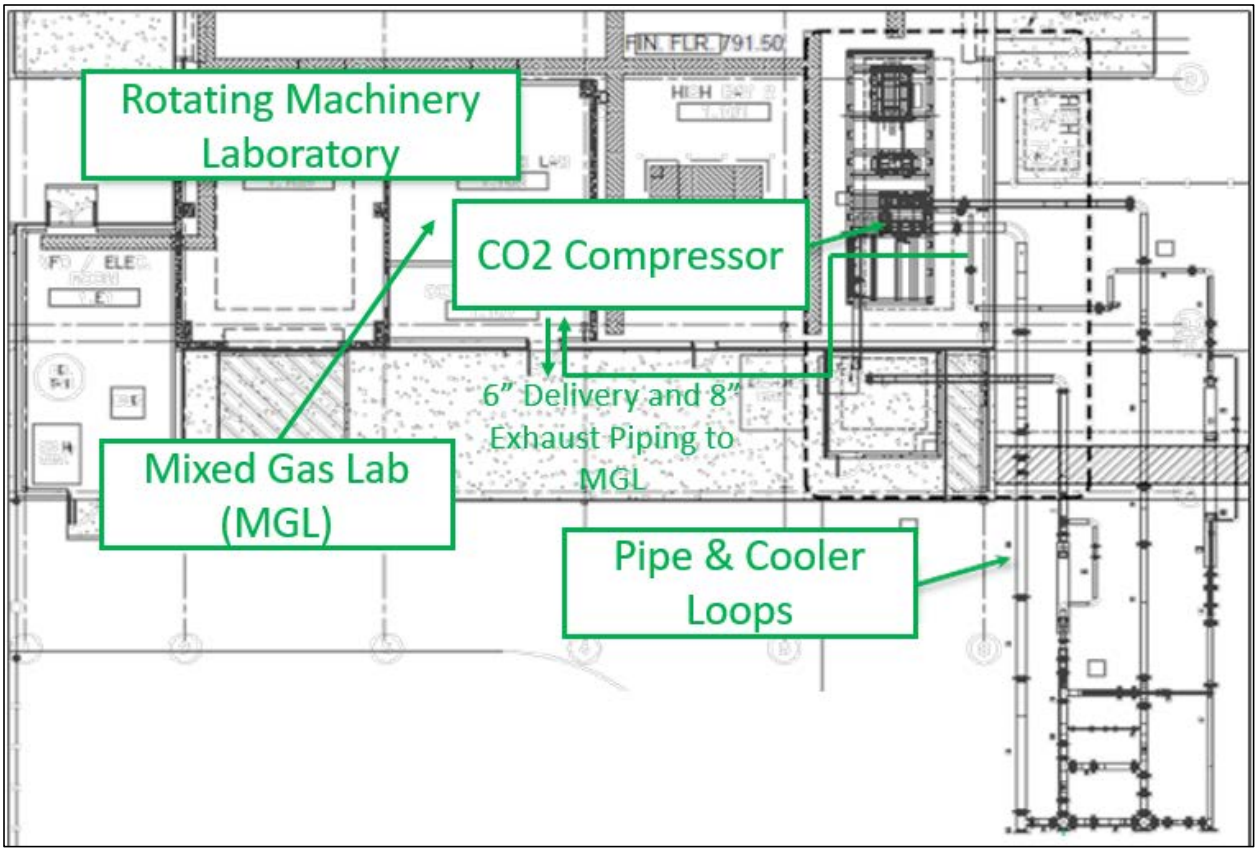

Figure 2-105. Anticipated Heater Location Prior to Recuperator Tests

2.6.2 SUBTASK 5.2 – PRELIMINARY DESIGN

In the following sections, the preliminary design will be described, major components will be discussed, and a budget for the detailed design and test loop procurement, construction, and operation will be given.

2.6.2.1 Test Loop Layout

The design for the full-scale tests is based upon the third test loop concept identified during the conceptual design phase (Concept #3, described in Section 2.6.1.3). A more detailed concept for the test loop was developed and is diagramed in Figure 2-106. In the diagram, green shading indicates equipment that is currently in place at the SwRI facility, red shading indicates equipment that would need to be purchased and installed, and yellow shading indicates equipment that exists but needs some modification to incorporate the equipment into the final test loop.

Several details are provided in the process diagram. Operating pressures and temperatures are given along with estimated average flow velocities in piping components. Preliminary calculations of pressure loss through piping sections are indicated along with the nominal pipe size and schedule. It should be noted that current estimates of pressure loss neglect any additional losses due to elbows, pipe reductions/expansions, or other flow restrictions. Thus, hours for detailed thermal and fluid design for the loop are included in the budgetary estimate. Finally, the required heating capacity of the two gas heaters and the required cooling capacity of the coolers are indicated.

In the test setup, the existing D-R compressor (see Section 2.6.1.2) would be used to compress gaseous CO_2 from a nearly atmospheric pressure of 1 bar at 46°C to a final pressure of approximately 18 bar and 200°C. This compression would utilize the existing shell-and-tube cooler to provide intercooling between the low-pressure and high-pressure stages. The mass flow for the indicated conditions is 7 kg/sec. Flow discharged from the compressor would be transported to the Mixed Gas Lab (MGL) through an existing 6” pipe and would expand to approximately 11 bar through an existing control valve.

Inside the MGL, the flow divides into three parallel (but not equal) flows. Figure 2-107 provides a more detailed look at the piping and instrumentation inside the MGL. First, an extraction flow of 1 kg/sec is diverted to a control valve where pressure is decreased to 1.8 bar (26.1 psia) prior to entering the OSRAM-Sylvania heater. The temperature of this stream is increased to approximately 816°C prior to entering the low-pressure side of the recuperator. The purpose of this flow is to replicate the low pressure and very high temperature conditions of the turbine exhaust. Another extraction stream is diverted to a small, 60 kW heater to warm the high-pressure CO_2 to the desired temperature of 253°C (487°F) prior to entering the high-pressure side of the recuperator. The flow rate of the extraction stream is carefully monitored and controlled with flow meters and control valves, respectively, to ensure the flow rates on either side of the recuperator are equal. The remaining 5 kg/sec flow of high-pressure CO_2 bypasses the recuperator and is mixed in with the recuperator discharge on the high-pressure side, so as to cool the high-pressure flow exiting the recuperator from 779°C to 304°C. The cooled, high-pressure stream then flows through an existing control valve to reduce pressure to approximately 1.7 bar, where it is then combined with the low-pressure recuperator outlet flow.

Recuperator Test Loop

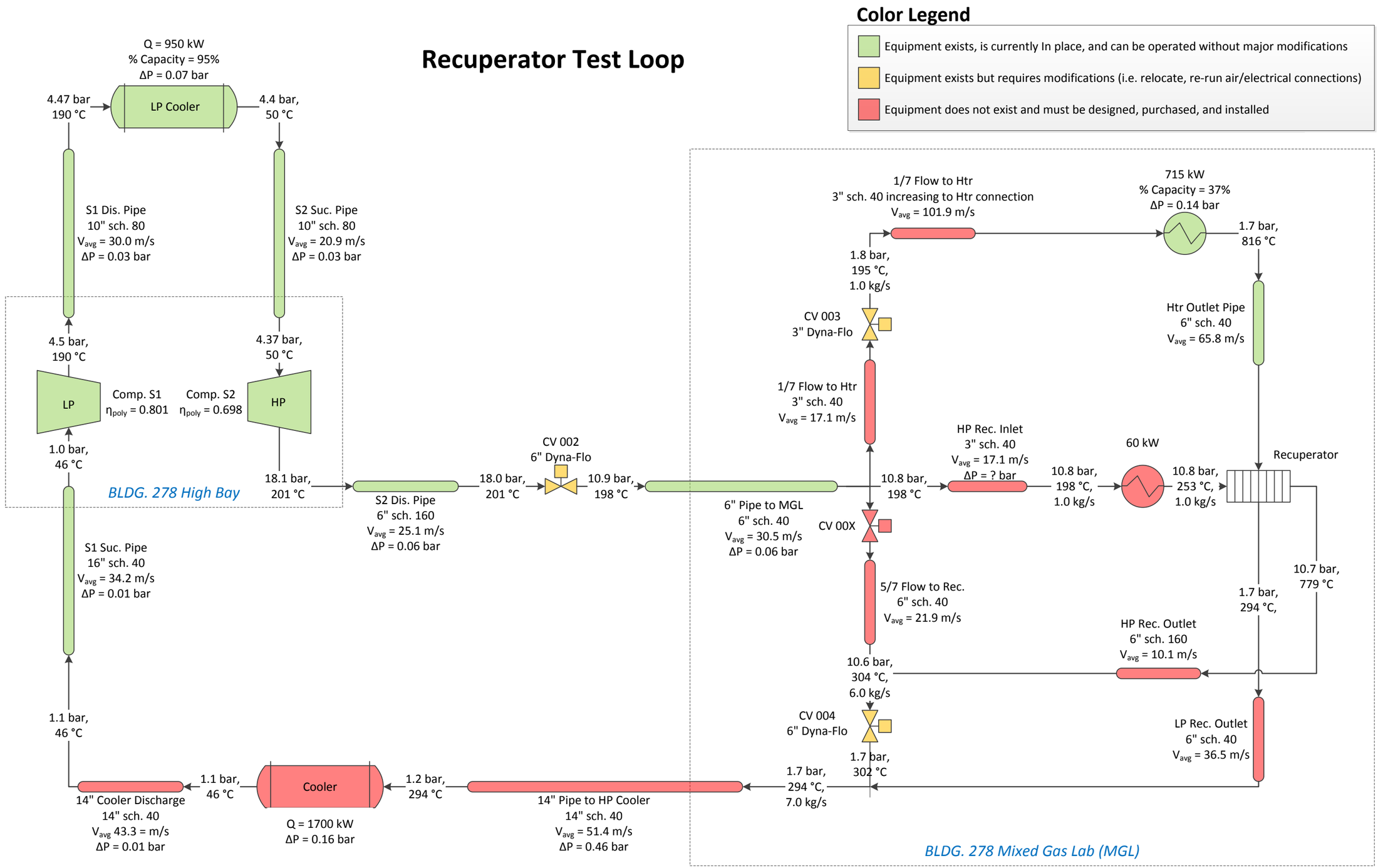

Figure 2-106. Preliminary Design of Recuperator Test Loop

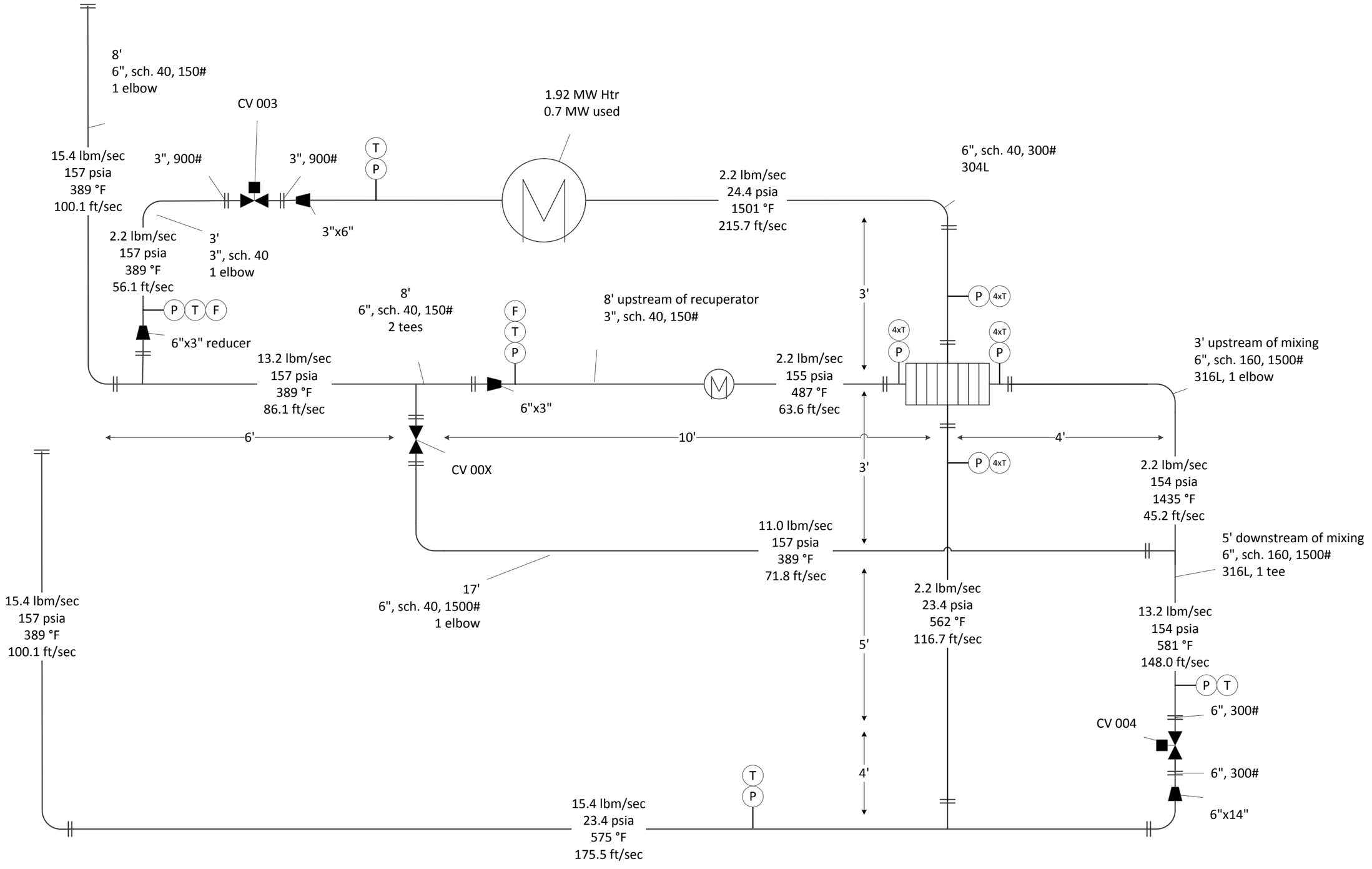

Figure 2-107. Diagram of Piping and Instrumentation inside MGL

The final steps in the process are to return the gas from the MGL to the existing pipe loop and then to cool the gas to the appropriate suction temperature. Due to the high temperature and low pressure of the flow leaving the MGL, a large 14" pipe is required to minimize pressure losses as the flow is returned to the compressor suction. A cooler is also required to cool the gas stream from 294°C to 46°C.

2.6.2.2 Required Major Components

The test loop described in the previous section requires the purchase of several new components. In the following paragraphs, a brief description of the required components is given along with sizing data and budgetary estimates. Existing loop components, described previously in Section 2.6.1.2, will be omitted.

2.6.2.2.1 Low Pressure Cooler

Gas leaving the MGL remains at an elevated temperature of nearly 300°C and must be cooled to an acceptable compressor inlet temperature. Diversified Manufacturing Inc. supplied a quotation for a shell-and-tube type heat exchanger capable of providing the required 1.7 MW of cooling.

On the tube side, CO_2 gas at 294°C and 1.4 bar enters the exchanger and exits at 46°C and 1.1 bar. On the shell side, cooling water is required at a rate of 329 gpm at an inlet temperature of 27°C and leaves the exchangers at 46°C. It should be noted that the cooling water system currently installed at the SwRI facility can handle 800 gpm. One of the existing coolers used for intercooling between LP compressor discharge and HP compressor suction, uses about 225 gpm. Therefore, the existing cooling system is sufficiently sized to provide cooling water to both coolers used for the recuperator test. The budgetary quotation provided by DMI is $27,973.

2.6.2.2.2 60 kW Heater for Recuperator High Pressure Inlet

To closely match the thermal conditions anticipated for the recuperator in operation, an additional heater is required. Gas entering the MGL is supplied at a temperature of 198°C and must be heated to 253°C. Chromalox provided a budgetary quote for a 480 V, 3-phase, 60 kW process heater. A drawing of the quoted heater is provide in Figure 2-108. Budgetary pricing for the heater and the required control panel is $26,584.

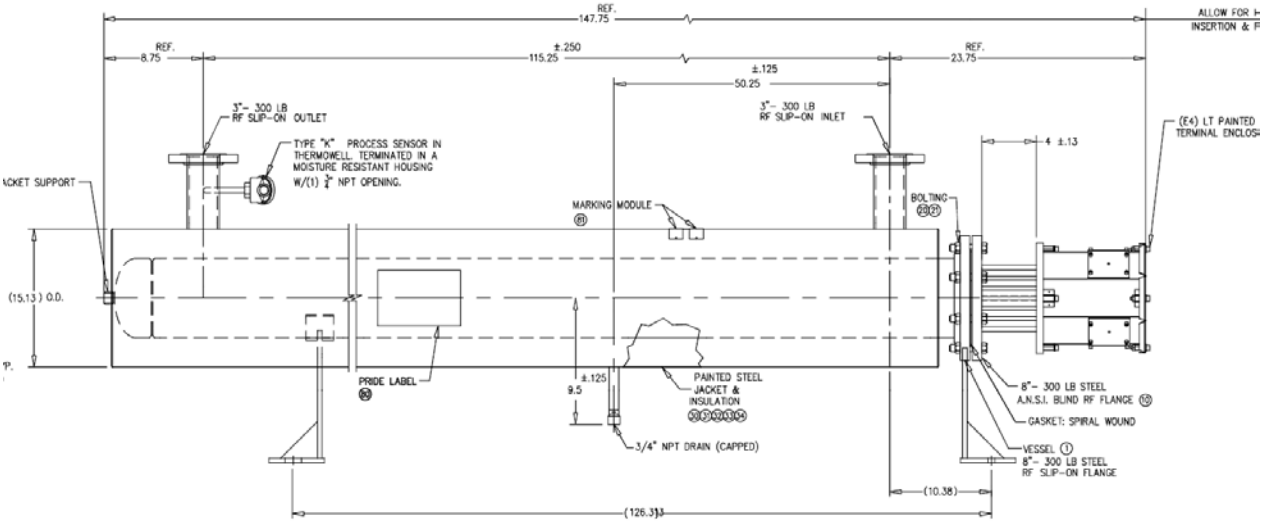

Figure 2-108. 60 kW Heater for Recuperator Inlet on High-Pressure Side

2.6.2.2.3 Control Valve for Recuperator High-Pressure Cooling Flow

Figure 2-106 and Figure 2-107 both indicate that a control valve will be used on the high-pressure bypass line within the MGL. This valve will be used to tune the steady flow rate of high-pressure gas between the two parallel streams and ensure that a constant 1 kg/sec flow is supplied to the recuperator. CVI Solutions provided a quote for a Dyna-Flo 6" control valve, model 570. A valve sizing report supplied along with the quotation indicates a valve flow coefficient of 420.7 and matches closely with estimates of 424.3 calculated with Equation 14. Budgetary pricing for the valve is $6,643 and includes the necessary electro-pneumatic positioner.

Additionally, CVI Solutions provided three sizing calculations for the existing control valves: CV002, CV003, and CV004. In all cases, the new process conditions were compatible with the existing valves.

2.6.2.2.4 Loop Piping

As indicated in Figure 2-106, several sections of pipe will be required for the test setup. Pipe diameters and schedules have been sized according to ASME B31.1 or B31.3 and are summarized in Table 2-38. In the table, nominal pipe diameters and the required schedules are indicated along with the assumed corrosion allowance of 0.030 inch. Furthermore, the pipe material is given. For the recuperator discharge piping on the high-pressure side, the elevated temperature and pressure necessitate the use of 316L. For all other pipes, carbon steel was selected. Finally, estimated lengths for the pipe sections are given.

Table 2-38. Required Piping for Recuperator Testing

Name	*Operating Conditions and Pipe Sizes*							*Pipe Design Calculations per ASME B31.1 or B31.3*			
	Fluid	ṁ	P	T	D	Sch	c	Ml	Material	Code	L
	-	lbm/s	psia	°F	in	-	in	-	-	-	ft
DOE NETL RECUPERATOR											
MGL - Supply Inlet	CO2	15.4	157	389	6	40	0.030	1	Carbon Steel, ASTM A106, Grade B	ASME B31.3-2008	8
MGL - Branch Line	CO2	13.2	157	389	6	40	0.030	1	Carbon Steel, ASTM A106, Grade B	ASME B31.3-2008	8
MGL - Flow to LP HTR	CO2	2.2	157	389	3	40	0.030	1	Carbon Steel, ASTM A106, Grade B	ASME B31.3-2008	3
MGL - Flow to HP HTR	CO2	2.2	157	389	3	40	0.030	1	Carbon Steel, ASTM A106, Grade B	ASME B31.3-2008	8
MGL - Cooling Flow	CO2	11.0	157	389	6	40	0.030	1	Carbon Steel, ASTM A106, Grade B	ASME B31.3-2008	17
MGL - HP Recup Disch	CO2	13.2	157	1435	6	160	0.030	2	Stainless, TP316L, ASTM A312	ASME B31.3-2008	8
MGL - LP Recup Disch	CO2	2.2	23	562	6	40	0.030	1	Carbon Steel, ASTM A106, Grade B	ASME B31.3-2008	12
MGL - Mixed Flow	CO2	15.4	23	577	14	40	0.030	1	Carbon Steel, ASTM A106, Grade B	ASME B31.3-2008	20
MGL - Outlet	CO2	15.4	23	577	14	40	0.030	1	Carbon Steel, ASTM A106, Grade B	ASME B31.3-2008	8
MGL to 278 Exterior	CO2	15.4	23	575	14	40	0.030	1	Carbon Steel, ASTM A106, Grade B	ASME B31.3-2008	45
278 Exterior to S1 Suction Piping	CO2	15.4	23	575	14	40	0.030	1	Carbon Steel, ASTM A106, Grade B	ASME B31.3-2008	130
CV002 Replacement Spool	CO2	15.4	157	389	6	160	0.030	1	Carbon Steel, ASTM A106, Grade B	ASME B31.3-2008	3
CV003 Replacement Spool	CO2	2.2	157	389	3	160	0.030	1	Carbon Steel, ASTM A106, Grade B	ASME B31.3-2008	2
CV004 Replacement Spool	CO2	15.4	65	374	6	80	0.030	1	Carbon Steel, ASTM A106, Grade B	ASME B31.3-2008	2

Additional features such as elbows, tees, and flanges, were included in an estimate of the piping cost. The current piping cost estimate is approximately $270,000 and includes estimated fabrication costs.

2.6.2.2.5 Loop Instrumentation

As indicated in Figure 2-107, instrumentation and data acquisition systems will be required to control the test loop and to collect data. Measurements of interest include temperature, pressure, flow rate, and mechanical strain for the recuperator assembly. Budgetary quotations were obtained for two vortex flow meters, for strain gauge conditioners, and for a temperature scanner. Catalog pricing was used to generate costs for thermocouples and the pressure transducers. Cost estimates based on historical pricing were generated for strain gauges and the data acquisition system. The current estimate for the data acquisition equipment and instrumentation is approximately $47,400.

2.6.2.3 Preliminary Schedule, Test Plan, and Budget

In the following paragraphs, the work necessary to perform a detailed test loop design, to construct the test loop, and then to commission the loop and perform the proposed tests is described.

2.6.2.3.1 Test Loop Detailed Design

The preliminary test loop design included additional details neglected in the concept design phase. Those details included estimates of pipe friction loss, temperature effects when determining pipe sizes, and component specs at operating conditions. Prior to constructing the test loop, additional detailed design will be required prior to constructing the loop. The detailed design element will include piping design, piping thermal analysis, and data acquisition planning.

The detailed piping design will be performed to identify the actual pipe dimensions required for the test loop. The result of this work will yield detailed pipe drawings for fabrication purposes and a three-dimensional model of the pipe network at the building 278 location. Furthermore, required pipe support locations and concrete footings will be identified in this design effort.

The piping thermal analysis will be conducted to account for thermal stresses induced under the high operating temperature conditions. This analysis will ensure that the piping structure in the MGL and the return piping will be designed and supported appropriately to tolerate the thermal growth.

The data acquisition design and planning work will ensure that the appropriate measurements are collected and that the selected instrumentation will provide an acceptable level of accuracy.

In total, these efforts will require a significant level of time and effort from engineering and from drafters along with oversight from senior level engineers and management. The estimated number of man-hours required to complete the design work is 460 hours and the budget estimate for this task is $75,000.

2.6.2.3.2 Test Loop Construction and Commissioning

Following the detailed design work, the test loop will be fabricated, assembled, and commissioned. This work will include the installation and setup of the data acquisition system, the fabrication and installation of the loop piping, and the installation of the components described previously. This task is labor intensive. The estimated number of man-hours to construct the loop and commission the facility is 1,100 hours with a labor budget of $130,000.

When the equipment costs and facility modification costs are included, the budget to procure equipment, construct the loop, and perform commissioning is $530,000.

2.6.2.3.3 Testing

A preliminary set of recuperator tests were identified that would simulate a variety of operational conditions and would investigate the thermal-hydraulic performance of the recuperator. The proposed tests and the anticipated man-hours to complete the tests are described in the following paragraphs.

Following commissioning, the first set of tests would be conducted at low operating temperatures and measure the pressure loss through the recuperator. At the low temperature condition, fluid density is the greatest and would provide an upper bound for the anticipated pressure drop through the recuperator. In total, these tests would last approximately one week and would require 120 man-hours.

The second set of tests would be operated at an intermediate temperature. These tests would be used to incrementally test the recuperator assembly for leaks and to identify other issues associated with elevated temperature operation. These tests would last approximately one week and would also require 120 man-hours.

The third set of tests would operate the loop at the full temperature condition. These tests would provide a majority of the thermal-hydraulic performance data for the recuperator assembly at conditions nearly identical to the intended application. These tests would occur over a two-week period and would require 236 man-hours.

An endurance test is also planned that would operate the recuperator test loop continuously for the period of one month. This test would be run at the full temperature and pressure conditions with the goal of identifying performance or mechanical issues associated with prolonged usage. Due the continuous operation of the test (twenty-four hours a day, seven days a week), shifts would be required. The total time usage for this test is 1,496 hours.

Following the endurance test, another set of tests would be run for two weeks in which the recuperator is subjected to cyclic operation. These tests would include both thermal cycling and flow cycling. These tests would require 276 man-hours to complete.

Finally, it is recognized that some disassembly and inspection will likely be needed at certain intervals during testing. Furthermore, following the cyclic tests, a final metallurgical inspection will be performed. In total, 372 man-hours have been included to perform the inspections and disassembly.

The budget for the tests is $408,000.

2.6.2.3.4 Total Budget for High-Temperature Recuperator Testing

The total budget for detailed test loop design, procurement, construction, and operation is estimated to be $1,013,000. This budgetary estimate includes all items except for the prototype subscale recuperator. The labor and material costs described in the previous sections are summarized in Table 2-39.

Table 2-39. Budget Summary for Full-Scale Recuperator Test Loop

Task Description	Labor Costs	Material Costs	Task Subtotal
Test loop detailed design	$75,000		***$75,000***
Test loop construction and commissioning	$130,000	$400,000	***$530,000***
Testing	$408,000		***$408,000***
Total			**$1,013,000**

2.7 MILESTONE STATUS

The milestone log shown in Table 2-40 displays the status of each project milestone.

Table 2-40. Milestone Log

MILESTONE LOG							
Budget Period	**Milestone Number**	**Task/Subtask Number(2)**	**Milestone Title/Description**	**Planned Start Date**	**Planned Completion Date**	**Actual Completion Date**	**Verification Method**
1	1	4.2	Completion of concept study and down-select of concepts for further detailed analysis	10/1/2014	3/31/2015	9/4/2015	Report
1	2	3.3	Completion of laboratory-scale material testing	10/1/2014	3/31/2015	5/15/2015	Report
1	3	4.3-4.4	Completion of preliminary design of high temperature heat exchanger	4/1/2015	2/29/2016	3/29/2016	Report
1	4	5.2	Completion of preliminary design for recuperator full-scale test loop	5/1/2015	2/29/2016	3/29/2016	Report
1	5	3.3	Statistically significant laboratory-scale corrosion testing of materials and coatings	10/1/2015	12/31/2015	3/29/2016	Report

3. PROJECT PRODUCTS

This section describes the research products developed from this project to date.

3.1 PUBLICATIONS AND PRESENTATIONS

A poster and accompanying paper were presented at the Supercritical CO_2 Power Cycles Symposium that was held in San Antonio, Texas in March 2016 and sponsored by DOE NETL. A copy of the poster is presented in Appendix A and the paper is presented in Appendix B.

3.2 WEBSITE(S) OR OTHER INTERNET SITE(S)

No websites or other Internet sites have resulted from the research to date.

3.3 TECHNOLOGIES OR TECHNIQUES

No technologies or techniques have resulted from the research to date.

3.4 INVENTIONS, PATENT APPLICATIONS, AND/OR LICENSES

No inventions, patent applications, or licenses have resulted from the research to date.

3.5 OTHER PRODUCTS

No other products have resulted from the research to date.

4. PROJECT PARTICIPANTS & ORGANIZATIONS

This project was completed by Southwest Research Institute (SwRI) in San Antonio, Texas. The SwRI project team efforts included all cycle modeling, material evaluation and testing, redesign analysis efforts, loop design, and economic modeling. Solar Turbines, Incorporated (San Diego, California) was a cost share partner, providing Mercury 50 recuperator design information as in-kind cost share for this project.

5. REFERENCES

[1] http://www.bls.gov/oes/current/oes514121.htm.

[2] http://www.bls.gov/ooh/architecture-and-engineering/mechanical-engineering-technicians.htm.

[3] Economist Intelligence Unit: Natural Gas (US$/mBtu), http://knoema.com/ncszerf/natural-gas-prices-long-term-forecast-to-2020-data-and-charts.

[4] Setlak, S. J., 2002, "Aerospace Structural Metals Handbook," Edition: 39.1.

[5] CRS Holdings Inc., 2006, "An Overview of Carpenter's High-Temperature Alloys," Source: www.cartech.com.

[6] Special Metal Corp, 2008, "Product Handbook of High-Performance Alloys," Source: www.specialmetals.com.

[7] High Temp Metals, Accessed Dec. 2014, "High Temp Metals Data Library," Source: www.hightempmetals.com/technicaldata.php.

[8] High Performance Alloys Inc., 2007, "High Temperature Alloys," Source: www.hpalloy.com/alloys/hightemperature.html.

[9] Haynes International, Accessed Dec. 2014, "High-Temperature Alloys," Source: www.haynesintl.com/htalloys.htm.

[10] Altemp Alloys, 2015, "Exotic, High Temperature Alloys & Super Alloys," Source: www.altempalloys.com/.

[11] Rolled Alloys, 2014, "Nickel Alloys," Source: www.rolledalloys.com/alloys/nickel-alloys/.

[12] Nickel Institute, 2011, "Nickel-Containing Materials – Properties," Source: www.nickelinstitute.org/NickelUseInSociety/MaterialsSelectionAndUse/Ni-ContainingMaterialsProperties.

[13] Mahaffey, J., Kalra, A., Anderson, M., Sridharan, K., Sept. 2014, "Materials Corrosion in High Temperature Supercritical Carbon Dioxide," The 4th International Symposium – Supercritical CO_2 Power Cycles.

[14] de Barbadillo, J. J., Baker, B. A., Gollihue, R. D., Sept. 2014, "Nickel-Based Superalloys for Advanced Power Systems – An Alloy Producer's Perspective," The 4th International Symposium – Supercritical CO_2 Power Cycles.

[15] Wright, I. G., Pint, B. A., Shingledecker, J. P., Thimsen, D., June 2013, "Materials Considerations for Supercritical CO_2 Turbine Cycles," Proceedings of ASME Turbo Expo 2013: Turbine Technical Conference and Exposition.

[16] Lee, H. J., Kim, H., Jang, C., Sept. 2014, "Compatibility of Candidate Structural Materials in High-Temperature S-CO_2 Environment," The 4th International Symposium – Supercritical CO_2 Power Cycles.

[17] Pint, B. A., Keiser, J. R., Sept. 2014, "The Effect of Temperature on the sCO_2 Compatibility of Conventional Structural Alloys," The 4th International Symposium – Supercritical CO_2 Power Cycles.

[18] Saari, H., Parks, C., Petrusenko, R., Maybee, B., Zanganeh, K., Sept. 2014, "Corrosion Testing of High Temperature Materials in Supercritical Carbon Dioxide," The 4th International Symposium – Supercritical CO_2 Power Cycles.

[19] Carlson, M., Conboy, T., Fleming, D., Pasch, J., June 2014, Scaling Considerations for SCO_2 Cycle Heat Exchangers, Proceedings of ASME Turbo Expo 2014: Turbine Technical Conference and Exposition.

[20] Rowlands, P. C., Garrett, J. C. P., Popple, L. A., Whittaker, A., Hoaskey, A., "The Oxidation Performance of Magnox and Advanced Gas-cooled Reactor Steels in High Pressure CO_2", Nuclear Energy, 25, 267-275 (1986).

[21] Courtesy of Solar Turbines, Incorporated.

[22] Abdulbasit, G. A., 2012, "Modeling of Fluid Flow in 2D Triangular, Sinusoidal, and Square Corrugated Channels," World Academy of Science, Engineering, and Technology, 6.

[23] Mylavarupu, S., 2011, "Design, Fabrication, Performance Testing, and Modeling of Diffusion Bonded Compact Heat Exchangers in a High-Temperature Helium Test Facility," Ph.D. Thesis, The Ohio State University.

[24] Agnew S. R., Liu K. C., Kenik E. A., Viswanathan S., January 2000, "Tensile and Compressive Creep Behavior of Die Cast Magnesium Alloy AM60B".

[25] Pint B. A., Brese, R. G., Keiser, J. R., March 2016a, "The Effect of O_2 and H_2O on Oxidation in CO_2 at 700°-800°C," The 5th International Symposium – Supercritical CO_2 Power Cycles.

[26] Pint B. A., Brese, R. G., Keiser, J. R., March 2016b, "The Effect of Temperature and Pressure on Supercritical CO_2 Compatibility of Conventional Structural Alloys," The 5th International Symposium – Supercritical CO_2 Power Cycles.

[27] Floreen, S., Fuchs, G. E., Yang, W. J., 1996, "The Metallurgy of Alloy 625," The Minerals, Metals & Materials Society.

6. APPENDIX A – sCO_2 SYMPOSIUM MATERIALS TESTING IN HIGH TEMPERATURE CO_2 POSTER

Comparative Testing of High Temperature Alloys for Supercritical CO_2 Applications: A Preliminary Evaluation

Larry Miller, Tim Allison, Todd Mintz and Abraham Mata (Southwest Research Institute)

Abstract

Increased interest in the use of sCO_2 as the working fluid in high-efficiency power cycles has created a need for new material testing parameters for the high-temperature materials available for use in the associated systems. The temperature ranges required for desirable high-efficiency sCO_2 cycles and the corrosive properties of the CO_2 fluid to which uncooled system components are exposed differ dramatically from that of the typical air-Brayton cycles that are commonly used today. Material properties and corrosion data for materials at these higher temperatures in a CO_2 environment are sparse and incomplete. This paper presents a look at the initial weight gain characteristics of some common high-temperature alloys and some high-temperature coating materials for a low-pressure CO_2 oxy-fuel Brayton cycle recuperator operating at 820° C. Although the near-atmospheric test pressure is significantly below sCO_2 cycle pressures, some components in sCO_2 applications may see high-temperature low-pressure CO_2 (e.g. advanced shaft-end seals) and comparative low-pressure results may provide insight into high-pressure behavior. The weight gain of each material is compared to Inconel 625 as this material is used in an existing air-Brayton cycle recuperator used as the baseline design for the low-pressure CO_2 Brayton cycle. The work presented in this paper only covers the first few hours of exposure and weight gain of these materials, but it does offer an initial look at the material behaviors and sets the stage for future long term testing in CO_2 environments and at the relevant temperatures for CO_2 and sCO_2 cycles.

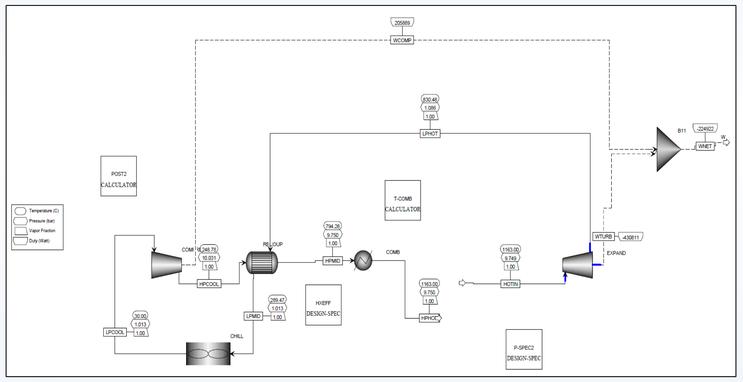

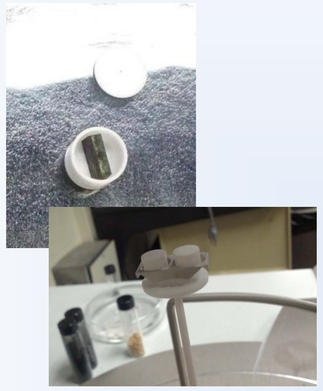

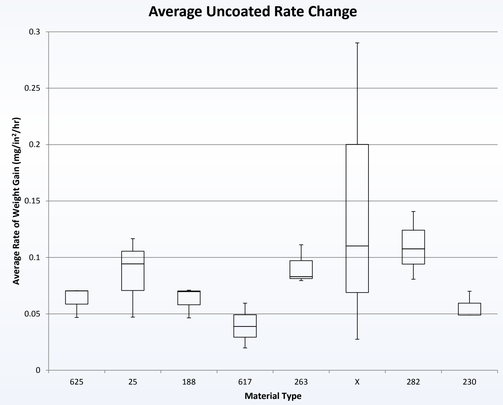

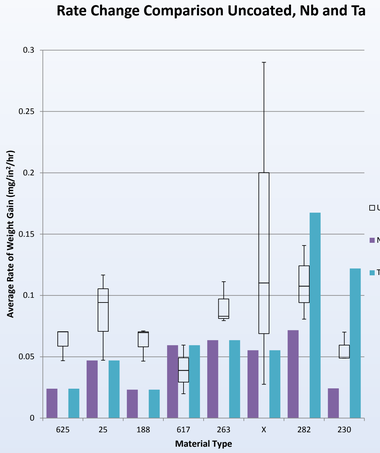

Results

Initial results show that alloys 188, 617 and 230 have rates of weight gain equal to or less than alloy 625, while alloys 25, 263, X and 282 may have higher weight gain rates. Standard deviations for these results are very high due to the small number of runs, which may not allow the discounting of any materials when moving forward with future testing.

SEM views of the 625 and 282 samples show initial oxidation and/or carburization as well as intergranular attack.

Tantalum coated samples showed higher rates than the uncoated samples in three materials (617, 282 and 230), while rates of niobium coated samples were all lower except with alloy 617.

Only one run was performed with each coated sample, so no statistical significance can be applied to these results.

Equipment

Test runs were carried out on a Netzsch model STA 449 F3 Jupiter Thermal Gravimetric Analyzer (or TGA).

Initial and final weights were recorded on a calibrated and conditioned Pinnacle Balance model # PI-225D.

Item: STA 449 F3 Jupiter – Simultaneous Thermal Analyzer TGA DSC
▪ Temperature range: -150°C to 2400°C
▪ Heating and cooling rates: 0.001 K/min to 50 K/min (dependent on furnace)
▪ Weighing range: 1 ug to 35 g
▪ TG resolution: 0,1 µg (over entire weighing range)
▪ DSC resolution < 1 µW (dependent on sensor)
▪ Measuring Range Cp measuring range: 0 to 5 J/(g*K)
▪ Atmospheres: inert, oxidizing, reducing, static, dynamic
▪ Switch valve for 2 purge gases and 1 protective gas
▪ Mass flow control for 3 gas channels (optional)
▪ Vacuum-tight assembly up to 10^{-4} mbar
▪ TGA-DSC and TGA-DTA sample carriers for real simultaneous operation

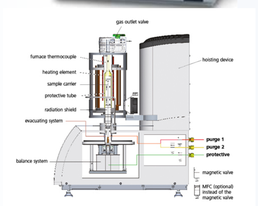

Materials

Eight different high temperature nickel alloys were evaluated. Each sample consisted of a 5mm x 3mm x 1mm cube.

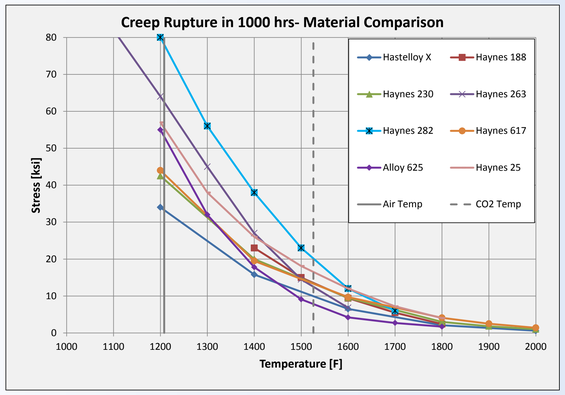

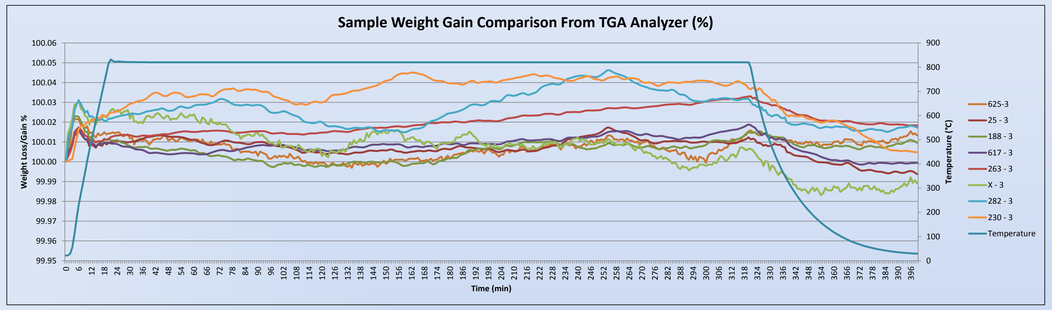

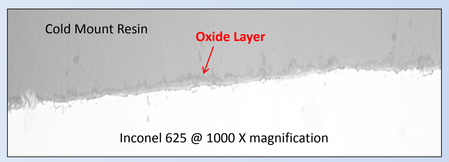

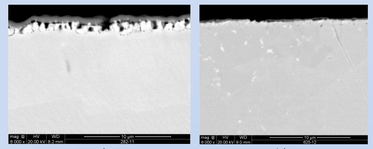

a) b)

Scanning Electron Microscope view of grain boundary attack on a) Haynes 282 and b) Inconel 625

Test Setup

Testing intended to be low cost, focused on oxidation rate of high-temperature alloys in a CO_2 environment.

Testing is comparative, measuring new materials against existing recuperator material (Alloy 625).

Three uncoated material runs performed and two coated material runs performed, one Niobium and one Tantalum.

Samples immersed in CO_2 environment at ambient pressure then heated at 40 ° C per minute up to 820° C where a five hour hold ensued. This was followed by a natural cool down back to ambient temperature.

Initial and final weights compared and weight gain rates (mg/in^2/hour) were calculated using surface area of each sample.

The calculated weight gain rates were compared to calculated rate for Inconel 625 samples.

Future Work

To refine this data, additional test runs can be performed to reduce the standard deviation and uncertainty.

Samples can be viewed with scanning electron microscopy (SEM) to determine the makeup of oxide layers formed in this environment.

Additional protective coatings can be tested with these base materials.

Longer term testing should be performed to identify oxidation rates and spalling/sluffing behavior over the expected life of the equipment.

Acknowledgement: "This material is based upon work supported by the Department of Energy under Award Number DE-FE0024104."

7. APPENDIX B – sCO_2 SYMPOSIUM MATERIALS TESTING IN HIGH TEMPERATURE CO_2 PAPER

The 5th International Symposium – Supercritical CO_2 Power Cycles
March 28-31, 2016, San Antonio, Texas

Comparative Testing of High Temperature Alloys for sCO_2 Applications: A Preliminary Evaluation

Larry Miller, Tim Allison, Todd Mintz, and Abraham Mata
Southwest Research Institute
San Antonio, TX

Abstract

Increased interest in the use of supercritical CO_2 (sCO_2) as the working fluid in high-efficiency power cycles has created a need for testing materials under high-temperature conditions used in the associated systems. The desired temperature range required for high-efficiency sCO_2 cycles differ dramatically from that of the typical air-Brayton cycles that are commonly used today. The temperature in these systems can be upwards of 820 °C. The system components exposed to this high temperature are uncooled and may undergo higher levels of corrosion or carburization. Corrosion data for materials at these higher temperatures in a CO_2 environment are sparse and incomplete. This paper presents a preliminary evaluation of the corrosion rate of some common high-temperature alloys and coating materials by monitoring the weight gain of these materials while being exposed to CO_2 at low pressure and 820 °C. Although the near-atmospheric test pressure is significantly below sCO_2 cycle pressures, some components in sCO_2 applications may see high-temperature low-pressure CO_2 (e.g. advanced shaft-end seals) and comparative low-pressure results may provide insight into high-pressure behavior. The weight gain of each material tested is compared to Haynes 625 as this material is already being used in existing air-Brayton cycle recuperators used as the baseline design for the low-pressure CO_2 Brayton cycle. The work presented in this paper only covers the first few hours of exposure and weight gain of these materials, but provides insight of how these materials behave. Furthermore, the work sets the stage for future long term testing in CO_2 environments and at the relevant temperatures for CO_2 and sCO_2 cycles.

Introduction

Interest in the use of supercritical CO_2 (sCO_2) as the working fluid in power generation cycles has risen dramatically in recent years due to the potential for high cycle efficiencies and compact heat exchangers and machinery. Heat exchangers in these cycles operate at high pressures, pressure differentials, and temperatures that may result in corrosion of metallic components. Although some sCO_2 corrosion data are available [Pint, Sept. 2014 (5)], additional corrosion testing at temperatures at or above 700°C is necessary to ensure long-term reliability of high-temperature power block components. Southwest Research Institute® is in the process of analyzing and redesigning a primary surface heat exchanger for use with a novel low-pressure CO_2 oxy-fuel Brayton cycle. This cycle, shown in Figure 1, maintains the pressures and turbine firing temperature of an existing industrial gas turbine, but achieves an efficiency above 47% with CO_2. This is significantly higher than the equivalent air Brayton cycle. Although the firing temperature is maintained, the turbine exit temperature is equal to 820 °C (1,508 °F), which is

higher than that of the existing air Brayton cycle. The goal of this redesign is to advance the existing recuperator design to operate in a high-temperature CO_2 environment at pressures up to 10 bar. A portion of this redesign effort involved short-term laboratory-scale testing on a variety of metal alloys and coatings in order to assess the risk of corrosion in the proposed cycle.

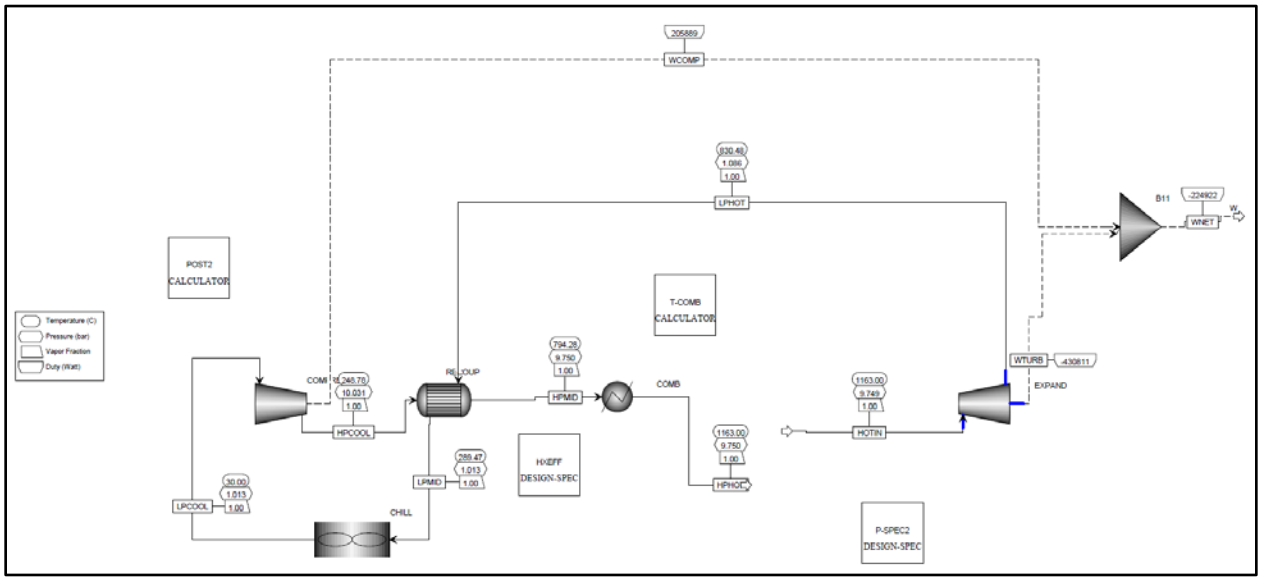

Figure 1. Recuperated Low-Pressure Oxy-Fuel CO_2 Brayton Cycle

An initial literature review was performed for the materials being tested which included a search for any information concerning operation at elevated temperatures in a CO_2 environment [Mahaffey, Sept. 2014 (1)]; [de Barbadillo, Sept. 2014 (2)]; [Wright, June 2013 (3)]; [Lee, Sept. 2014 (4)]; [Pint, Sept. 2014 (5)]; [Saari, Sept. 2014 (6)],. Currently, most material testing for sCO_2 applications has been performed at temperatures around 600 °C and at much higher pressures, thus information regarding the corrosion rates of materials in the higher temperature environments at low pressures is not readily available.

The testing presented in this paper, though short in duration, offers some insight into the comparative rate of initial corrosion/oxidation that can be expected between different types of high temperature materials when exposed to a CO_2 environment near 820 °C. This testing does not include any weight loss that might occur over long durations of exposure. Additional testing with a much longer duration would be required to understand the change in corrosion rate with time.

Materials

The materials used in this testing were selected with four criteria in mind. First, the materials had to have sufficient strength at high working temperature, specifically up to 820 °C. The material had to be easily procurable. The sheet rupture life at elevated temperatures needed to be sufficiently high to allow for a long operation life of the recuperator. Finally, the material had to have good formability, which was dependent upon its nickel content. Using these criteria, the extensive list of high-

temperature materials available on the market were narrowed down to the following 8 materials: Hastelloy X, Haynes 188, Haynes 230, Haynes 25, Haynes 263, Haynes 282, Haynes 617, and Haynes 625.

The test equipment selected for the performance of this testing uses crucibles that are 3 mm deep and have an inner diameter of only 5.75 mm (see Figure 2). To fit this available volume, the samples of each material were cut to approximately 5 mm x 3 mm x 1 mm cubes using a wire EDM machine. All samples used in the final testing results were deburred and polished with 600 grit sanding strips to obtain a uniform surface finish on all samples. To ensure the surface area of each sample was known, two measurements were made on each set of parallel faces and the averages of those measurements were used to calculate volumes and surface areas. Each sample was cleaned with acetone and DI water prior to testing to ensure no contamination was present on the samples.

Figure 2. Sample Measuring 3 mm x 5 mm x 1 mm Inside the Crucible

Test Setup

The test materials were exposed to the high temperature CO2 environment using a Thermogravimetric Analysis (TGA) method to measure weight loss/gain in an exposure environment. The weight loss/gain testing was performed using a Netzsch STA 449 F3 TGA machine with a silicon carbide furnace and alumina crucibles. An example of this equipment can be seen in Figure 3 with the actual test setup shown in Figure 4. Specifications for the STA 449 F3 are presented in Table 1. The silicon carbide furnace used has a maximum temperature of 1,600 °C and uses forced air as the cooling mechanism. The main focus of this testing was to view a comparative weight loss/gain for each of the subject material. Each material's weight loss/gain was compared to the original recuperator material, Haynes 625. A greater weight gain for one sample over such a short period could indicate a higher rate of oxidation for that material in the operating environment.

Background research into the possible oxidation and carburization rates of some of the materials being tested lead to an initial testing time of 5 hours [Special Metals Corp., March 2005 (8)]. It was assumed that this duration at the required temperature would allow enough oxidation to occur on each sample to allow for a meaningful weight gain/loss comparison with the chosen testing equipment.

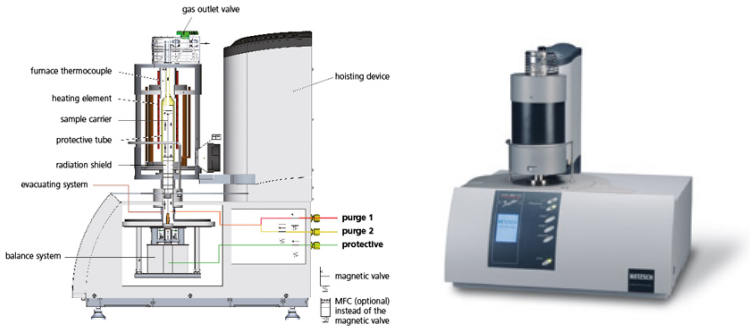

Figure 3. Jupiter 449 F3 TGA Machine Available on SwRI Campus

a. b.

Figure 4. a. and b. Sample Crucibles Mounted in Netzsch TGA Machine

Table 1: STA 449 F3 Technical Specifications

Item: STA 449 F3 Jupiter – Simultaneous Thermal Analyzer TGA DSC
Temperature range: -150°C to 2400°C
Heating and cooling rates: 0.001 K/min to 50 K/min (dependent on furnace)
Weighing range: 1 ug to 35 g
TG resolution: 0,1 µg (over entire weighing range)
DSC resolution < 1 µW (dependent on sensor)
Measuring Range Cp measuring range: 0 to 5 J/(g*K)
Atmospheres: inert, oxidizing, reducing, static, dynamic
Switch valve for 2 purge gases and 1 protective gas
Mass flow control for 3 gas channels (optional)
Vacuum-tight assembly up to 10^{-4} mbar
TGA-DSC and TGA-DTA sample carriers for real simultaneous operation

Three initial test runs were made with each material. These first runs were performed using the base material with no protective coating. A fourth run was performed with the base material coated with a layer of niobium, and a fifth run was performed with the base material coated with a layer of tantalum. The program used to test these samples provided an initial temperature ramp rate of 40 °C per minute

up to 820 °C. The temperature was then held at 820 °C for 5 hours, at which time the program was allowed to cool back to ambient temperature. The weight and temperature were recorded until the material had cooled back down to the set ambient temperature. An example of the results obtained from one of these tests can be seen in Figure 5.

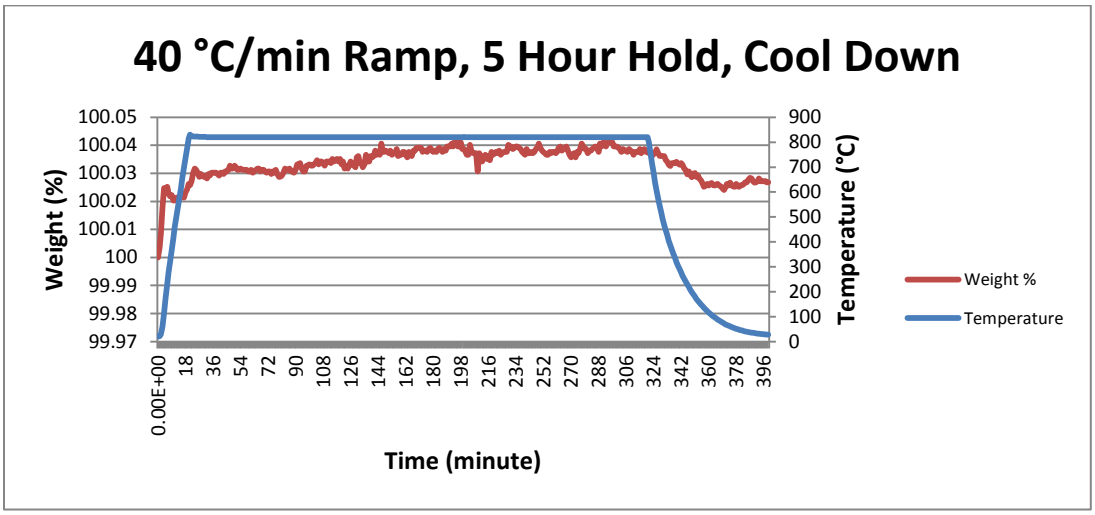

Figure 5. Test Program with 40 K/min Ramp Rate, 5 Hour Hold and Cool-down to Ambient

Initial runs with this program revealed anomalies which affected the weight measurements acquired from the TGA machine. Natural phenomenon, such as buoyancy effects, and inadequate sample preparation lead to large initial weight loss and intermittent negative weight gain readings with the TGA machine. To overcome these anomalies, sample preparation procedures were implemented which required a thorough cleaning of each sample with acetone and isopropyl alcohol prior to testing. In addition, pre and post weight measurements were made using a Pinnacle Balance by Denver Instruments, model PI-225D, which is calibrated and kept in a conditioned area, free of temperature swings external vibrations and high air circulation. With these procedural implementations the variability in sample data was greatly reduced. After testing and weight gain measurements, the samples were examined using high magnification and a Scanning Electron Microscope (SEM) with Energy-dispersive X-ray spectroscopy (EDS) to more fully understand how the material behaved in the exposure tests.

Results

The results obtained from the testing equipment showed weight loss/gain for each sample in mg and in weight % change. For initial comparison purposes the change in weight % for each sample was inserted into a single graph for each set of tests (see Figure 6). Though this graph gives some sense of how the materials react in the environment of interest, when compared to each other, minor anomalies can occur within the chamber that may affect the exact weight measurements obtained. In addition, the weight change comparison with the TGA raw data is not a true comparison between the individual samples because the surface area is not included as a parameter of weight change. Since the initial weight and size of each sample varied, the results needed to be converted to a form that was not biased

by these differences. To accomplish this, the weight loss/gain rates per surface area were calculate and compared. This rate was calculated using the initial measured weight and the final measured weight as these were deemed to be more accurate than the TGA readout. The initial and final measured weights were measured using the same scale, the PI-225D Pinnacle Balance.

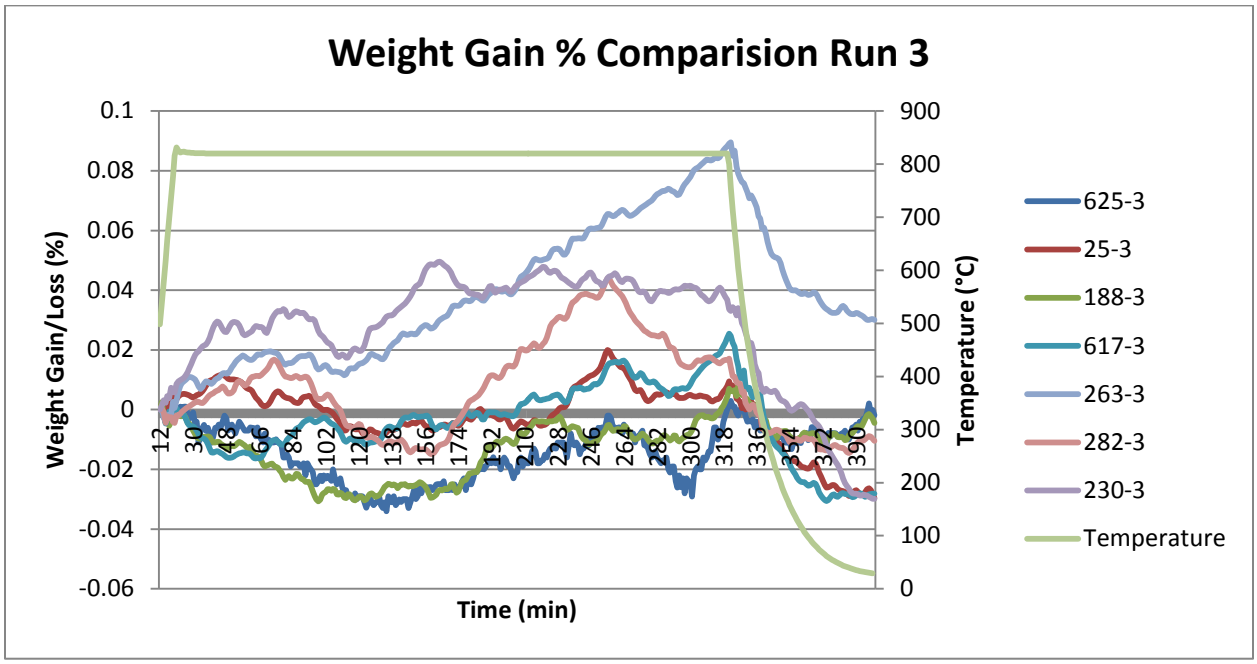

Figure 6. Weight gain profile comparison of each material tested in Run -3

Figure 7 shows the average rate changes in milligrams per in^2 per hour and the standard deviations for each material in the three uncoated test runs. The results of these runs showed that alloys 188, 617 and 230 have weight gain rates equal to or less than alloy 625.Alloys 25, 263, X and 282 had higher initial weight gain rates. However the standard deviation with these three runs is quite high. The large standard deviations arise from the large variation in weight gain seen between the three initial runs. More runs of each material would need to be made before ruling out any of these materials for future use. Also, though the results of this testing show that alloys 25, 263, X and 282 have a much higher initial (5 hour) oxidation rate, the long term oxidation rate of some of these materials may still be acceptable making them a viable option moving forward. Of course the viability of each of these materials also depends on cost and on the individual mechanical properties of each material.

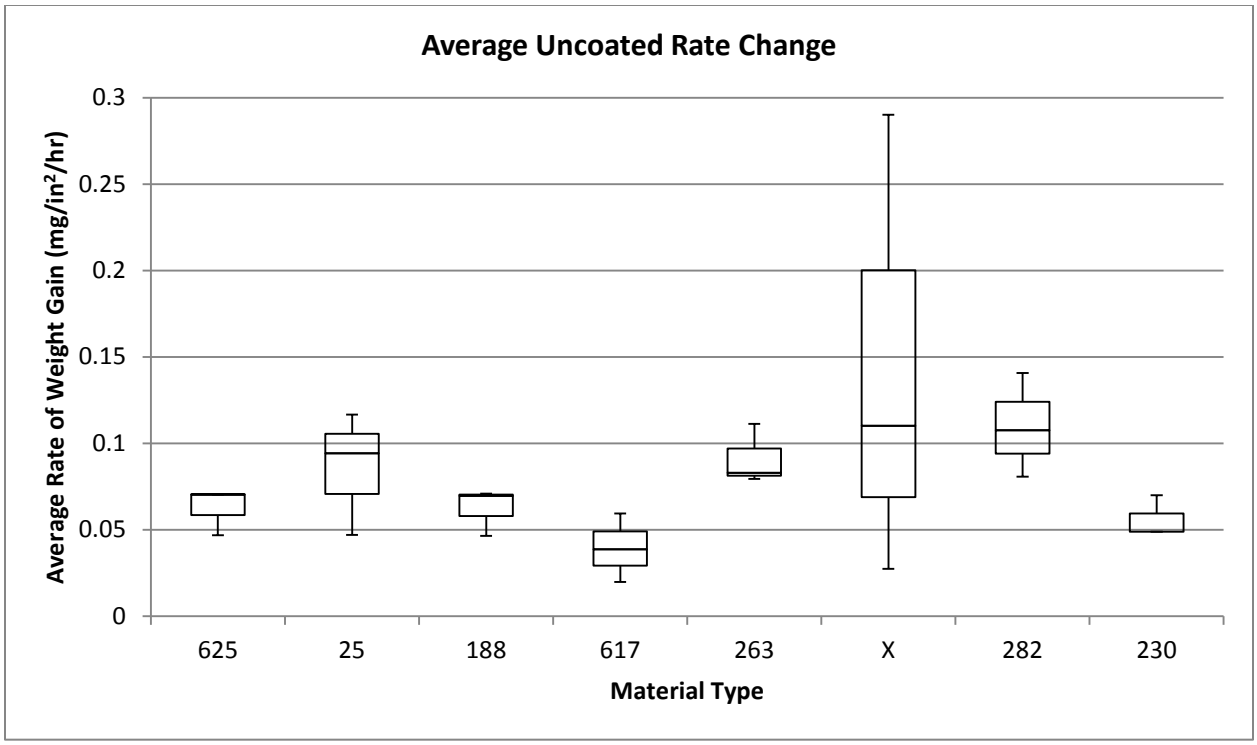

Figure 7. Average weight change with standard deviations

High magnification images were taken of some of the samples in an effort to measure the thickness of the oxidation layer on the samples. Figure 8 shows the oxidation layer on one of the alloy625 samples. Typical oxidation layer thicknesses measured via visual magnification ranged from around 0.5 microns up to 2 microns. Using these oxide layer thicknesses and the surface area of the samples, and assuming most of the oxidation is a Chromium(III) Oxide (Cr_2O_3), the minimum and maximum weight gain for several samples were calculated and compared to the measured weight gains. The measured weight gains for all the samples were within these calculated values.

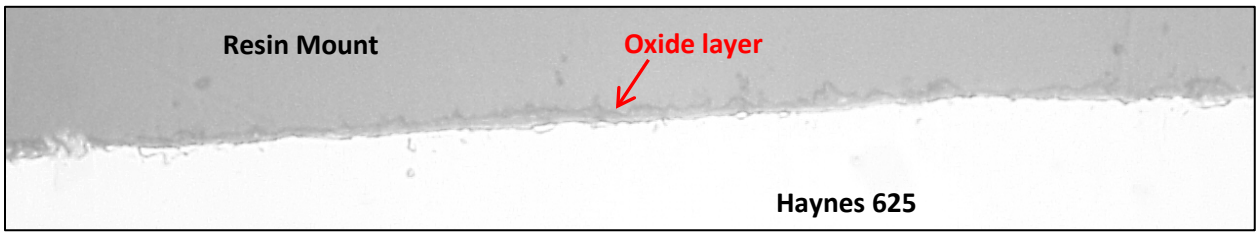

Figure 8. 1000X magnification of 625 oxidation layer

The Haynes 625 and Haynes 282 samples were also viewed using Scanning Electron Microscopy (SEM). The results of these scans are still being evaluated. However the images from these scans clearly show some form of intergranular attack occurring on the Haynes 282 sample with a more modest grain boundary attack on the Haynes 625 (Figure 9).

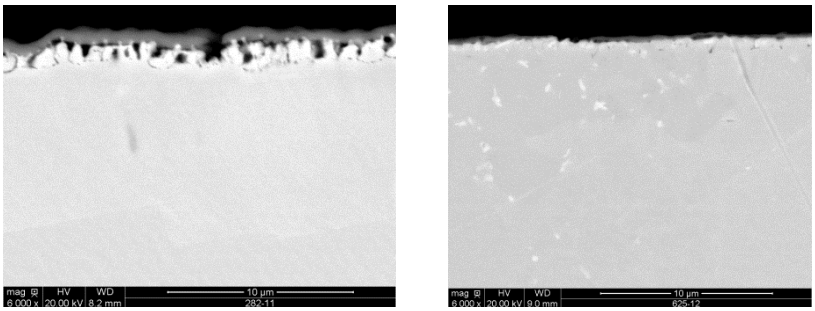

a) b)

Figure 9. SEM view of intergranular attack on a) Haynes 282 and b) Haynes 625

Two sets of test samples with protective coatings were prepared for additional testing. The first set of materials was coated with niobium and the second set was coated with tantalum. The deposition process used on these samples was a Plasma Vapor Deposition . These samples were tested using the same weight balance and TGA equipment that was used for the uncoated tests. Figure 10 shows the weight gain comparison between the uncoated, niobium coated, and tantalum coated samples.

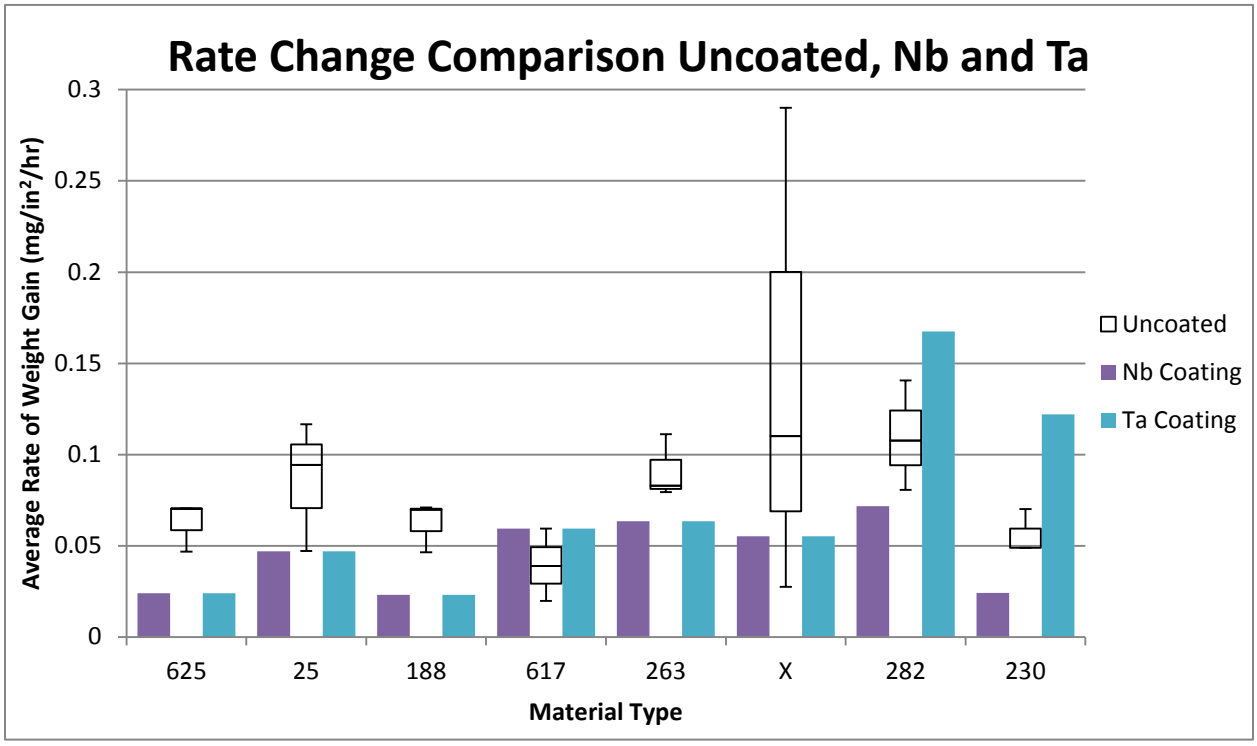

Figure 10. Weight Gain Rate Comparison for Average Uncoated, Niobium Coated and Tantalum Coated Samples

The results of this comparison show that the tantalum coated samples appear to have a higher rate of weight gain on alloys 617, 282 and 230, whereas the niobium coated samples show decreased weight gain rates in seven of the eight samples with the only increased rate of weight gain occurring in alloy 617. These results are, however, from only one run of the niobium and tantalum samples, and thus no statistical significance can be associated with these results.

From the results of the short exposure tests, it would appear that when compared to the 625 alloy, alloys 188, 617 and 230 appear to have corrosion properties that suggest they may be good candidates for use in the high temperature CO_2 recuperator. However the mechanical properties, cost, and availability of the material still need to be considered. In addition, it would appear that the use of niobium and tantalum coatings may be beneficial and effectively expand the list of usable materials in this environment.

It must be kept in mind that this testing provides only a comparative view of the initial weight change rate of these materials (five hours) while this equipment is expected to run for thousands or even hundreds of thousands of hours. In addition, some of these initial rates of weight gain may decrease drastically with time while others may remain high leading to a much shorter life under these conditions. An example diagram of oxidation leading to breakaway is presented in Figure 11. As can been seen in the figure, to fully understand how any of these materials would perform for the life of the recuperator, testing should be performed for a much longer time frame (typically 10,000 or 100,000 hours) in this environment and material boundary effects should be investigated.

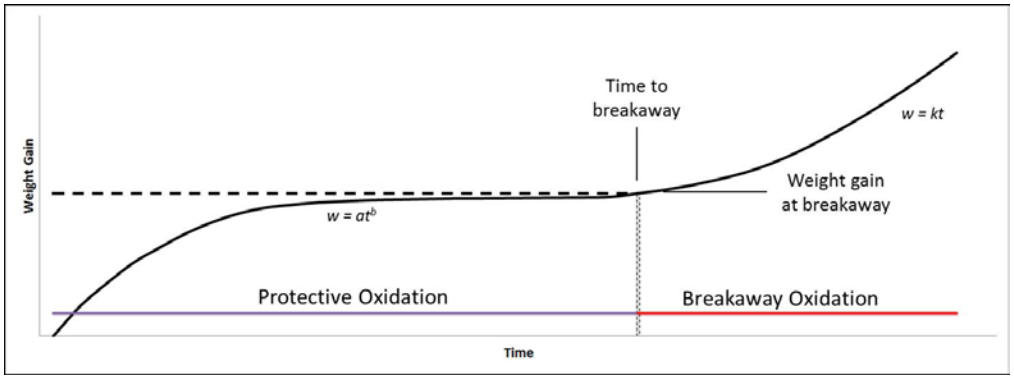

Figure 11. Diagram of Oxidation Leading to Breakaway Growth [Rowlands (7)]

Future Work

There are still a number of unanswered questions that remain after conducting this preliminary evaluation of materials that may be used in a CO_2 Brayton cycle. To provide additional insight into how the materials behave in this environment, additional test runs with these same materials can be performed to reduce the size of the standard deviation and provide a more accurate assessment of the degradation rate. An additional item that would be beneficial is to examine the current samples tested and further determine the type of oxides forming on each of these materials in a low pressure CO_2 environment at elevated temperatures. This may provide more insight into the degradation mechanism and help predict how the materials would degrade in the high temperature CO_2 and sCO_2 environments of interest. Additional testing could also be performed with protective coatings including the Niobium and Tantalum that were presented here, but also including other protective coatings that may improve corrosion rates of base materials (chromes, ceramics, etc.).

Finally, to gain a better understand of how these materials will act over the life of the recuperator, longer term testing of these materials should be performed. These long term tests could provide a map the oxidation rates over the expected life of the recuperator and would show which materials were susceptible to spalling or sluffing off of the protective oxidation layer, which occurred after 1,500 hours in other testing with similar materials [Gibbs, June 2011 (9)].

Acknowledgement

"This material is based upon work supported by the Department of Energy under Award Number DE-FE0024104."

Disclaimer

References

[1] Mahaffey, J., Kalra, A., Anderson, M., Sridharan, K., Sept. 2014, “Materials Corrosion in High Temperature Supercritical Carbon Dioxide,” The 4th International Symposium – Supercritical CO_2 Power Cycles.

[2] de Barbadillo, J. J., Baker, B. A., Gollihue, R. D., Sept. 2014, “Nickel-Based Superalloys for Advanced Power Systems – An Alloy Producer’s Perspective,” The 4th International Symposium – Supercritical CO_2 Power Cycles.

[3] Wright, I. G., Pint, B. A., Shingledecker, J. P., Thimsen, D., June 2013, “Materials Considerations for Supercritical CO_2 Turbine Cycles,” Proceedings of ASME Turbo Expo 2013: Turbine Technical Conference and Exposition.

[4] Lee, H. J., Kim, H., Jang, C., Sept. 2014, “Compatibility of Candidate Structural Materials in High-Temperature S-CO_2 Environment,” The 4th International Symposium – Supercritical CO_2 Power Cycles.

[5] Pint, B. A., Keiser, J. R., Sept. 2014, “The Effect of Temperature on the sCO_2 Compatibility of Conventional Structural Alloys,” The 4th International Symposium – Supercritical CO_2 Power Cycles.

[6] Saari, H., Parks, C., Petrusenko, R., Maybee, B., Zanganeh, K., Sept. 2014, "Corrosion Testing of High Temperature Materials in Supercritical Carbon Dioxide," The 4th International Symposium – Supercritical CO_2 Power Cycles.

[7] Rowlands, P. C., Garrett, J. C. P., Popple, L. A., Whittaker, A., Hoaskey, A., "The Oxidation Performance of Magnox and Advanced Gas-cooled Reactor Steels in High Pressure CO_2", Nuclear Energy, 25, 267-275 (1986).

[8] Special Metal Corp, March 2005, "Publication Number SMC-029, Inconel® Alloy 617," Source: www.specialmetals.com.

[9] Gibbs, J., June 2010, "Corrosion of Various Engineering Alloys in Supercritical Carbon Dioxide," Massachusetts Institute of Technology.